DEVELOPMENT OF HIGH-PERFORMANCE CATALYST-COATED MEMBRANES FOR PRESSURE-DIFFERENTIAL PROTON EXCHANGE MEMBRANE WATER ELECTROLYSERS

By

Dehua Hou

A thesis submitted to the

University of Birmingham

for the degree of

DOCTOR OF PHILOSOPHY

School of Chemical Engineering

College of Engineering and Physical Sciences

University of Birmingham

January 2025

Abstract

The proton exchange membrane water electrolysis (PEMWE) has emerged as a key technology in sustainable hydrogen production, offering high efficiency and integration potential with renewable energy systems. The catalyst-coated membrane (CCM) serves as the core component of PEMWEs, and the development of high-power performance CCMs is critical for enabling large-scale commercial deployment of this technology. This PhD research systematically investigates the optimisation of testing protocols, CCM fabrication processes, and hydrogen crossover mitigation strategies to address the challenges associated with proton exchange membrane water electrolysers under differential pressure conditions.

Initially, the research focuses on establishing a standard testing protocol to ensure consistent and reliable evaluation of CCMs. This involves investigating the influence of the geometric area and assembly force during the assembly of the testing cell, as well as optimising key operational parameters, including water flow rates, clamping forces and conditioning procedures. Following the optimisation of the testing protocol, materials used for the PEMWE single cell are explored, including membranes, porous transport layers, catalysts, and ionomers. After material selection, CCM fabrication processes are further studied, from the catalyst ink formulation and processing to spray-coating techniques and hot pressing procedures. This optimisation significantly improves CCM performance. The optimised CCMs surpass the DOE's 2022 targets, making progress toward the ambitious goals set for 2026.

Building upon this foundation, a key innovation of this work is the introduction of a platinum functional layer at the anode/membrane interface, deposited via sputter

coating, to mitigate hydrogen crossover. Experimental results demonstrate a 73% reduction in hydrogen crossover at atmospheric pressure and a 66% reduction at 10 bar differential pressure, highlighting the layer's effectiveness across varying operating pressures. To further understand hydrogen permeation mechanisms, a diffusion-based qualitative analysis model is developed to provide theoretical insights into the influence of functional layer placement and gas transport properties. Furthermore, accelerated stress tests are designed to simulate dynamic load conditions to evaluate the durability of the functional layer for PEMWEs under differential pressures. The tests confirm the robustness of the functional layer, which retains 94% of its hydrogen crossover mitigation capability at 0.25 A/cm^2 and 99% at 2.50 A/cm^2 after the equivalent of 100 hours of operation.

Acknowledgment

After years of study, I have finally arrived at this milestone. I have never considered myself particularly gifted; my abilities are modest, and my knowledge limited. But regardless, I have reached this point.

First and foremost, I want to extend my deepest gratitude to my supervisor, Professor Du. It has been an honour to undertake my doctoral research under his guidance. His unwavering support both academically and personally has been invaluable and cannot be fully expressed in words.

I am also profoundly grateful to my parents. Their sacrifices and unconditional support have made this journey possible, and for that, I remain deeply indebted. Each time I reflect on their dedication, I am reminded that no words or actions could ever truly repay such kindness.

To my friends, Yang, Yichang, Elvin, Bernardo, Kun, James, Millon, Jinxin, Jingze, and Kelly, thank you for accompanying this path with me. Your companionship has made this journey far less solitary, and I consider myself fortunate to have walked alongside you. I once read that names inscribed together stand the test of time. I want to write your name here to acknowledge how much you mean to me.

Finally, to myself, I hope you can be braver in the following journey.

List of publications

Peer-reviewed Journal Papers

1. **Dehua Hou**, Shangfeng Du, Current status and challenges in high-differential pressure proton exchange membrane water electrolysis, *Under preparation*
2. **Dehua Hou** , Geng Qiao , Liqiu Liu , Xiaoqiang Zhang , Yichang Yan and Shangfeng Du, Challenges in scaling up testing of catalyst coated membranes for proton exchange membrane water electrolyzers. Front Energy Res 13 (2025) 1557069. https://doi.org/10.3389/FENRG.2025.1557069/BIBTEX.
3. **Dehua Hou**, Liqiu Liu, Geng Qiao, Xiaoqiang Zhang, Yichang Yan, Yang Li, Shangfeng Du, Platinum functional layer for hydrogen crossover mitigation in proton exchange membrane water electrolysers. Chemical Engineering Journal 512 (2025) 162524. https://doi.org/10.1016/J.CEJ.2025.162524.

Peer-reviewed Conference Papers

1. Geng Qiao, Chaomurilige, Gaoqun Zhang and **Dehua Hou**, Materials study for proton exchange membrane water electorlyzers for hydrogen production with intermittent renewable power, The 8th International Conference on Energy and Environmental Science (ICEES 2024), Chongqing, China, 5-7 January, 2024.
2. Alexandra Brochoire, **Dehua Hou**, Shangfeng Du, Exploring facile oxygen evolution reaction one-dimensional catalyst synthesis using K_2PtCl_6, The Electrochemical Society PRiME 2024, Honolulu, United States, 6-11 October, 2024.
3. Aurimas Turkus, Vahid Nasrollahi, **Dehua Hou**, Tahseen Jwad, Mitchell Leering, Sundar Marimuthu, Shangfeng Du, Stefan Dimov, Porous transport layers with novel design for performance improvements of PEM electrolysers, 7th World

Congress on Micro and Nano Manufacturing, Pattaya, Thailand, 16-19 September, 2024.

Conference Presentations

1. 'Evaluation of commercial materials for PEM water electrolysers'. 31th CSCST-SCI conference, Surrey, UK, 3-4 September, 2024, ***Oral presentation***.
2. 'Evaluation of commercial materials for proton exchange membrane water electrolyser'. Midlands green hydrogen community projects, Birmingham, UK, 10 April, 2024, ***Poster presentation***.
3. 'A study in commercial components for proton exchange membrane water electrolyser'. Early Career Development Network Conference, Birmingham, UK, 7 June, 2024, ***Poster presentation***.
4. 'Benchmark fabrication at MEA Level for PEM water electrolysis'. 2023 world fuel cell conference, London, UK, 11-13 December, 2023, ***Oral presentation***.
5. 'Iridium-based catalysts for Oxygen evolution reaction (OER) in PEMWE application'. 30th CSCST-SCI conference, London, UK, 6-7 September, 2023, ***Oral presentation***.
6. 'Benchmark commercial Iridium-based catalysts for proton exchange membrane water electrolysers'. 29th CSCST-SCI conference, Birmingham, UK, 6 September, 2022, ***Poster presentation***.

Table of contents

List of figures

List of tables

Abbreviations

PEMWE	Proton exchange membrane water electrolysis
MW	Megawatt
GW	Gigawatt
LHV	Lower heating value
AWE	Alkaline water electrolysis
AEMWE	Anion exchange membrane water electrolysis
SOEC	Solid oxide electrolysis cell
PEM	Proton exchange membrane
HER	Hydrogen evolution reaction
OER	Oxygen evolution reaction
BP	Bipolar plate
PTL	Porous transport layer
LEL	Lower explosive limit
UFL	upper flammability limit
AST	Accelerated stress testing
PFSA	Perfluorosulfonic acid
CL	Catalyst layer
GDL	Gas diffusion layer
LSV	Linear sweep voltammetry
CV	Cyclic voltammetry
GC	Gas chromatography
MS	Mass spectrometry (MS)
I/C	Ionomer-to-catalyst
SPSf	Sulfonated polysulfone
SPEEK	Sulfonated poly(ether ether ketone)
SPPs	Sulfonated poly(phenylene sulfone)
TPA	Tungstophosphoric acid
MEA	Membrane electrode assembly
CCM	Catalyst-coated membrane
CCS	Catalyst-coated substrate

DMD	Direct membrane deposition
SEM	Scanning electron microscopy
XCT	Micro-X-ray computed tomography
XRF	X-ray fluorescence mapping
DLS	Dynamic light scattering
IPA	Isopropanol
PTFE	Polytetrafluoroethylene
ECSA	Electrochemical surface area
EIS	Electrochemical impedance spectroscopy
OCV	Open-circuit voltage
TEM	Transmission Electron Microscope
ICP-MS	Inductively Coupled Plasma – Mass Spectrometry
XPS	X-ray Photoelectron Spectroscopy
NREL	National Renewable Energy Laboratory
GDE	Gas diffusion electrode

Chapter 1

Introduction

1 Introduction

The transition to renewable energy is essential for achieving carbon neutrality, but its intermittent nature and fluctuating output pose significant challenges for daily energy distribution and utilisation [1,2]. Hydrogen has emerged as a promising solution due to its ability to store excess renewable energy, serving as a flexible energy carrier. Currently, most hydrogen production relies on fossil fuels, with green hydrogen accounting for only a small fraction [3,4]. To address this gap, advanced technologies are needed to enable the efficient and sustainable production of green hydrogen. The proton exchange membrane water electrolysis (PEMWE) has garnered attention as a leading solution for producing green hydrogen, offering advantages such as high energy efficiency, compact design, and compatibility with renewable energy sources, making it particularly suitable for this green hydrogen production [(5)]. Moreover, PEMWE can operate under high differential pressures, which simplifies downstream processes by eliminating the need for additional compression stages [5–8]. This reduces energy losses and allows direct storage of high-density hydrogen, making PEMWE particularly advantageous for industrial applications and large-scale energy storage [9,10]. Additionally, the ability to produce pressurised hydrogen ensures seamless integration with existing hydrogen infrastructure, further highlighting its versatility for energy grids, transportation, and chemical industries.

Since its early development, the PEMWE technology has advanced significantly. The first pilot PEM water electrolysis plant was introduced in 2000, marking the beginning of commercialisation [11]. In 2013, Hydrogenics achieved a milestone by installing the first 1 MW-level PEMWE system, demonstrating the maturity of the technology for industrial applications. As a further step in this progress, it is reported that Linde will

start up the world's largest PEMWE plant by 2025, with a capacity of 35 MW. According to IRENA, the current focus is on scaling PEMWE technology from the megawatt (MW) level to the gigawatt (GW) level to meet growing industrial-scale hydrogen demand, targeting cost reductions below $200/kW, durability exceeding 50,000 operational hours, and efficiency improvements reaching 80% of lower heating value (LHV) [12,13]. The timeline of major developments in the application of PEMWE is illustrated in Figure 1.1. With its inherent advantages and the recent impressive achievements, PEMWE stands as a promising technology for driving the transition towards a hydrogen-based energy economy.

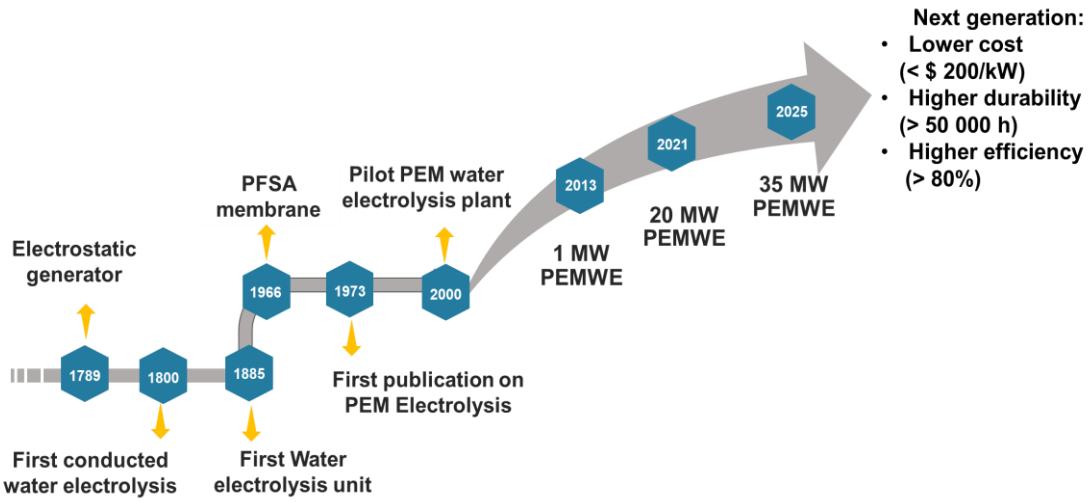

Figure 1.1 Timeline of major developments in the application of PEMWE [12,13].

1.1 Fundamental of water electrolysis

Water electrolysis is an electrochemical process that employs direct current to split water into hydrogen and oxygen gases. Based on operating temperature, it can be broadly categorised into low-temperature (below 100°C) and high-temperature techniques. Low-temperature methods include alkaline water electrolysis (AWE), anion exchange membrane water electrolysis (AEMWE), and proton exchange membrane water electrolysis (PEMWE), while high-temperature solid oxide electrolysis cell

(SOEC) operates at elevated temperatures. The typical schematics of these water electrolysis techniques are illustrated in Figure 1.2.

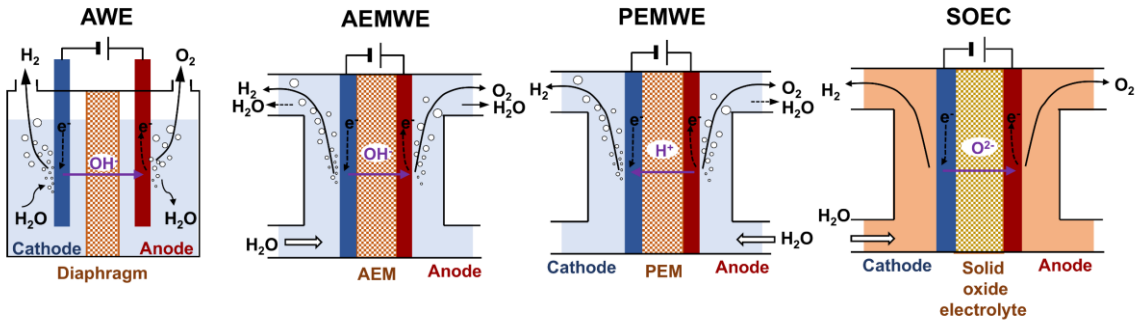

Figure 1.2 Schematics of different water electrolysis techniques.

Among these approaches, SOEC achieves the highest efficiency (75–85%) by operating at high temperatures, which reduces Gibbs free energy and lowers the thermoneutral voltage, thereby decreasing the electrical energy required for water splitting [14,15]. However, SOECs face challenges such as complex heat management, limited stability, and sluggish start-up times. Currently, SOEC technology remains at the laboratory scale, hindering its commercial application [16,17]. AWE, a mature and widely used technology, operates in an alkaline environment using a concentrated liquid electrolyte and a diaphragm to separate gases. It offers long-term stability and low catalyst costs but is limited by lower current densities, low hydrogen purity, and restricted operation under high pressure compared to PEMWE [18–20]. AEMWE builds on AWE by replacing the diaphragm with an anion-conducting membrane, which reduces ohmic resistance and improves gas separation. Despite these advantages, the technology remains in the laboratory stage due to challenges such as limited membrane durability [21–23].

In contrast, PEMWE demonstrates distinct advantages in performance and durability. Its proton-conducting membrane exhibits significantly higher ionic conductivity than

hydroxide-conducting membranes, attributed to the greater intrinsic transport of protons (H^+) compared to hydroxide ions (OH^-) [24]. This characteristic enhances ion transport efficiency, resulting in current densities exceeding 2 A/cm^2, enabling rapid hydrogen production. Additionally, proton exchange membranes exhibit exceptional chemical and mechanical stability, which extends the system lifetime and ensures reliable performance under demanding operational conditions [25,26]. Beyond its high performance and stability, PEMWE is highly compatible with renewable energy sources. It can handle dynamic energy inputs across a wide load range, from partial loads (5%) to overloads (up to 150%) [17,25,27]. This flexibility allows PEMWE to maintain stable performance under the fluctuating and intermittent conditions characteristic of renewable energy, ensuring reliable hydrogen production [27–32].

Another standout feature of PEMWE is its capability to operate under high differential pressures. By working at a differential pressure up to 180 bar, PEMWE allows for the direct production of compressed hydrogen, effectively decreasing the energy required for external compression [33,34]. This not only simplifies system design but also reduces maintenance requirements and lowers operational costs. Operating at higher pressures facilitates hydrogen storage and distribution, further highlighting its suitability for industrial applications and large-scale energy storage [6,35,36].

The combined advantages of PEMWE, including efficient ion transport, high current density, adaptability to dynamic energy inputs and high-pressure operation, make it an exceptional technology for hydrogen production. This unique combination of features positions PEMWE as a cornerstone technology in the advancement of a hydrogen-based energy sector. The specifications of all water electrolysis techniques are summarised in Table 1-1.

Table 1-1 Characteristics of the four types of water electrolysers [8,12,37–39].

	AWE	AEMWE	PEMWE	SOEC
Maturity	Mature	Laboratory stage	Commercial	Laboratory stage
Electrolyte	KOH 5 ~ 7 M	DVB polymer	PFSA membrane	Yttria-stabilized Zirconia
Operating temperature [°C]	70 ~ 90	40 ~ 60	50 ~ 80	700 ~ 850
Operating Pressure [bar]	< 30	< 35	≤ 180	1
Nominal current density [A/cm^2]	0.2 ~ 0.8	0.2 ~ 2	1 ~ 3	0.3 ~ 1
Voltage range [V]	1.4 ~ 3	1.4 ~ 2	1.4 ~ 2.3	1 ~ 1.5
Efficiency LHV [%]	50 ~ 68	52 ~ 67	50 ~ 68	75 ~ 85
Stack costs 1MW [$/KW]	200 ~ 400	320 ~ 600	700 ~ 900	> 2,000
lifetime stack [h]	60,000	> 5,000	50,000 ~ 80,000	< 20,000

1.2 Principle of PEMWE

The PEM water electrolysers are characterised by a thin solid ion-conducting membrane, known as proton exchange membrane (PEM) or polymer electrolyte membrane. Figure 1.3 illustrates the structure of a PEM water electrolyser [40].

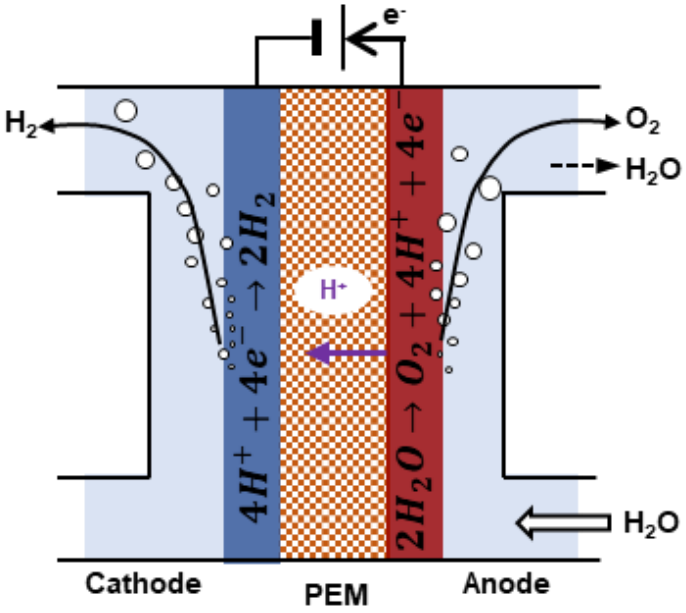

Figure 1.3 Schematic of the PEMWE with electrode reactions.

A PEM water electrolyser cell involves two key half-reactions: the hydrogen evolution reaction (HER) at the cathode and the oxygen evolution reaction (OER) at the anode [41,42]. The overall electrochemical reaction can be expressed as:

$$2H_2O(l) \rightarrow 2H_2(g) + O_2(g) \quad (1)$$

At the anode, water is split into protons and oxygen:

$$2H_2O \rightarrow O_2 + 4H^+ + 4e^-, \quad E_a^0 = 1.229\,V \quad (2)$$

Protons formed at the anode pass through the proton exchange membrane and move to the cathode, where the HER occurs:

$$4H^+ + 4e^- \rightarrow 2H_2, \qquad E_c^0 = 0.000\,V \quad (3)$$

Under standard conditions (T=25 °C; pressure=1 atm), the minimum voltage required for water splitting, known as the reversible cell voltage, is 1.23 V [43]. In PEMWE, HER involves a two-electron transfer process, making it kinetically faster than the four-

electron OER which has a higher energy barrier [38,44,45]. As a result, the OER acts as the rate-determining step, requiring a higher operational voltage to overcome this barrier. In practical applications, the actual voltage required for water splitting exceeds the reversible cell voltage due to several irreversible resistances within the electrolyser. The potential (η) can be categorised as activation resistances, ohmic resistances, and mass transfer resistances [25], all contributing to deviations from the thermodynamic equilibrium (Figure 1.4).

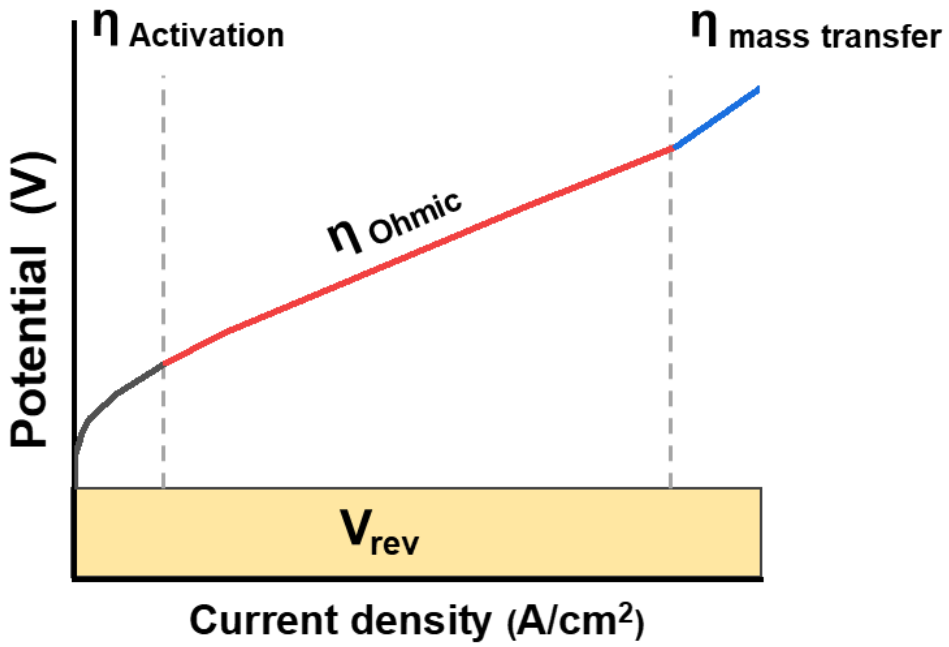

Figure 1.4 Potential with the dominated current density region with a typical polarisation curve for PEMWEs.

1) Activation resistance:

At low current density, activation dominates and represents the energy required to drive electrochemical reactions at the electrode surfaces [46]. This resistance, referred to as η_{act}, arises from both electrodes. However, the anode contributes significantly more to activation resistance due to the inherently sluggish OER kinetics, which is inherently more complex than the HER. The OER mechanism involves multiple reaction steps. A

widely accepted model introduced by Rossmeisl et al. describes this process as a series of four proton-electron transfer steps, as shown in Figure 1.5 [47,48]:

$$H_2O + * \rightleftharpoons H^+ + HO^* + e^- \quad \text{(Step 1)}$$

$$HO^* \rightleftharpoons H^+ + O^* + e^- \quad (Step\ 2)$$

$$O^* + H_2O \rightleftharpoons H^+ + HOO^* + e^- \quad (Step\ 3)$$

$$HOO^* \rightleftharpoons * + O_2 + e^- + H^+ \quad (Step\ 4)$$

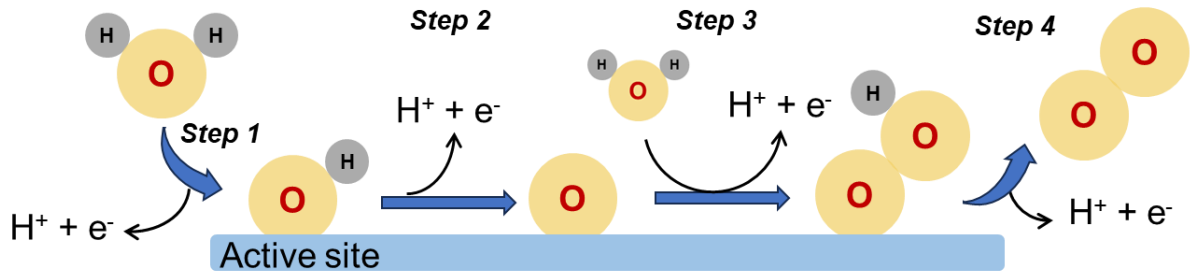

Figure 1.5 OER mechanism from Rossmeisl et al [47,48].

These reversible redox reactions occur on the catalyst surface, where the forward and reverse reaction rates are balanced at thermodynamic equilibrium, resulting in zero net current. This balance determines the exchange current density, which is influenced by the activation barrier. Reducing the activation barrier can increase the exchange current density. This can be achieved by raising the operating temperature or improving the quantity and quality of active reaction sites on the catalyst surface. Since different materials exhibit varying exchange current densities, the selection and optimisation of electrode materials are crucial for improving kinetics of reactions. Thus, developing high-performance catalysts with improved activity and durability is essential for reducing activation resistances, thereby boosting the overall performance of the electrolysers [42].

2) Ohmic resistance:

Ohmic resistance (η_{ohm}) occurs due to the resistance encountered by electrons moving through the electrodes and other components of the electrolyser, as well as protons crossing the membrane. This resistance follows Ohm's law, increasing proportionally with the applied current and becoming more significant at moderate current densities [46,49]. A key contributor to ohmic resistance is the membrane's resistance, which contributes substantially to potential loss, especially at higher current density [50]. While employing thinner membranes effectively reduces ohmic resistance, it increases hydrogen crossover, posing safety risks due to the flammability of hydrogen-oxygen mixtures, particularly under high differential pressure conditions [51].

Interfacial resistance, another critical factor, arises at the contact points between components due to imperfect contact or surface roughness [52]. Techniques such as optimising materials and applying surface coatings, such as gold or platinum, to bipolar plates (BPs) and porous transport layers (PTLs) have proven effective at reducing resistance while simultaneously improving component durability [53].

3) Mass transfer resistance:

At high current density, the reaction is mainly limited by the transport of reactants, as the reaction kinetics are extremely fast [54]. A high flow rate is required to ensure sufficient reactant supply. Mass transfer resistances (η_{mass}) can arise not only from insufficient reactant supply but also from the accumulation of excess produced gas. The gas bubbles generated during the operation can block the active sites, lowering the utilisation of catalysts, and obstructing the reactant transport channels, limiting the water supply. These effects intensify at high current densities, where bubble formation is more extensive. Furthermore, insufficient removal of hydrogen increases the risk of

hydrogen crossover [55].

As a result, optimising component design is essential to mitigating these resistances and improving power performance. In real condition, the actual cell voltage in a PEMWE exceeds the theoretical reversible cell voltage due to several irreversible resistances, expressed as follows [56]:

$$V_{cell} = V_{rev} + \eta_{act,anode} + \eta_{act,cathode} + \eta_{ohm} + \eta_{mass} \quad (4)$$

Where:

- $\eta_{act,anode}$ and $\eta_{act,cathode}$ are the activation resistances at the anode and cathode, respectively,
- η_{ohm} represents the ohmic resistances, and
- η_{mass} represents the mass transport resistances.

These resistances can be attributed to two main sources: catalyst performance and cell component design. Thus, the development of advanced electrocatalysts and the optimisation of cell components to mitigate these resistances are crucial steps in enhancing PEMWE performance.

However, as the application of differential pressure PEMWEs progresses, specific quantifications of how the differential pressure affects the activation, ohmic, and mass transport resistances remain underexplored. Current findings primarily focus on the general polarisation curve, where increased pressure is observed to reduce cell efficiency and increase cell potential [9,34,57,58]. The chapter 2 will delve into the specifics of cell components, highlighting the reported strategies for reducing these resistances and improving system performance.

1.3 Economic analysis of PEMWEs

To better understand the economic feasibility of water electrolysis technologies, it is essential to evaluate their associated costs relative to their efficiency. Figure 1.6 presents a comparative analysis of efficiency and costs for various electrolysis methods based on IRENA and DOE data [12,37,38]. SOEC demonstrates the highest efficiency, reaching 75% to 80%, with projections to exceed 90% by 2030. However, this high efficiency comes at a significant cost, with 1 MW stacks costing over $2000 per kW. AWE, one of the earliest developed technologies, offers a cost advantage of approximately $300 per kW but achieves the lowest efficiency, ranging from 50% to 68%, highlighting a clear trade-off between cost and performance. AEMWE, a hybrid technology that integrates the benefits of AWE and PEMWE, provides moderate efficiency and cost. Despite its promise, AEMWE remains in the research phase, with current efforts focusing on improving catalyst performance. Its practical application is still far from realization. Among all the technologies, PEMWE represents a balanced approach, with efficiencies ranging from 50% to 68%, combined with moderate costs. This technique demonstrates strong potential for improvement, with efficiencies anticipated to reach up to 80% by 2030. Compared to AWE, although PEMWE requires higher capital investment, its lower operating costs and greater hydrogen production rates make it economically competitive. The high hydrogen purity (> 99.9%) eliminates the need for additional purification steps, while its ability to operate under high differential pressure reduces the reliance on external compressors. Additionally, its long-term stability lowers maintenance costs, further enhancing its economic viability [8,39,59,60]. These advantages position PEMWE as the leading candidate among low-temperature electrolysis technologies.

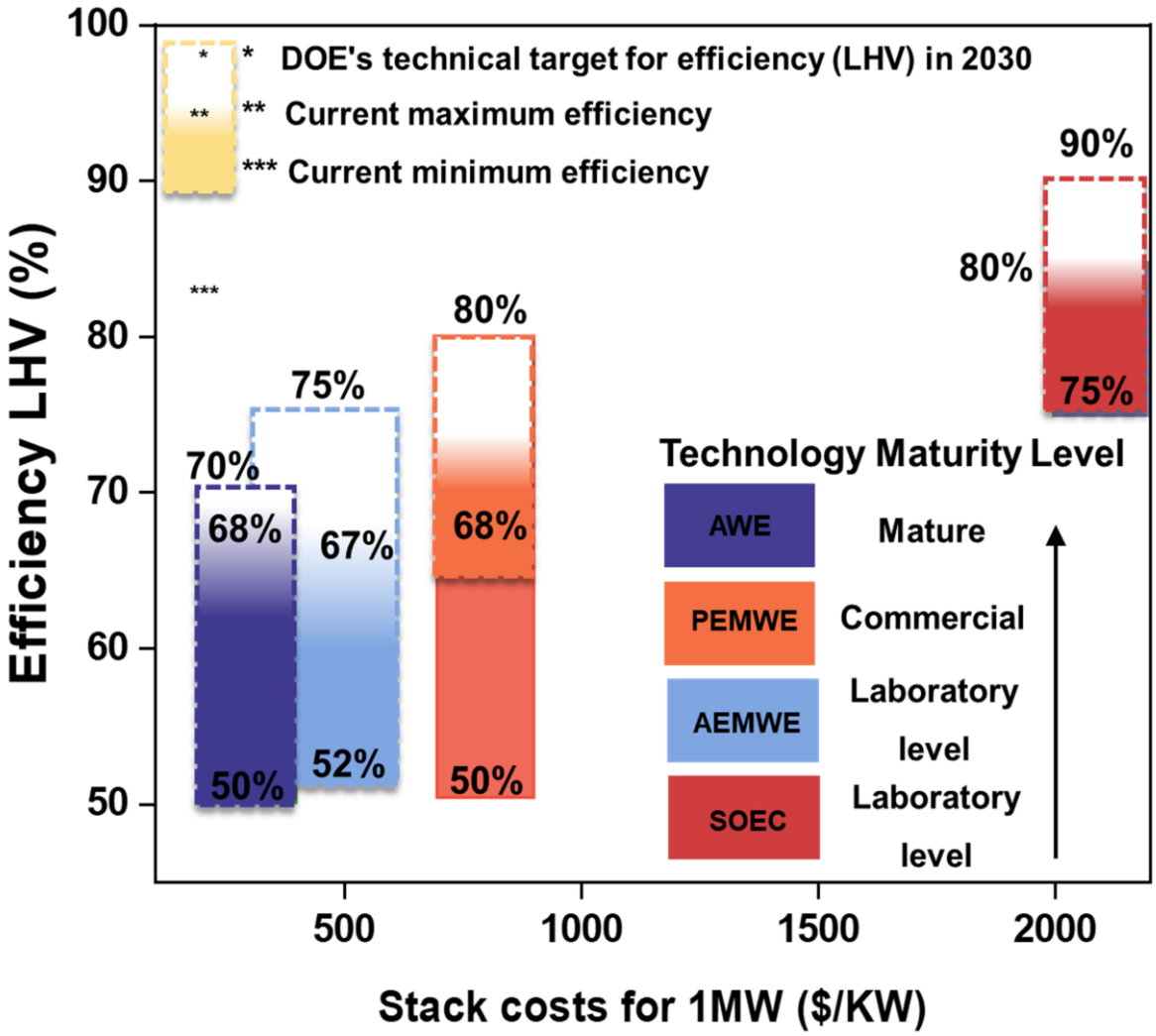

Figure 1.6 Cost comparison of water electrolysis technologies [12,37,38].

PEMWE demonstrates strong technical potential, and several advancements have been made in optimising key components like the catalyst-coated membrane (CCM), porous transport layers (PTLs), and bipolar plates (BPs). However, significant economic barriers continue to limit its feasibility for large-scale applications. The high cost of noble metal catalysts, coupled with the overall expense of these components, remains a substantial obstacle to the widespread adoption of this technology [61]. A detailed cost breakdown of PEMWE stacks (Figure 1.7) reveals that BPs and PTLs contribute 51% and 17% to the total cost, respectively, largely due to the reliance on

titanium-based materials. Meanwhile, the CCMs account for 23% of the stack cost, with its breakdown showing the membranes at 5%, catalysts at 8%, and fabrication processes comprising 10% [61–63]. These cost distributions highlight the importance of targeted strategies to reduce expenses, such as developing alternative materials for BPs and PTLs. Continued research and development are essential for lowering capital costs and improving the overall efficiency of the PEMWEs.

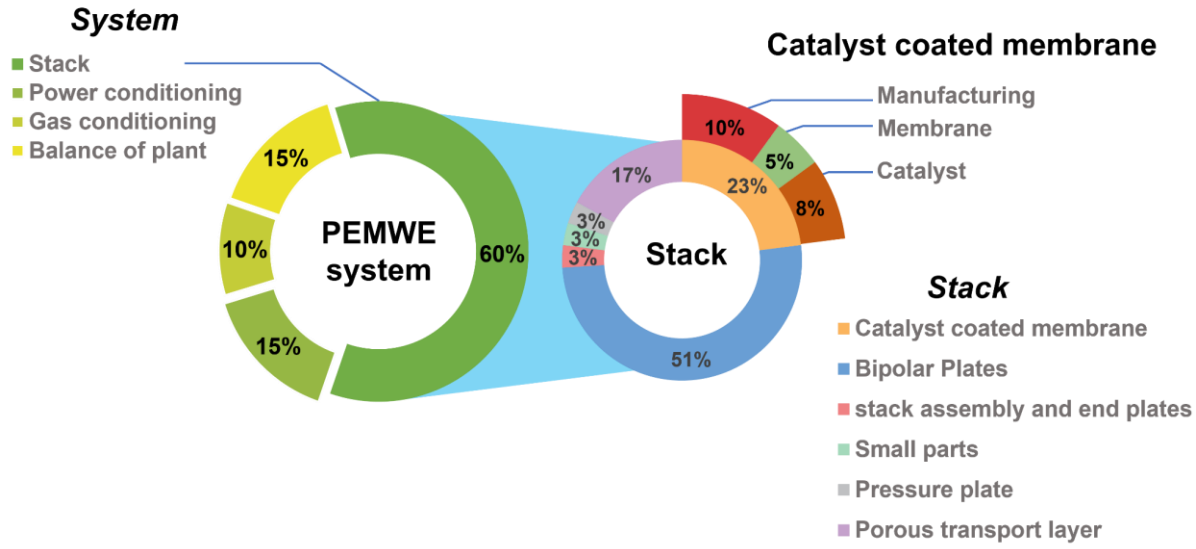

Figure 1.7 Scheme of a PEMWE system cost breakdown [61,62].

1.4 Challenges and Opportunities for PEMWE

Generally, PEMWE offers numerous advantages, but its drawbacks cannot be ignored. The challenging operating conditions of PEMWE significantly narrow the selection of suitable materials. PEMWE operates at extremely acidic conditions, with pH levels typically below 2. In addition to enduring such corrosive environments, the materials must be capable of withstanding high operation voltage (greater than 2 V) [17,26,38]. As a result, only materials with exceptional chemical stability and mechanical robustness are suitable for such demanding conditions. Thus, PEMWE systems heavily depend

on noble metal catalysts such as iridium and platinum for the CCMs, and corrosion-resistant materials like titanium are required for PTLs and BPs, significantly increasing overall system costs. Moreover, the adoption of fluorinated membranes increases costs while posing additional environmental and regulatory challenges.

In addition to these challenges are characteristic of the standard PEMWE system, operating under high differential pressure introduces additional advantages and challenges. The high differential pressures refer to a configuration where pressure is applied to the cathode while the anode operates at atmospheric pressure, resulting in asymmetric pressure conditions. One primary advantage of the high differential pressure PEMWE lies in its ability to produce high pressure hydrogen directly within the electrolyser, effectively reducing or eliminating the post-requirement for mechanical compressors and significantly lowering energy consumption [39]. Furthermore, high-pressure operation also enhances gas purity by facilitating water vapour condensation, minimising the need for additional drying processes [64].

However, high pressure conditions pose several challenges, primarily affecting system safety, component durability, and integration with renewable energy sources. The differential pressure across the membrane increases hydrogen crossover into the oxygen side, which becomes hazardous when hydrogen concentration exceeds 4 vol%, the lower explosive limit (LEL) for H_2 in O_2 gas [65–67]. The asymmetric high-pressure conditions also accelerate the degradation of main components, resulting in membrane rupture, corrosion of metal components such as BPs and PTLs [68,69]. Lastly, integrating high differential pressure PEMWE with renewable energy sources also introduces challenges in maintaining stable pressure and temperature under fluctuating power inputs [70–72].

1.5 Aims and Objectives

The aim of this thesis is to optimise the fabrication processes of catalyst-coated membranes for proton exchange membrane water electrolysers, with a particular focus on enabling safe and high-performance operation under differential pressure conditions. To achieve this, the objectives of the thesis are as follows:

- Establish a robust and reproducible test platform for evaluating PEMWE performance.
- Optimise CCM fabrication procedures, including catalyst ink formulation, spraying technique, and hot-pressing conditions.
- Develop and evaluate a platinum functional layer for mitigating hydrogen crossover.

1.6 Thesis overview

This thesis investigates the development and optimisation of PEMWEs under high differential pressure operations. **Chapter 1** provides an overview of the PEMWE fundamentals, including its key components, along with the advantages and challenges for high differential pressure operation. **Chapter 2** reviews recent advancements in addressing the impacts of high-pressure difference on the PEMWEs, highlighting mitigation strategies and potential pathways for future improvement. **Chapter 3** outlines the methodologies used for physical characterisation and single-cell testing, establishing a robust framework for experimental investigations. **Chapter 4** focuses on the assembly and optimisation of the testing setups, including both small-scale and large-scale configurations, to establish reliable benchmark conditions for subsequent studies. Following this, **Chapter 5** explores the systematic optimisation of the CCM fabrication processes, from the catalyst ink formulation to the ultrasonic

spray-coating process, ultimately establishing a reproducible benchmark fabrication method for high-performance CCMs. Building on these efforts, **Chapter 6** examines strategies for mitigating hydrogen crossover under high differential pressure operation, incorporating sputter coating techniques to introduce platinum interlayers that significantly reduce hydrogen permeability. Accelerated stress testing (AST) is employed to evaluate the long-term stability of these designs under realistic operational conditions, providing critical insights into their practical applicability. Finally, **Chapter 7** concludes the thesis by summarising the key findings and contributions while offering recommendations for future research directions.

Chapter 2

Literature review

The work presented in this chapter is unpublished at the time of writing.

2 Literature review

Chapter 1 provided an overview of PEMWEs, including the fundamental principles and the associated economic considerations. It highlighted the key challenges of PEMWEs and also discussed the opportunities for advancing this technology. These challenges underline the need for innovative solutions required to improve the efficiency and durability of PEMWEs, particularly under high differential pressure operating conditions. Thus, this chapter focuses on reviewing the latest developments and the remaining limitations of the key PEMWE components. The impact of high differential pressure operation on these components is then discussed in detail, along with the strategies to overcome the raised challenges. Finally, the strategies to fabricate high-performance CCM and mitigate hydrogen crossover are explored for addressing the existing shortcomings.

2.1 Basic component of PEMWEs

To achieve high energy efficiency PEMWEs, the optimisation of the key components is essential. The primary components of a PEMWE include bipolar plates (BPs), porous transport layers (PTLs), proton exchange membranes (PEMs), and electrocatalysts [26]. Each of these plays a critical role in the electrolysis process. In practical applications, individual cells are assembled into stacks to achieve high voltages and large amounts of gas production. Figure 2.1 illustrates the schematic of a PEMWE single cell.

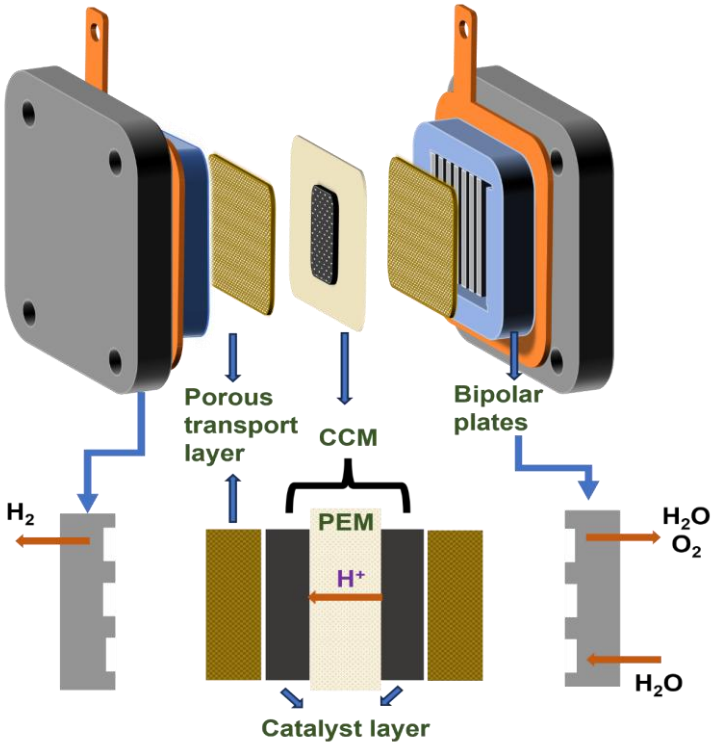

Figure 2.1 Schematic of a PEMWE single cell.

The membrane functions as a proton conduction media while separating the anode and cathode compartments [73]. The most widely used membrane material is perfluorosulfonic acid (PFSA), represented by Nafion®. Three key characteristics determine the membrane performance: water uptake, proton conductivity, and gas permeability [74,75]. Water uptake is critical for achieving efficient proton transport, as a

high hydration rate enables fast ionic mobility within the membrane structure. Research indicates that the conductivity of the Nafion® membrane improves linearly as the water uptake increases [76]. However, an excessive water content also increases gas permeability, leading to high hydrogen crossover rate and potential safety risks, especially under high differential pressure operation conditions [74,75,77].

The porous transport layer (PTL) is located between the catalyst layer (CL) and the bipolar plate, serving multiple purposes. It facilitates the water transport to catalyst layers and removal of the generated gases [78]. Additionally, it provides mechanical support to the catalyst coated membrane (CCM) [79–81]. At the cathode side, the potential of the hydrogen evolution reaction (HER) is 0 V vs. RHE, which is comparable to that in fuel cells, allowing the use of porous carbon-based materials such as carbon paper or carbon cloth as the PTL. These materials are often referred as the gas diffusion layer (GDL) in PEM fuel cells [82]. In contrast, the anode side experiences a high potential and acidic environment, making carbon unsuitable as the PTL material. Instead, titanium is usually employed due to its excellent corrosion resistance. Generally, the thickness, porosity, and pore size of the PTL are key properties that impact its performance. A thinner PTL typically offers better performance by lowering ohmic resistance and mass transport resistances. Porosity and pore size are interrelated factors that influence mass transportation and ohmic resistance, requiring careful consideration to balance these effects [83,84]. The optimisation of PTL surface structure is essential for achieving uniform reactant distribution and enhancing overall system efficiency.

The bipolar plate (BP) performs multiple functions, including providing mechanical stability to the stack, distributing reactants across the electrodes, and managing heat

[25,85]. BP materials must exhibit low electrical resistance, high mechanical stability, and effective thermal conductivity [85]. Although graphite is commonly used in fuel cells for its excellent conductivity, it is unsuitable for PEMWE applications due to rapid degradation under high potential. This degradation increases surface contact resistance, contaminates catalysts, and risks system failure [86]. As a result, titanium has become the material of choice for PEMWEs due to its superior corrosion resistance.

Additionally, the design of flow fields formed by flow channels engraved on BPs is critical. The shape and geometry of these channels directly impact the uniformity of reactant distribution and heat management. Improper design can result in uneven mass and heat distribution, Localised overheating, and performance degradation, especially in large-scale PEMWE systems [87]. Common flow field configurations include point flow fields, parallel flow fields, serpentine flow fields, and combined flow field structures. Although high differential pressure operation mitigates the need for mechanical hydrogen compression and improves system efficiency, it also introduces several technical challenges, including hydrogen crossover and material degradation, particularly hydrogen embrittlement in metallic components [88–90]. The following sections examine these challenges in detail and discuss the strategies currently being explored to address them.

2.2 Hydrogen crossover in asymmetric pressure condition

Hydrogen crossover is a persistent issue in PEMWEs operating under asymmetric pressure. When a pressure gradient exists across the membrane, hydrogen migrates from the cathode to the anode side, a phenomenon known as hydrogen crossover [39,91]. As hydrogen has a wide flammability range in pure oxygen, with a lower flammability limit (LFL) of 4% and an upper flammability limit (UFL) of 94%, the mixing of hydrogen

and oxygen can significantly increase explosion risks and elevate impurity gas concentrations [92,93]. A schematic representation of mass transport within the cell is illustrated in Figure 2.2.

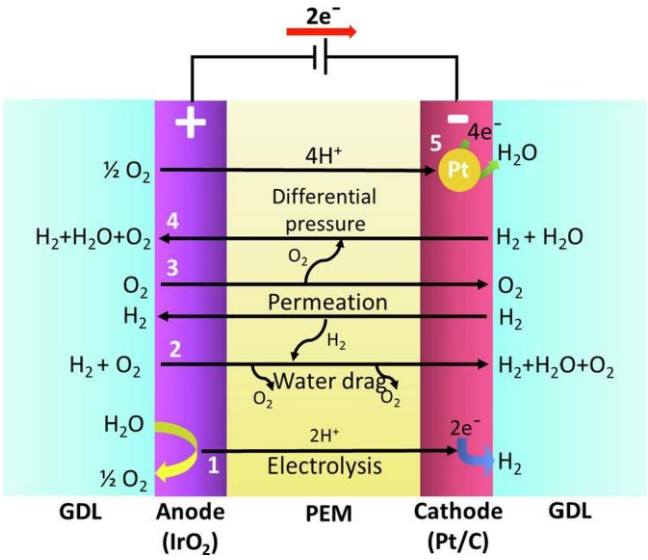

Figure 2.2 Schematic diagram of the water-gas transport mechanism in an operating PEMWE [39].

The key mass transport pathways in a PEMWE cell are as follows [91]:

1) Electrolysis reaction: hydrogen and oxygen are generated at the cathode and anode, respectively, while protons migrate from the anode to the cathode.
2) Water transport: dissolved hydrogen is carried from the anode to the cathode along with water transport.
3) Gas transport: generated gases permeate through the membrane via diffusion and osmosis.
4) Pressure-driven permeation: a higher differential pressure accelerates hydrogen and water permeation across the membrane.
5) Catalytic recombination: permeated oxygen reacts with cathodic Pt catalysts to

form water.

Hydrogen transportation mechanism in both membrane and cathode catalyst layer remains poorly understood. In particular, gas permeability properties, especially for non-Nafion® membranes, have not yet been well established. Therefore, the following discussion focuses on Nafion® membrane. In membranes, hydrogen transport occurs through both the ionomer (solid phase) and the pore phase, as illustrated in Figure 2.3 (a). Ito et al. reported that hydrogen permeability in a fully hydrated membrane is approximately ten times higher than in a dry Nafion® membrane [75]. This increase is attributed to the formation of water channels within the pore phase when Nafion® is hydrated. Since gas transport in the water phase is significantly faster than in the solid phase, higher water uptake in Nafion® increases its overall gas permeability [75,94,95].

In addition to membrane, hydrogen transport within the cathode catalyst layer plays a crucial role in crossover behaviour. At the hydrogen generation site in the cathodic catalyst layer, the concept of supersaturation is introduced, as depicted in Figure 2.3 (b). It is assumed that the generated hydrogen initially dissolves into water. The dissolved gas follows Path A, exiting the catalyst layer and transitioning into the vapour phase. However, due to the complex pathway, hydrogen cannot be released efficiently, leading to the local concentration higher than the theoretical equilibrium value. This phenomenon intensifies at higher current densities, where increased generation raises hydrogen levels further. The resulting elevated concentration gradient between the cathode and membrane enhances hydrogen permeation though the membrane into the anode, ultimately increasing crossover (Path B) [96,97].

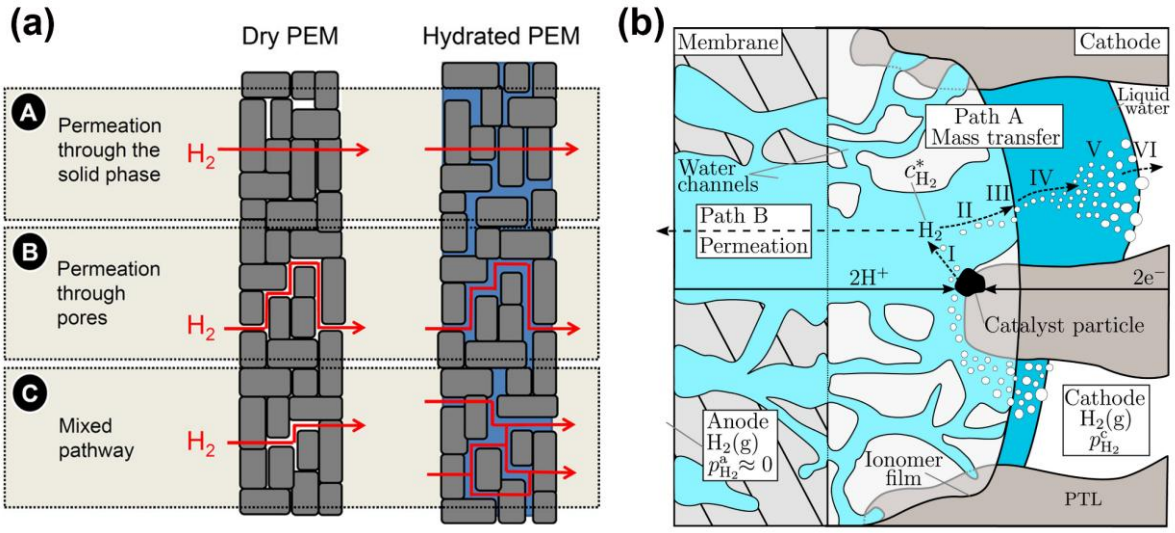

Figure 2.3 (a) Sketch of hydrogen transportation in the dry and hydrated membranes [95]; and (b) schematic of hydrogen transportation in the membrane /cathode interface [96].

To quantify hydrogen crossover, the permeation rate ($N_{H_2}^{Perm}$) is linked to the hydrogen concentration at the anode outlet ($\mathrm{X}_{H_2\ in\ O_2}$) using the following equation [98]:

$$\mathrm{X}_{H_2\ in\ O_2} = \frac{N_{H_2}^{Perm}}{N_{O_2}^{Anode} + N_{H_2}^{Perm}} \tag{7}$$

Where, $N_{O_2}^{Anode}$ represents the oxygen flux at the anode, determined using Faraday's law:

$$N_{O_2}^{Anode} = \frac{i}{4F} \tag{8}$$

Where i is the current density and F is the Faraday constant. Given that oxygen permeation from the anode to the cathode is negligible [99–101], the hydrogen flux can be

determined as:

$$N_{H_2}^{Perm} = \frac{i}{4F} \times \frac{\mathrm{X}_{H_2\ in\ O_2}}{1 - \mathrm{X}_{H_2\ in\ O_2}} \tag{9}$$

The hydrogen concentration at the anode outlet ($\mathrm{X}_{H_2\ in\ O_2}$) can be measured using electrochemical and non-electrochemical techniques. Electrochemical methods, such as linear sweep voltammetry (LSV) and cyclic voltammetry (CV), are commonly applied in the PEM fuel cell systems. In these methods, permeated hydrogen is oxidised to water at the platinum electrode, generating a current signal that correlates with the hydrogen crossover rate. While electrochemical methods offer simplicity, their accuracy is sensitive to variations in scan rate [102]. In contrast, non-electrochemical methods, including gas chromatography (GC) and thermal conductivity analyser, provide direct and continuous detection of trace hydrogen in the anode exhaust. Although requiring expensive equipment, they offer higher accuracy under diverse testing conditions, making them more reliable for studying hydrogen permeation [39,102–105].

Beyond quantifying hydrogen crossover, understanding the key factors that influence its magnitude is crucial for PEMWE optimisation. Hydrogen crossover is influenced by both operating conditions and cell configuration. The primary operating conditions influencing hydrogen permeation are current density and operating pressure. At high current densities, although the absolute hydrogen permeation increases, the corresponding rise in oxygen flux dilutes its concentration in the anode, reducing the measured hydrogen fraction there. In contrast, at low current densities, despite low hydrogen permeation, the reduced oxygen flux results in a high relative hydrogen concentration at the anode. Thus, hydrogen crossover mitigation efforts focus on the

low current density range. In terms of pressure effects, hydrogen crossover increases with the higher differential pressure due to an increased hydrogen concentration gradient between the cathode and anode [98,106,107]. The detailed discussion will be presented in Section 2.3.

In addition to these operating conditions, cell configuration also impacts the hydrogen crossover, particularly mechanical compression, cathode ionomer content, and membrane thickness [99]. Stähler et al. investigated the effect of cathode PTL compression and observed that at very low current densities, hydrogen crossover remained largely unaffected by compression, while at higher current densities, increased compression was strongly associated with increased hydrogen crossover. At a current density of 3.5 A/cm^2, the hydrogen crossover was six times higher for 45% compression of PTLs compared to 12.5% compression. While at low current density (below 0.25 A/cm^2), the hydrogen crossover was nearly the same under different compression ratios [106]. Similarly, Martin et al. reported that increased compression at high current densities led to greater hydrogen crossover. Their results showed that at 3.5 A/cm^2, hydrogen crossover was twice as high for PTLs compressed by 42.5% compared to those compressed by only 5% [108].

Another critical factor influencing hydrogen crossover is the ionomer-to-catalyst (I/C) ratio in the cathode catalyst layer. Studies have shown that hydrogen crossover flux increases with higher cathode I/C ratios [98,109]. Zhang et al. prepared CCMs with different I/C ratios on the cathode side and found that at 1 bar, the hydrogen crossover reached 3% at 0.5 A/cm^2 for an I/C ratio of 0.69, which is three times than that observed at an I/C ratio of 0.35, where only 1% crossover occurred. Their analysis indicated that the mass transfer coefficients were 2 mm/s and 15 mm/s for I/C ratios of 0.69 and 0.35,

respectively. This result suggests that a higher ionomer content increases the tortuosity of pore volume in the catalyst layer, hindering hydraulic gas transport through the pore network. This leads to increased hydrogen supersaturation in the catalyst layer, which further results in increased hydrogen crossover [98,109]. The combined effects of compression and ionomer content can be further interpreted through the supersaturation model. As generated hydrogen becomes trapped due to insufficient transport pathways, excess hydrogen permeates through the membrane to the anode side. However, a fundamental trade-off exists between proton conductivity and hydrogen transport. As demonstrated by the DOE Hydrogen Program, which found that increasing the I/C ratio improves catalyst layer uniformity due to enhanced catalyst dispersion [110].

To mitigate hydrogen crossover, several strategies have been explored. The first method is adjusting the cell operation, such as reducing the pressure and increasing the current density. However, these adjustments limit the operational flexibility of PEMWEs and are impractical when coupled with variable renewable energy sources. Increasing membrane thickness is another approach, as it provides a greater diffusion barrier, but this also raises costs and increases ohmic resistance, which negatively impacts overall efficiency. Another method involves introducing a physical barrier to impede mass transport. Materials such as graphene oxide [111] and hexagonal boron nitride [112] have shown potential in reducing gas crossover. However, research on these materials has primarily been conducted in PEM fuel cells rather than in PEMWEs. Additionally, such barrier layers often introduce additional resistance, ultimately reducing cell performance.

Currently, a widely adopted method for hydrogen crossover mitigation is the

incorporation of platinum-based recombination catalysts within the anode to promote hydrogen and oxygen recombination. Since iridium does not efficiently oxidise hydrogen, the ability to mitigate hydrogen crossover is predominantly attributed to platinum [105]. The recombination catalysts are normally introduced into either the membrane or anode catalyst layer. The first configuration is a sandwich construction, where a platinum interlayer is introduced onto the membrane surface, followed by casting an ionomer layer or pressing an additional membrane over it to form a sandwiched structure (Figure 2.4 (a) and (b)). Studies have shown that positioning the platinum interlayer closer to the anode is more effective in reducing hydrogen content. For instance, with a platinum loading of 20 μg/cm^2, the hydrogen content in the anode stream was reduced from 2.8% to 0.2% at a current density of 0.5 A/cm^2 under 10 bar differential pressure (Figure 2.4 (c) and (d)). When the platinum was positioned in the middle of the membrane or closer to the cathode, the hydrogen crossover increased to 1.5 % and 2.6%, respectively [113–116]. This approach has been validated on large-area CCMs (32.5 × 32.5 cm^2), achieving long-term stability exceeding 5,000 hours, proving its feasibility for industrial deployment [115]. However, the additional ionomer layer or membrane increases the overall membrane thickness, leading to higher ohmic resistances [116–120]. Furthermore, the complex fabrication process requires thoroughly control of the spraying and parameters, raising the manufacturing cost [107,121]. Reports also showed that the added interfaces in this structure may introduce cavities, potentially leading to pinholes or electrical shorts during operation [122,123]. These issues can negatively impact both efficiency and durability.

An alternative approach to the platinum interlayer method is the direct integration of recombination catalysts into the anode catalyst layer, simplifying the fabrication

process (Figure 2.4 (e)). Briguglio et al. incorporated a PtCo layer between the PEM and the anode catalyst layer (unmixed configuration), reducing hydrogen crossover from 2.7% to 2.2% at 0.5 A/cm^2 under 20 bar differential pressure [124]. They also mixed the PtCo with iridium to form catalyst layer, instead of forming a pure PtCo layer, refer as the mixed configuration. This mixed catalyst approach further lowered hydrogen crossover to 1.5% under the same conditions. However, it resulted in a reduction in electrochemical performance compared to the unmixed configuration. At 3 A/cm^2, the unmixed configuration required a voltage of 1.8 V while the mixed configuration needed 1.9 V [125]. Pantò et al. validated the durability of this approach, demonstrating stable CCM operation over 3,500 hours at 4 A/cm^2, with a degradation rate of 9 μV/h, well below the 14 μV/h threshold generally considered acceptable for PEMWE systems [26,126].

It is worth noting that corporate research is ahead of academic efforts in this area, with many published patents related to recombination interlayers. Companies are actively exploring high differential pressure PEMWEs for hydrogen production. Some commercial CCMs have achieved hydrogen crossover concentrations below 0.5% at 20–30 bar differential pressures, although specific design details are usually not provided [113,127–129].

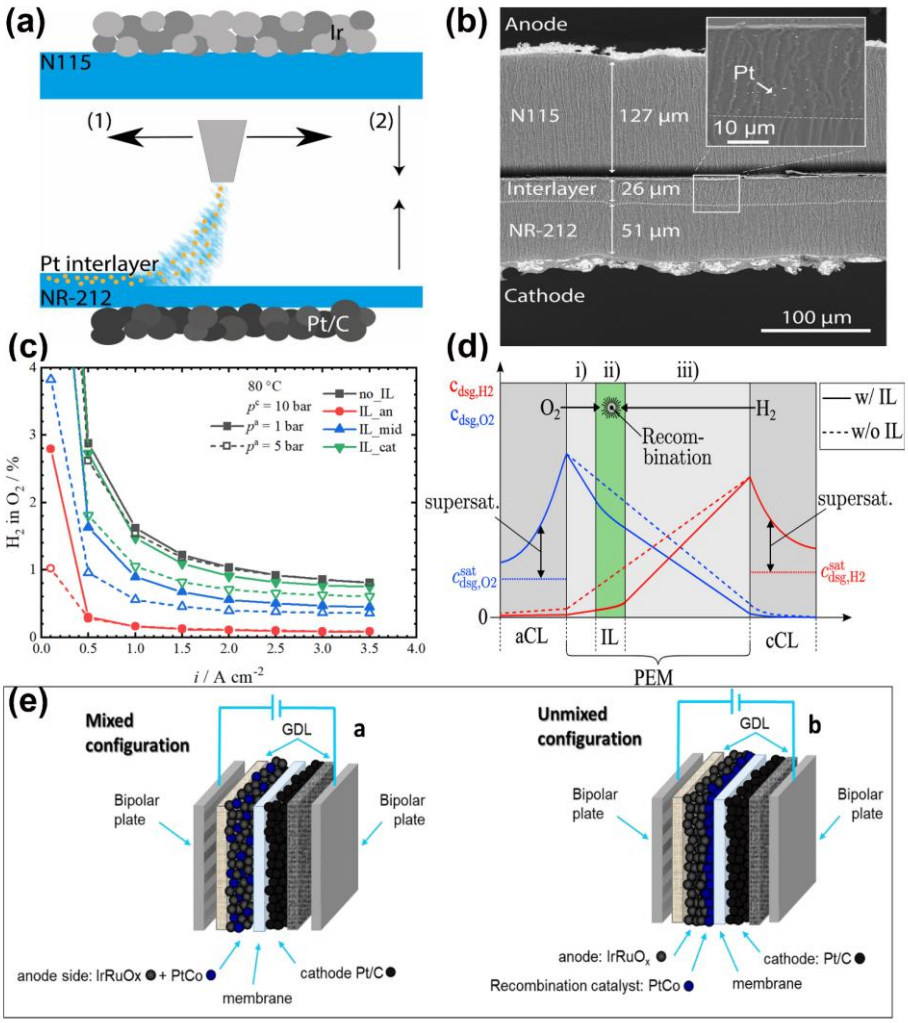

Figure 2.4 Overview of hydrogen crossover mitigation strategies. (a) Schematic of Pt interlayer fabrication [116]. (b) A cross-sectional SEM image of the CCM, showing the interlayer structure [116]. (c) Comparison of hydrogen crossover under 9 bar and 5 bar differential pressure with the Pt interlayer positioned at different locations: near the anode (IL_an), within the membrane (IL_mid), and near the cathode (IL_cat) [114]. (d) Model illustrating the effect of Pt interlayers on hydrogen recombination and suppression [130]; (e) Structural comparison between mixed and unmixed configurations for recombination catalyst integration [125].

While the performance and characteristics of the PEMWE components have been

extensively studied under atmospheric conditions, high-pressure operation introduces additional challenges that significantly affect both performance and durability. The following sections examine the specific challenges faced by the key components, including membranes, PTLs, BPs and CCMs, under atmospheric and high differential pressure conditions, along with the corresponding mitigation strategies.

2.3 Fundamentals and challenges of membrane

Perfluorosulfonic acid (PFSA) membranes are the most widely used in PEMWE due to their high proton conductivity and chemical stability. However, their high cost, accounting for up to 21% of the total CCM expenditure, and their fluorine-based backbone pose significant disposal challenges for large-scale adoption [131,132]. To improve performance, Solvay developed the short-sidechain Aquivion® membrane, which exhibits twice the proton conductivity of Nafion®, reaching 0.2 S/cm^2 [133,134]. Siracusano et al. reported that under identical fabrication conditions, the CCMs incorporating Aquivion® membrane achieved a current density of 2.4 A/cm^2 at 1.8 V, whereas Nafion®-based CCMs reached only 1.5 A/cm^2 [135].

Besides, hydrocarbon-based polymers have been investigated as potential alternatives to PFSA, such as sulfonated polysulfone (SPSf), sulfonated poly(phenylene sulfone) (sPPs), and sulfonated poly(ether ether ketone) (SPEEK) [136–138]. Despite their cost advantage, these materials still fall short of PFSA in terms of both performance and durability. For example, the SPSf membrane only shows proton conductivity of 69 mS/cm^2 at 80°C. At 1.8 V, CCMs incorporating SPSf and SPEEK achieved current densities of 1.35 A/cm^2 and 1 A/cm^2, respectively [139,140]. Although Klose et al. reported that sPPs membranes significantly improved current density to 3.5 A/cm^2 at 1.8 V, which is approximately 2.3 times higher than that of the PFSA-

based membrane, their durability remains a concern. The lower stability of the C–H bond in hydrocarbon membranes, compared to the C–F bond in PFSA membranes, results in significantly higher degradation rates. The sPPs-based CCM exhibited a degradation rate of 850 μV/h and electrical shorting after only 60 hours, whereas the PFSA-based CCM showed a degradation rate of 300 μV/h over 100 hours at a current density of 1 A/cm^2 [141,142].

In addition to material selection, membrane thickness also plays a crucial role in determining overall performance, influencing proton conductivity, gas crossover, and mechanical durability. Phan et al. prepared CCMs with three membranes of varying thickness: NR212 (50 μm), N115 (125 μm) and N117 (183 μm), as shown in Figure 2.5. At a current density of 3.0 A/cm^2, the cell potential differences were 136 mV and 241 mV when comparing NR212 with N115 and N117, respectively, demonstrating that thinner membranes enhanced the cell performance. However, thinner membranes also resulted in significantly higher hydrogen crossover. For instance, NR212 exhibited a significantly higher crossover rate of 1.58 mA/cm^2·bar, compared to 0.72 mA/cm^2·bar and 0.54 mA/cm^2·bar for N115 and N117, respectively [143].

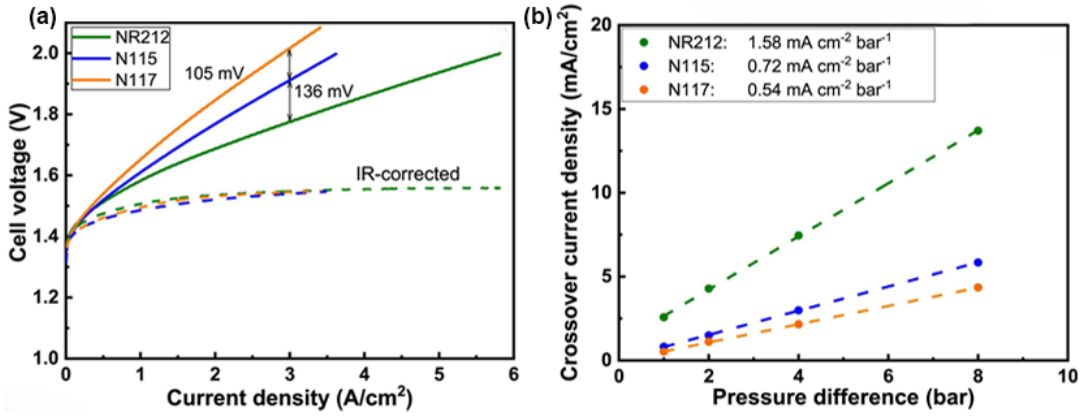

Figure 2.5 (a) Polarisation curves and (b) hydrogen crossover for CCMs with varying membrane thickness (NR212: 50 μm, N115: 125 μm, N117: 175 μm) [143].

These differences in hydrogen permeation directly impact the operating pressure range. To ensure system safety, the hydrogen volume fraction in oxygen must remain below 2%, as indicated by the dashed red line in Figure 2.6. The results show that without additional treatments, N117 membrane provides a broader operating pressure range compared to NR212, especially at high pressure and low current density [144]. Moreover, membrane thickness also influences long-term stability; at 3 A/cm^2, the degradation rates for NR212 and N117 are 0.55 mV/h and 0.24 mV/h, respectively [143].

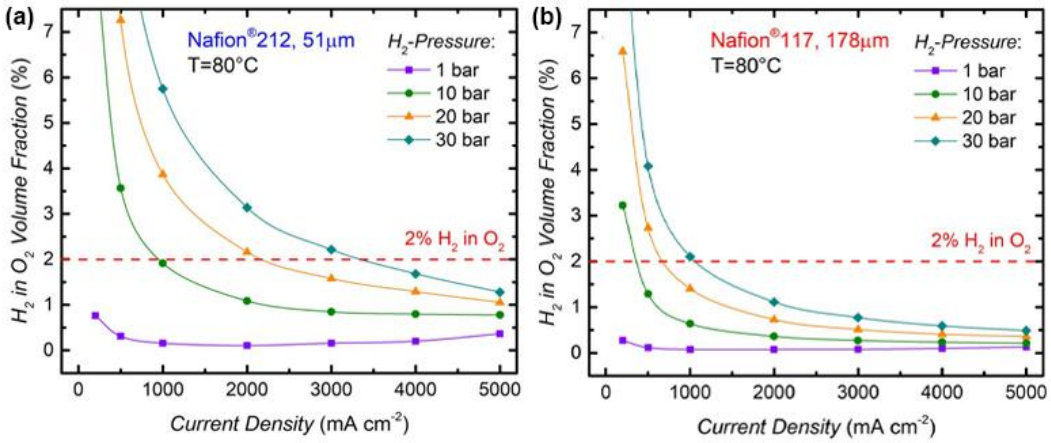

Figure 2.6 Hydrogen crossover as a function of current density for NR212 (a) and N117 (b) under varying cathode pressures (1, 10, 20, and 30 bar) [144].

As mentioned above, water uptake is critical for efficient proton transport, but excessive water content increases hydrogen crossover and potential safety risks, especially under high-pressure conditions [74,75,77]. In fact, membranes are always fully hydrated due to continuous contact with water reactants, making hydrogen crossover unavoidable. In practical operation, thicker membranes ranging from 120 to 200 μm are often employed to improve mechanical strength and reduce gas crossover under high differential pressure operation conditions. However, this comes at the expense of higher ohmic resistance, as the membrane resistance contributes over 70% of the total

ohmic resistances. These findings highlight the importance of selecting an appropriate membrane thickness to balance efficiency, safety, and durability. The optimal choice depends on the specific application and operational requirements [17,36,38,145].

Beyond membrane thickness and permeability considerations, degradation presents another challenge under high differential pressure conditions. Among all components in PEMWEs, the membrane is considered the most vulnerable during long-term operation, with degradation occurring due to mechanical, chemical, and thermal factors [68,146]. Mechanical degradation is the primary factor affecting membrane performance during the early stage (within the first 1,000 hours). Under differential pressure conditions, membranes experience continuous mechanical stress, which is further exacerbated by the high assembling force required to maintain a sealed environment [147,148]. This stress leads to the formation of cracks, especially in stress concentration areas such as the interfaces between PTL and membranes, as seen in Figure 2.7 [147,149]. Aggravating this issue, swelling under hydrated conditions causes the membrane creep, further increasing the risk of cracking [150,151]. These structural failures not only compromise membrane integrity but also increase hydrogen permeation, leading to potential risks during operation [146].

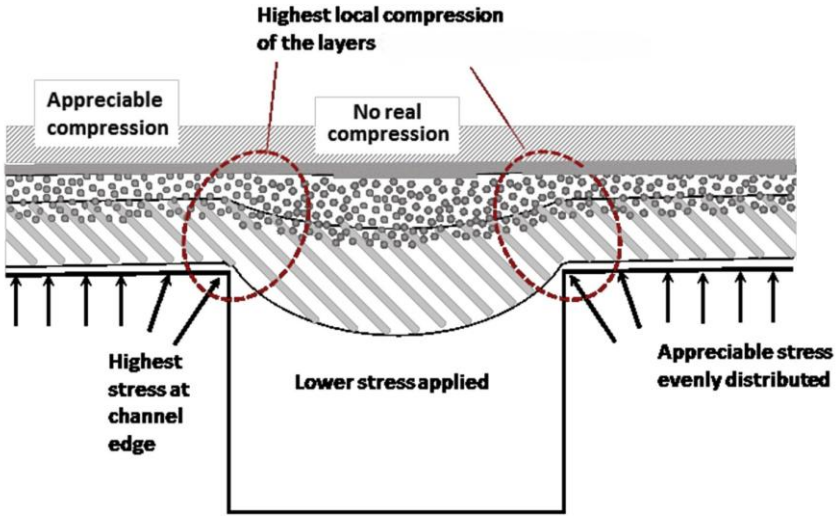

Figure 2.7 Localised compression of CCM caused by the grooved channels in bipolar plates [152].

Chemical degradation is primarily caused by permeated hydrogen radicals (H•) reacting with oxygen at the anode/membrane interface, generating intermediate radicals such as HO_2• and •OH, along with hydrogen peroxide. These reactive species attack the membrane backbone, leading to membrane thinning and the release of sulphur and fluoride species [146,153,154]. This degradation becomes more serious under higher differential pressure, as greater hydrogen crossover accelerates radical formation [155,156]. Kuhnert et al. reported a direct correlation between hydrogen crossover and fluoride emission. After a membrane stability test, hydrogen crossover increased by 13%, while the fluoride emission rate rose by 8.5%, indicating that the increased hydrogen permeation accelerates chemical degradation [157]. Moreover, uneven water distribution and non-uniform current densities result in localised hotspots, accelerating thermal degradation [158].

To address these challenges, several strategies have been explored. Operating solutions such as optimised clamping mechanisms, have been investigated to ensure

uniform mechanical compression and minimise the risk of mechanical failure. Besides, various additives have also been investigated to enhance the mechanical stability of the PFSA membranes. As previously discussed, polysulfone can reduce membrane creep, exhibiting a water swelling ratio of only 5 wt% compared to 33 wt% for Nafion® 115. Jang et al. employed a SPEEK membrane cross-linked with tungstophosphoric acid (TPA), achieving a tensile strength of 75.01 MPa, significantly higher than the 43 MPa of Nafion® 117. However, despite improved mechanical strength, this structure achieved a current density of only 1 A/cm^2 at 1.8 V, highlighting the trade-off between durability and performance [159].

For chemical degradation, mitigating hydrogen crossover is a key approach to limiting radical-induced damage [160]. Hydrocarbon-based membranes, with their lower water uptake and narrower water channels, restrict hydrogen transport and further reduce permeation [118,141,159,161]. Huang et al. used the PFSA with imidazole terminal groups composite membrane, which reduced hydrogen crossover at 0.5 A/cm^2 from 0.083 vol% to 0.035 vol% [161]. Similarly, the previously discussed sPPs CCM demonstrated a threefold reduction in hydrogen crossover compared to PFSA membranes [141]. These findings suggest that hydrocarbon-based membranes present a promising solution to the inherent limitations of the PFSA membranes, offering more favourable low gas crossover characteristics [33]. However, despite these advantages, long-term performance of these modified membranes is still a question, and fundamental studies on their physical properties, including proton, water, and gas migration, remain insufficient [17].

2.4 Fundamentals and challenges of porous transport layers

An optimised PTL structure is essential for achieving uniform distribution of water,

gases, and current within an electrolyser, thereby enhancing electrolysis performance. Porosity is a key parameter affecting PTL performance. A high porosity facilitates mass transport but reduces the contact area with the catalyst layer, leading to increased interfacial resistance. According to the literature, the optimal PTL porosity ranges from 30% to 50% [82,162,163]. Weber et al. investigated PTLs with different porosities. The found for PTLs with a thickness of 200 μm, the required voltages to reach a current density of 1.8 A/cm^2 were 2.1 V (43% porosity), 2.4 V (26% porosity), and 2.98 V (9% porosity) [164].

As discussed previously, titanium is the primary material used for PTLs. To prevent the titanium oxidisation under highly oxidative and acidic conditions and improve the electrical conductivity, Ti-based PTLs are typically coated with noble metals such as platinum or gold. Rakousky et al. reported that sputtering a 200 nm Pt layer onto PTLs significantly improved stability, reducing the degradation rate to 12 μV/h over 380 hours, compared to 108 μV/h for uncoated PTLs at 2 A/cm^2 [165,166]. Kang et al. applied a 180 nm gold layer via electroplating, which reduced the ohmic resistances from 0.0925 Ω cm^2 to 0.0700 Ω cm^2 and also showed good stability, with a degradation rate of 0.4 μV/h over 100 hours at 0.2 A/cm^2 [167]. Given its excellent electrical conductivity, the National Renewable Energy Laboratory applied a 100 nm gold on the PTLs and BPs [168].

However, despite their high conductivity, platinum and gold are not fully stable under the anodic condition of PEMWEs, as they can undergo oxidation over time. Thus, very thick coatings are required to extend their lifetime [169,170]. To address this limitation, Liu et al. introduced an iridium coating using a sputtering technique, as iridium is the most corrosion-resistant metal, and its oxide also maintains good electrical conductivity

[171,172]. Their finding showed that a 7 nm iridium layer (0.005 mg/cm^2) reduced ohmic resistance by 21%, from 0.283 Ω cm^2 to 0.222 Ω cm^2. Despite using 40 times less noble metal, the iridium coated PTLs exhibited an enhanced performance, increasing the current density from 1.2 A/cm^2 to 1.5 A/cm^2 at 1.8 V compared with uncoated PTLs. Additionally, a 4000-hour stability test demonstrated that the PTLs coated with 0.1 mg/cm^2 iridium remained nearly unchanged in performance, whereas PTLs with a 0.18 mg/cm^2 gold coating showed a 50% decline at 2 V [169,173,174].

Under high differential pressure conditions combined with strong clamping forces. PTLs are subjected to non-uniform forces due to the channel-rib configuration. Similar to the membrane, these compressive stresses can lead to PTL deformation, as shown in Figure 2.8 (a). Additionally, the coarse surface structure of PTLs can cause indentations in the catalyst layer and damage to the fragile membrane, potentially resulting in pinholes (Figure 2.8 (b)) [175,176]. Therefore, achieving an optimal clamping force is critical to minimizing mechanical deformation while maintaining electrochemical performance.

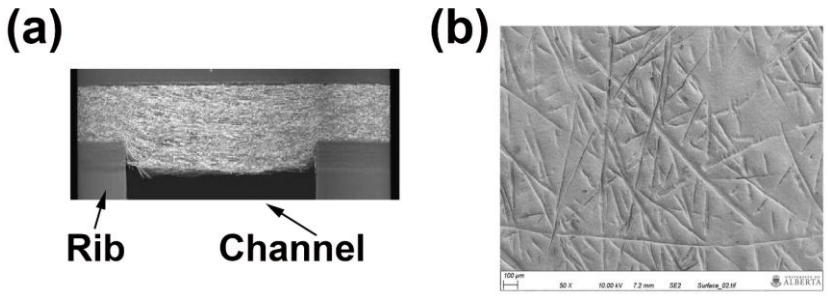

Figure 2.8 (a) Compression effects on PTLs adjacent to flow channels under 30-bar compression [176]; (b) A SEM image of catalyst layer surface showing indentations caused by PTL compression [175].

Considering that the titanium-based PTLs are rigid materials, they are less effective at redistributing compression forces compared to softer materials like carbon paper. This limitation makes achieving uniform pressure distribution more challenging. To date, most studies investigating the influence of clamping pressure on PEMWE performance have focused primarily on the cathode-side GDL rather than the complete PTL configuration.

For cathode-side analysis, carbon-based GDLs have been extensively studied due to their compressibility. Borgardt et al. concluded that optimal performance can be achieved when the cell operates at an average clamping pressure of 2.0–3.0 MPa on the active area [177]. Using the same configuration, Cruz Ortiz et al. investigated the different compression levels of 20%, 40% and 60%, corresponding to clamping pressure of 1 MPa, 2.15 MPa and 3 MPa, respectively. They found that as the compression increased, the ohmic resistance decreased, with overpotential at 3 A/cm^2 dropping from 203 mV to 169 mV and further to 151 mV. However, excessive compression (> 40%) led to significant membrane deformation and increased mass transfer overpotential from 28 mV (20% and 40% compression) to 55 mV (60% compression). This doubled increase in mass transfer resistance negated its advantage in reducing contact resistance, demonstrating that compressing carbon paper should be less than 40% to provide a balance between minimising membrane deformation and maintaining good performance [178].

Beyond compression studies on GDLs, PTL compression effects have also been investigated. Liu et al. used modelling software to simulate the behaviours of titanium PTLs under compression. They examined three different compression ratios: 10%, 20%, and 30%. The porosity of PTLs decreased from 75.9% (uncompressed) to 73.8%

(10% compression), 71.2% (20% compression) and 68.2% (30% compression). Using an electrochemical model, they demonstrated that compression improved electrochemical performance, as the cell voltage decreased from 2.107 V (0% compression) to 2.060 V (30% compression) at a current density of 1.6 A/cm^2 [179].

Despite these findings, studies on clamping pressure effects under varying PTL conditions, particularly for the rigid titanium-based PTLs, remain limited. Further research is needed to address this gap, focusing on understanding the interplay between clamping pressure, mechanical deformation, and electrochemical performance, particularly under high differential pressure conditions.

2.5 Fundamentals and challenges of bipolar plates

Similar to PTLs, titanium is also widely used for BPs due to its excellent corrosion resistance. However, it encounters the same challenge of forming a passivating oxide layer under high humidity and voltage, which increases contact resistance. Additionally, titanium is susceptible to corrosion when exposed to fluoride ions, especially under high differential pressure operation [39]. To mitigate these issues, as for PTLs, noble metal coatings, such as gold and platinum, are commonly applied to enhance durability and maintain stable performance [180–182].

Apart from material selection, the design of flow channels engraved on BPs is also important. The shape and geometry of these channels influence the distribution of reactants and heat across the cell. Improper designs can lead to uneven mass transfer, localised overheating, and performance losses, particularly in large-scale systems [87]. Various configurations have been investigated, including point, parallel, serpentine, and combined flow fields. Li et al. studied the effects of three flow field configurations: serpentine, parallel, and cascade on both anode and cathode sides (Figure 2.9). On

the cathode side, the serpentine flow field improved water distribution and membrane hydration, resulting in the lowest ohmic resistance. As for the anode side, the cascade configuration effectively facilitated oxygen bubble removal, improved water utilisation, and exhibited the lowest overpotential among all tested designs [183].

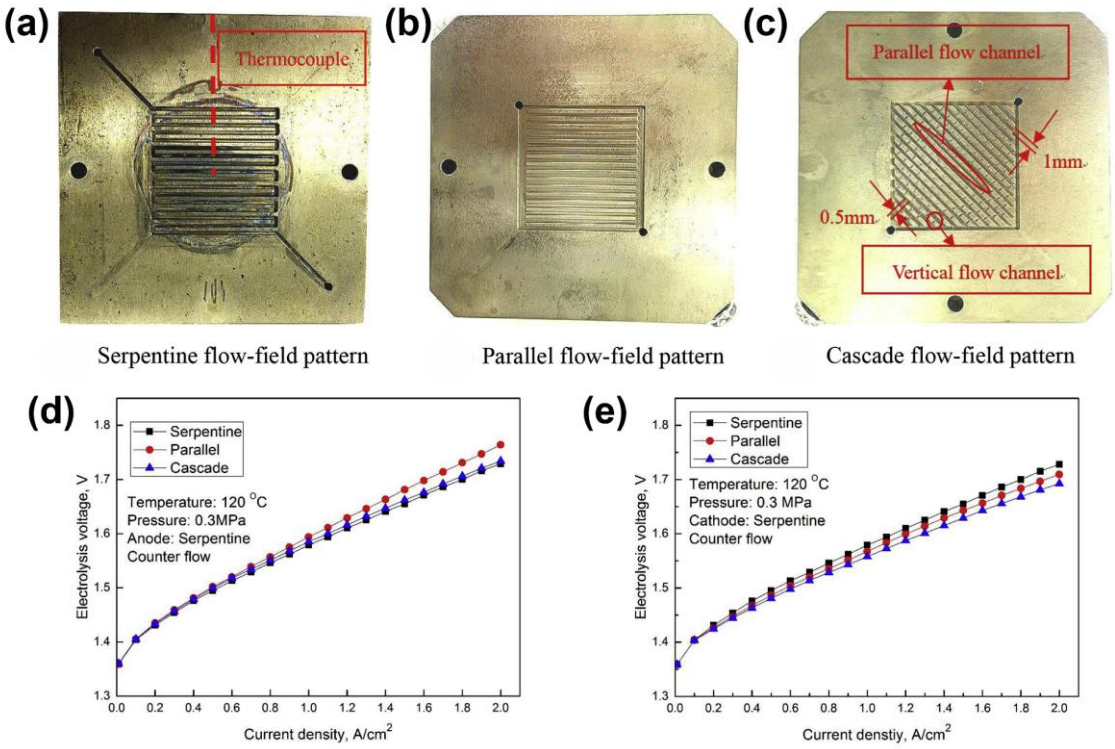

Figure 2.9 Comparison of three flow field patterns: (a) serpentine, (b) parallel, and (c) cascade flow field; (d) Polarisation curves obtained under different flow field patterns at cathode side, and (e) Polarisation curves obtained under different flow field patterns at anode side [183].

Beyond the influence on the electrochemical performance, the flow field design also plays a role in stress distribution. For instance, Liu et al. introduced a point flow channel design to optimise stress distribution, which was tested in a 50 cm^2 electrolysis cell at 2 A/cm^2, showing a voltage reduction of 40 mV compared to serpentine design. In

addition, the SEM analysis of the catalyst layer revealed that improved pressure distribution mitigated mechanical stress, reducing surface indentations and cracks [184].

In addition to corrosion, hydrogen embrittlement presents another significant challenge. Due to the small atomic radius of hydrogen, it can easily penetrate metal components and recombine to form molecular hydrogen. When the internal hydrogen pressure exceeds the mechanical strength of the metal, cracking occurs, eventually leading to fracture failure. This challenge becomes more severe under high-pressure conditions, particularly on the cathode side [185,186]. Long-term studies have shown that titanium BPs can absorb over 1000 ppm of hydrogen within 500 hours under 20 bar differential pressures, with mechanical failure occurring at approximately 8000 ppm due to excessive hydride formation [187,188].

Traditionally, gold and platinum coatings are applied to mitigate hydrogen embrittlement in titanium components. Alternative coatings such as titanium diboride (TiB_2) have also shown promise in providing better long-term stability. He et al. conducted a 20-day corrosion test on TiB_2 coatings, which exhibited a resistance of approximately 19 $m\Omega/cm^2$ after testing, significantly lower than the European target (25 $m\Omega/cm^2$) [189].

Although efforts have been made to develop coatings that address both corrosion and hydrogen embrittlement in bipolar plates, progress remains largely confined to laboratory-scale studies, hindered by the absence of standardised evaluation methods [36,91]. Future research should focus on addressing these gaps to ensure the long-term reliability of bipolar plates in industrial PEMWE systems.

2.6 Fundamentals and challenges of MEA fabrication

The membrane electrode assembly (MEA), which is central to a PEMWE, comprises a proton exchange membrane, the anodic catalyst layer and the cathodic catalyst layer [73]. The fabrication process of MEAs is crucial in defining the overall performance of a PEMWE. Fabrication methods are categorised into catalyst-coated membrane (CCM) and catalyst-coated substrate (CCS) approaches, based on where the catalyst layer (CL) is applied to [190–192]. With the CCS process, the catalyst is deposited onto the PTL surface. While CCM techniques directly deposit the catalyst onto the membrane, improving the contact between the membrane and the catalyst layer. This direct deposition minimises interfacial resistance, improves proton conductivity, and offers superior performance compared to the CCS approach. Zenyuk et al. applied X-ray computed tomography to evaluate the interfacial structures of the two configurations. Their research demonstrated that the CCM configuration achieved higher connectivity between catalyst particles and the membrane than the CCS sample, showing an advantage of 200 mV at a current density of 1 A/cm^2 [193,194]. This direct contact structure minimises the interfacial impedance, enhancing proton conductivity and durability of the CCM. As a result, the CCM method has become the standard method in both industrial and academic applications. Besides these two conventional approaches, some novel methods have also been developed. Holzapfel et al. introduced a direct membrane deposition (DMD) method, which deposits the membrane onto the PTL. Although its performance is not comparable to those made by traditional methods, it provides an alternative route to simplify the MEA fabrication process [195]. Beyond fabrication methods, various fabrication techniques have also been reported, including ultrasonic spraying [196], roll-to-roll processing [197], and hand brushing [53]. Ultrasonic spraying, widely adopted for laboratory-scale applications, offers precise control over

catalyst layer deposition, ensuring consistency and reproducibility. With a high degree of design flexibility, it is also employed to develop new MEA configurations, including low-loading catalyst layers [198–200]. Meanwhile, roll-to-roll processing (slot-die, gravure, and knife) enables continuous operation, increases production efficiency, and reduces costs, making it well-suited for both laboratory and large-scale applications (Figure 2.10) [25,197]. The rational selection of fabrication methods is fundamental to improving MEA quality and, consequently, the overall performance of PEMWEs.

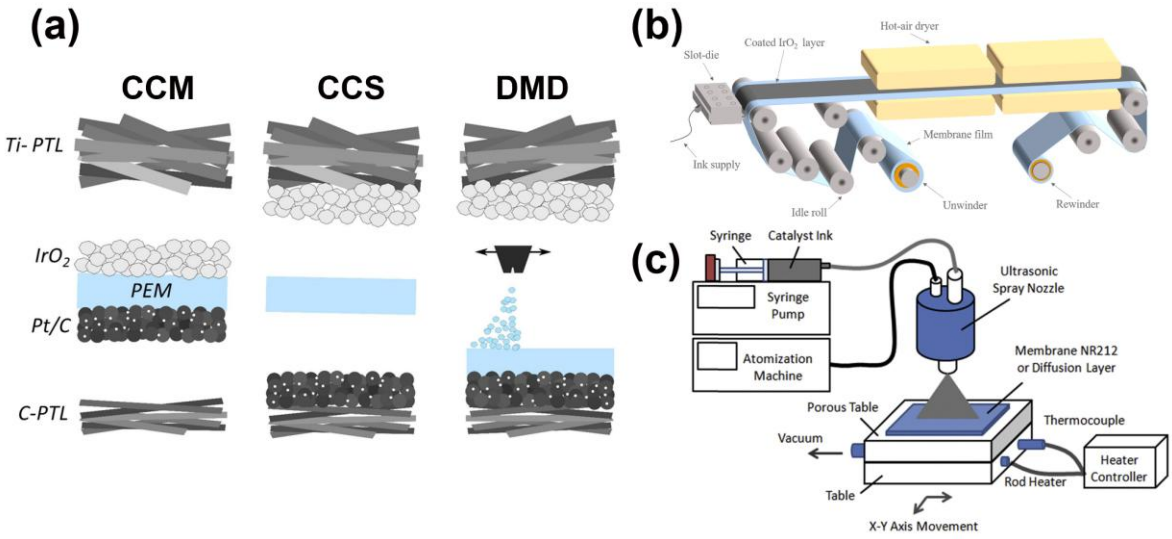

Figure 2.10 (a) Schematic diagram of different MEA fabrication techniques and methods: catalyst-coated membrane (CCM), catalyst-coated substrate (CCS) and direct membrane deposition (DMD) methods [199]; (b) roll-to-roll coating (R2R) [197], and (c) ultrasonic spraying coating [198].

Although fabrication advances have significantly enhanced MEA performance, the scalability of PEMWEs remains constrained by the high cost of critical materials used in the catalyst layers. To address this, research efforts have increasingly focused on optimising catalyst utilisation and reducing catalyst loading without sacrificing performance. Due to the fast HER kinetics, reducing Pt loading on the cathode shows

little impact, whereas Ir loading on the anode remains critical due to the sluggish OER kinetics, making it the primary focus of the optimisation efforts. Ir is an extremely scarce metal, with annual global production of only about 7-8 tonnes, mostly obtained as a by-product of platinum and palladium mining [201]. In comparison, the global supplies of gold and platinum supplies are approximately 40 and 10 times higher, respectively [202]. This scarcity of Ir poses a significant challenge for the large-scale PEMWE deployment [201]. Currently, the iridium loading in PEMWEs ranges from 2 to 5 mg/cm^2, but studies suggest that reducing iridium loading to at least 0.05 to 0.1 mg/cm^2 would enable sufficient global supply to support gigawatt-scale PEMWE deployment [65,203–205]. Thus, developing a low-loading iridium catalyst layer is another research direction.

However, directly reducing iridium content can significantly affect performance. A thinner catalyst layer suffers from poor in-plane conductivity, and in extreme cases, isolated catalyst regions become deactivated, reducing catalyst utilisation. Additionally, an uneven catalyst layer can lead to poor interfacial contact with the PTL, increasing ohmic resistances and reducing overall efficiency [206–209]. In addition to performance limitations, low-loading CCMs also exhibit higher degradation rates. For example, an optimised CCM containing 1.6 mg$_{Ir}$/cm^2 showed a degradation rate of 5 μV/h over 1000 hours at 1A/cm^2, only one-third of that observed in a low loading CCM with 0.5 mg$_{Ir}$/cm^2 [210].

Current optimisation methods can be summarised into several categories: development of low-loading iridium catalyst inks, the introduction of conductive layers, the design of structured catalyst layers, and the synthesis of supported iridium catalysts. The first method focuses on developing low-loading iridium catalyst inks, requiring precise control of the ink formulation, catalyst particle size, and coating

procedures to achieve uniform deposition. Taie et al. employed multiple physical characterisation techniques, including scanning electron microscopy (SEM), micro-X-ray computed tomography (XCT), X-ray fluorescence (XRF) mapping, and dynamic light scattering (DLS) to optimise catalyst ink and catalyst layer (Figure 2.11 (a)). The optimised CCMs with well distributed and continuous CL achieved a current density of 1 A/cm^2 at 1.7 V with an ultralow iridium loading of just 0.011 mg/cm^2, highlighting the potential of process optimisation to improve PEMWE performance [211,212]. The second method introduces a conductive layer between the catalyst layer and the PTL to address the high interfacial resistance [213]. Kwan et al. demonstrated that depositing platinum within the PEM and catalyst layer, achieving a significant performance enhancement of 400 to 600 mV at 2 A/cm^2 with an iridium oxide loading of 1.2 mg/cm^2 [214]. Their method grows Pt nanoparticles chemically within the membrane, enhancing electronic pathways and enabling hydrogen recombination. In contrast, this work introduces a sputtered Pt interlayer directly on the membrane, allowing controlled thickness. It also evaluates the performance of the platinum layer under differential pressure, which was not addressed in their work. Similarly, ultrasonic spraying of Pt nanoparticles onto the PTL surface enabled a catalyst layer with iridium loading of 0.1 mg/cm^2 and 0.4 mg/cm^2 of Pt to achieve performance comparable to that of a high-loaded (1 mg$_{Ir}$/cm^2) CCM (Figure 2.11 (e)) [215]. In addition to platinum, IrOx nanofibres have also been explored as conductive additives. It was demonstrated that with a total iridium loading of 0.2 mg/cm^2, the cell achieved performance comparable to that of CCM containing 1.2 mg/cm^2 of iridium (Figure 2.11 (c)) [208].

The third method involves structured catalyst layer design to improve in-plane conductivity and mass transport. Tian et al. employed magnetron sputtering to form a

conical gradient ionomer structure with just 20 μg/cm^2 of iridium (Figure 2.11 (d)). This approach achieved an electrochemical active area 8.7 times larger than that of a conventional CCM with 1.0 mg/cm^2. At 2.0 V, the gradient-structured CCMs attained a current density of 3.36 A/cm^2 compared to 2.62 A/cm^2 for the conventional CCM. The gradient structure was believed to facilitate efficient proton transport and rapid oxygen bubble release by forming numerous vertically aligned channels (conical structure). This design also enhanced catalyst utilisation [216].

Beyond cell-level modifications, catalyst-level engineering provides another method for reducing Ir loading while maintaining performance. One approach involves designing catalysts with low packing density and/or reduced Ir content without compromising CL thickness. Supporting materials have been introduced to decrease Ir packing density (Figure 2.11 (b)). Pham et al. synthesised IrO_2 coated TiO_2 core-shell microparticles, achieving 1 A/cm^2 at 1.67 V with an iridium loading of 0.4 mg/cm^2, whereas bulk iridium required 1.2 mg/cm² to reach the same performance [217]. Similarly, Shi et al. utilised cerium oxide as support, incorporating 0.3 mg/cm^2 of iridium. This design achieved a current density of 3 A/cm² at 1.72 V and demonstrated durability over 6000 hours, with a degradation rate of only 1.33 μV/h [218].

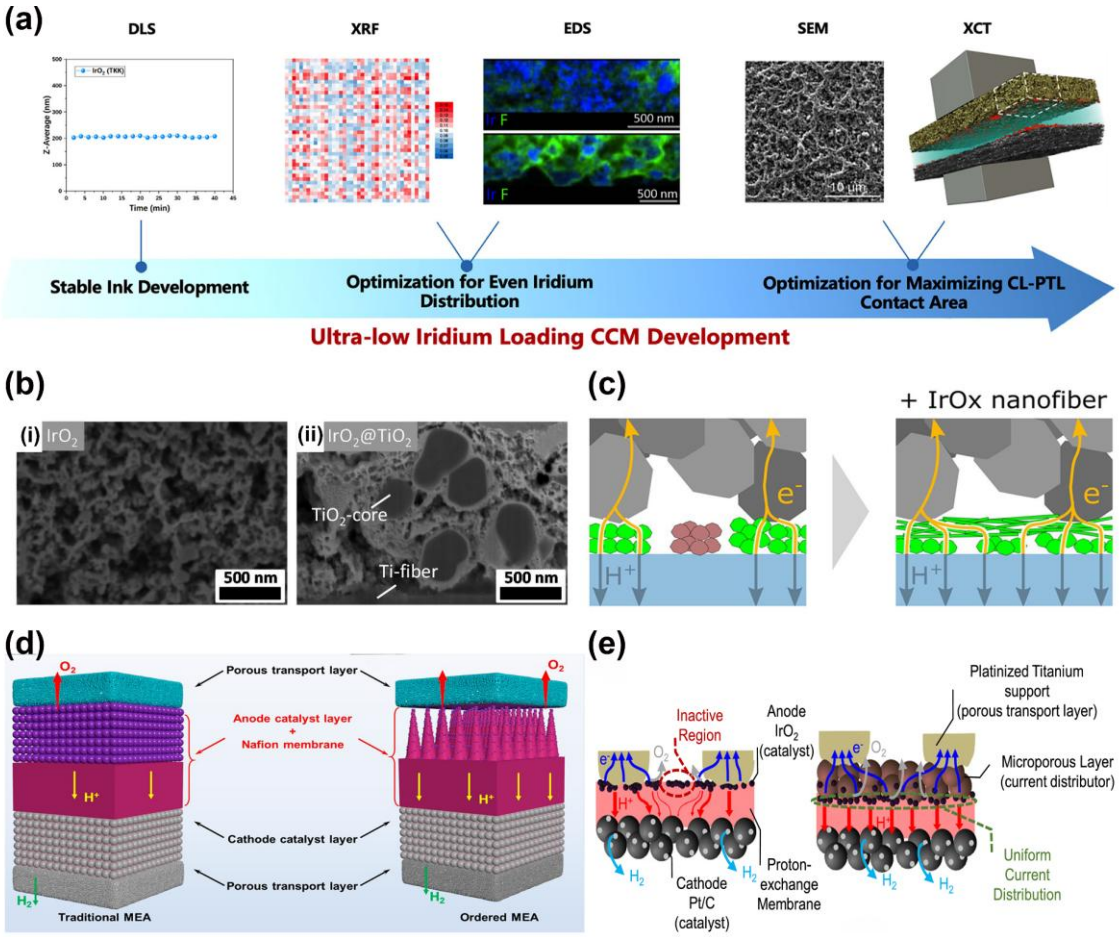

Figure 2.11 Strategies for developing low iridium loading CCMs. (a) Ink formulation optimisation using various physical characterisation techniques, including DLS, XRF, EDS, SEM, and XCT [211,212]. (b) Using TiO_2 support material to maintain catalyst layer structure and density [219]. (c) IrO_x nanofibres as a conductive layer between the PEM and PTL[208]. (d) Ordered ionomer distribution within the catalyst layer [216]. (e) Pt nanoparticles as a conductive interlayer to enhance electron transport [215].

While various strategies have been developed to optimise low-loading CCMs, their long-term stability remains a concern, particularly under high differential pressure conditions. In addition to the degradation mechanisms discussed in the previous sections, asymmetric pressure introduces additional mechanical stress on the catalyst layer. This increases mass transfer resistance and induces irreversible structural

damage, leading to overall performance deterioration [184,220]. Huang et al. demonstrated that increasing the cathode pressure from 1 bar to 30 bar significantly raises the CCM decay rate from 31.4 μV/h to 479 μV/h, representing a nearly 15-fold increase. Additionally, high pressure distribution induces uneven mechanical stress on the catalyst layer, causing surface cracking that further accelerates degradation [221]. The mechanism of this degradation is illustrated in Figure 2.12.

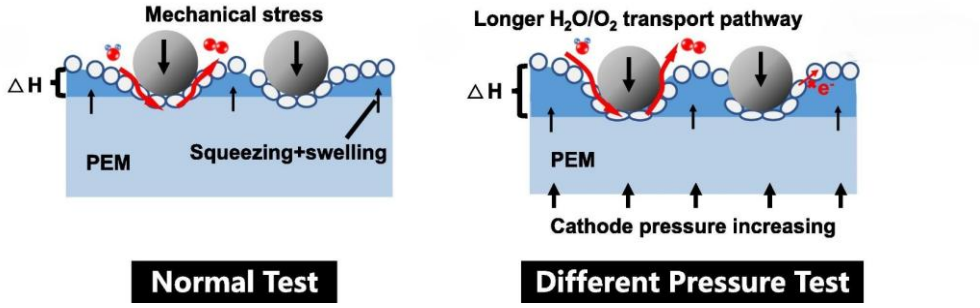

Figure 2.12 Schematic diagram of the cross section of the CCM under the influence of pressure difference [220].

As illustrated in Figure 2.12, structural of CL has a minimal changes under atmospheric pressure conditions. However, with the increasing cathodic pressure, greater mechanical stress is applied on the catalyst layer, extending the transport pathways for water and vapour, and resulting in higher mass transport resistance [209,211,220]. Combined with the previously discussed adverse effects of asymmetric pressure on the membrane, these factors collectively contribute to the accelerated degradation of CCMs. To address this problem, a mesh flow channel (with uniformly distributed square pores of approximately 0.2 mm) has been tested to replace the conventional serpentine design to minimise stress. At a differential pressure of 30 bar, this adjustment reduced the degradation rate from 479 μV/h to 114 μV/h. These findings highlight the differential pressure as a major contributor to CCM degradation. However, even with structural optimisations, degradation under high pressure remains inevitable

when compared to atmospheric operation (31.4 μV/h) [220].

Based on the above discussion, asymmetric pressure impacts not only individual components but also the overall system performance. Therefore, future designs must adopt a cell-level perspective to comprehensively optimise all components, ensuring reliable operation under high differential pressure conditions.

2.7 Summary and perspectives

Proton exchange membrane water electrolysis has emerged as a key technology for green hydrogen production. Advances in membrane modification, PTL surface treatments, and catalyst layer engineering have demonstrated promising improvements in efficiency and durability. However, several challenges remain, as most studies focus on isolated components rather than evaluating their integrated performance within a complete PEMWE cell. This limitation, coupled with insufficient long-term stability data under high-pressure conditions, continues to hinder the transition from laboratory-scale research to industrial deployment.

This chapter has reviewed critical factors influencing PEMWE performance, with a particular emphasis on the challenges introduced by high differential pressure operation. The discussion covered membrane integrity, PTL and BP degradation mechanisms, and CCM durability, highlighting their respective roles in determining overall system efficiency and stability. Various mitigation strategies have been explored, including platinum interlayers for hydrogen recombination, structural modifications to improve catalyst utilisation, and optimised mechanical compression to minimise degradation. While these strategies offer potential solutions, further research is needed to address unresolved challenges, particularly in material stability under high-pressure conditions, interfacial degradation, and scalable fabrication techniques. These will be

part of this PhD research and the efforts will be crucial for advancing durable and efficient high differential pressure PEMWE systems suitable for large-scale hydrogen production.

Chapter 3

Materials and Experiments

3 Materials and Experiments

This chapter describes the experimental procedures employed in this study, focusing on the fabrication of the catalyst-coated membrane (CCM) and the engineering of the electrolyser testing setup. Section 3.1 introduces the specific materials used in these experiments. The main CCM fabrication techniques, including airbrushing, ultrasonic spraying, and decal transferring, are explained in detail in Section 3.2. Section 3.3 covers the electrochemical measurements, such as half-cell test, and single-cell test. Additionally, Section 3.4 presents the physical characterisation methods, including TEM, SEM, XRD, and XPS analyses.

3.1 Chemicals and materials

To facilitate the large-scale fabrication of CCM, commercially available chemicals and materials were selected. These materials were sourced from various suppliers, including the Fuel Cell Store, Ion Power, Sigracet, Bekaert, and others. The details of the materials used are summarised below:

Polymer electrolyte membranes

All membranes were procured from the Fuel Cell Store:

- Nafion® 115, 117, and 212 membranes.
- Fuma-Tech® FS-990-PK and F-10120-PK membranes.
- Aquivion® E98-09S and E98-15S membranes.

Catalysts

- Ir black, supplied by Johnson Matthey.
- PtIrRu and IrO_2 catalyst blacks, purchased from the Fuel Cell Store.
- Ir and IrO_2 catalyst black, from Fisher Scientific, UK.

- Pt/C from Tanaka (TEC10E50E, 46.2 wt% Pt on high surface area carbon).
- Pt/C from the Fuel Cell Store (10% FC,10% Platinum on Carbon XC-72).
- Pt/C from the Fuel Cell Store (20% FC, 20% Platinum on Carbon XC-72).

Ionomer dispersions

The ionomer dispersions used were purchased from the Fuel cell store:

- 25 wt% Aquivion (D98-25BS) and Nafion® D520.

Solvents

The solvents were sourced from Sigma-Aldrich:

- Isopropanol (IPA,≥ 99.5%) and ethanol (≥ 99.8%).

Gas diffusion layers (GDLs) and porous transport layers (PTLs)

The GDLs and PTLs used included:

- Sigracet 25BA and 39BB GDLs from the Fuel Cell Store.
- Toray TGP-H-090 GDL from the Fuel Cell Store.
- Platinised Ti-based PTLs with porosities of 30%, 50%, and 70% from the Fuel Cell Store.
- Platinised Ti-based PTLs with porosities of 56%, 63%, and 77% from Bekaert.
- Ti-based PTLs with porosities of 30% from Anhui Contango New Energy Technology

The water used in the report was deionised to 18 MΩ cm purity using a Millipore water system.

3.2 Fabrication of catalyst-coated membranes (CCMs)

The fabrication of CCMs involves several critical steps to ensure proper adhesion and performance of the catalyst layer on polymer electrolyte membrane (PEM). A brief overview is shown in Figure 3.1. The detailed procedures, including membrane pre-

treatment, catalyst ink preparation, spraying, and hot pressing, are introduced in the following sections.

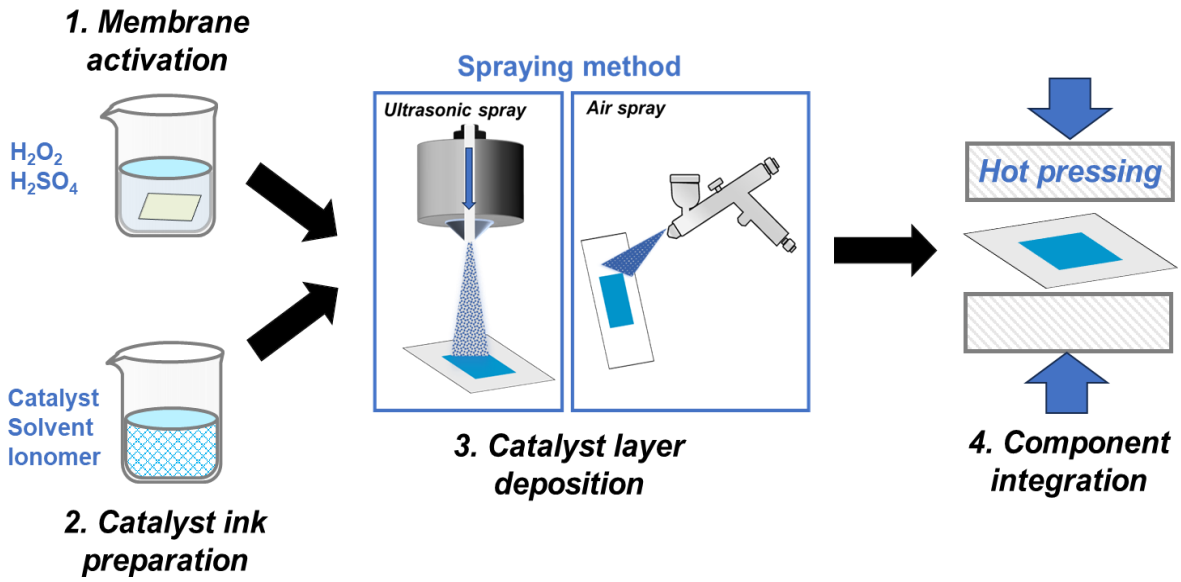

Figure 3.1 Overview of CCM fabrication processes.

3.2.1. Membrane pre-treatment

Before preparing CCM, PEM requires pre-treatment. The hydrophilic (-SO_3H) functional groups within the hydrated membrane form clusters, containing sulfonic acid groups, water, and protons. These clusters, which expand as water content increases, are connected by channels that facilitate proton conductivity [222,223]. The effectiveness of the pre-treatment process is critical for minimising proton transport resistance. The pre-treatment involves a series of activation steps to fully prepare the membrane:

1. Organic impurities removal: The membrane was heated in a 10% (v/v) hydrogen peroxide (H_2O_2) aqueous solution at 80°C for 2 hours to eliminate organic impurities such as glycerol, organic processing additives and some polymerization residues [224].

2. Rinsing: After the H_2O_2 treatment, the membrane was heated in deionised water at 80°C for 1 hour to remove any residual H_2O_2.
3. Protonation: The most crucial step is protonating the membrane using an acid. The membrane was immersed in a 0.5 M sulphuric acid (H_2SO_4) solution at 80°C for 2 hours.
4. Final rinsing: It was then rinsed in deionised water at 80°C for 1 hour to ensure the complete removal of H_2SO_4 traces.
5. Preservation: After the above pre-treatment steps, the membrane was stored in deionised water to maintain its hydration. This ensures that the membrane is ready for immediate use in future experiments without the need for reactivation.

Nafion® 212 was supplied with protective layers; therefore, no activation procedure was required.

3.2.2. Catalyst ink preparation

For the preparation of catalyst inks, catalysts were first dispersed in a solvent prior to the CCM fabrication. The main components of the catalyst ink include the catalyst, ionomer and solvent (isopropyl alcohol or ethanol). The detailed optimisation of variables such as the catalyst solid content, ionomer content, and solvent ratio will be discussed in Chapter 4, and this section presents the optimal recipes for the catalyst inks. The catalysts used for the cathode and anode were 46.2 wt% Pt/C catalyst from TANAKA (TKK) and iridium black from Johnson Matthey (JM), respectively. The preparation process of the catalyst inks is as follows:

Anode catalyst ink:

24 mg of iridium black was added to a mixed solvent of 1000 μL (IPA and water in a 4:1 volume ratio), along with 20.87 μL of 25 wt% Aquivion D98-25BS ionomer dispersion to give an I/C ratio of 25:100.

Cathode catalyst ink:

7 mg of 46.2 wt% Pt/C was mixed with 1000 μL of the same solvent (IPA and water in a 4:1 ratio), and 16.8 μL of 25 wt% Aquivion D98-25BS ionomer dispersion to give an I/C ratio of 69:100. The ionomer content was calculated as the mass of the dry ionomer divided by the total mass of the dry ionomer and catalyst (based on the metal mass). So, the optimal ionomer content in the catalyst ink was 25 wt% at the anode and 69 wt% at the cathode.

To obtain a homogeneous dispersion, the catalyst ink was initially ultrasonicated in an ultrasonic bath (GT sonic-D6) for 30 minutes. This was followed by further ultrasonication using a Sonics VCX-130 ultrasonic tip for an additional 5 minutes in an ice bath to prevent overheating. For the ultrasonic tip, the parameter settings were meticulously defined: the amplitude was set at 30%, and the pulse duration was configured to alternate between 5 seconds on and 5 seconds off.

3.2.3. Catalyst layer spraying method and devices

After the catalyst ink was prepared, it was sprayed immediately onto PEM or a substrate to form a catalyst layer. Two types of equipment were used in this thesis: an air spray gun or an ultrasonic spray machine.

Air spray method

The first spraying method used a spray gun (SPARMAX SP-35) under a nitrogen carrier gas at a pressure of 3 bar, with a gas flow rate of 2 mL/min. The detailed schematic diagram of the airbrush spraying process is shown in Figure 3.2.

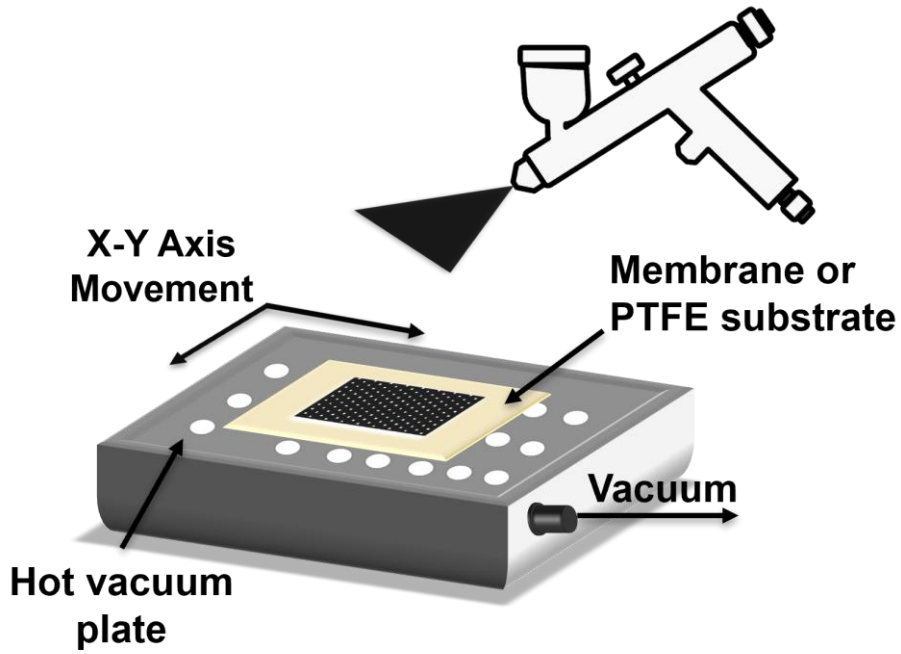

Figure 3.2 Schematic diagram of the air brush spraying for fabricating CCMs.

To ensure efficient drying of the catalyst ink, the hot plate was maintained at 70 °C. Specific cover films with a square empty areas of 5 cm^2, 25 cm^2, and 50 cm^2 were used to cover the substrate, allowing for precise spraying of the active area. During the spraying, the vacuum pump was used to create a vacuum to hold the substrate as well as the gasket. To minimise the potential disturbance of catalyst particles caused by the gas flow, the distance between the spray nozzle and the hot plate surface was carefully maintained at 5 to 6 cm. The nozzle movement followed a coordinated pattern along the x and y axes for each successive layer to ensure uniform spraying of the catalyst layer across various substrates, and the axis movement was manually controlled during the coating process.

Ultrasonic spray

The ultrasonic spraying machine used in this study was the Nadetech spray coating machine. In this system, the catalyst ink was stored in a syringe and delivered to the nozzle via a micro-pump. An ultrasonic wave (at a frequency of 85 kHz) was introduced at the nozzle to shatter droplets and spray them onto the substrate. The whole system is controlled by the central computer, which has a built-in program named ”ND-SP spray coater”. The detailed schematic diagram illustrates the ultrasonic spraying process in Figure 3.3.

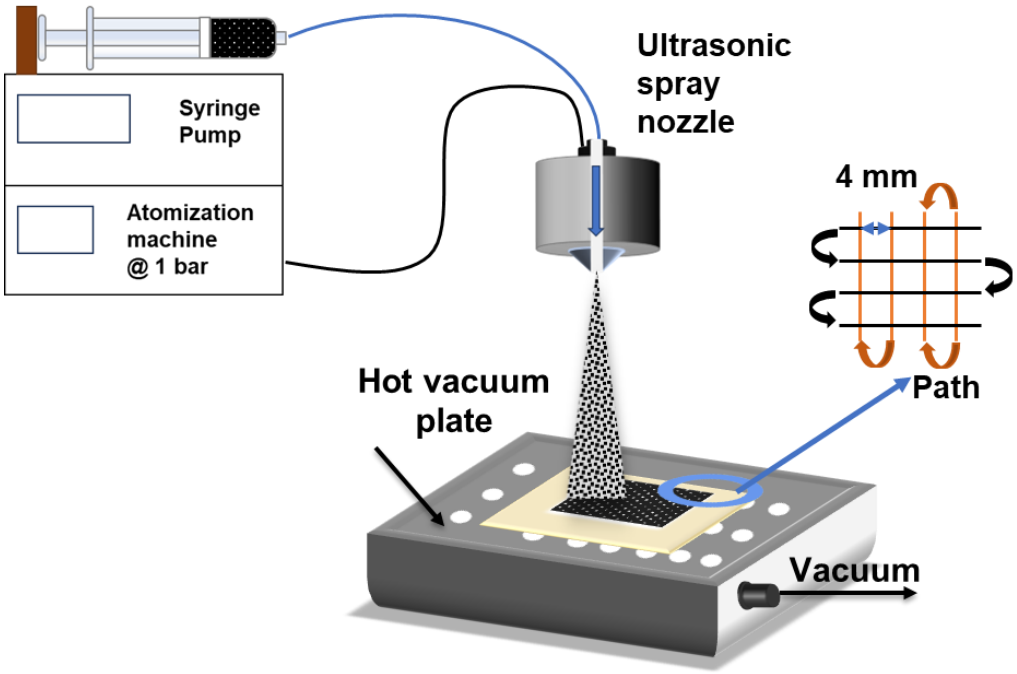

Figure 3.3 Schematic diagram for the ultrasonic spray coating to fabricate CCMs.

The ultrasonic spray coating system purchased from Nadetech is shown in Figure 3.4.

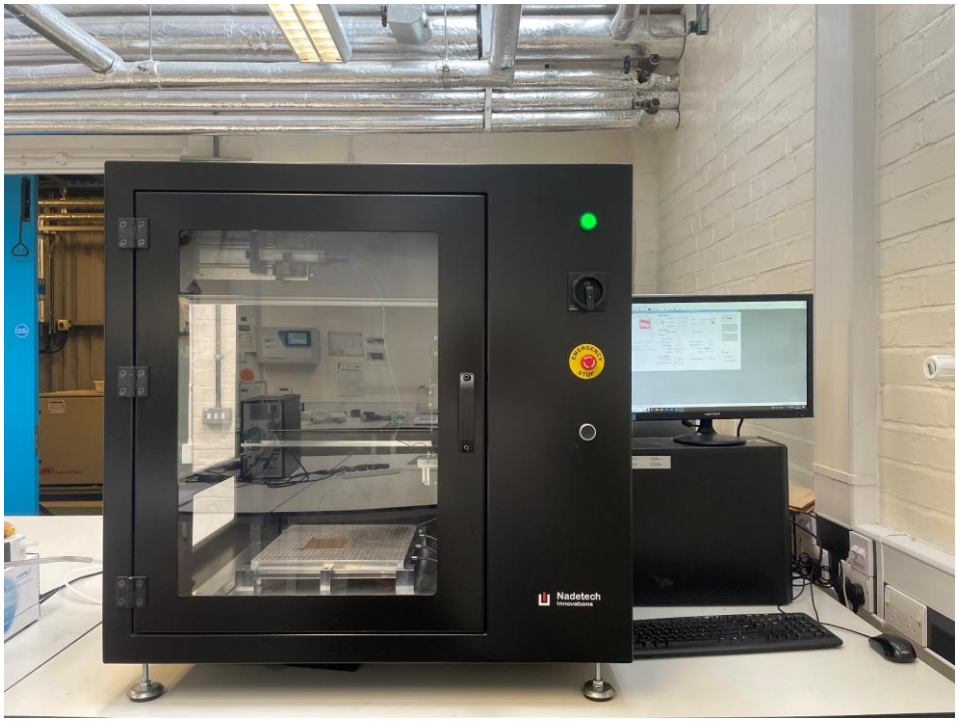

Figure 3.4 Ultrasonic spray coating machine.

Several preliminary experiments were conducted to investigate the effects of different parameters on catalyst layer formation, which will be discussed in Chapter 4. The optimal spraying parameters were determined as follows:

Gas Supply: Compressed nitrogen at a pressure of 1 bar was introduced into the air-focusing shroud to assist spray formation.

Movement Control: The nozzle movement was managed by an x-y-z stage, and its movement was automatically guided along a predefined path, as shown in Figure 3.3.

Spray Pattern: A meander-shaped spray pattern with a 4 mm pitch was utilised for uniform coverage.

Flow Rate: The catalyst ink spraying rate was 15 mL/h.

Nozzle Speed: The nozzle is moved at a speed of 1000 mm/min to ensure even deposition.

Substrate Heating: The membrane substrate was placed on a hot plate maintained at 85 °C to facilitate rapid drying of the sprayed catalyst layer. An example of the parameter settings as configured in the software is shown in Figure 3.5.

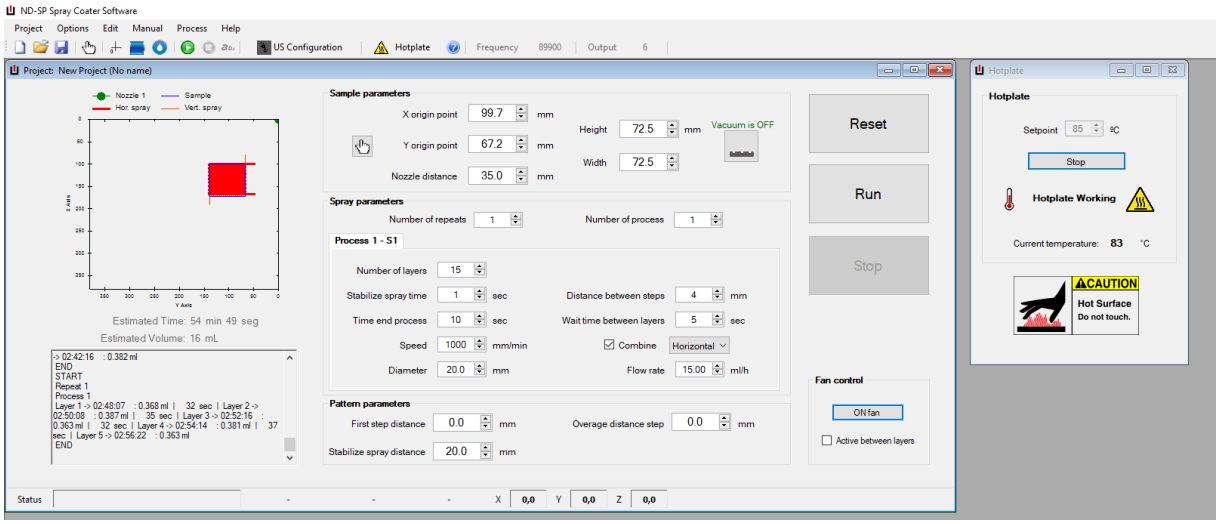

Figure 3.5 Parameter setting for the ultrasonication spraying.

During the spraying process, the nozzle moves alternately in longitudinal and transverse directions. The first layer is applied with a transverse spray (Y-axis direction), followed by a longitudinal spray (X-axis direction) for the next layer, and so on. Each layer of spraying consists of multiple passes with a step size of 4 mm. The "nozzle distance" parameter in the software defines the vertical distance the nozzle moves downward from its starting point. For example, a setting of 50 mm results in a 35 mm distance between the nozzle tip and the membrane surface, given a maximum descent of 85 mm. For the cathode and anode catalyst layers, nozzle distances of 50 mm and 35 mm were selected, respectively.

Under air spraying, a 5 cm^2 CCM takes approximately 30 minutes to complete. In contrast, ultrasonic spraying takes around 40 minutes for the same area, while the preparation of a 50 cm^2 CCM requires approximately 1.5 hours. Considering the catalyst loss during the spraying process, an excess amount of catalyst ink needs to

be prepared. Based on the current experiments, both methods resulted in approximately 60% catalyst loss.

CCM fabrication procedures

To determine the most effective method for fabricating CCMs, two approaches were tested using the described spraying equipment: decal transfer and direct coating.

In the decal transfer method, catalyst ink was sprayed onto a polytetrafluoroethylene (PTFE) sheet, which served as the decal substrate, with the cathode coated first, followed by the anode. The coated substrates were dried at 50°C for at least 1 hour, then assembled with membrane and hot-pressed at 160 lb/cm^2 for 180 seconds. Hot-pressing temperatures were set to 135°C for Nafion/Fuma-Tech membranes and 185°C for Aquivion membranes. After cooling, the PTFE substrate was peeled off to transfer the catalyst layer to the membrane. However, incomplete transfer of the catalyst layer often impacted consistency, limiting the method's reliability.

In the direct coating method, the membrane itself replaced the PTFE substrate, eliminating the catalyst transfer step. Catalyst ink was sprayed directly onto the membrane with loading of 2 mg_{Ir}/cm^2 for the anode and 0.5 mg_{Pt}/cm^2 for the cathode. After coating both sides, the CCM was dried in an oven at 50°C for at least 1 hour. The CCM was then hot-pressed using the same procedure as the decal method to enhance CCM stability. Following performance evaluation, the direct coating method demonstrated superior results compared to the decal method and was subsequently adopted for the later stages of the research.

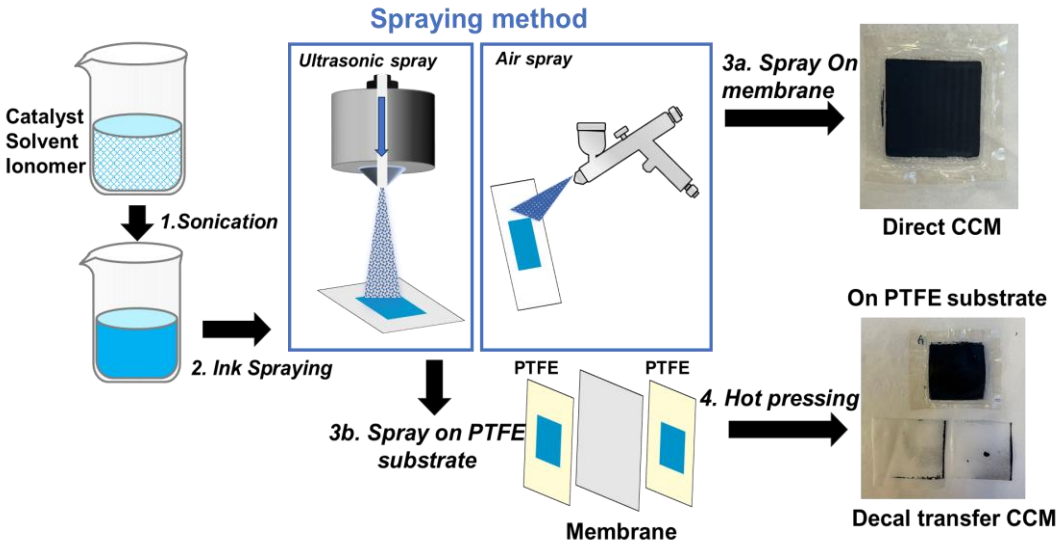

Figure 3.6 Two different CCM fabrication processes.

3.3 Electrochemical characterisation

3.3.1. Electrochemical surface area (ECSA) measurement

To quickly optimise the ionomer content in the cathodic Pt catalyst layer, the half-cell GDE testing method was employed. Compared to the PEMWE single cell test, the GDE test avoids the complex fabrication process of CCMs, saving time and preventing interference from other electrolyser components. The ionomer content was adjusted to 69 wt%, 45 wt%, 25 wt%, 20 wt%, and 15 wt%, with other conditions consistent during the CCM catalyst ink preparation. The catalyst was sprayed onto the GDL (39BB) and tested in an ex-situ GDE half-cell (FlexCell, Gaskatel), as shown in Figure 3.7, and the ECSA was calculated.

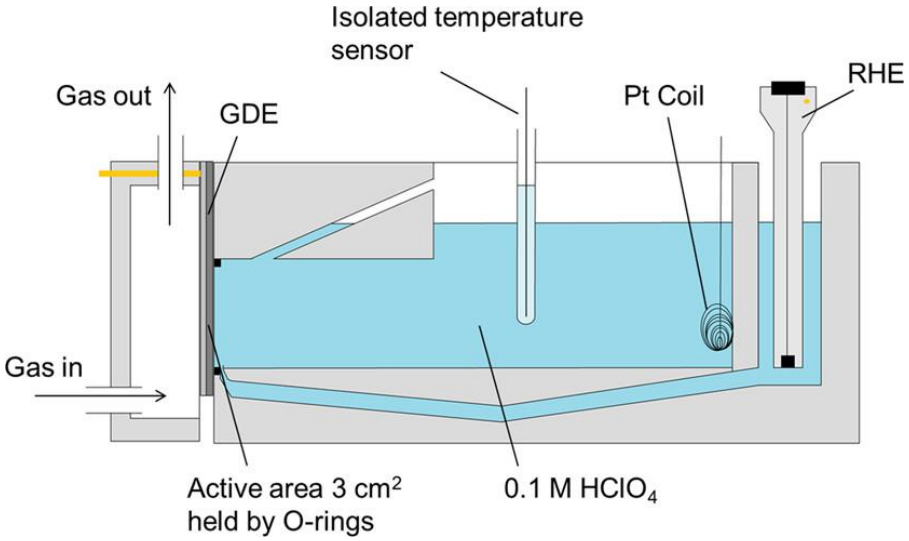

Figure 3.7 Cross-sectional view of the FlexCell setup [225].

The measurement was conducted in a 1.0 M $HClO_4$ electrolyte, with N_2 gas purged for at least 20 min to remove dissolved oxygen. The testing protocol included 100 CV cycles at a rate of 100 mV/s within a potential range of 0.05 V to 1.2 V versus the RHE. Then three slow cycles were performed at 20 mV/s to record data for calculating ECSA of the electrode. A typical CV scan for ECSA measurement is illustrated in Figure 3.8:

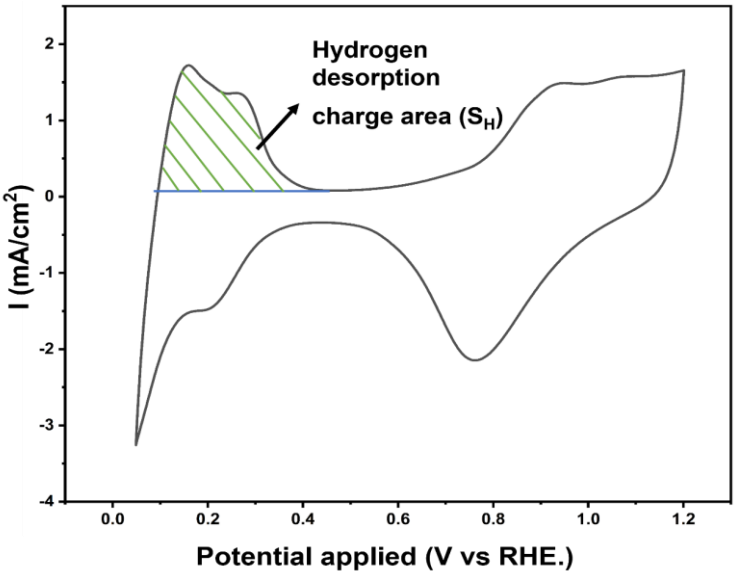

Figure 3.8 CV measurement of the Pt/C catalyst GDE.

The number of electrons measured during hydrogen desorption or absorption process corresponds to the active sites on the catalyst surface. This is defined as the ECSA (m^2 / g) and can be calculated by [226]:

$$ECSA = \frac{Q_H(C)}{210\ (\mu C \cdot cm^2) \times L(mg\ cm^{-2}) \times A_g(cm^2)} \times 10^5 \quad (5)$$

In this equation: $Q_H(C)$ represents the hydrogen desorption charge (in coulombs), and L is the Pt loading on the electrode, A is the geometric area of the electrode. To simplify the calculation further, the equation can also be expressed as:

$$ECSA = \frac{\frac{S_{area}}{v}}{0.21\ (mC \cdot cm^2) \times M_{pt}} \quad (\mathbf{6})$$

Where: S_{area} is the area of hydrogen desorption charge, which can be obtained by integrating the current vs. potential plot (CV curve) in the hydrogen desorption region.

v is the scan rate of CV measurement, and

M_{pt} is mass loading of Pt on the electrode.

3.3.2. PMEWE performance testing (5 cm^2)

To evaluate the CCM performance in an electrolyser, the experiments were conducted using a LeanCat single cell with a 5 cm^2 active area. D.I. water was pumped to the anode side at a flow rate of 10 mL/min using a peristaltic pump. The cell components were assembled with 4 screws, ensuring uniform contact pressure by tightening each screw to 3.5 N·m. Temperature was maintained at 80°C using a controller that monitored the anode, cathode, and inlet water temperatures. The detailed electrolyser system is shown in Figure 3.9 and Figure 3.10

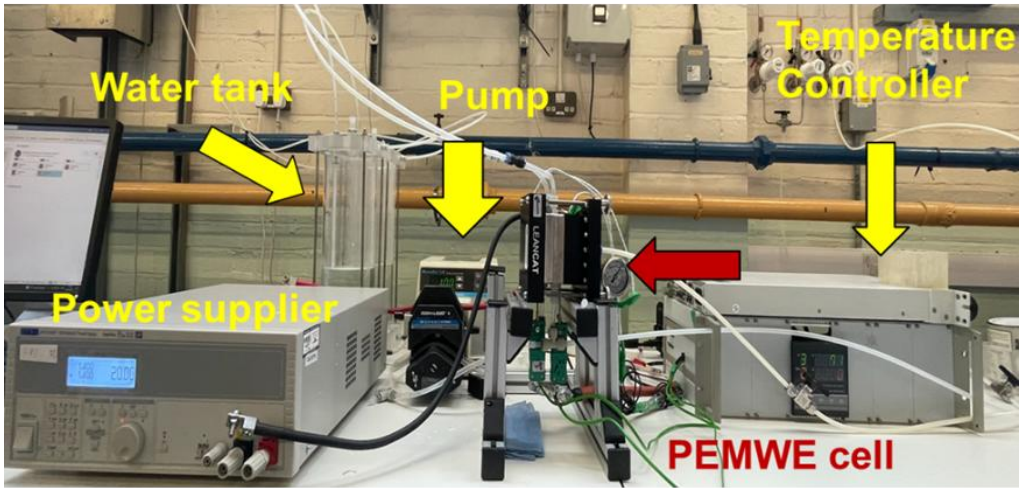

Figure 3.9 Schematic diagram of the testing device with a 5 cm^2 LeanCat testing cell.

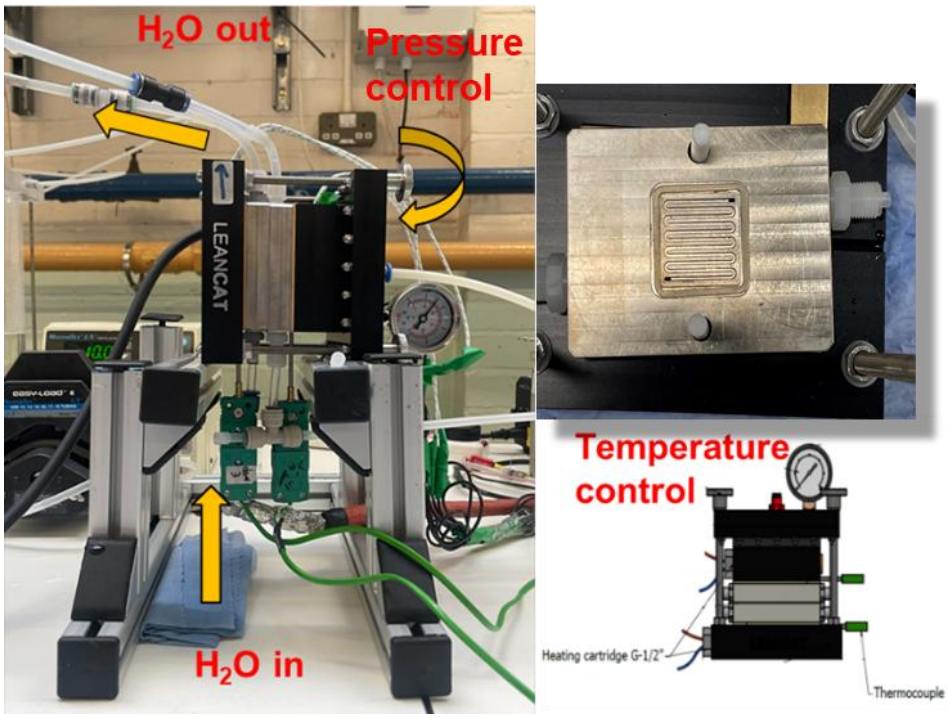

Figure 3.10 Detailed assembling of the testing cell.

Before testing, the electrolysis cell was operated using a conditioning protocol with 20 times of polarisation curve scans to activate the CCM. Polarisation curves (V vs. *j*) were recorded with the constant voltage mode with the cell voltage adjusted stepwise by the power supply and the corresponding current density recorded after 1-minute

intervals. Electrochemical impedance spectroscopy (EIS) analysis was performed with a potentiostat (IviumStat.XRi) at 1.5 V under different conditions, varying the frequency from 100 kHz to 0.1 Hz with an amplitude of 10 mV. The summarised operating conditions are listed below:

Table 3-1 Experimental operating conditions applied.

Condition	Setpoint
Active area	5 cm^2
Cell temperature	80 °C
Water temperature at Anode	80 °C (inlet)
Water flow rate at Anode	10 mL/min
Water quality	Millipore water system (18 MΩ cm)
Assembling	3.5 N·m (4 M6 screws)

3.3.1. PMEWE performance testing (50 cm^2)

The CCM with a large active area was evaluated under high current density and high-pressure conditions using Horiba-Fuelcon Evaluator C50-EC PEM water electrolysis testing system. The 50 cm^2 electrolyser testing cell, provided by Contango (Figure 3.11), can withstand pressures up to 35 bar and features a parallel flow field with 2 mm wide and deep channels. The test station supports pressure differences up to 50 bar and operating temperatures up to 90 °C. The power supply delivers a maximum current of 600 A and a maximum voltage of 30 V. Cell temperature was controlled by the anode water, with a flow rate of 2 mL/(min cm^2) to ensure uniform temperature distribution and sufficient reactant supply to the anode. No flow was applied to the cathode side during

operation. Additionally, thermal insulation cotton covered the electrolyser cell to maintain the target temperature during long-term testing. An ULTRA CLEAR® TP ultrapure water system ensured a consistent supply of high-purity water, while water conductivity sensors monitored water quality at both the anode and cathode inputs. A schematic of the test setup is shown in Figure 3.12.

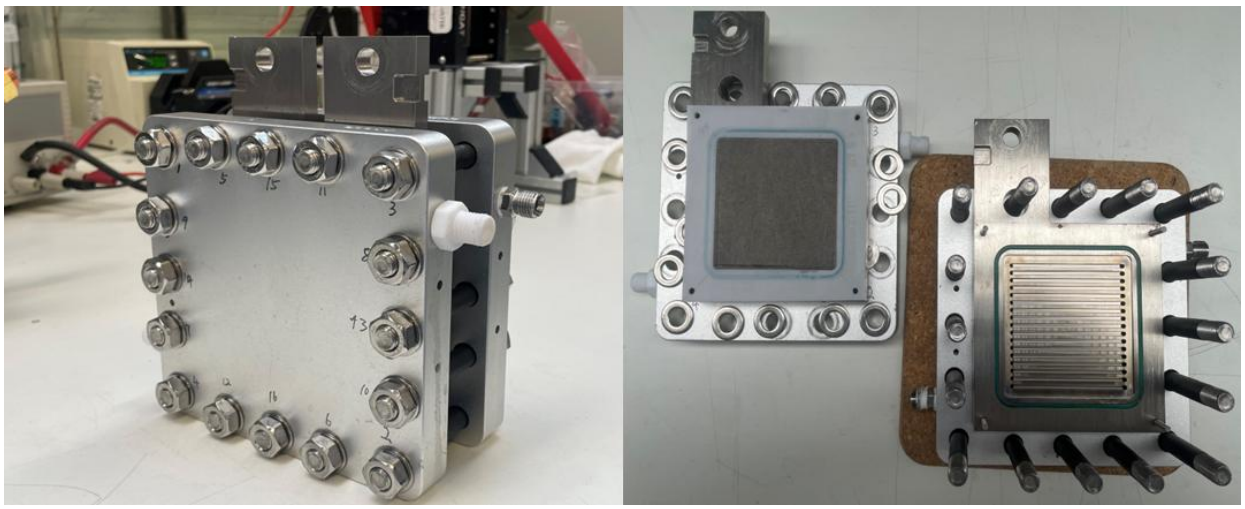

Figure 3.11 Image of the electrolyser testing cell used in HoribaFuelCon testing system.

Figure 3.12 Image of the HoribaFuelCon testing system.

The CCM assembling steps followed the same procedure as that for the small electrolyser cell. On each side of the CCM, 250 μm platinised PTLs were placed, followed by 250 μm PTFE gaskets for proper sealing and leak prevention. The assembly was tightened progressively, starting at 2 Nm and increasing to 4 Nm, 7 Nm, and finally 10 Nm, to ensure uniform pressure distribution. The cell was tested at 70°C or 80°C, with a conditioning protocol applied to activate the CCM before recording polarisation curves, following the same procedures as described for the small electrolyser testing cell. To evaluate performance under high-pressure conditions, the cathode-side pressure valve was manually adjusted (P1090) to the desired value by using the software TestWork (Figure 3.13). The cell was operated at 1.8 V to generate hydrogen until the cathode pressure reached the target level. During operation, the hydrogen content sensor (thermal conductivity sensor) integrated in the testing system continuously monitored the hydrogen content in the anode to ensure safety. Once the

target pressure was achieved, further measurements were performed.

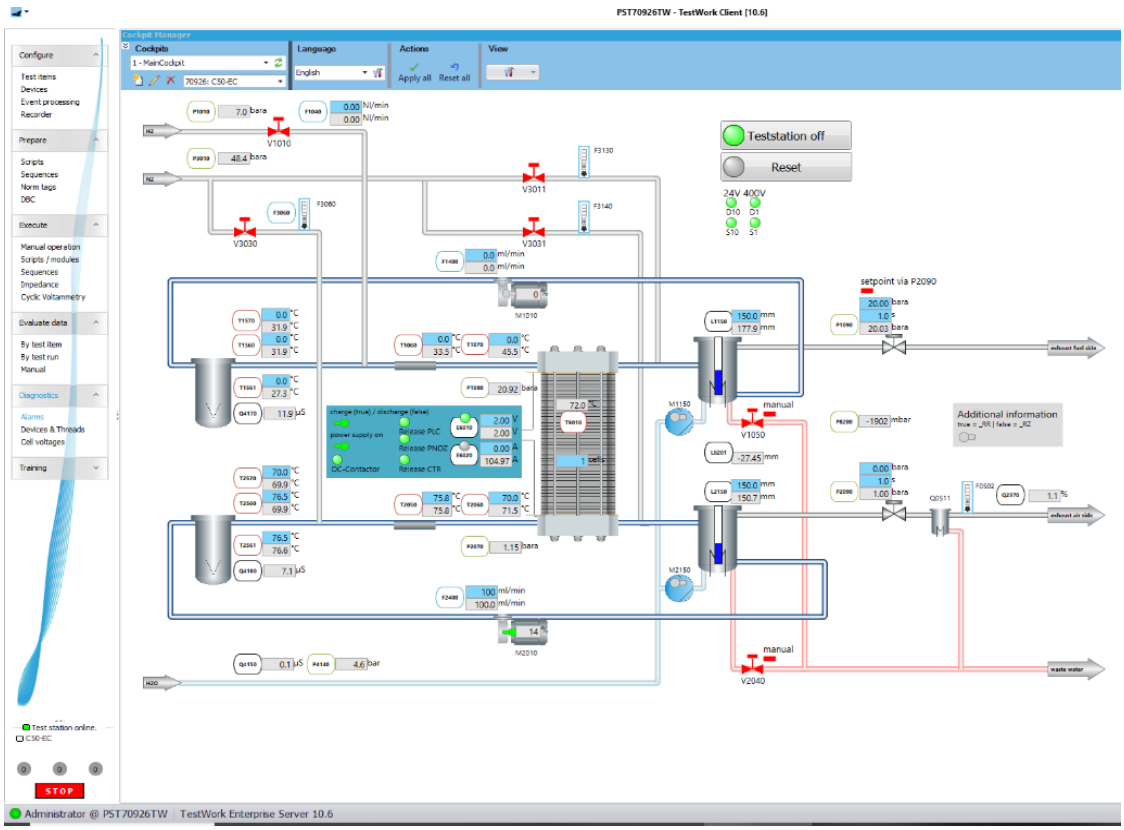

Figure 3.13 Screenshot of a process control software interface (TestWork).

3.3.2. Hydrogen crossover testing

Considering the lower explosive limit (LEL) for hydrogen/oxygen mixtures of 4 vol%, the hydrogen concentration in the anode exhaust was continuously monitored for safety using a Michell XTC601 gas sensor integrated in the Horiba test system. This sensor measures the thermal conductivity of the anode outlet gas to determine hydrogen concentration, with a range of 0–5% and an accuracy of ±2%. A flow diagram illustrating the hydrogen crossover testing system is provided in Figure 3.14:

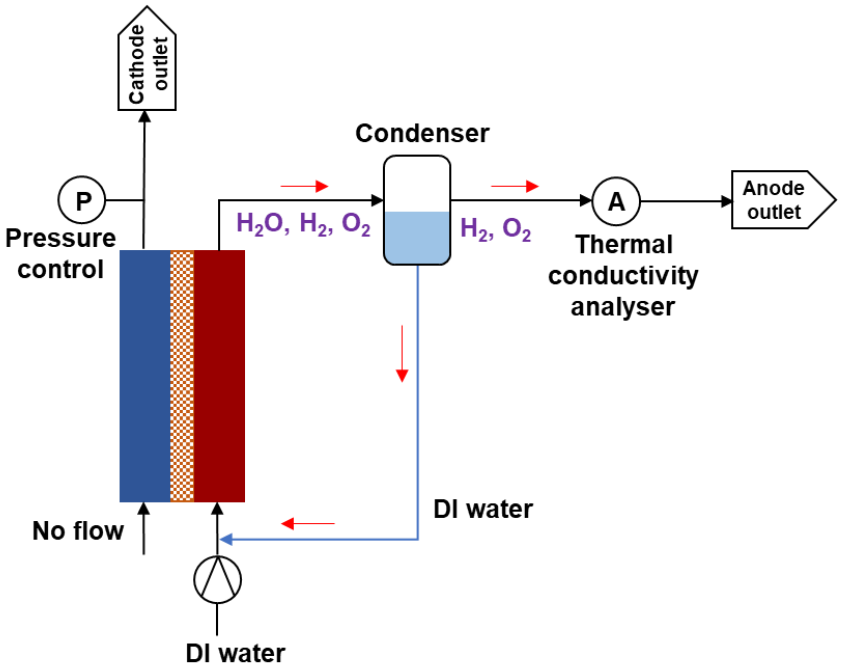

Figure 3.14 Flow diagram of the hydrogen crossover testing in the system.

Before initiating hydrogen permeability tests, the electrolyser and associated pipelines were purged with nitrogen. The operating parameters, including cell temperature, pressure, water flow rate, and water temperature, were set to the desired values and stabilized. Hydrogen content in the oxygen was measured at various differential pressures, achieved by adjusting the cathode pressure while maintaining the anode at 1 bar. The cell was operated in constant current mode, with six current densities ranging from 0.25 to 2.5 A/cm^2. Each step was maintained until the hydrogen crossover stabilised, which required longer times at lower current densities due to the slower gas production rates. For example, steady state was achieved in 6 hours at 0.25 A/cm^2, while at 2.5 A/cm^2, it took only 1 hour.

3.3.3. Accelerated stress testing (AST)

To assess catalyst stability under realistic operating conditions while reducing testing time, an accelerated stress test protocol was employed. The AST cycled between high

and low current densities with idle periods at open-circuit voltage (OCV) to simulate fluctuations encountered when coupling the electrolyser with renewable energy sources. The electrolyser was maintained at 80°C, with a cathodic pressure of 11 bar and an anodic pressure of 1 bar. The anode was continuously pumped with 100 mL/min of deionised water to ensure proper hydration. The AST cycle consisted of three phases: 10 minutes at 3 A/cm^2 (high current), 10 minutes at 0.1 A/cm^2 (low current), and 10 minutes at 0 A/cm^2 (OCV). Each cycle lasted 30 minutes, and the test was conducted for 200 cycles.

3.4 Physical characterisation

3.4.1. Scanning Electron Microscopy (SEM)

The scanning electron microscopy (SEM) analysis was used to observe the microstructure and thickness of the catalyst layer. It was performed using Hitachi TM3030 at an accelerating voltage of 15 kV to image the catalyst layer and porous transfer layer surface. Images were used to measure the catalyst layer thickness and to study the catalyst layer microstructure. The SEM samples were prepared by breaking the CCMs in liquid nitrogen.

3.4.2. Transmission Electron Microscope (TEM)

The transmission Electron Microscope (TEM) analysis was used to analyse the morphology and distribution of the commercial electrocatalyst particles at the nanoscale. To conduct TEM analysis, the electrocatalysts were initially dispersed in IPA using sonication, a drop of the solution was then pipetted onto a Cu grid (CF300-CU) containing a holey carbon film. The electrocatalysts were then left to dry in air and analysed using Jeol 2100 TEM at 200 kV.

3.4.3. Inductively Coupled Plasma – Mass Spectrometry (ICP-MS)

ICP-MS was conducted to measure the catalyst loading of Pt and Ir in the CCMs. A piece of 2 cm^2 CCM were dissolved in 10 mL (50%) of Aqua Regia solution in autoclave at 90 °C for 10 hours. The aqua regia solution was made by diluting 9.45 mL of HCl (37%, Sigma Aldrich) and 3.3 mL HNO_3 (70%). The solution was allowed to cool down and then diluted to approximately 500 parts per billion as well as filtering through a 0.22 um filter to remove any particulate matter. Then the sample was loaded to ICP-MS device (Perkin Elmer Nexion 300X, USA) with a plasma strength of 1500 W. The catalyst loading is determined based on the results of the ICP. To ensure analytical accuracy, each condition was measured by ICP using three independently prepared samples.

3.4.4. X-ray Photoelectron Spectroscopy (XPS)

The X-ray Photoelectron Spectroscopy analysis was used to understand the platinum interlayer coated on the membrane. The measurement was performed with a NEXSA spectrometer (ThermoFisher Scientific) using a 72 W micro focused monochromatic Al Kα source. The results were calibrated using the C 1s peak at 284.8 eV as a reference.

3.4.5. Dynamic light scattering (DLS)

Dynamic Light Scattering was used to assess the stability of the catalyst ink and analyse the particle size distribution of the dispersion. ζ-Potential and particle size analyses were conducted using a Malvern Zetasizer Ultra (1310/103). All tests were performed at 25°C. The zeta potential was calculated using the Helmholtz–Smoluchowski equation. To ensure measurement repeatability, all tests were repeated five times, with error bars in the figures denoting the standard deviation. The

experiments were conducted with diluted iridium inks at a concentration of 0.1 wt%. This section employs the particle size distribution by intensity as it provides more accurate insights into the particle size distribution within the ink.

Chapter 4

Benchmarking set up and testing for PEM water electrolysers

The work presented in this chapter has been accepted as *'Challenges in Scaling Up Testing of Catalyst Coated Membranes for Proton Exchange Membrane Water Electrolyzers'* to Frontiers in Energy Research: Front Energy Res 13 (2025) 1557069. https://doi.org/10.3389/FENRG.2025.1557069/BIBTEX.

4 Benchmarking set up and testing for PEM water electrolysers

The performance of a PEM water electrolyser is influenced by a variety of factors, including assembling force, water flow rate, porous transport layer (PTL) properties, and membrane selection. Variability in these parameters not only impacts experimental reproducibility but also affects critical performance indicators such as current density, voltage efficiency, and system stability [227,228]. For instance, improper assembling force can result in uneven contact between components, while inappropriate water flow rates may lead to insufficient membrane hydration and overall performance. These complexities highlight the necessity of a systematic approach to optimise key parameters and establish robust testing protocols. This chapter investigates the influence of these variables on electrolyser performance, focusing on the development of an optimised setup for both small-area (5 cm^2) and large-area (50 cm^2) PEMWE single cell testing. Key parameters, including the assembling force, gasket selection, water flow rates, PTL porosity, and membrane thickness, are systematically investigated to identify optimal configurations. By addressing these factors, this study aims to provide a reliable framework for benchmarking PEMWE performance and ensuring reproducibility across different experimental setups.

4.1 Experimental set-up

With limited prior experience in PEMWE in our research group, the initial setup and optimisation were undertaken to systematically investigate the influence of each key component, with the aim of identifying an optimal configuration to achieve best performance in the electrolyser test. The tests began with a comprehensive analysis of the primary factors using a 5 cm^2 electrolyser (LeanCat), After determining the

optimal conditions, these findings were further validated in the large electrolyser with HoribaFuelCon testing system. An overview of the key PEMWE cell components used in the experimental setup is illustrated in Figure 4.1.

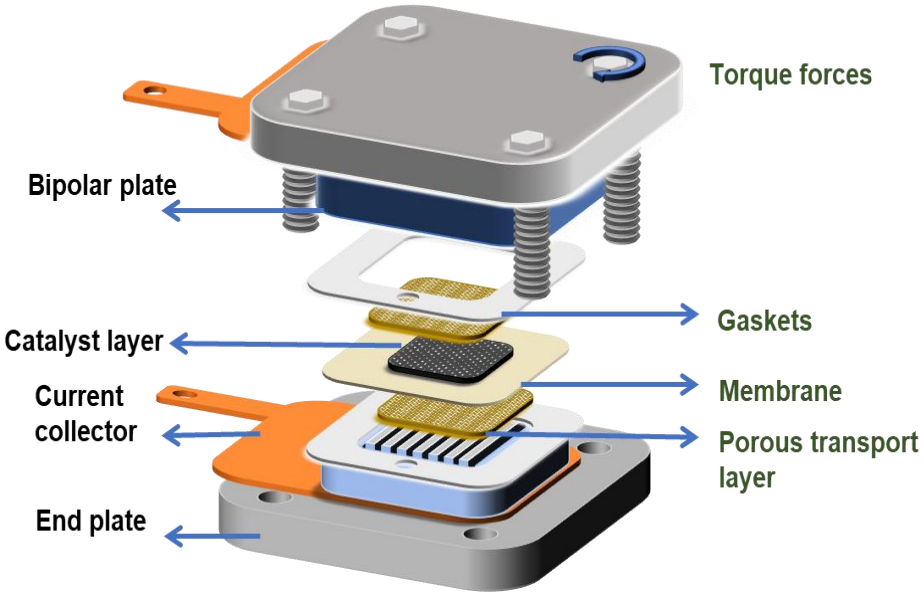

Figure 4.1 Overview of key PEMWE cell components for experimental setup.

4.2 Assembling force

When assembling a CCM in the testing cell, the applied force plays a critical role in performance. To examine the effect of the assembling force, the torque on the screws was tightened, ranging from 2 to 4 N·m. In this study, the polarisation performance of the CCM was evaluated at each torque setting, while all other operating conditions were kept consistent with the standard protocol. To minimise external variables, a commercial CCM (Fumea EF-10) was used, with an anode Iridium catalyst loading of 2 mg_{Ir}/cm^2 and a cathode Pt/C loading of 0.5 mg_{Pt}/cm^2.

To achieve uniform contact across the entire area of the cell components, the assembling force was carefully controlled. The cell was tightened incrementally, beginning with a lower torque value and gradually increasing to the target force. This

staged tightening process helps to evenly distribute pressure across the membrane and PTL, minimising potential issues such as uneven stress distribution or deformation, which could degrade performance or even damage the cell.

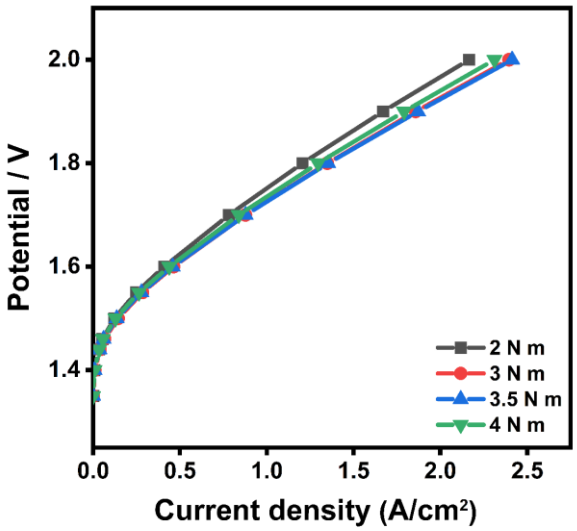

Figure 4.2 Polarisation cures for the CCM under different assembling force.

A comparison of the current density at 1.8 and 2 V are shown in Figure 4.3.

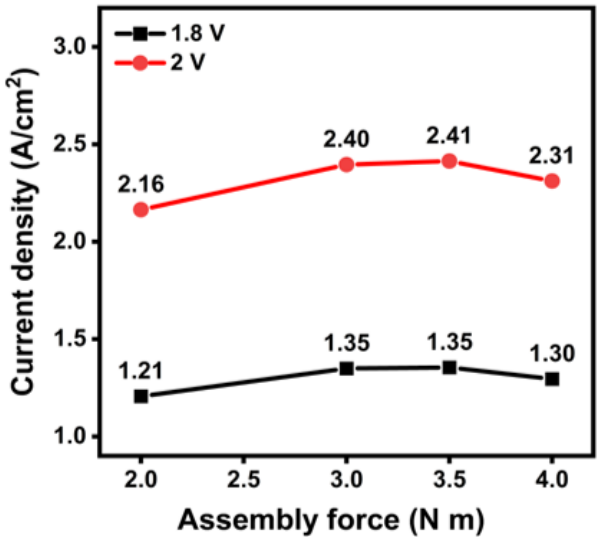

Figure 4.3 Comparison of the current density at 1.8 V and 2.0 V for the testing cell assembled at different torque forces.

As shown in Figure 4.2, the cell current density increases with the assembling force, particularly between 2 to 3 N·m, where the current density at 1.8 V increases notably from 1.21 A/cm^2 to 1.35 A/cm^2. A further increase in torque force provides minimal benefit. When comparing 3 N·m and 3.5 N·m, there is no notable increase, with current density peaking at 2.41 A/cm^2 and 1.35 A/cm^2 at 1.8 V and 2 V respectively, at 3.5 N·m. Beyond this point, a slight decrease in current density occurs, dropping to 1.3 A/cm^2 and 2.31 A/cm^2 at 4 N·m for 1.8 V and 2 V, respectively. This trend suggests that excessive assembling torque force can negatively affect the cell performance. An optimal assembling force enhances the physical contact between the PTL, catalyst layer, and flow field plates, thus enhancing interfacial contact. This observation is consistent with other studies, which report that the optimal clamping pressure reduces the ohmic resistance [177,229,230]. On the other hand, insufficient assembling force may lead to gas leakage and poor interfacial contact, while excessive force poses a risk of damaging the CCM. Based on these results, in the following testing, cells are tightened with a torque force of 3.5 N·m.

4.3 Gasket effect

Besides the assembling force, the gasket plays a critical role as a sealing material to prevent the leakage of water and the generated gases. Proper gasket compression can optimise the interfacial contact between components, contributing to a better performance [231,232]. In this study, PTFE gaskets of various thicknesses (300 μm, 250 μm, and 150 μm) were tested with 250 μm-thick PTLs. This experiment is based on the previous assembling force experiments, and the polarisation curves for each gasket thickness are shown in Figure 4.4.

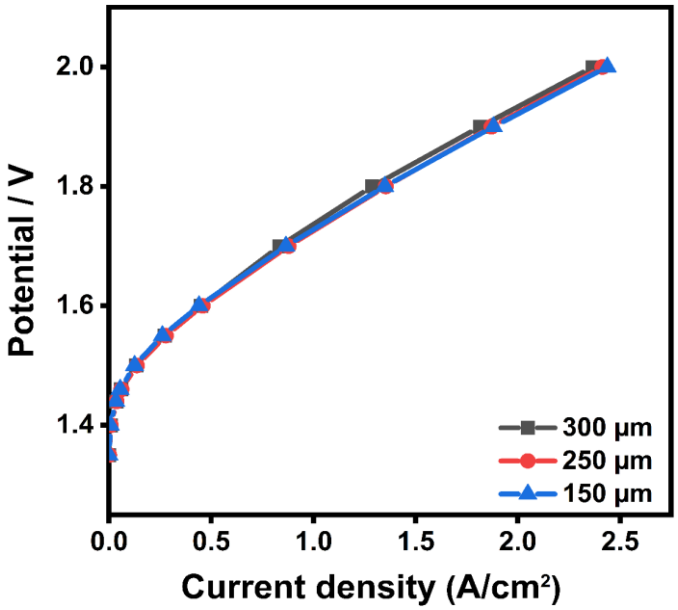

Figure 4.4 Polarisation curves obtained using PTFE gaskets of different thicknesses (300 µm, 250 µm, 150 µm),

The results indicate that gasket thickness has a negligible effect on the overall electrolyser performance. Among all the tested gaskets, the 250 µm gasket exhibits the highest performance among all the gaskets. A thinner gasket (less than 150 µm) causes excessive pressure on the PTL surface leading to deformation of both PTLs and CCMs. Conversely, a much thicker gasket (greater than 300 µm) required an extremely high assembling force; otherwise it would result in poor contact between the CCM, PTL, and the flow field plate. Additionally, it cannot provide a proper sealing, leading to water leakage. A previous study determined that an assembling force between 2 MPa and 3 MPa is ideal for PEM water electrolysers, as it provides sufficient compression for the PTL [177]. In this work, four M6 screws with a torque of 3.5 N·m achieves a pressure of 2.4 MPa, and the 250 µm PTFE gasket under this pressure provides the optimal compression for the PTLs.

4.4 Water Flow Rate

Water flow rate is another critical variable that can impact PEMWE performance. While some studies suggest that water flow rate has a relatively minor effect on the electrolyser, it can help maintain the temperature control and ensuring uniform water distribution within the system, both of which can impact overall performance [233]. Similar to the assembling force, this variable also has an optimal range. An insufficient water flow rate may fail to maintain the membrane hydration and can lead to overheating, whereas an extremely high water flow rate can accelerate catalyst loss through dissolution or erosion effects [229,234–236].

In this investigation, the commercial CCM (Fumea EF-10) was used. The flow rate was adjusted to 5, 10, 15, 20 and 30 mL/min, corresponding to 1 to 6 mL/(min·cm^2) based on the 5 cm^2 effective CCM area. A series of polarisation curves were recorded accordingly, as shown in Figure 4.5. To ensure stable operating conditions, the electrolyser was allowed to equilibrate for 30 minutes at each flow rate before recording the polarisation curve.

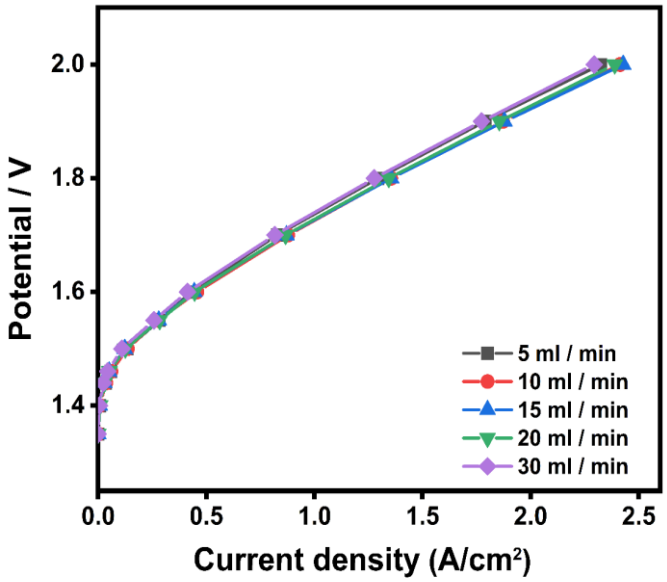

Figure 4.5 Polarisation curves recorded at different water flow rates (5, 10, 15, 20, 30 mL/min).

The results indicate only minor variations in cell performance across the different water flow rates, with a slight decline observed at the lowest (5 mL/min) and highest (30 mL/min) flow rates. For intermediate flow rates between 10 and 25 mL/min, performance remains nearly constant. This trend may be associated with the flow-field design of the bipolar plate. A higher flow velocity can alter the water flow regime, exerting a greater impact on the cell than the mass transport enhancement provided by the increased flow rate. Consequently, performance deterioration may occur at excessively high flow rates [234]. Based on these observations, an optimal flow rate of 10 mL/min, equivalent to 2 mL/(min·cm^2), is selected for further experiments. This rate provides a balance between performance and the operational demands of the water recycle pump and aligns with the flow rate range specified in the “EU Harmonised Protocols for Testing of Low Temperature Water Electrolysers” [236].

4.5 Porous transport layer

The PTL serves a critical function between the flow field plate and the catalyst layer, facilitating both the transfer of water and the removal of produced gases. The properties of PTLs vary significantly due to differences in material composition, porosity, and surface coating, all of which influence single cell performance [25]. In this section, selected PTLs were examined and categorised into two main types: titanium-based PTLs (surface platinization), and carbon-based GDLs. The titanium-based PTLs include various forms from the Fuel Cell Store:

- Ultra-thin sintered: thickness of 0.25 mm, porosity of 33%
- Fibre felt: thickness of 0.25 mm, porosity of 56%.
- High porosity fibre felt: thickness of 0.25 mm, porosity of 73%.

Additionally, some widely used titanium-based PTLs produced by Bekaert include:

- 05N-0.15: thickness of 0.15 mm, porosity of 63%.
- 05N-0.25: thickness of 0.25 mm, porosity of 77%.
- 10N-0.25: thickness of 0.25 mm, porosity of 56%.

The carbon-based GDLs assessed include Toray TPG-H-090 (0.28 mm), SGL 39BB (0.315 mm) and 25BA (0.235 mm). Due to the vulnerability of carbon-based GDLs to corrosion under the high anode voltage, they are restricted to the cathode side [237,238].

To ensure a consistent evaluation, the commercial CCM (Fumea EF-10) was employed. Throughout the testing, the cell assembly was maintained at an assembling force of 3.5 N·m, and all other relevant parameters were kept constant. Three platinised Ti-based PTLs from the Fuel Cell Store were compared at the anode side, with the 33% porosity PTL used at the cathode side. The polarisation curves are shown in Figure 4.6.

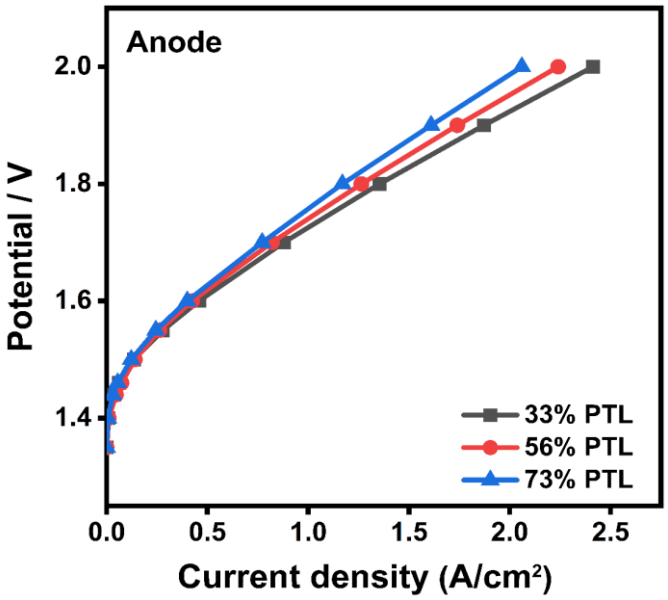

Figure 4.6 Polarisation curves obtained using PTLs from Fuel Cell Store with different porosity at the anode side.

It can be concluded that the performance decreases as porosity increases. The platinised ultra-thin titanium porous transport layer with a porosity of 33% at the anode side shows the highest performance. At 1.8 V, the PTLs with the porosity of 56% and 73% exhibit a decrease in performance by 13.6% and 31.2%, respectively, compared to the 33% porosity PTL. Further performance tests were conducted on the anode side for four different PTL models produced by Bekaert and compared to the best-performing 33% porosity PTL from the Fuel Cell Store. The test results are shown in Figure 4.7. In this experiment, the 33% porosity PTL was also used on the cathode side.

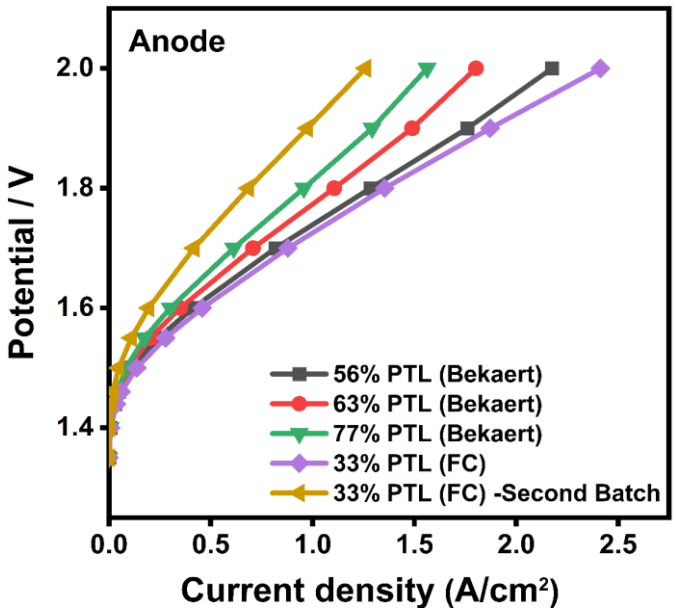

Figure 4.7 Polarisation curves under various Bekaert PTLs at the anode side.

The Bekaert PTLs exhibit a similar trend to those from the Fuel Cell Store: performance decreases as porosity increases. At 1.8 V, the current densities are 1.28 A/cm^2 (56% porosity), 1.10 A/cm^2 (63% porosity) and 0.95 A/cm^2 (77% porosity). Among all Bekaert PTLs, 56% porosity PTL shows the highest performance. However, its performance remains lower than that of the 33% porosity PTL from the Fuel Cell Store, which achieves a current density of 1.35 A/cm^2. However, subsequent experiments reveal significant batch-to-batch variability in Fuel Cell Store PTLs. For instance, in a second batch, the 33% porosity PTL only reaches 0.68 A/cm^2 at 1.8 V, indicating a lack of reliability. Therefore, for all subsequent experiments, the 10N-0.25 (56% porosity) PTLs from Bekaert are used as the anode PTL due to its more consistent performance.

After analysing the porosity effect on the anode side, the effect of PTLs at the cathode side is also examined. Three Bekaert Ti-based PTLs and three GDL-based GDLs were investigated at the cathode side using the commercial CCM (Fumea EF-10). The recorded results are presented in Figure 4.8. The Ti-based PTLs exhibit superior

performance compared to the carbon-based GDLs. This improved performance can be attributed to the higher electrical conductivity of titanium compared to carbon materials. Additionally, the performance trend of Ti-PTLs on the cathode side follows a similar pattern to that observed at the anode side.

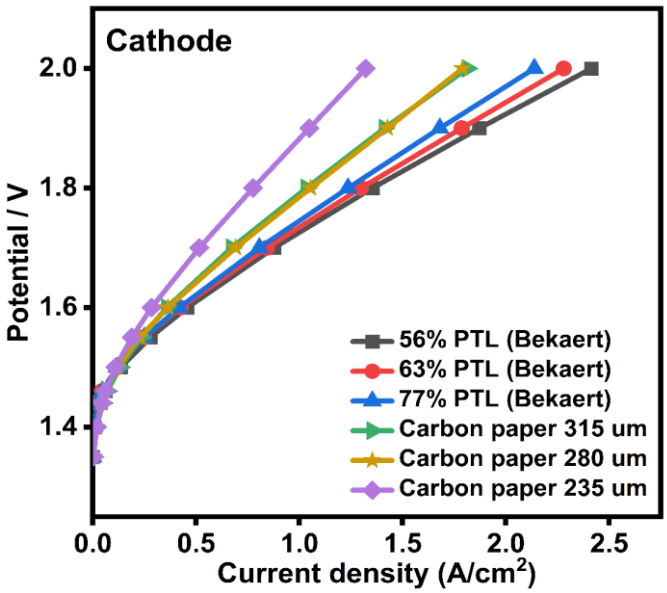

Figure 4.8 Polarisation curves for the test with various PTLs and GDLs at the cathode side.

To gain a deeper understanding of the effect of porosity, the surface structures of PTLs with different porosities were imaged by the SEM analysis, as shown in Figure 4.9. The low-porosity titanium-based PTLs are primarily composed of sintered titanium, whereas the high-porosity carbon-based or titanium-based PTLs exhibit a fibrous structure. The SEM images clearly show that the low-porosity PTLs have a denser surface structure and a larger contact area compared to high-porosity PTLs.

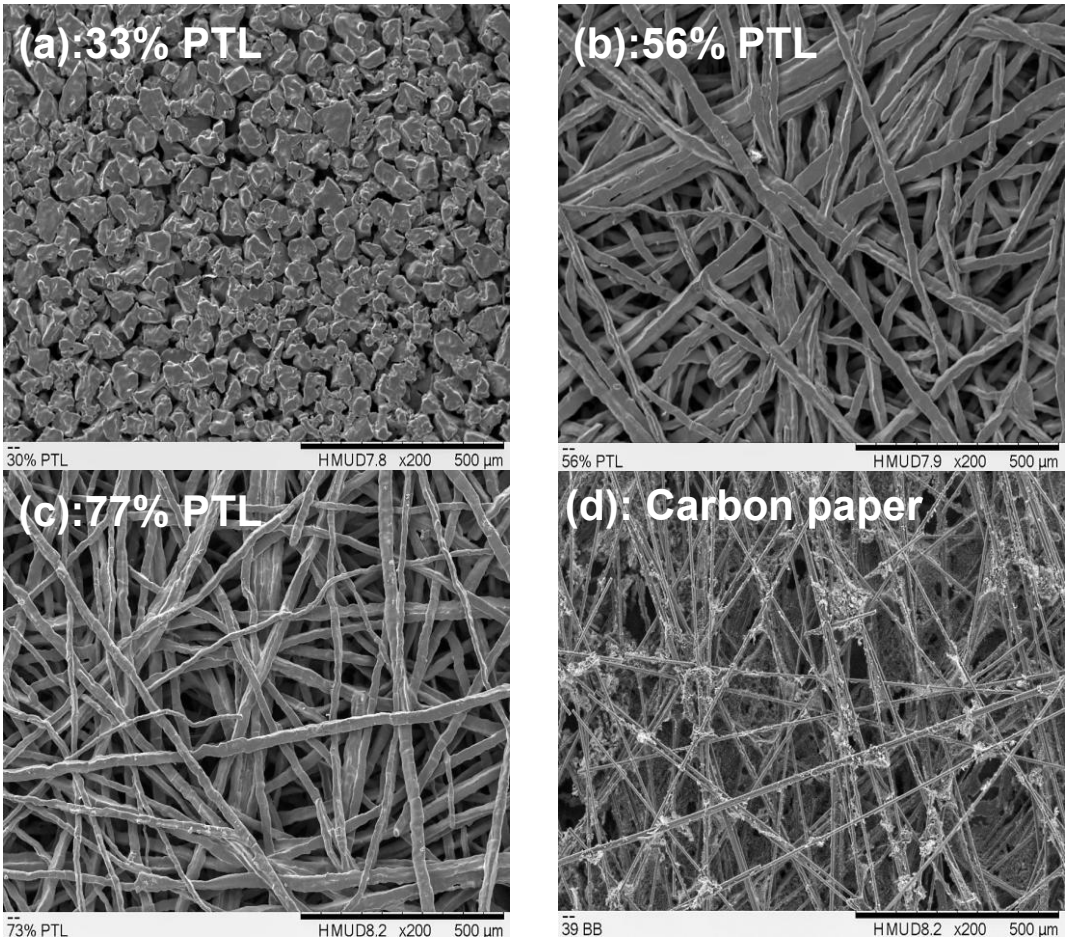

Figure 4.9 SEM images of different PTL surfaces: (a) platinum-coated titanium felt with 33% porosity from Fuel Cell Store; (b) platinum-coated titanium felt with 56% porosity from Bekaert; (c) platinum-coated titanium felt with 73% porosity from Bekaert; (d) carbon paper 39BB from Fuel Cell Store.

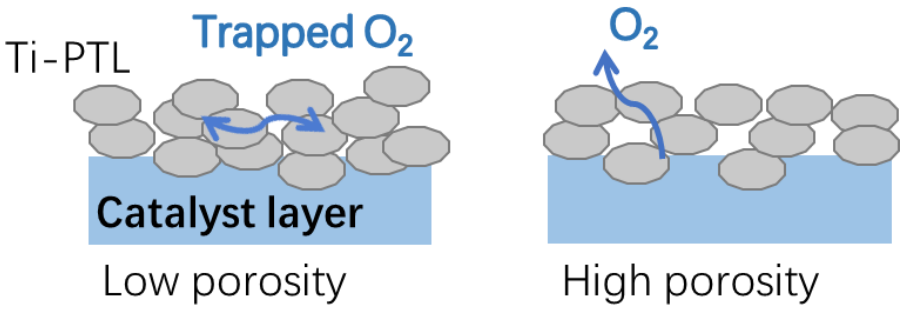

Figure 4.10 Illustration of the effect of the PTL porosity on gas release.

An illustration of the effect of porosity on gas release is presented in Figure 4.10. The

observed performance variations can be attributed to the differences in interfacial contact resistance and gas transport properties. PTLs with lower porosity offer a larger contact area between the PTL and the flow field plate, as well as between the PTL and the catalyst layer, leading to reduced interfacial resistance. However, gas transport is also affected by PTL porosity. Larger porosity facilitates the removal of generated gases, whereas lower porosity may trap gases, resulting in increased mass transport resistance. Previous studies suggest that the optimal porosity range for PTLs is between 30% and 50% [239], while some reports indicate that larger porosities may be beneficial for high current density operation under high differential pressure [141,240].

In this study, only porosity data were available for the commercial PTL materials used, while other structural parameters such as pore size, distribution, and tortuosity were not provided by the supplier. Although the performance trends were discussed primarily based on porosity, it is important to acknowledge that these additional properties also influence mass transport and interfacial contact [241,242].

Therefore, based on these findings, the 56% porosity PTL from Bekaert is selected for further experiments, as it balances the gas transportation and interfacial contact resistance.

4.6 Membrane selection

The membrane is the key component in the CCM, and various membranes with different structures and thicknesses are available from different manufacturers. To evaluate the effect of the membrane thickness, six membranes with different thicknesses, sourced from three suppliers, were tested by a self-fabricated CCM. The specific thicknesses of these membranes are listed in Table 4-1. All membranes were pre-treated according to standard activation procedures to maximise proton

conductivity and ensure reliable baseline measurements. All CCMs were prepared using the decal transfer method to ensure consistent catalyst loading across samples. The anode contained an Ir loading of 2.5 mg_{Ir}/cm^2, and the cathode employed a Pt/C catalyst with a loading of 0.5 mg_{Pt}/cm^2. The ionomer content was specified as 33 wt% for the anode and 69 wt% for the cathode. In the cathode, Pt nanoparticles are dispersed on porous carbon supports rather than being exposed directly. As a result, not all Pt particles are naturally in contact with ionomer. A higher ionomer content is required to ensure more uniform coverage of the catalyst surface, facilitating efficient proton transport to a greater number of active Pt sites [98]. The results of CCM testing are presented in Figure 4.11.

Table 4-1 Membrane specification and the corresponding CCM testing results.

Membrane	**Suppliers**	**Thickness (μm)**	**1.8 V (A/cm^2)**	**2 V (A/cm^2)**
Nafion 212	Chemours	50	1.61	2.94
E98 - 09S	Solvay	90	1.30	2.23
FS - 990 - PK	Fumatech	85-105	1.28	2.14
Nafion 115	Chemours	127	1.27	2.10
E98 - 15S	Solvay	150	1.15	1.95

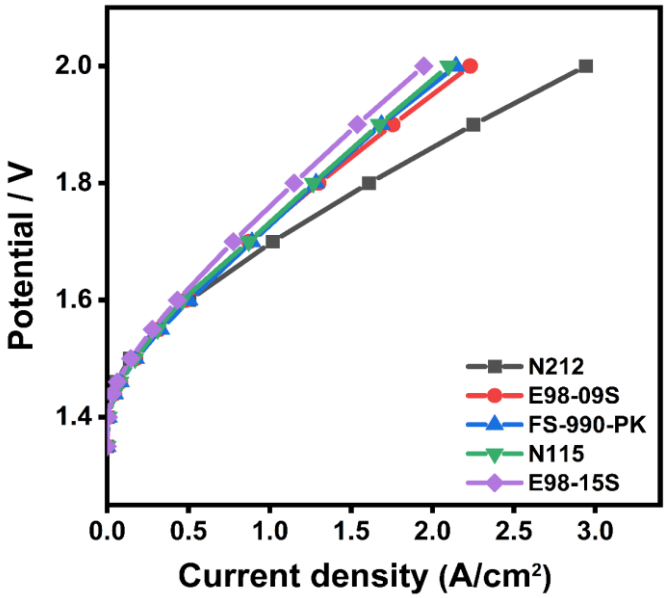

Figure 4.11 Polarisation curves for the CCMs with different membranes.

Based on the polarisation curve results, it can be observed that the performance of the CCM correlates with the thickness of the selected membrane. In other words, the thinner the membrane, the higher the current density generated. This observation aligns with previous findings that proton conductivity increases as the membrane thickness decreases [145]. For N212 (50 μm), which is the thinnest, reaches a current density of 1.61 A/cm^2 at 1.8 V, indicating that thinner membranes enhance electrochemical performance. Conversely, E98-15S membrane from Aquivion® (150 μm), the thickest, the lowest performance, with a current density of only 1.15 A/cm^2 at 1.8 V. These results confirm that increasing membrane thickness reduces proton conductivity, leading to a decline in electrochemical performance.

However, in practical applications, especially for high differential pressure PEMWEs, thinner membranes result in higher gas crossover. Therefore, a good balance between the performance and the gas crossover is essential. Generally, relatively thick membranes (120–200 μm), such as Nafion® 115 and 117, are used in PEMWEs to

ensure low gas crossover and mechanical robustness [38,145]. Thus, considering that the cell operates under a differential pressure of 10 bar or higher in the following experiments, E98-15S membranes are selected for the following experiments to minimise gas crossover while maintaining performance.

4.7 Testing and conditioning method

For PEMWEs, conditioning CCMs is essential for reaching the best performance, and this process may require several hours or even days. The conditioning serves three purposes: (1) removing impurities within the CCMs, (2) activating the catalysts and establishing efficient pathways for water and gas transport, and (3) hydrating the membranes to enhance proton conductivity. However, there is no standardised conditioning procedure for CCMs, and existing protocols involve applying a sequence of stepped potentials or currents to maximize performance. To study the impact of different conditioning methods on CCM performance, a home-made CCM was selected, with the anode contained an Ir loading of 2.5 mg_{Ir}/cm^2, and the cathode employed a Pt/C catalyst with a loading of 0.5 mg_{Pt}/cm^2.The ionomer content was specified as 33 wt% for the anode and 69 wt% for the cathode. Additionally, each conditioning method was tested with a freshly prepared CCM.

1) Excess voltage conditioning method

In this experiment, a high voltage (2.2 V) was applied to the electrolyser for 3 hours to activate the CCM. Studies have reported that applying a high voltage can accelerate activation processes [243]. The polarisation curves for this method are presented in Figure 4.12.

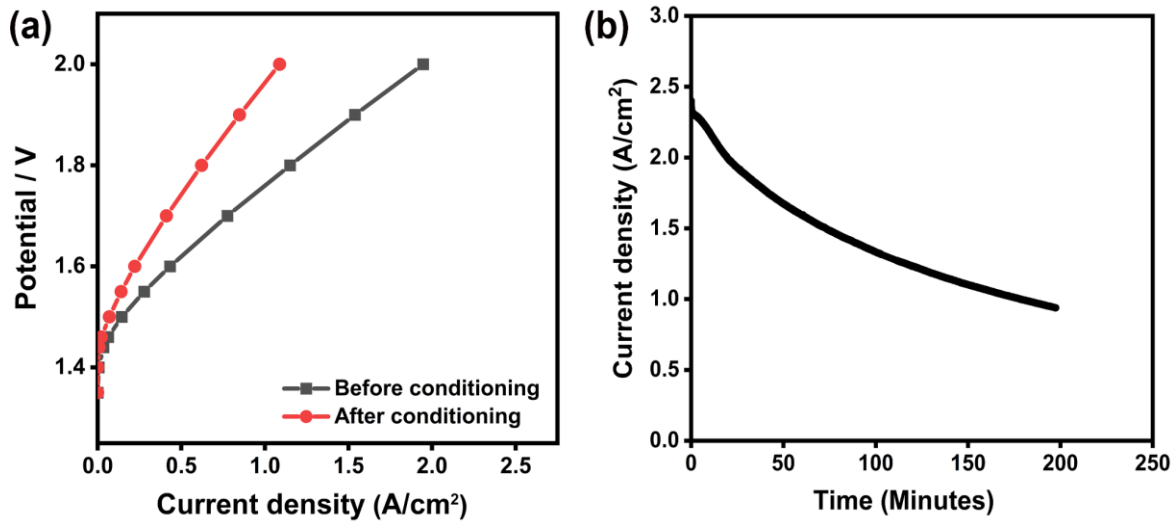

Figure 4.12 (a) Polarisation curves before and after the excess voltage conditioning; (b) The current density decay over time during the conditioning at 2.2 V.

It is obvious that applying a high voltage negatively affects CCM performance. The current density at 1.8 V declines significantly, from 1.15 A/cm^2 to 0.62 A/cm^2. Besides, the conditioning process has been monitored, as shown in the Figure 4.12 (b). Similarly, the current density at 2.2 V decreases dramatically from 2.4 A/cm^2 to 0.9 A/cm^2, without signs of stabilisation. Some studies have indicated that high current or voltage can accelerate catalyst dissolution, thereby reducing both the stability and performance of PEMWE [244,245]. Iridium-based catalysts are relatively stable but begin to dissolve above 1.8 V, forming unstable Ir(III) complexes that rapidly degrade through electrochemical reactions [246]. Although this conditioning method has been reported to be effective for specific CCMs, it was not suitable for the CCM used in this study, which employed iridium black (JM) as the catalyst.

Thus, considering the negative effects observed, this conditioning method is not considered for further use.

2) Step conditioning method

The second conditioning method, adapted from protocols developed by the National Renewable Energy Laboratory (NREL), applies a series of constant current and constant voltage steps [247,248]. The specific steps are as follows:

- 1 hour at 0.2 A/cm^2 (current-controlled)
- 1 hour at 1 A/cm^2 (current-controlled)
- 30 min at 2 V (voltage-controlled)
- 2 hours at 1.7 V (voltage-controlled)

The polarisation curves obtained with this method are given in Figure 4.13.

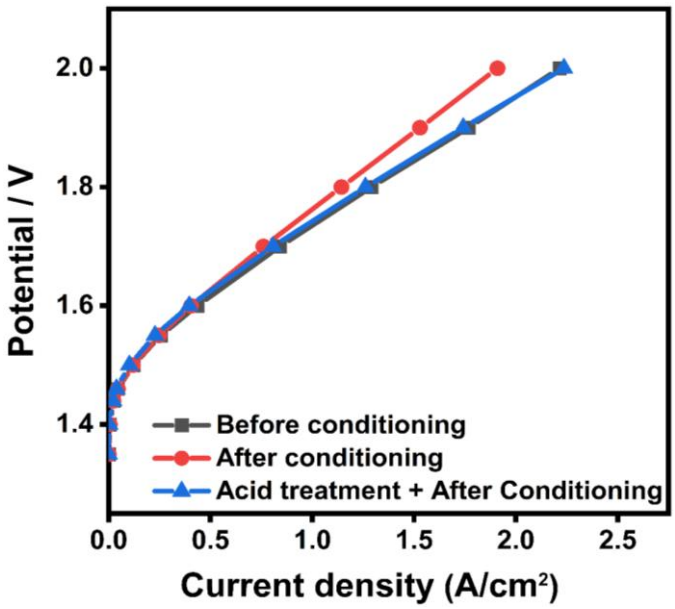

Figure 4.13 Polarisation curves before and after using step conditioning.

With this conditioning method, the CCM shows a performance decline, with the current density decreasing from 1.29 A/cm^2 to 1.14 A/cm^2, a reduction of approximately 11.6%. Compared to the first method, this method uses a moderate voltage (2 V), which may result in less degradation. However, signs of catalyst detachment were observed after conditioning. Other reports suggest that immersing the CCM in sulfuric acid can restore

the CCM performance, so the conditioned CCM was immersed in 0.5 M H_2SO_4 at room temperature for 24 hours [249,250]. After acid treatment, the CCM appears to have regained its initial performance, as shown in Figure 4.13. Based on these results, this conditioning method does not fully enhance CCM performance.

To further investigate the conditioning mechanism, an old commercial CCM (EF-10), which had not undergone prior activation, was assembled in the electrolyser. This CCM was subjected to two conditioning steps: (1) a 10-minute conditioning at a current density of 0.2 A/cm^2 (low current conditioning) and (2) a 10-minute conditioning at 1 A/cm^2 (high current conditioning). The polarisation curves of different conditioning step and the fully conditioned CCM (standard) are shown in Figure 4.14, with a detailed view of the low current range (Figure 4.14 (b)).

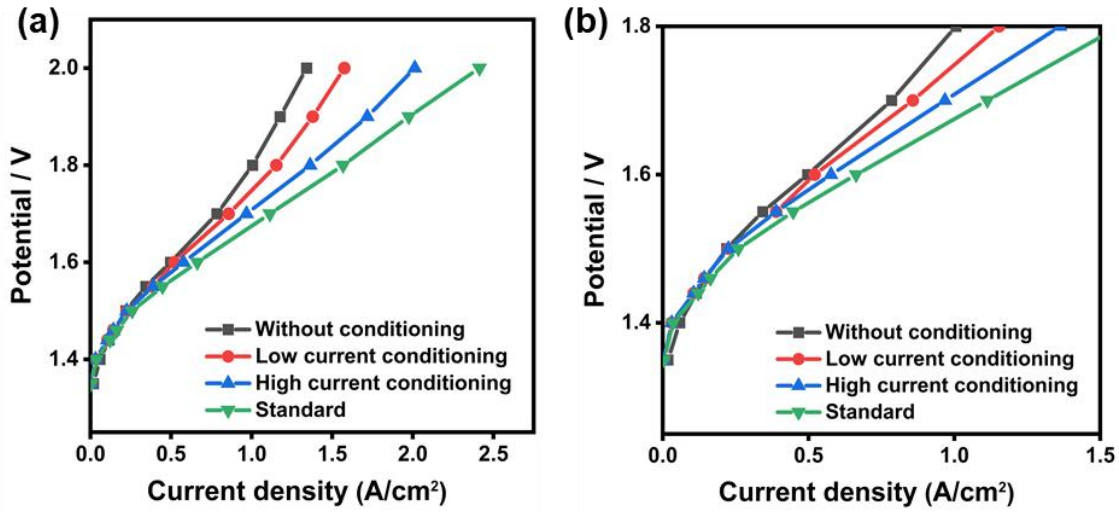

Figure 4.14 (a) Polarisation curves for different conditioning steps; (b) Magnified view of the low-current region.

The results indicate that the initial conditioning step primarily activates the CCMs in the low current range (< 0.5 A/cm^2), while the second step significantly enhances the

performance at the high current density region (> 1.5 A/cm^2), suggesting that the activation process primarily occurs within these operational ranges. Based on these findings, it can be inferred that conditioning is effectively achieved by exposing the CCM to different current ranges. However, only setting the conditioning at some fixed current or voltage with prolonged operation may not fully activate the CCMs. Thus, a more efficient activation strategy would involve a linear voltage sweep from 1.3 V to 2.0 V, ensuring activation across the full operational range. Additionally, multiple short-duration scans (e.g., 1-minute intervals) rather than extended conditioning periods (e.g., 2 hours) may reduce potential degradation effects while still achieving complete activation.

3) Linear voltage sweep conditioning method

Based on the above conclusions and mechanism study, a simplified conditioning method was developed. This method applies a linear voltage sweep from 1.3 V to 2.0 V, repeated 20 times under constant voltage control, with each voltage step held for 1 minute. The corresponding voltage profile during conditioning is shown in Figure 4.15 (a). The total conditioning time is approximately 3 hours. The performance of the prepared CCM after applying this method is demonstrated in Figure 4.15 (b).

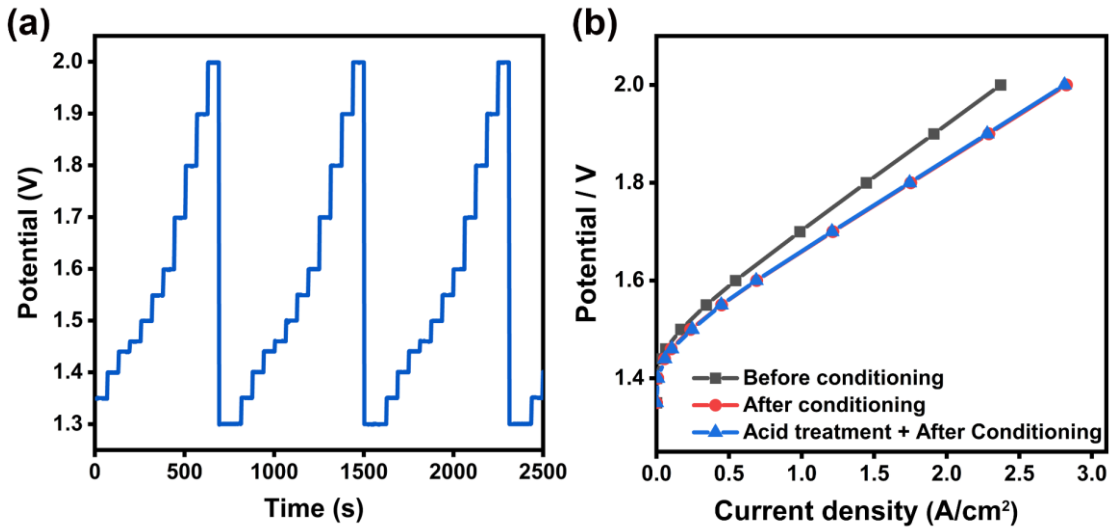

Figure 4.15 (a) Voltage profile during the conditioning (only the first three of 20 total cycles are shown for clarity); (b) Polarisation curves before and after linear voltage sweep conditioning.

The performance shows an increasing trend, with the CCM improving by approximately 21% at 1.8 V, and the acid treatment seems to have a negligible effect on the CCM, which means that this method can maximise the CCM performance. These results demonstrate that this conditioning method is more effective than previously tested methods. Since the CCMs used in this experiment were freshly prepared, aggressive or long-period activation methods were unnecessary. Therefore, this linear voltage sweep conditioning is selected for subsequent experiments, ensuring efficient activation while minimising performance degradation caused by high voltages and extended conditioning times.

4.8 Cell testing with 50 cm^2 active area

Based on the optimal setup conditions identified in previous sections, the homemade 50 cm^2 CCM was assembled in a large electrolyser testing cell from Contango, China. The initial testing revealed extremely poor performance, with a current density of only

0.72 A/cm^2 at 1.8 V. To improve the interfacial contact between PTL and catalyst layer, a series of new assembling methods were designed as illustrated in the Figure 4.16.

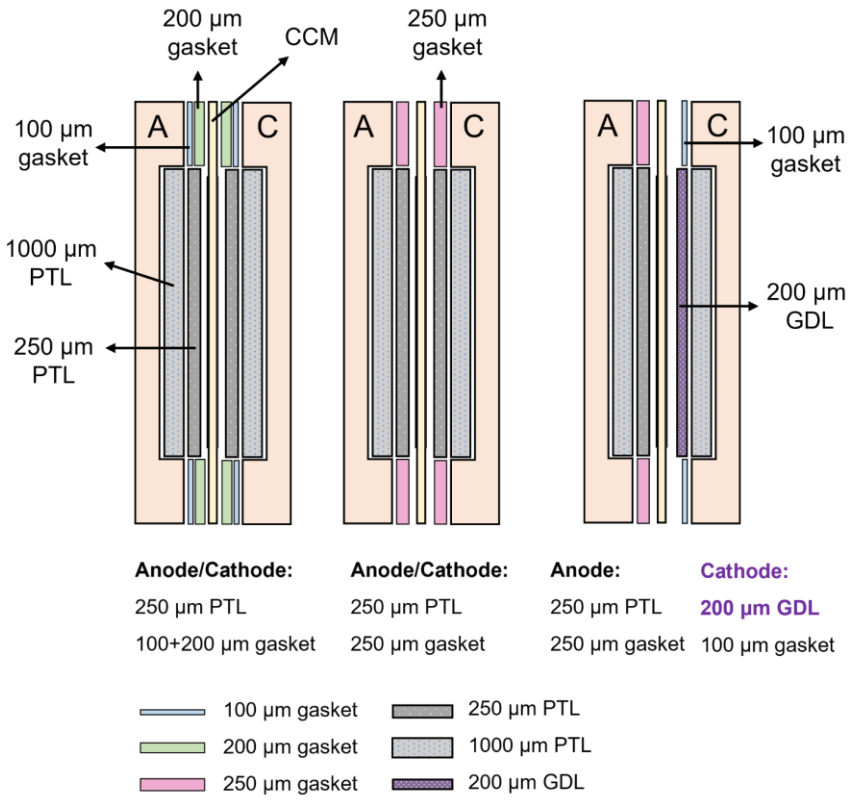

Figure 4.16 Cross-sectional views of different assembly methods for the 50 cm^2 electrolyser testing cell.

In the images above, 'A' and 'C' represent the anode and cathode, respectively. The main difference among the three assembling methods is the arrangement of the PTL and the thickness of the gasket, with all methods using the same assembling torque of 10 N·m (as recommended by the manufacturer). Below is a discussion of each assembling method and its impact on CCM performance:

- **Assembling method 1**: This method uses a thicker PTFE gasket with 300 μm to prevent excessive compression of the PTL. Based on the previous results, a gasket thicker than the PTL may cause inadequate contact between components

and even result in leakage. However, the large electrolyser normally requires a high assembling force to achieve a uniform contact across the entire area, which is essential for optimal thermal, electrical, and mass transport distribution. A higher torque may compensate for this limitation.

- **Assembling method 2**: This method is based on the optimal configuration identified in previous experiments, using a PTFE gasket and PTL of equal thickness (0.25 mm). By ensuring uniform pressure distribution and effective mechanical sealing, this method balances contact resistance and component stability, which may contribute to improved performance.
- **Assembling method 3**: This configuration, recommended by the manufacturer, the titanium PTL is replaced with a carbon-based GDL. Due to its higher compressibility, the GDL allows for more even pressure distribution. However, over-compression of the GDL can significantly reduce its porosity, hindering gas transport and potentially compromising overall CCM performance.

Based on the above analysis, it is clear that material compressibility, applied force, and electrical contact distribution significantly influence overall electrolyser performance. Notably, the issue of membrane swelling also requires consideration, especially for the large area CCMs. During operation, the membrane absorbs water, potentially changing its thickness and shape. This change may result in uneven contact distribution and is the main reason for the poor performance observed in initial tests. Thus, in the practical application, especially for large electrolysers or stacks, the CCM should be sealed to prevent membrane swelling and to maintain optimal contact [232,251,252].To test the effect of the different assembling methods on electrochemical performance, CCMs with 50 cm^2 active area were prepared using the same fabrication process, and the resulting

polarisation curves are shown in figure 4.17.

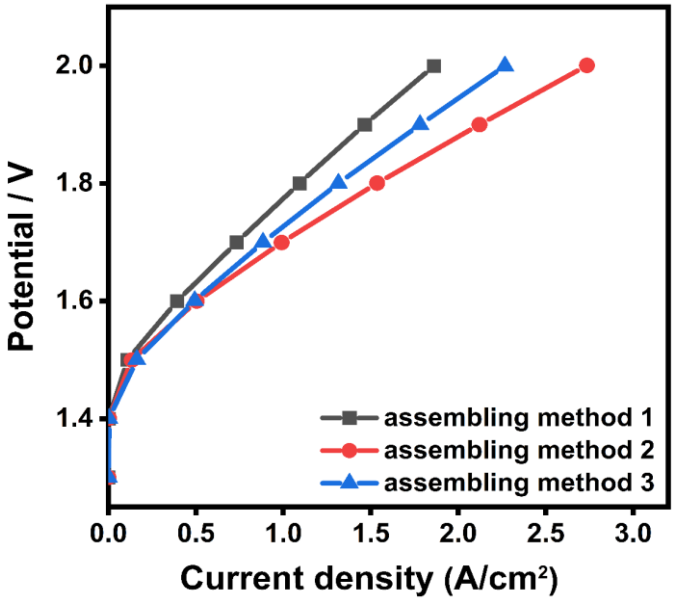

Figure 4.17 Polarisation curves under different assembling methods for the 50 cm^2 CCMs.

Obviously, the second assembling method exhibits a better performance which is consistent with findings from 5 cm^2 testing rig, where the PTL and PTFE gasket had the same thicknesses. In this configuration, the current density reaches 1.54 A/cm^2 at 1.8 V, indicating that a moderate compression ratio optimises performance. The first method performs the worst performance due to the use of a thicker PTFE gasket. Under the same assembling torque, the excess thickness of the PTFE causes insufficient contact between the catalyst layer and PTL, resulting in higher contact resistance and reduced electrochemical performance. At 1.8 V, this method achieves a current density of only 1.17 A/cm^2. In contrast, the third method, which employs a GDL on the cathode, achieves a current density of 1.32 A/cm^2 at 1.8 V. Although the more uniform pressure distribution appears to improve performance, the lower electrical conductivity of the GDL limits further enhancement. In summary, the second

assembling method is the most recommended configuration due to its superior electrochemical performance, which is selected as the standard assembly method for 50 cm^2 electrolyser cell testing in the following experiments.

In addition to the assembly method, the assembling force also needs to be considered. To investigate the impact of different torques on CCM performance, assembling torques of 4, 6, 8, and 10 N·m were applied, with the resulting polarisation curves shown in Figure 4.18.

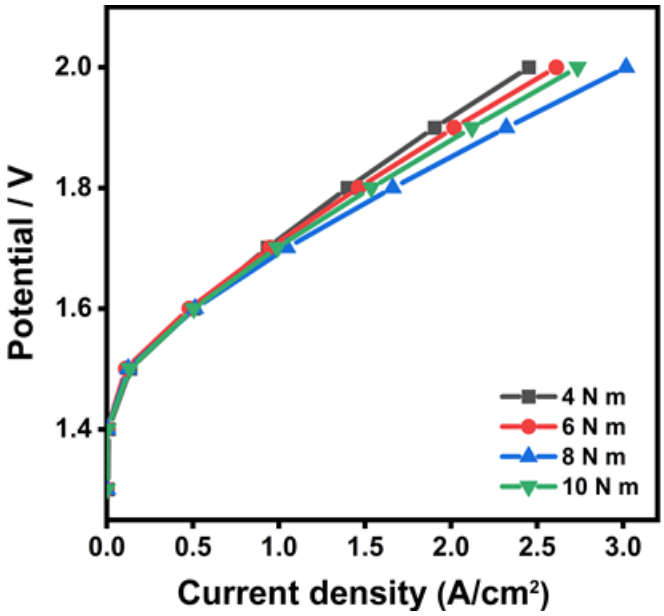

Figure 4.18 Polarisation curves under different torques for the 50 cm^2 CCM.

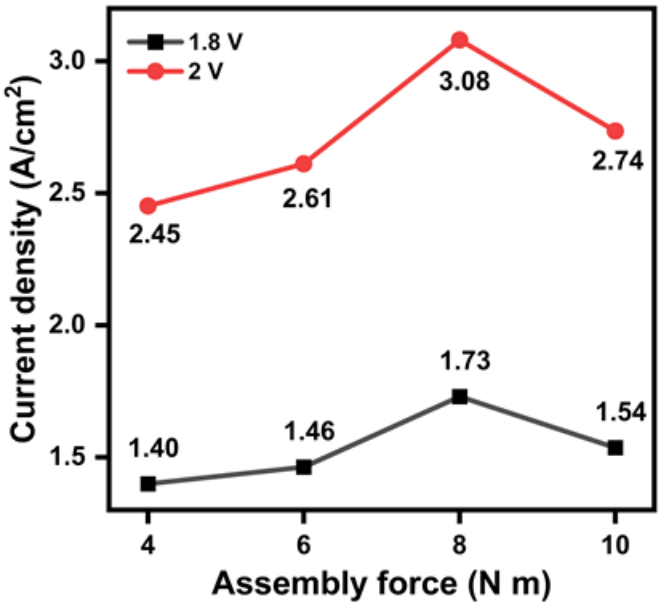

Figure 4.19 Comparison of the current density at 1.8 V and 2.0 V for the 50 cm^2 testing cell assembled at different torque forces.

The above figures (Figure 4.18 and Figure 4.19) indicate that as the torque increases from 4 N·m to 8 N·m, the performance of the CCM improves, with current density rising from 1.4 A/cm^2 to 1.73 A/cm^2 at 1.8 V. However, a further increase in the torque to 10 N·m leads to a decrease in current density, decreasing to 1.54 A/cm^2. Additionally, gas leakage needs to be considered in future experiment. According to the manufacturer's technical manual, the recommended torque range is between 10 N·m and 15 N·m with carbon-based GDL. An increase in assembling force was attempted (12 N·m), causing the CCM to adhere to the PTL and resulting in damage to the CCM. In this study, an attempt to further increase assembling force resulted in the CCM adhering to the titanium-based PTL, causing mechanical damage to the CCM. Additionally, the bipolar plate, with a thickness of only 10 mm, may be susceptible to deformation during long-term testing under higher torque conditions. Although the best performance was

observed at 8 N·m, a torque of 10 N·m was ultimately selected for assembling the 50 cm^2 electrolyser to ensure proper sealing under future high-pressure operation and to comply with the minimum torque recommended by the supplier.

Therefore, the optimal assembling configuration uses the same thickness (0.25 mm) of PTFE gaskets and PTLs, with an assembling force of 10 N·m, as presented in Figure 4.20. This assembling method aligns with the initial configuration used in the 5 cm^2 electrolyser testing cell, demonstrating the best balance between performance and stability for the 50 cm^2 electrolyser testing cell.

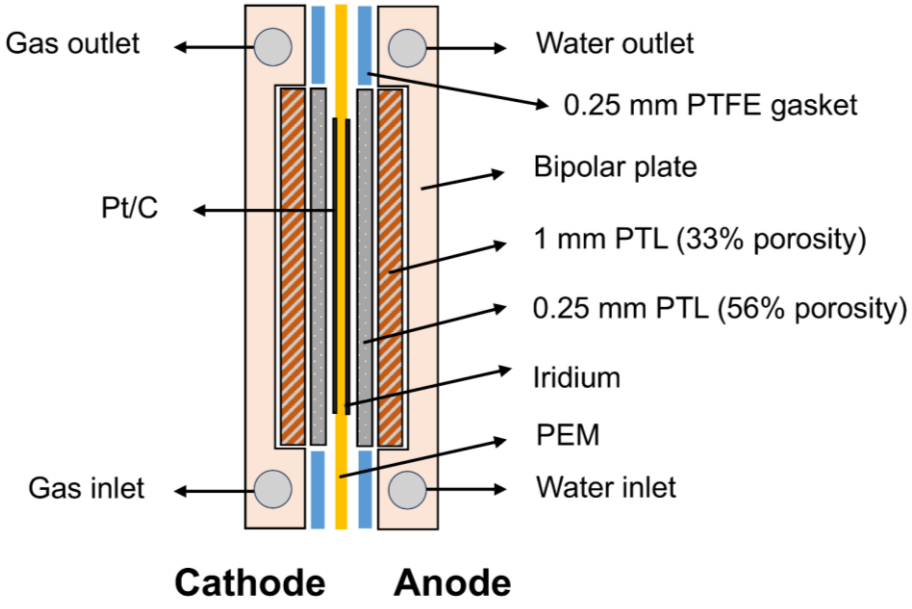

Figure 4.20 Illustration for the optimal assembling method for the 50 cm^2 electrolyser.

4.9 Conclusions

This chapter discusses the benchmarking setup and conditioning procedures for PEM water electrolyser single cell test, providing a standardised testing protocol for future experiments. The study initially evaluated the impact of the assembling method and force, concluding that an assembly torque of 3.5 N·m and a PTFE gasket thickness of 0.25 mm provided the best performance.

Besides, the optimal operating conditions were analysed includes porous transport layer, membrane and water flow rate. The PTL experiment demonstrates that titanium based-PTLs perform better than carbon-based PTLs due to their lower electrical resistance. Among the tested PTLs, the PTL with 56% porosity (10N-0.25 from Bekaert) was selected for its balance between conductivity and mass transfer.

The membrane thickness has a significant effect on overall electrolyser performance: the thinner the membrane, the higher the current density. However, considering the hydrogen crossover issue under a high differential pressure, the thicker membrane (Aquivion E98-15S, 150 μm) was chosen. In contrast, water flow rate exhibits minimal influence on performance, an optimal flow rate of 10 mL/min, equivalent to 2 mL/(min·cm^2),was employed consistent with the European Commission results.

Regarding the conditioning method, three approaches were analysed in this study, with the linear voltage sweep conditioning method demonstrating the significant improvement after application. After applying the optimised configurations obtained in the 5 cm^2 electrolyser cell test, these settings were adapted for the 50 cm^2 electrolyser testing cell with an assembly torque of 10 N·m, while other parameters remained unchanged.

In summary, this chapter provides an in-depth understanding of how the key factors influence the overall performance of PEMWEs, offering a benchmark testing protocol to guide future testing and support the development of high-performance CCMs.

Chapter 5

From catalysts to electrodes in PEM water electrolysers

5 From catalysts to electrodes in PEM water electrolysers

Chapter 4 outlined the standardised setup parameters and procedures for reliably benchmarking the PEM water electrolyser. Based on the previous findings, this chapter delves into the CCM fabrication process, including catalyst ink preparation, catalyst layer deposition, and component integration, with the objective of improving CCM performance. A schematic illustration of the CCM fabrication process is shown in Figure 5.1

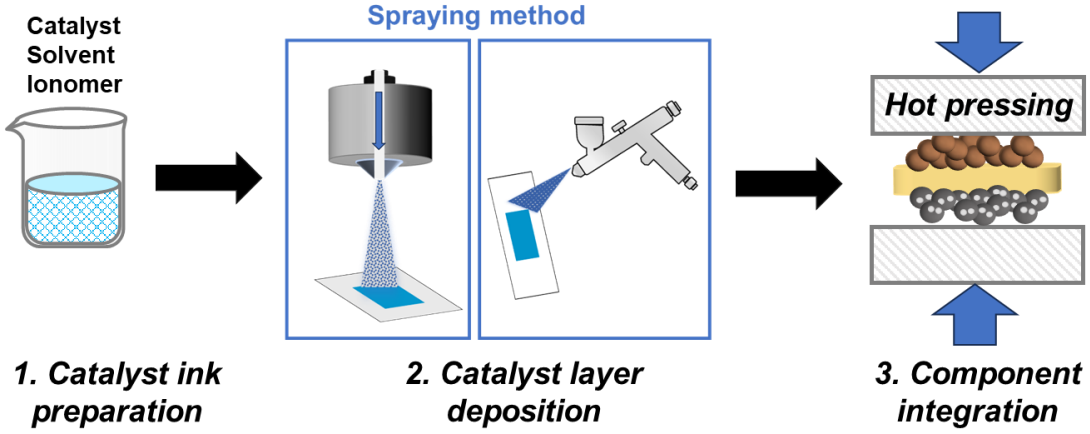

Figure 5.1 Basic fabrication process for CCMs.

5.1. Anode catalyst ink optimisation

To optimise the catalyst ink for fabricating CCMs, various commercial catalysts were evaluated for both the oxygen evolution reaction (OER) and hydrogen evolution reaction (HER). To control the variables, the CCMs were fabricated via decal transfer method, with a metal loading of 2.5 mg_{Ir}/cm^2 for the anode and the catalyst loading of 0.5 mg_{Pt}/cm^2 for the cathode. The ionomer content was set at 33 wt% and 69 wt% for the anode and cathode, respectively. All the CCM tests were conducted in the 5 cm^2 electrolyser testing cell.

5.1.1 Catalyst selection for OER

Four different commercial catalysts were evaluated in this work, including iridium black from Johnson Matthey (Iridium-JM), IrO_2 (IrO_2-FC) and platinum-iridium ruthenium alloy black (PtIrRu-FC) from the Fuel Cell Store; and IrO_2 from ThermoFisher Scientific (IrO_2-thermo). The polarisation curves for CCMs incorporating these catalysts are shown in Figure 5.2.

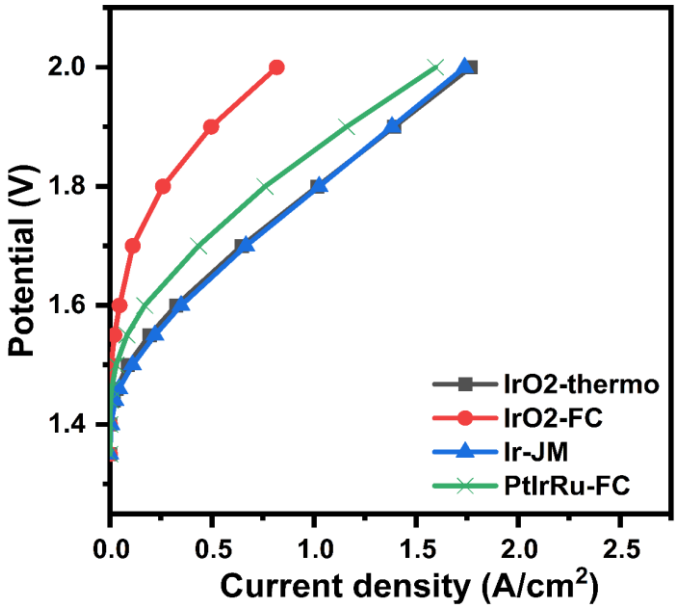

Figure 5.2 Polarisation curves for the CCMs with different OER catalysts at the anode.

Both JM Iridium black and IrO_2 from ThermoFisher show similar electrochemical performance, reaching 1.30 A/cm^2 at 1.8 V. PtIrRu catalyst exhibits lower performance, and IrO_2 from the Fuel Cell Store displays the poorest performance, with a current density of only 0.3 A/cm^2 at 1.8 V. According to the suppliers, the iridium black has a smaller X-ray crystallite size of about 2-3 nm. Both IrO_2 catalysts have an average particle size smaller than 20 nm, and PtIrRu has an X-ray crystallite size of 5-10 nm. To further understand the morphology of the catalysts, TEM analysis (Figure 5.3)

shows that all samples exhibit extensive aggregation, making it difficult to distinguish clear differences in particle size. Iridium black from JM was chosen primarily because it is commercially available in sufficient quantities to support consistent experimentation. Based on electrochemical performance, it was selected for subsequent OER studies.

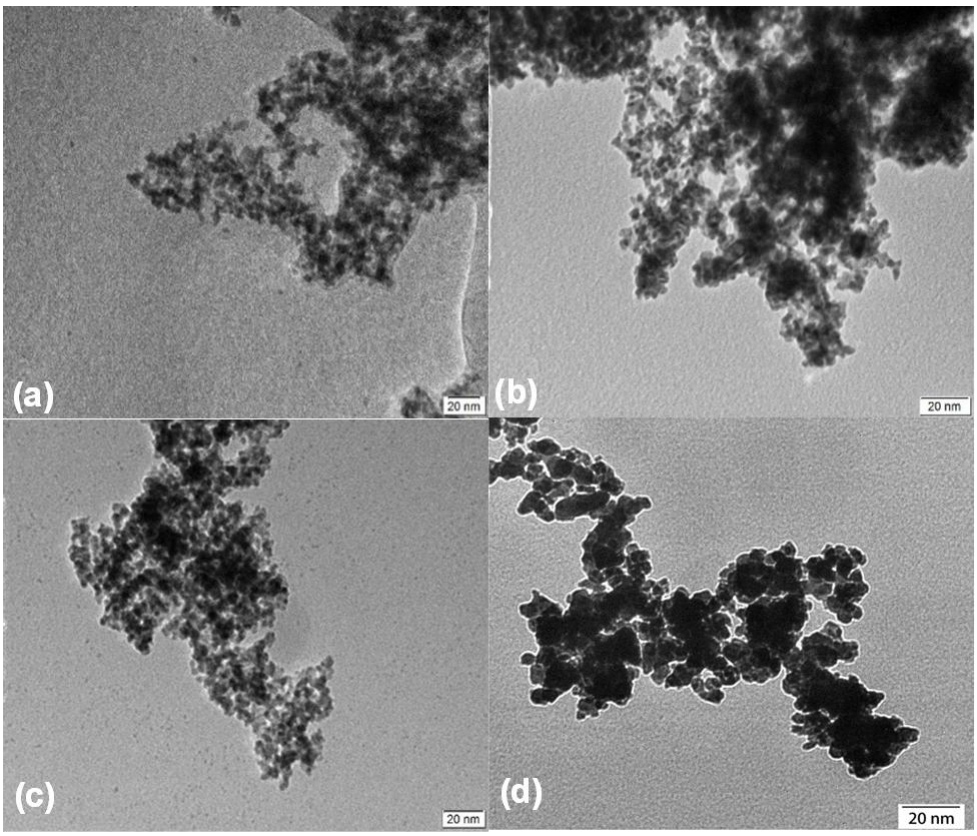

Figure 5.3 TEM images of (a) Iridium black from the Johnson Matthey, (b) IrO_2 from the Fuel Cell Store, (c) PtIrRu and (d) IrO_2 from ThermoFisher.

Thus, the next step focuses on optimising the formulation of the anode catalyst ink to further enhance dispersion stability and electrode performance.

5.1.2 Catalyst dispersion optimisation

5.1.2.1 Solvent optimisation

The solvent serves as a dispersion medium and will evaporate completely after forming the catalyst layer (CL). It can significantly affect the ionomer-catalyst interaction, and the structural integrity of the CL. Isopropyl alcohol (IPA) combined with water is the most commonly used solvent system for catalyst ink preparation for PEMFCs and PEMWEs. This was also adopted for this work, and the IPA-to-water ratio was systematically investigated to identify the optimal recipe for preparing catalyst ink. In this experiment, 24 mg of iridium black was dispersed into 1000 µL of a mixed IPA-water solvent, along with 20.87 µL of ionomer dispersion (D98-25BS). The particle size distribution and zeta potential analysis of the inks prepared with different IPA-to-water ratios are presented in Figure 5.4.

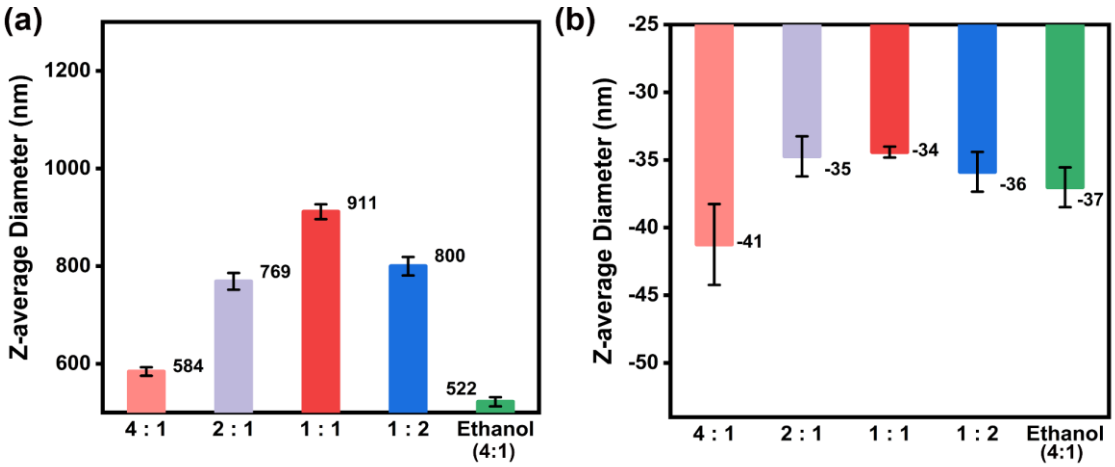

Figure 5.4 (a) Particle size distribution; and (b) zeta potential of the catalyst inks prepared with various IPA: H_2O ratios and ethanol: H_2O at 4:1 ratio.

The results indicate that an IPA-to-water ratio of 4:1 exhibits the smallest agglomerate size (584 nm) and the highest zeta potential value (-43 mV). In contrast, the 1:1 ratio shows the largest particle size and the lowest zeta potential, suggesting poor dispersion stability. These findings confirm that the 4:1 ratio of IPA:H_2O promotes

uniform ionomer-catalyst interaction, which is critical for forming a high-quality catalyst layer. For comparison, the catalyst ink using ethanol (4:1 of ethanol:H_2O) as the solvent was also analysed. Although it produces a smaller agglomerate size of 522 nm, the zeta potential value drops to approximately -37 mV, indicating worse dispersion stability than IPA-to-water ratio of 4:1 sample. The catalyst inks prepared with different IPA:H_2O ratios (4:1 and 1:1) and with ethanol:H_2O at a 4:1 ratio were used to spray the anode CL and then tested in the electrolyser, as shown in Figure 5.5. The CCM fabricated using an IPA:H_2O ratio of 4:1 shows the best performance, achieving a current density of 1.1 A/cm^2 at 1.8 V, which is 22% and 32% higher than that of the CCMs prepared with an IPA:H_2O ratio of 1:1 and ethanol:H_2O at a 4:1 ratio, respectively. Besides, the CL formed using ethanol-based ink exhibited significant cracking compared to those prepared with the IPA system. Such cracks can lead to reduced performance and stability during electrolyser testing. Based on these observations, a 4:1 IPA:H_2O solvent ratio was selected for catalyst ink preparation, as it provides the best balance between particle dispersion and stability.

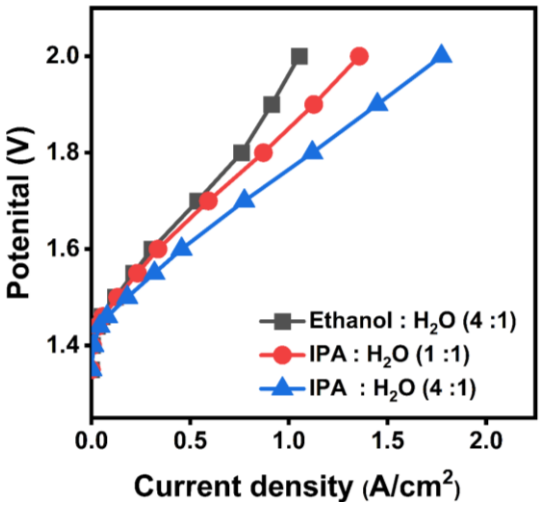

Figure 5.5 Polarisation curves for the CCMs prepared with catalyst inks prepared with various IPA: H_2O ratios and ethanol: H_2O at 4:1 ratio at the anode.

5.1.2.2 Anode catalyst loading

It is crucial to identify the optimal catalyst loading for the PEMWE application to maximise electrochemical performance. The effect of iridium loading is investigated in this study, with values controlled at 0.5, 1.0, 2.0, and 2.5 mg_{Ir}/cm^2, and the ionomer content is fixed at 33 wt% to the catalyst, while all other parameters remain unchanged.

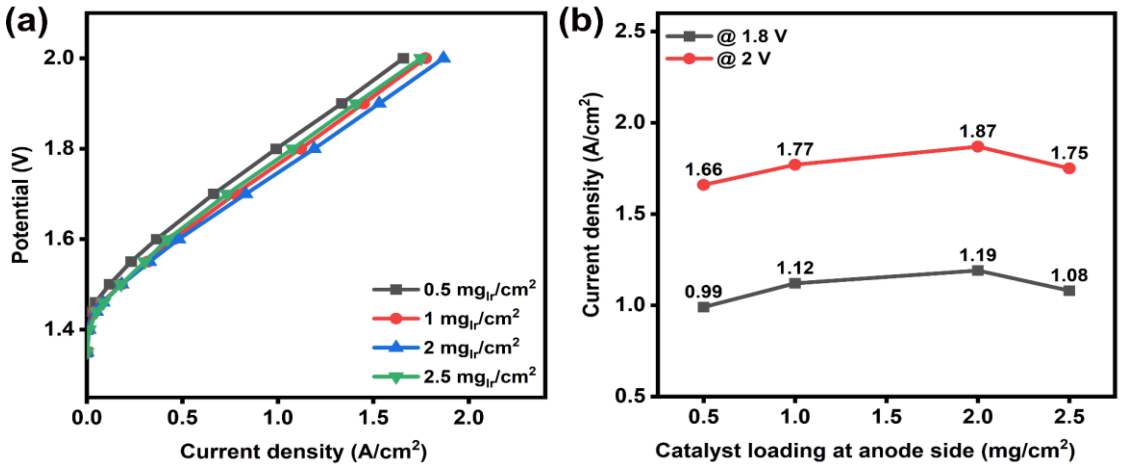

Figure 5.6 (a) Polarisation curves for CCMs with different catalyst loadings at the anode side; (b) Current density at 1.8 V and 2 V as a function of the catalyst loading.

At 1.8 V, as the catalyst loading increase, the current density rises from 0.99 A/cm^2 to 1.12 A/cm^2 at 1 mg/cm^2, reaching a peak of 1.19 A/cm^2 at 2 mg/cm^2, before slightly decreasing to 1.08 A/cm^2 at 2.5 mg/cm^2 (Figure 5.7). At the lowest catalyst loading, the performance is limited by an insufficient number of catalytic sites, which hinders the oxygen evolution reaction (OER). Increasing the catalyst loading to 2 mg/cm^2 provides more active sites, improving the utilisation of the iridium and enhancing the electrochemical activity. However, as the catalyst loading exceeds 2 mg/cm^2, the additional material forms a thicker catalyst layer, resulting in increased ohmic and mass transfer resistance, which ultimately reduces performance despite the higher catalyst

amount. Based on these findings, an anode catalyst loading of 2 mg_{Ir}/cm^2 was identified as the optimal value for achieving the best electrochemical performance.

5.1.2.3 Ionomer-to-catalyst ratio

The ionomer is a critical part of the catalyst layer, as it (i) enhances proton conductivity from active sites to the membrane, (ii) increases the electrochemical surface area, (iii) binds catalyst particles, and (iv) ensures the mechanical stability of the catalyst layer during both fabrication and operation. [253,254]. In addition, the ratio of ionomer to catalyst (I/C ratio) plays a crucial role in determining both the microstructural and macroscopic properties of the catalyst ink, which significantly influence the catalyst layer structure [255–257].

To investigate the ionomer content effect, various ionomer contents were selected for the anode side: 33 wt%, 25 wt%, 20 wt% and 15 wt% to fabricate CCMs. These weight ratios correspond to the dry ionomer content relative to the total catalyst mass. The catalyst loading was maintained at 2 mg_{Ir}/cm^2 for the anode and 0.5 mg_{Pt}/cm^2 for the cathode. The ionomer content was set at 69 wt% for the cathode. The current densities recorded at 1.8 V and 2 V for these ionomer contents are shown in Figure 5.7 (b).

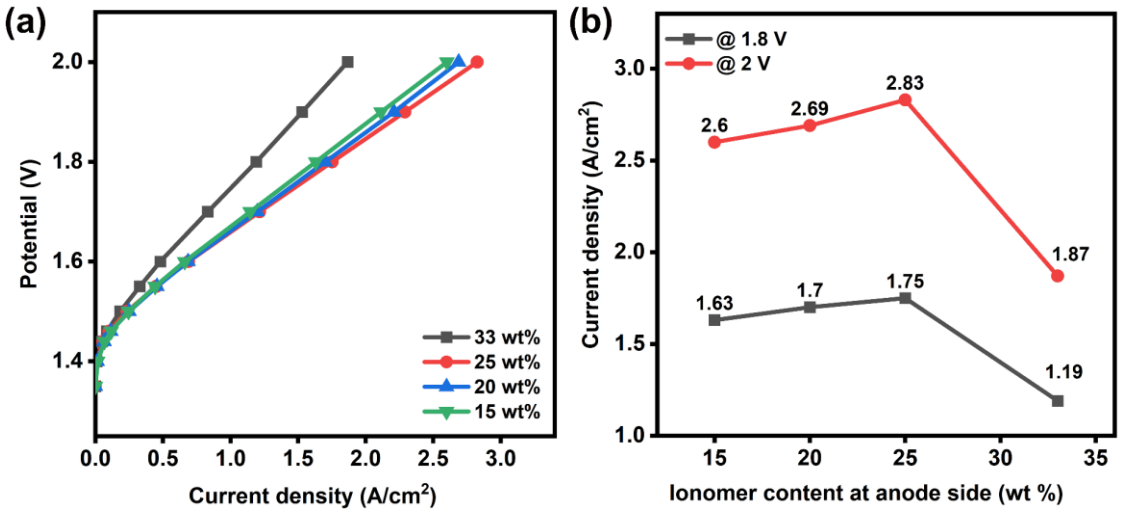

Figure 5.7 (a) Polarisation curves for the CCMs with different ionomer contents (15 wt%, 20 wt%, 25 wt%, and 33 wt%) at the anode side, the iridium catalyst loading was fixed at 2 mg/cm^2; (b) local view of current density at 1.8 V and 2 V for the CCMs with various ionomer contents.

It is observed that the CCM with 25 wt% ionomer content exhibits the highest performance across all samples, and a similar trend is observed at both 1.8 V and 2 V. Using 1.8 V as an example, the current density shows a clear variation with ionomer content increases. Starting from 1.63 A/cm^2 at 15 wt%, the current density increases to a peak value of 1.75 A/cm^2 at 25 wt%, representing an improvement of approximately 7.4%. However, when the ionomer content increases further to 33 wt%, the current density decreases sharply to 1.19 A/cm^2, marking a 31.9% reduction from the peak value. The ionomer facilitates the proton transport within the catalyst layer, enhancing the effective reaction sites and reducing ohmic resistances [26]. This trend reveals that within the optimal range of ionomer content; higher ionomer loading enhances performance. However, an excessively high ionomer content may overfill the pores in the electrode, leading to higher mass transfer resistance and increased

electrical resistance [255]. To explore the underlying mechanisms, electrochemical impedance spectroscopy (EIS) analysis was conducted. The results for the four CCMs are presented in Figure 5.8.

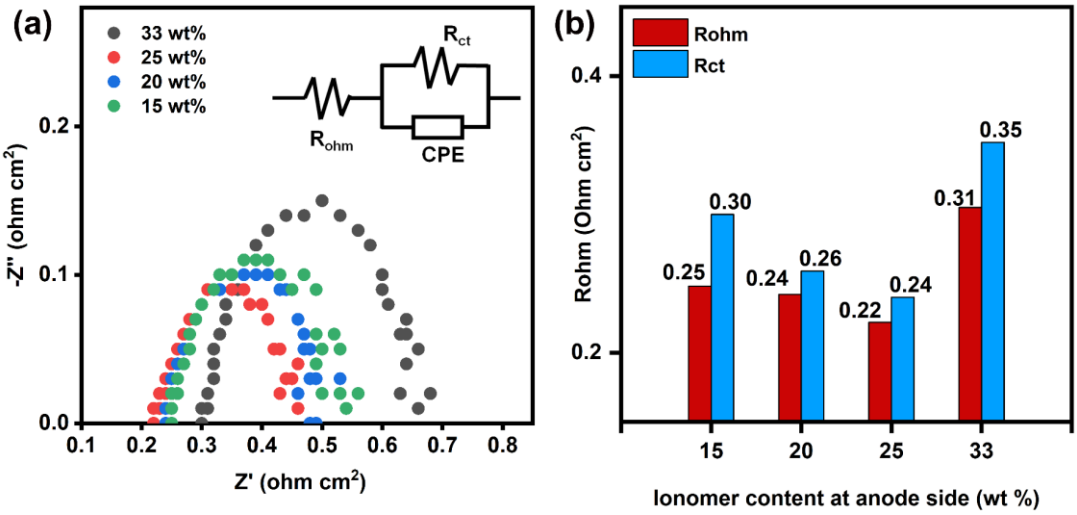

Figure 5.8 (a) Nyquist plots of the CCMs with different ionomer contents (15 wt%, 20 wt%, 25 wt%, and 33 wt%) at the anode side, recorded at 1.5 V; (b) Breakdown of ohmic resistance (Rohm) and charge transfer resistance (Rct) for each ionomer content.

The ionomer content of 25% demonstrates the lowest ohmic resistance of 0.22 Ohm·cm^2, whereas the CCM with 33% ionomer content exhibits the largest ohmic resistance, approximately 0.3 Ohm·cm^2. The CCMs with ionomer contents of 15 wt% and 20 wt% display moderate resistance, reflecting that insufficient ionomer distribution within the catalyst layer limits overall efficiency. Consequently, 25 wt% ionomer content is selected as the optimal value for fabricating CCMs at the anode side. To further examine catalyst ink dispersion at various ionomer contents, particle size and zeta potential analyses were conducted using the dynamic light scattering (DLS) technique, with results shown in Figure 5.9

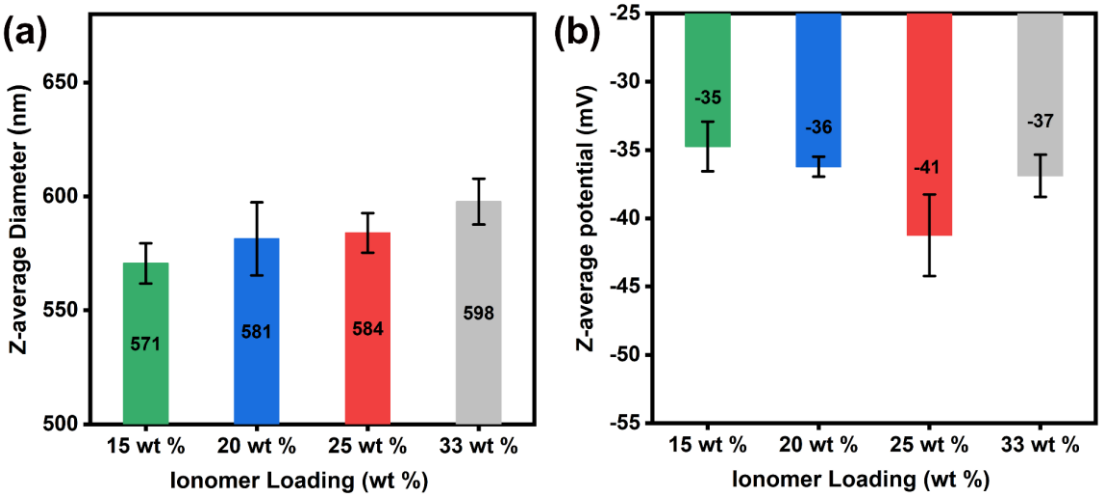

Figure 5.9 (a) DLS analysis of the Ir catalyst ink with various ionomer contents: particle size distribution, and (b) Zeta potential.

The catalyst particle size increases slightly with increasing ionomer content, ranging from 571 nm at 15 wt% to 598 nm at 33 wt%. This gradual increase is expected, as the ionomer encapsulates catalyst particles, leading to larger aggregate sizes. As for the zeta potential, the catalyst ink with 25 wt% ionomer content achieves the highest zeta potential value of -41 mV, compared to -35 mV, -36 mV, and -37 mV for 15 wt%, 20 wt%, and 33 wt%, respectively. A higher absolute zeta potential indicates better dispersion stability, as it reduces particle agglomeration and enhances the uniformity of the catalyst ink. These findings demonstrate that the optimised 25 wt% ionomer content, combined with the appropriate solvent system, not only enhances electrode performance but also ensures superior dispersion stability. This highlights the critical role of ink formulation in achieving high-quality catalyst layers for PEMWE systems.

5.1.3 Anode catalyst layer (CL) analysis

With the optimal OER catalyst ink formulation determined, the structural integrity and surface morphology of the catalyst layers were further evaluated using the SEM

analysis to confirm their stability and uniformity. The thickness of the catalyst layers was measured using ImageJ software. Measurements were taken at ten different locations per image, and multiple images were analysed to ensure accuracy. To eliminate any potential errors caused by image tilt, the thickness of the proton exchange membrane was also measured and compared against the manufacturer's specifications. CCMs were subjected to 20 polarisation cycles prior to SEM sample preparation and analysis.

5.1.3.1 Anode catalyst layer surface SEM analysis

Figure 5.10 shows the surface morphology of the anode catalyst layer. After testing, new cracks appear on the catalyst layer surface, which are most likely a result of expansion and shrinkage during the operation load cycles, as well as the release of oxygen bubbles generated within the CL. In addition, some indentations are visible in Figure 5.10 (b), which may have been caused by the PTL pressing against the CL during assembling.

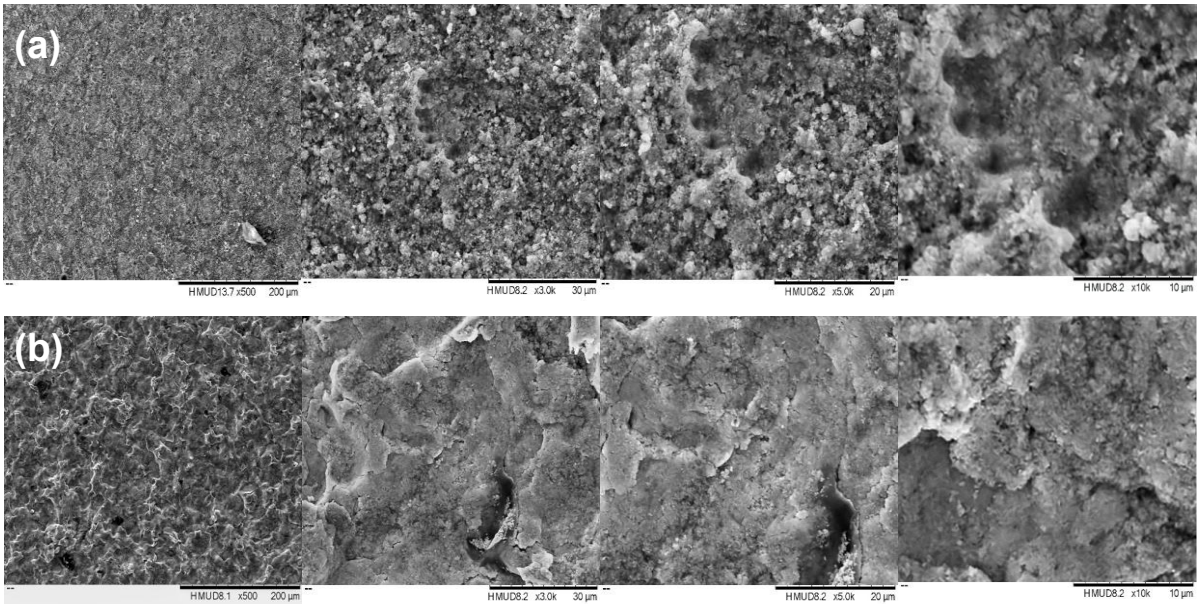

Figure 5.10 (a) Surface SEM images of the anode catalyst layer before; and (b) after testing at various magnifications.

5.1.3.2 Anode catalyst layer cross-sectional SEM analysis

The cross-sectional SEM analysis revealed that the measured thickness of the CL is 6.64 ± 1.01 µm before testing and 6.72 ± 1.04 µm after testing (Figure 5.11). Considering that catalyst loading was not entirely uniform across all samples, the observed deviation is negligible. This suggests that the thickness of the CL remained effectively unchanged after the testing. Additionally, the catalyst layer appears continuous and uniform, with no significant breaks or disruptions observed, confirming the mechanical integrity of the CL after testing.

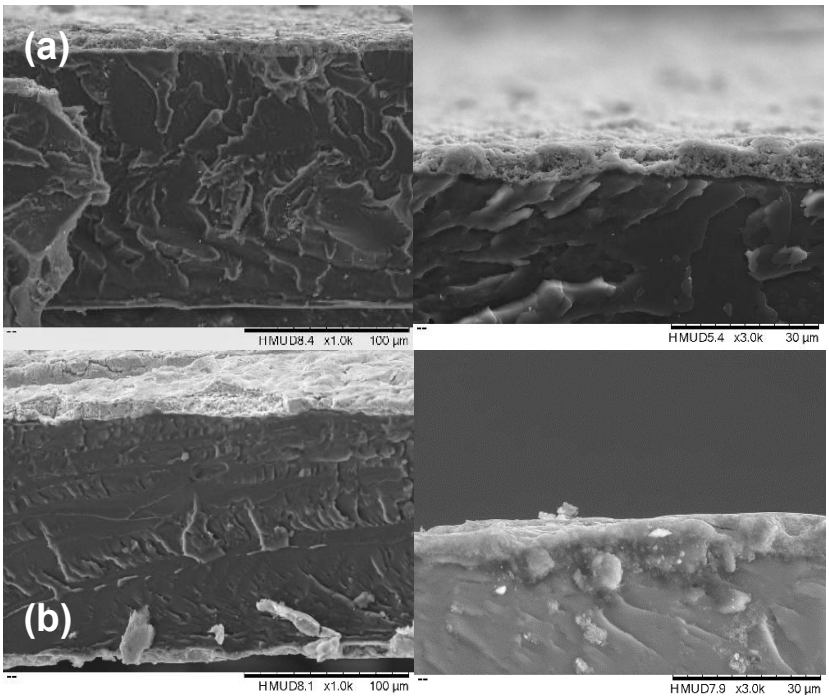

Figure 5.11 Cross-section SEM images of the anode catalyst layer (a) before and (b) after testing.

In summary, the optimisation of the catalyst selection, ink formulation, and catalyst layer structure collectively improve the stability and performance of the anode catalyst layer for OER. Iridium black (JM) was selected as the catalyst due to its superior performance and uniform dispersion. The optimal solvent system consists of isopropyl alcohol and water in a 4:1 ratio, with the ionomer loading of 25 wt%. Specifically, 24 mg of iridium black is dispersed in 1000 µL of the mixed solvent along with 20.87 µL of 25 wt% Aquivion D98-25BS ionomer dispersion. To normalise the content, the catalyst ink is prepared with a mass ratio of 1 : 1 : 35.36 for iridium, 25 wt% Aquivion D98-25BS ionomer dispersion, and solvent mixture. These findings provide a solid foundation for further investigation of the OER at the anode side, ensuring the overall efficiency of the PEMWE cell.

5.2. Cathode catalyst ink optimisation

Three different commercial HER catalysts were evaluated in this work, all of which are commonly used in PEM fuel cells, including Pt/C from TANAKA (TKK TEC10E50E, 46.2 wt% Pt on high surface area carbon); Pt/C (10 wt% and 20 wt% Pt on XC-72 carbon) from Fuel Cell Store. All CCMs were fabricated using the airbrush method, with an iridium loading of 2 mg_{Ir}/cm^2 for the anode and a Pt/C catalyst loading of 0.5 mg_{Pt}/cm^2 for the cathode. The anode catalyst ink was prepared using the previously optimised recipe, while the ionomer content was set at 69 wt% for the cathode. Aquivion E98-15S was used as the PEM, and the Bekaert PTL with 56% porosity was employed on both sides. The polarisation curves for the CCMs prepared with these three catalysts are shown in Figure 5.12.

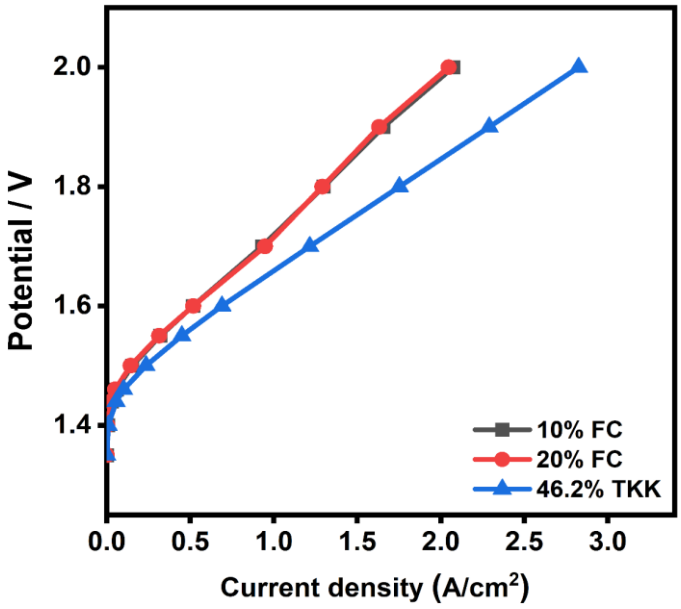

Figure 5.12 Polarisation curves of the CCMs prepared with three different HER catalysts: TKK Pt/C (46.2 wt%), Pt/C (10 wt%), and Pt/C (20 wt%).

Both Pt/C catalysts from Fuel Cell Store show very similar electrochemical performance, achieving 1.30 A/cm^2 at 1.8 V. However, the TKK catalyst demonstrates

a higher performance, achieving a current density of 1.75 A/cm^2 at 1.8 V. According to the supplier, the surface areas of the 10 wt% and 20 wt% Pt/C catalysts from Fuel Cell Store are 120 m^2/g and 100 m^2/g, respectively, with both catalysts having X-ray crystallite sizes of approximately 2–3 nm. Similarly, the TKK catalyst has a surface area of 100 m^2/g and an X-ray crystallite size of 2–3 nm. TEM image analysis was conducted to further investigate the morphology of the catalysts, and the results are presented in Figure 5.13.

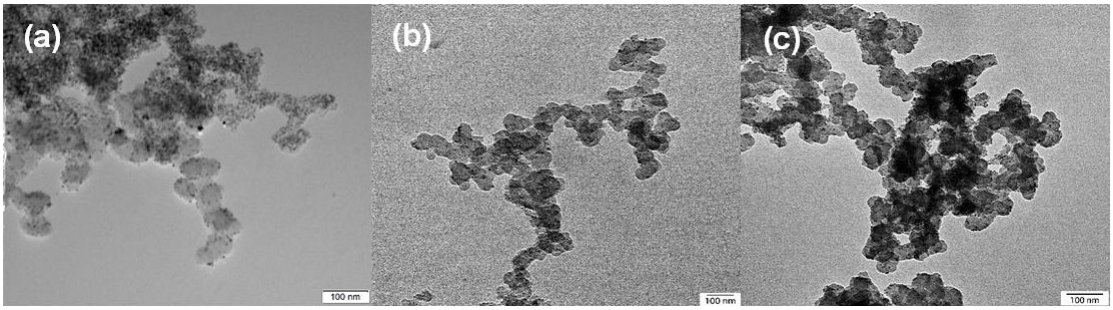

Figure 5.13 TEM images of (a) TKK Pt/C (46.2%); (b) Pt/C (10%);and (c) Pt/C (20%) from Fuel Cell Store.

The TEM images indicate well-dispersed Pt nanoparticles across the carbon support, with no significant agglomeration observed. This suggests effective dispersion of Pt nanoparticles by the carbon support, especially when compared to iridium-based samples. However, the differences in Pt loading have important implications for the electrode structure and performance. For the same platinum loading, the 10 wt% or 20 wt% Pt/C catalyst requires a much greater total mass of catalyst to achieve the same Pt loading as the TKK (46.2 wt%). This higher mass results in a thicker catalyst layer, which increases mass transport resistance and leads to performance limitations at higher current densities. This effect is particularly evident in the polarisation curves, where the slope for the 10 wt% and 20 wt% Pt/C catalyst increases significantly at high

current densities. Moreover, the thicker catalyst layer required for 10 wt% Pt/C increases material usage, making it less practical for large-scale applications. Based on these considerations, the TKK Pt/C catalyst was selected for subsequent research to optimise catalyst ink formulation and electrode structure for improved HER performance. Its higher Pt weight percentage enables a thinner catalyst layer, reducing mass transport limitations and improving high-current-density performance.

5.2.1 Catalyst dispersion optimisation

5.2.1.1 Solvent optimisation

The selection of the solvent for catalyst ink preparation is critical for the dispersion of HER catalysts, as it directly influences the microstructure of the electrode and, consequently, the performance and long-term stability of PEM water electrolysers. Previous studies have demonstrated a positive correlation between the IPA content and the performance of cathode catalyst layers. Microstructural analysis revealed that increasing the IPA content significantly reduces the size of catalyst secondary agglomerates, thereby enhancing the electrochemical performance of the electrodes [258,259]. Building on this knowledge from fuel cell studies, the same solvent system was adapted for PEMWE applications. Similar to the OER catalyst ink, HER catalyst ink was prepared using a 4:1 mixture of IPA and water.

5.2.1.2 Cathode catalyst loading

At the cathode side, the hydrogen evolution reaction is significantly faster compared to the oxygen evolution reaction. Therefore, the platinum loading at the cathode is typically maintained at a very low level, generally below 0.5 mg/cm^2. In this study, two CCMs were fabricated using the direct spraying method, with a metal loading of 2

mg/cm^2 for the anode and platinum catalyst loadings of 0.2 mg$_{Pt}$/cm^2 and 0.5 mg$_{Pt}$/cm^2 for the cathode, respectively. All other conditions were kept consistent with previous discussion.

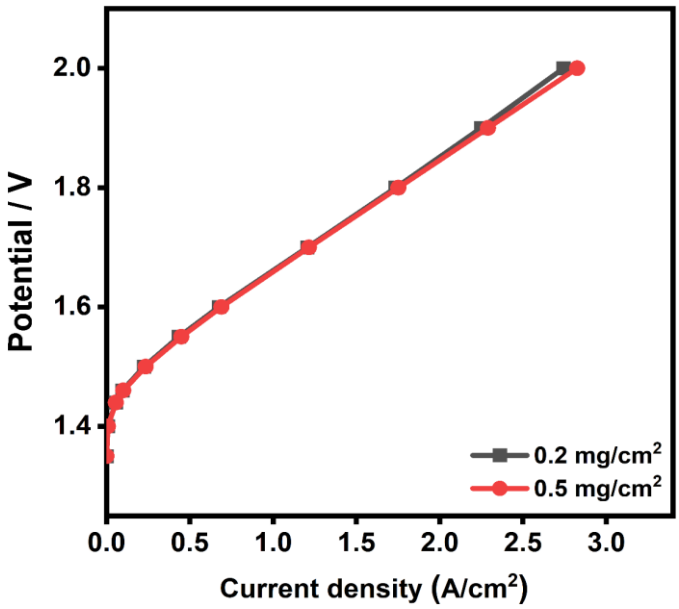

Figure 5.14 Polarisation curves of the CCMs with different platinum loadings (0.2 mg$_{Pt}$/cm^2 and 0.5 mg$_{Pt}$/cm^2) at the cathode side.

The polarisation curves for the two CCMs are presented in Figure 5.14. The results indicate no significant difference in performance between the two platinum loadings, although the higher loading of 0.5 mg$_{Pt}$/cm^2 demonstrates slightly better performance. Drawing on knowledge from fuel cell studies, higher platinum loadings are often associated with improved stability. Therefore, considering both performance and long-term stability, a platinum loading of 0.5 mg$_{Pt}$/cm^2 was selected as the optimal value for the cathode side in this study.

5.2.1.3 Ionomer-to-catalyst ratio

In the complex operating environment of an electrolyser, the electrochemical performance is determined not only by the intrinsic properties of the anode and cathode

catalysts but also by various other factors. To evaluate the effect of the ionomer content on catalytic activity while minimising external environmental influences, this study first conducted ex-situ half-cell gas diffusion electrode (GDE) tests, and the electrochemical surface area (ECSA) was calculated accordingly. Catalyst inks with varying I/C ratios (69 wt%, 45 wt%, 25 wt%, 20 wt%, and 15 wt%) were prepared and directly sprayed onto SGL 39BB carbon paper. The platinum catalyst loading was controlled at 0.5 mg_{Pt}/cm^2.

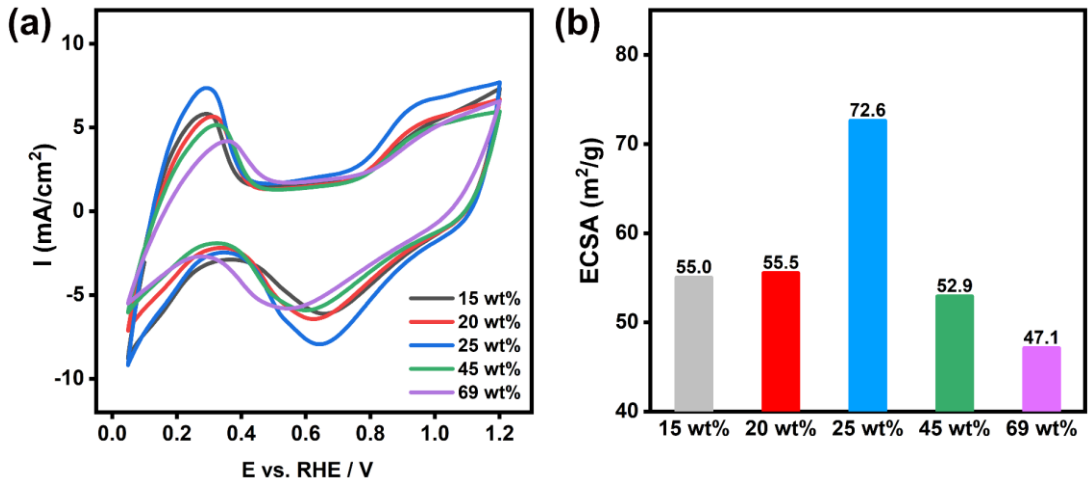

Figure 5.15 Ex-situ GDE test: (a) CV plots in 1.0 M $HClO_4$ with a scan rate of 20 mV/s; and (b) comparison of the ECSA for all GDEs calculated from the Pt-H desorption peaks.

Based on the ex-situ GDE test results (Figure 5.15), the highest ECSA is obtained at 25 wt% ionomer content, with an ECSA value of 72.6 m^2/g_{Pt}. Increasing the ionomer content from 15 wt% to 25 wt% enhances ECSA, increasing from 55 m^2/g_{Pt} to 72.6 m^2/g_{Pt}. However, further increasing the ionomer content to 69 wt% results in a substantial decline in ECSA to 47.1 m^2/g_{Pt}. Below 25 wt%, the increasing ionomer content improves proton transport, leading to enhanced ECSA. At lower ionomer

contents (<25 wt%), the proton-conducting network is insufficiently developed, limiting catalytic activity. However, excessive ionomer content overfills the electrode pores, which negatively impacts ECSA. To validate these findings under practical conditions, full-cell tests were conducted using CCMs prepared with I/C ratios of 25 wt%, 45%, and 69 wt% at cathodes. In these tests, the anode catalyst loading was 2 mg_{Ir}/cm^2, while the cathode Pt/C catalyst loading was maintained at 0.5 mg_{Pt}/cm^2. The polarisation curves for the CCMs are shown in Figure 5.16.

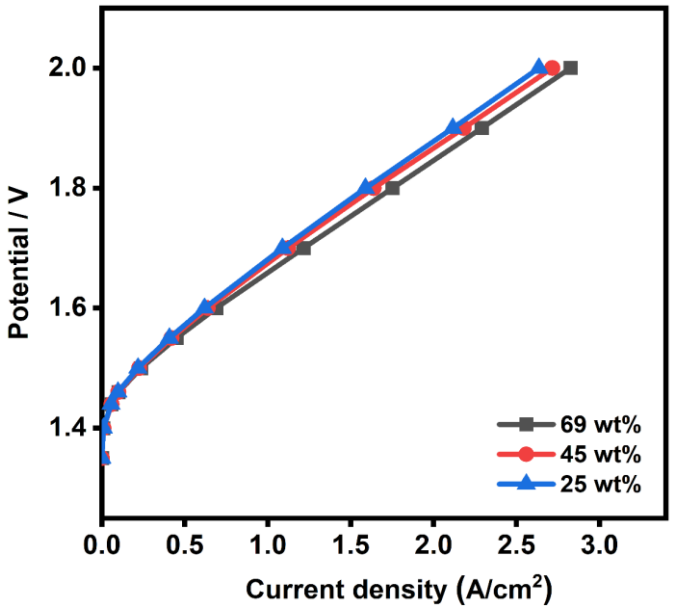

Figure 5.16 Polarisation curves of CCMs with different ionomer-to-catalyst ratios (69 wt% and 25 wt%) at the cathode side.

Interestingly, exhibiting the highest ECSA in ex situ GDE tests, the 25 wt% I/C ratio does not lead to the best performance in full-cell operation. Instead, the 69 wt% I/C ratio delivers superior performance, particularly at medium and high current densities. While the polarisation curves for all ionomer ratios overlap in the low current density range, indicating similar catalytic activity, the 69 wt% CCM outperforms the others in the high current density region. This discrepancy between half-cell and full-cell

performance highlights the importance of assessing ionomer content under real operating conditions. While the ex situ GDE test provides insights into catalyst kinetics by isolating reaction mechanisms, a full-cell test accounts for a more comprehensive range of factors, including reaction kinetics, ohmic resistance, and mass transport limitations. The improved performance of the 69 wt% I/C ratio in the full-cell setup can be attributed to its ability to maintain a continuous proton-conducting network while also enhancing gas diffusion under more complex electrolyser operating conditions, same conclusions have also been reported in the DOE's reports [110]. Additionally, a CCM with an increased I/C ratio (100 wt%) was tested in the full cell. As expected, its performance dropped significantly, with the current density declining from 1.75 A/cm^2 (69 wt%) to 1.3 A/cm^2 at 1.8 V. This trend aligns with findings from the anode I/C ratio studies, where excessive ionomer content led to performance deterioration due to pore blockage and increased transport resistance. Given that full-cell tests provide a more accurate representation of operational conditions, an I/C ratio of 69 wt% was chosen for subsequent cathode catalyst ink formulations.

In addition to carbon-supported platinum (Pt/C) catalysts, the interaction between unsupported platinum black (Pt) catalysts and ionomers was also investigated. Using the same testing methodology described above, a series of I/C ratios (100 wt%, 75 wt%, 50 wt%, and 25 wt%) were selected to prepare platinum black catalyst inks, which were directly sprayed onto 39BB carbon paper. The platinum loading was maintained at 0.5 mg$_{Pt}$/cm^2, and ex-situ half-cell GDE tests were conducted.

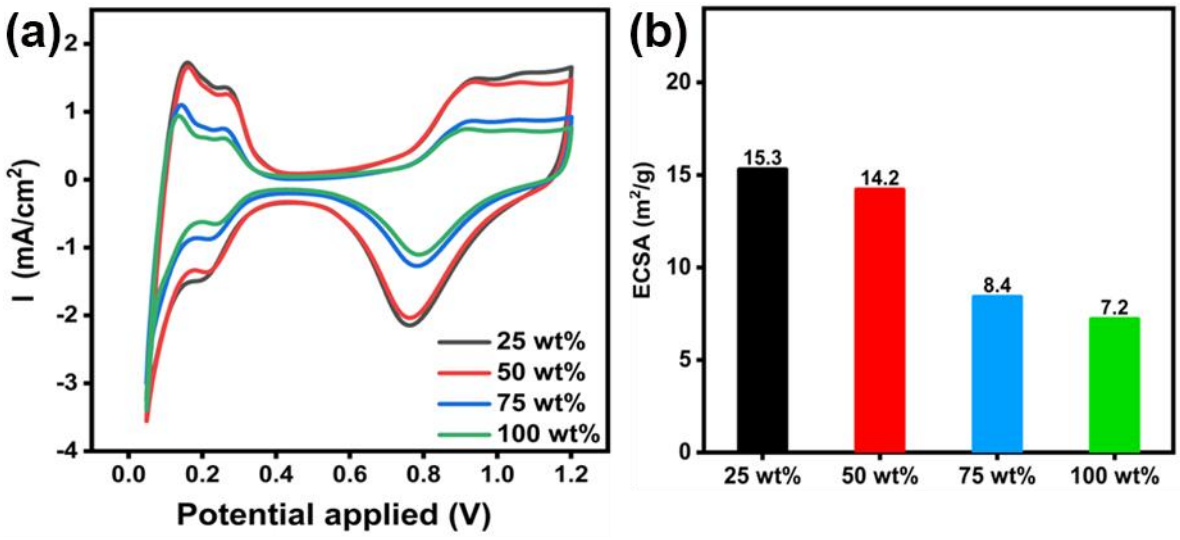

Figure 5.17 (a) CV curves recorded in 1.0 M $HClO_4$ at a scan rate of 20 mV/s; (b) ECSA values calculated from the Pt-H desorption peak for GDEs with different I/C ratios.

As shown in Figure 5.17, ECSA decreases as the ionomer content increases from 25 wt% to 100 wt%, dropping from 15.3 m^2/g_{Pt} to 7.2 m^2/g_{Pt}. Additionally, platinum black exhibits a much lower ECSA compared to Pt/C, despite having the same catalyst loading. The ECSA of Pt/C is 3.6 times higher than that of platinum black. This reduction in ECSA is primarily attributed to the lack of a carbon support in platinum black, resulting in severe agglomeration. A similar phenomenon is observed in unsupported iridium catalysts, where the formation of larger aggregates limits the number of exposed active sites, ultimately reducing catalyst utilisation and overall performance.

To assess full-cell performance, CCMs were then fabricated using these I/C ratios and tested in full cells, with their performance compared to the best-performing Pt/C CCM (I/C ratio: 69 wt%). The polarisation curves are presented in Figure 5.18. Under the same catalyst loading conditions, platinum black CCMs exhibit significantly inferior

performance compared to Pt/C-based CCMs. The best-performing platinum black CCM achieves a current density of only 1.29 A/cm^2 at 1.8 V, whereas the Pt/C CCM reaches 1.75 A/cm^2, representing a 35.6% decrease in performance. Furthermore, the performance of platinum black CCMs shows a strong correlation with their ECSA results. As the I/C ratio increases, the ECSA decreases. This reduction is accompanied by a corresponding drop in electrochemical performance from 1.29 A/cm^2 to 0.56 A/cm^2 at 1.8 V.

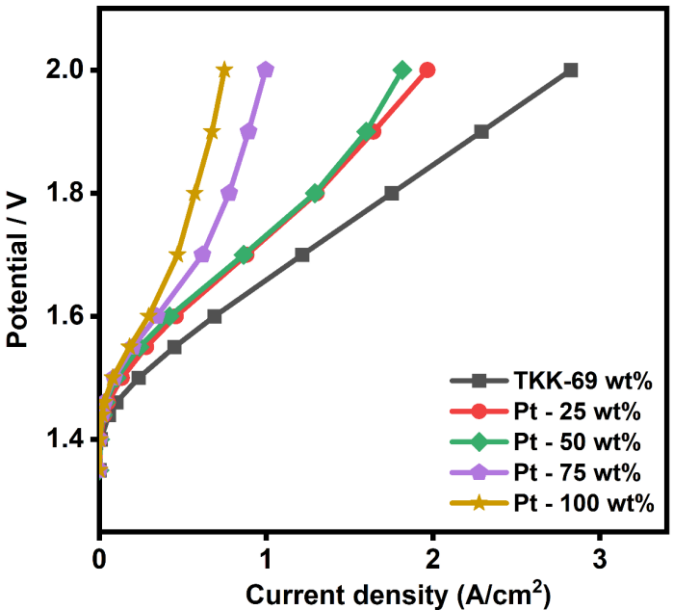

Figure 5.18 Polarisation curves of CCMs prepared with platinum black catalysts at different I/C ratios, compared with the best-performing Pt/C CCM (I/C ratio: 69 wt%).

In summary, the primary disadvantage of platinum black catalysts is their low ECSA which results in limited accessible active sites. This issue is also observed in unsupported iridium catalysts, where high loadings (2 mg$_{Ir}$/cm^2) are necessary to achieve adequate activity. This limitation is attributed to the limited surface active sites due to the large particle size. These findings highlight the importance of improving catalyst dispersion to enhance the accessibility of active sites and improve overall cell

performance in both HER and OER systems.

5.2.2 Cathode catalyst layer (CL) analysis

5.2.2.1 Cathode catalyst layer surface SEM analysis

Similar to the anode CL, the cathode CL exhibits a higher number of cracks after testing, as seen in Figure 5.19. These cracks are likely caused by mechanical stresses during operation and the release of hydrogen gas within the layer. Additionally, some catalyst agglomeration is observed after testing, which could further contribute to the uneven distribution of active sites and potentially impact long-term performance. In addition, all SEM characterisation was performed on samples that had undergone 20 polarisation cycles.

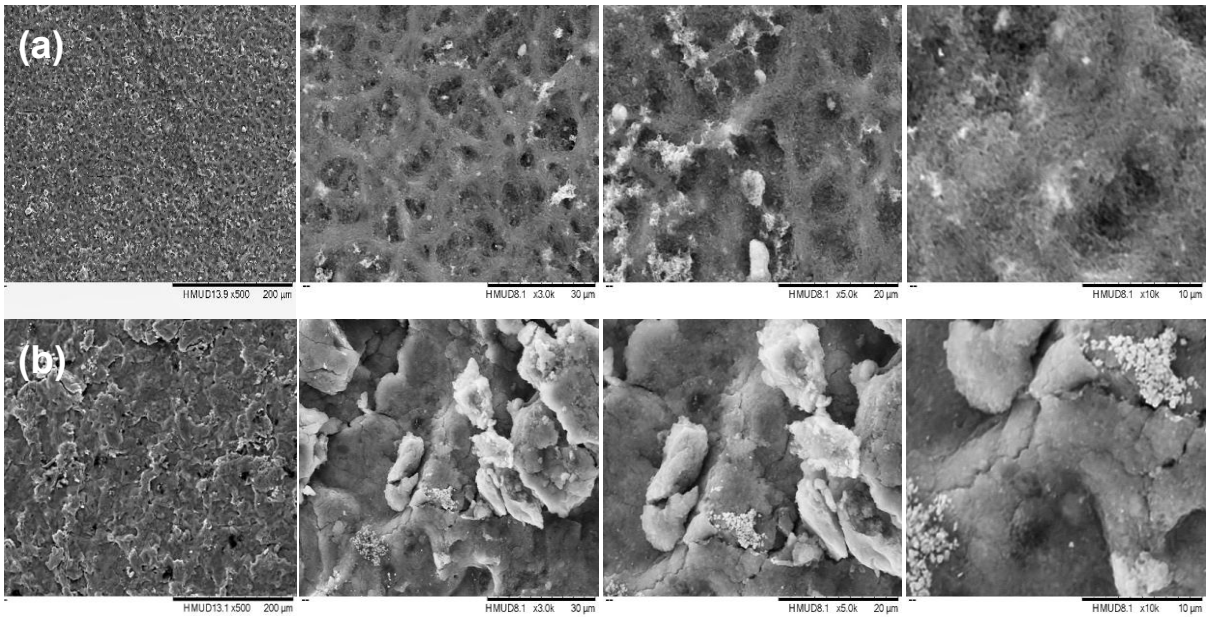

Figure 5.19 Surface SEM images of the cathode catalyst layer (a) before and (b) after testing at various magnifications.

5.2.2.2 Cathode catalyst layer cross-sectional SEM analysis

Cross-sectional SEM images (Figure 5.20) reveal that the cathode catalyst layer thickness increases from 8.30 ± 0.66 μm before testing to 9.66 ± 1.42 μm after testing. This increase in thickness is likely due to ionomer swelling during operation, which persists even after drying. Another contributing factor may be the increase in porosity caused by hydrogen gas release during operation. Despite these structural changes, the catalyst layer remains continuous without significant interruptions or detachment, indicating good mechanical stability.

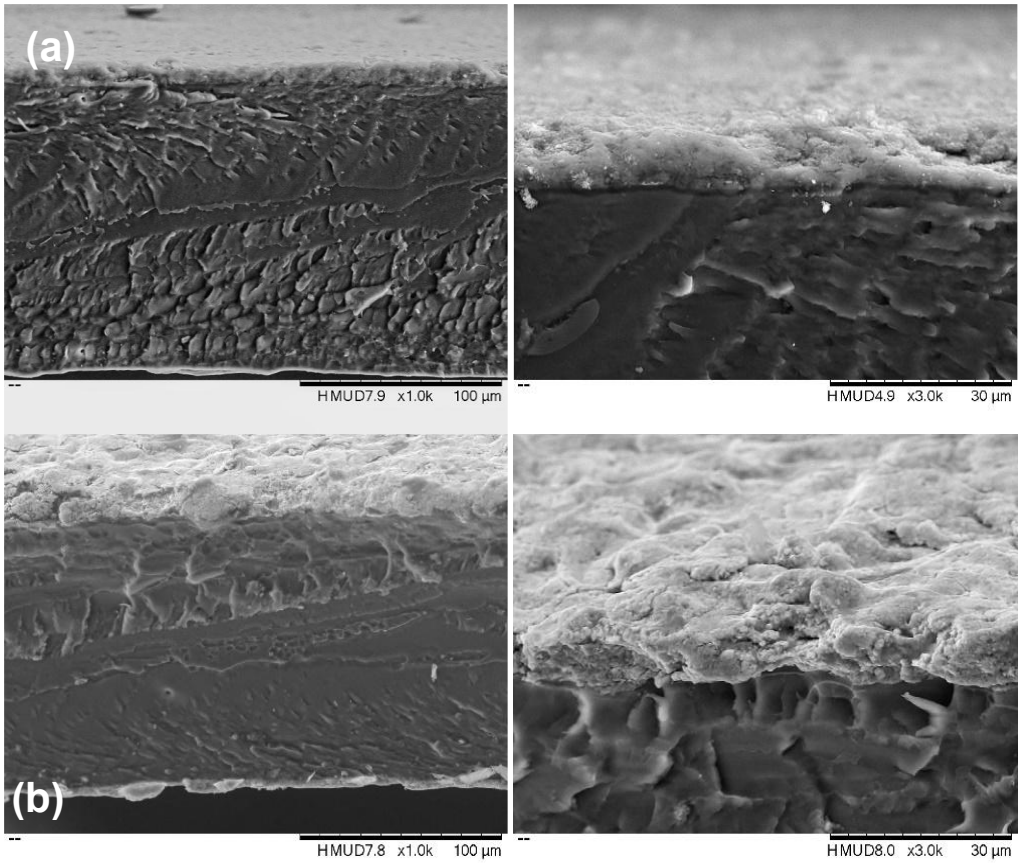

Figure 5.20 Cross-section SEM images of the cathode catalyst layer (a) before and (b) after testing.

In summary, Pt/C (46.2 wt%, TKK) is selected as the cathode catalyst. The optimal formulation for the HER cathode ink consists of 7 mg of 46.2 wt% Pt/C, 1000 μL of a

mixed solvent (isopropyl alcohol and water in a 4:1 ratio), and 16.8 μL of 25 wt% Aquivion D98-25BS ionomer dispersion. To normalise the content, the catalyst ink is prepared with a mass ratio of 1 : 2.76 : 121.26 for Pt/C, 25 wt% Aquivion D98-25BS ionomer dispersion, and solvent mixture.

5.3. Post-treatment for CCM (Hot pressing)

Hot pressing is a widely employed technique for assembling CCMs, ensuring robust interfacial contact between the catalyst layers and the proton exchange membrane. This process also promotes bonding between ionomers and catalysts by applying heat and pressure to facilitate coalescence at the interface [260]. However, hot pressing significantly alters the structural and porosity characteristics of CCMs, influencing their mechanical stability and electrochemical performance. Excessive heat and pressure can also dehydrate the proton exchange membrane, reducing proton conductivity and potentially causing irreversible performance loss [74,92].

Initially, CCMs were fabricated using the direct spraying method without the hot-pressing. However, it was observed that these CCMs exhibited significantly reduced stability, with noticeable performance degradation over the repeated testing cycles. This instability is primarily attributed to catalyst detachment during operation, with a significant portion of the detached catalyst becoming trapped in the PTLs. To evaluate the effect of hot pressing, the anode PTLs of the tested CCMs were sonicated in isopropyl alcohol after operation to check the lost catalyst particles (Figure 5.21).

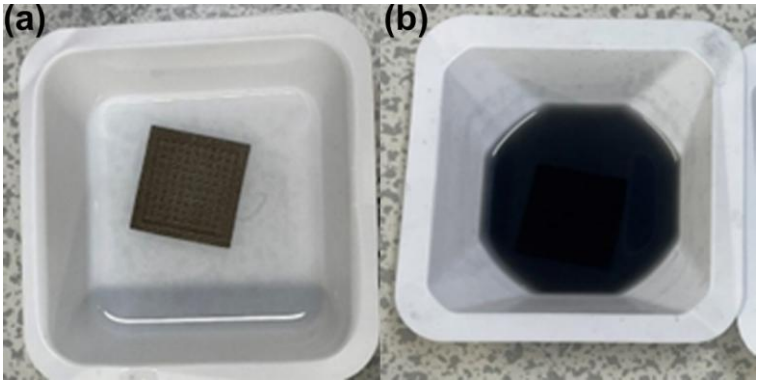

Figure 5.21 Washing solution of the PTL from a (a) hot-pressed CCM; (b) and a non-hot-pressed CCM.

The results demonstrate that the CCM subjected to hot pressing exhibits significantly less catalyst detachment, whereas the CCM without hot pressing loses up to 50 percent of its catalyst, as visually evident from the darker washing solution. Although the hot pressing improves catalyst retention within the catalyst layer, it also causes a decrease in cell performance recorded (Figure 5.22). Two self-made CCMs were prepared under identical conditions, with the only difference being whether they underwent hot pressing.

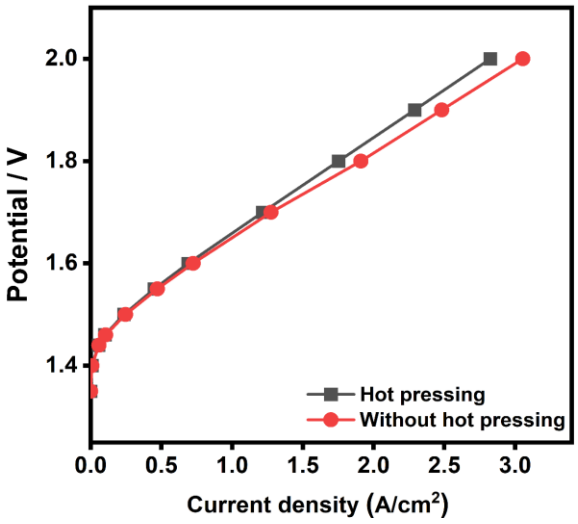

Figure 5.22 Polarisation curves of the CCMs with and without hot pressing.

The non-hot-pressed CCM demonstrates consistently higher current density compared to the hot-pressed CCM across the entire range of potentials, with the difference becoming more significant at higher current densities. At 1.8 V, the non-hot-pressed CCM achieves a current density of 1.91 A/cm^2, whereas the hot-pressed CCM reaches only 1.75 A/cm^2, representing a performance decrease of approximately 8.38%. Similarly, at 2.0 V, the current density for the non-hot-pressed CCM is 3.15 A/cm^2, compared to 2.82 A/cm^2 for the hot-pressed CCM, resulting in a 10.48% reduction. These findings indicate that hot pressing negatively impacts electrochemical performance, particularly at high operating voltages. However, hot pressing is still required to ensure the stability and reproducibility of testing results. Added to that, all CCMs discussed in Sections 5.1 and 5.2 underwent hot-press treatment to ensure stability and reproducibility. To further investigate and optimise the hot-pressing conditions, the subsequent sections will analyse the influence of the hot-pressing time, pressure, and temperature on catalyst layer structure and overall performance.

5.3.1 Hot-pressing temperature

Temperature selection is a critical factor in optimising the hot-pressing process. For Aquivion® membranes, the glass transition temperature (Tg) ranges from 160°C to 195°C. A suitable pressure temperature ensures sufficient ionomer flexibility and bonding while maintaining structural integrity. Based on this, 160°C and 185°C were chosen to investigate their effects on CCM microstructure and electrochemical performance. Two CCMs were prepared under identical conditions, with the hot-pressing pressure of 800 lb and a duration of 180 seconds. The polarisation curves for both CCMs are presented in Figure 5.23.

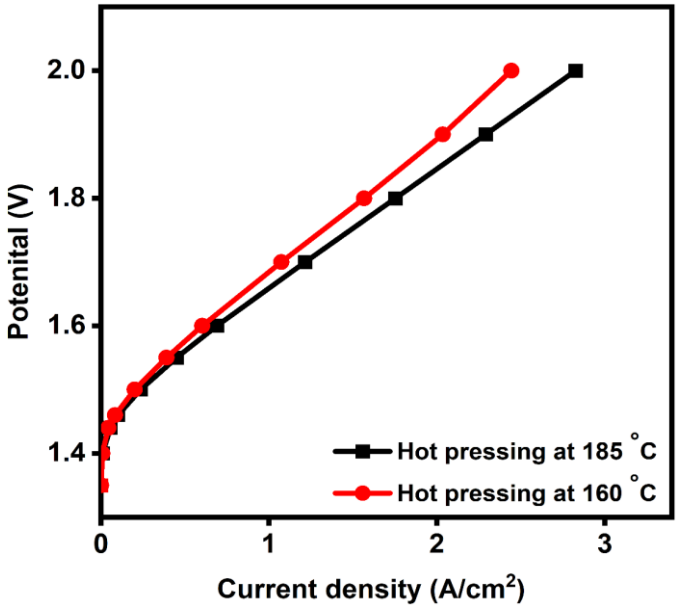

Figure 5.23 Polarisation curves of the two CCMs with different hot-pressing temperature. All samples were prepared with an anode catalyst loading of 2 mg_{Ir}/cm^2 and a cathode loading of 0.5 mg_{Pt}/cm^2.

The CCM hot-pressed at 185°C achieves a current density of 1.75 A/cm^2 at 1.8 V. In comparison, the CCM hot-pressed at 160°C reaches only 1.57 A/cm^2. Besides, post-test washing of the anode PTL revealed significant catalyst detachment from the CCM hot-pressed at 160°C, while the CCM processed at 185°C remains intact without any observable detachment. This indicates that higher hot-pressing temperature is necessary to promote superior structural integrity and adhesion. A further consideration is the temperature stability of the hot press, as fluctuations can occur, especially at higher settings. When set to 190°C, the actual temperature sometimes exceeds 195°C. If the hot-pressing temperature surpasses this value, local overheating may result in visible carbonisation of the CCM, turning it black. To prevent potential degradation while ensuring optimal adhesion and mechanical stability, 185°C was chosen as the maximum hot-pressing temperature. To further investigate the influence of hot-

pressing temperature on the catalyst layer, SEM analysis was performed on the two CCMs, as shown in Figure 5.24.

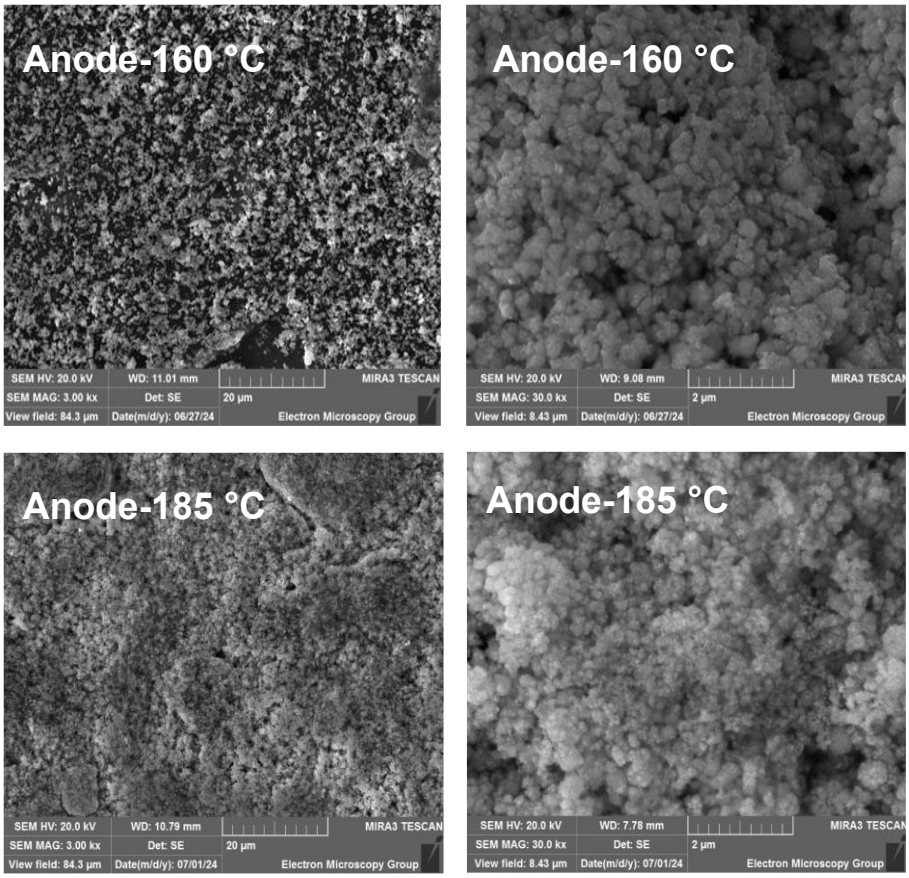

Figure 5.24 SEM images of the anode catalyst layer for the CCMs hot processed at 160°C (top) and 185°C (bottom) under different magnifications.

At higher magnification, the sample hot-pressed at 185°C shows fewer large agglomerates compared to the 160°C sample, where finer clusters are observed across the catalyst layer. Although the contrast is not pronounced, this trend suggests that higher temperature hot-pressing may generate a more uniform microstructure. This difference may be attributed to the ionomer becoming more flexible near its glass transition temperature (~185°C), which facilitates partial redistribution within the catalyst layer. This redistribution could improve interfacial contact and structural

uniformity, leading to enhanced mechanical stability and more effective utilisation of active sites [260–262]. These morphological differences provide a plausible explanation for the enhanced electrochemical performance observed in the 185 °C sample.

The cathode catalyst layers processed at 160°C and 185°C were also examined to investigate the effect of hot-pressing temperature, as shown in Figure 5.25. Unlike the anode catalyst layers, the differences between the two cathodes are relatively minor. At lower magnification, both cathodes exhibit smooth surfaces without significant defects or visible cracks. Although the high-magnification SEM image of the 185 °C sample appears to show more void-like structures than that of the 165 °C sample, these may arise from local delamination or cracking during cross-sectional sample preparation. Notably, these structures are not observed consistently across the sample and do not correlate with performance degradation. On the contrary, the 185 °C sample exhibited better electrochemical performance, suggesting that any local voids did not compromise bulk interfacial contact or proton transport. These findings further support the selection of 185°C as the optimal hot-pressing temperature for CCM fabrication.

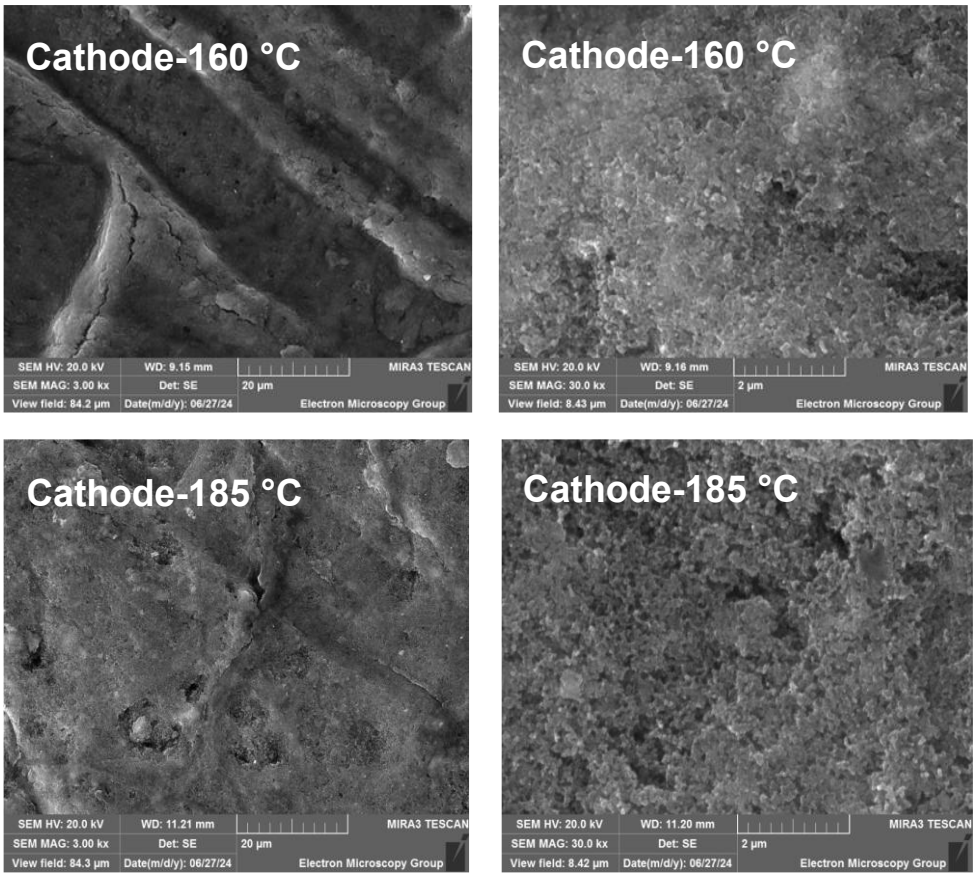

Figure 5.25 SEM images of the cathode catalyst layer for the CCMs hot processed at 160°C (top) and 185°C (bottom) under different magnifications.

5.3.2 Hot-pressing pressure

In addition to the influence of hot-pressing temperature, the applied pressure also plays a significant role. A suitable pressure ensures effective contact between the catalyst layer and membrane, while excessive pressure alters the catalyst layer structure, which may hinder reactant transport and reduce reaction efficiency. To investigate these effects, three CCMs were prepared under identical conditions but subjected to different hot-pressing pressures: no pressure (0 lb), 800 lb, and 1600 lb. The corresponding polarisation curves are presented in Figure 5.26.

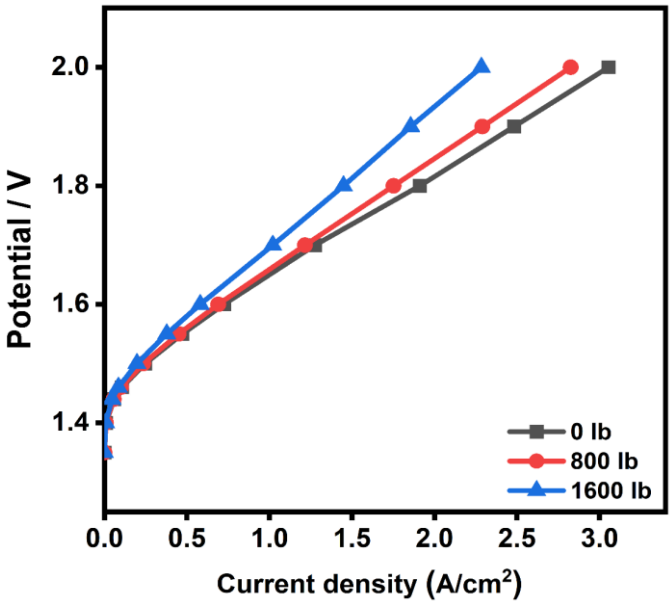

Figure 5.26 Polarisation curves of the CCMs with different hot-pressing pressure.

Some polarisation curves results were discussed in the Section 5.2.1, where the CCMs pressed at 0 lb and 800 lb were referred to as non-hot-pressed and hot-pressed CCMs, respectively. An additional CCM was tested under double the pressing force (1600 lb) for comparison in this work. As previously discussed, the CCM pressed at 800 lb exhibited improves performance compared to the non-hot-pressed sample. However, when the hot-pressing pressure increases to 1600 lb, performance declines significantly, with the current density dropping to 1.45 A/cm^2 at 1.8 V, representing reductions of 17% and 8% to the non-hot-pressed and 800 lb-pressed CCMs, respectively. Previous studies have shown that excessive pressure alters the microstructure of the catalyst layer, reducing catalyst layer thickness under excessive pressure results in a denser structure, which further increases transport resistance and limits electrochemical activity [263,264].

These CCMs were subsequently analysed using SEM to study the structural differences of the anode catalyst layer (Figure 5.27).

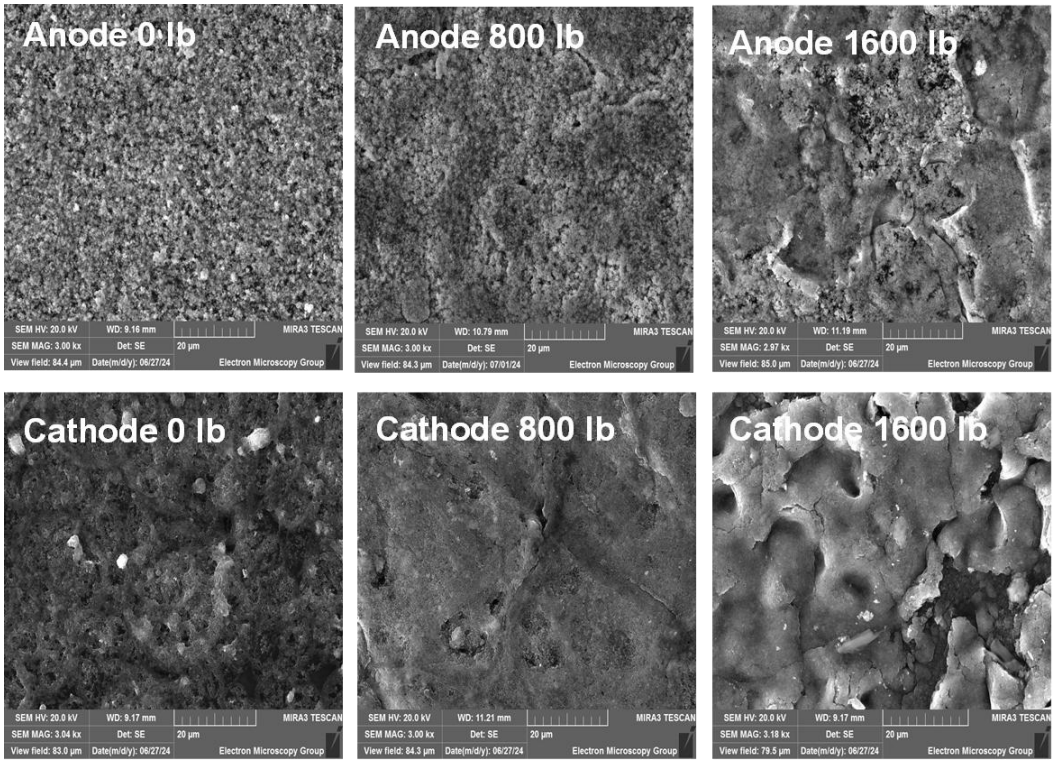

Figure 5.27 SEM images of the anode catalyst layer for the CCMs prepared under different hot-pressing pressures (0 lb, 800 lb, and 1600 lb).

The SEM images show that the catalyst layers of 0 lb and 800 lb exhibit similar structural characteristics, with only a slight reduction in porosity at 800 lb. At 1600 lb, more cracks appear on the surface, and severe catalyst agglomeration is observed. These structural disruptions suggest that excessive pressure damages the catalyst layer, which may negatively impact overall performance. The cross-section images are shown in Figure 5.28.

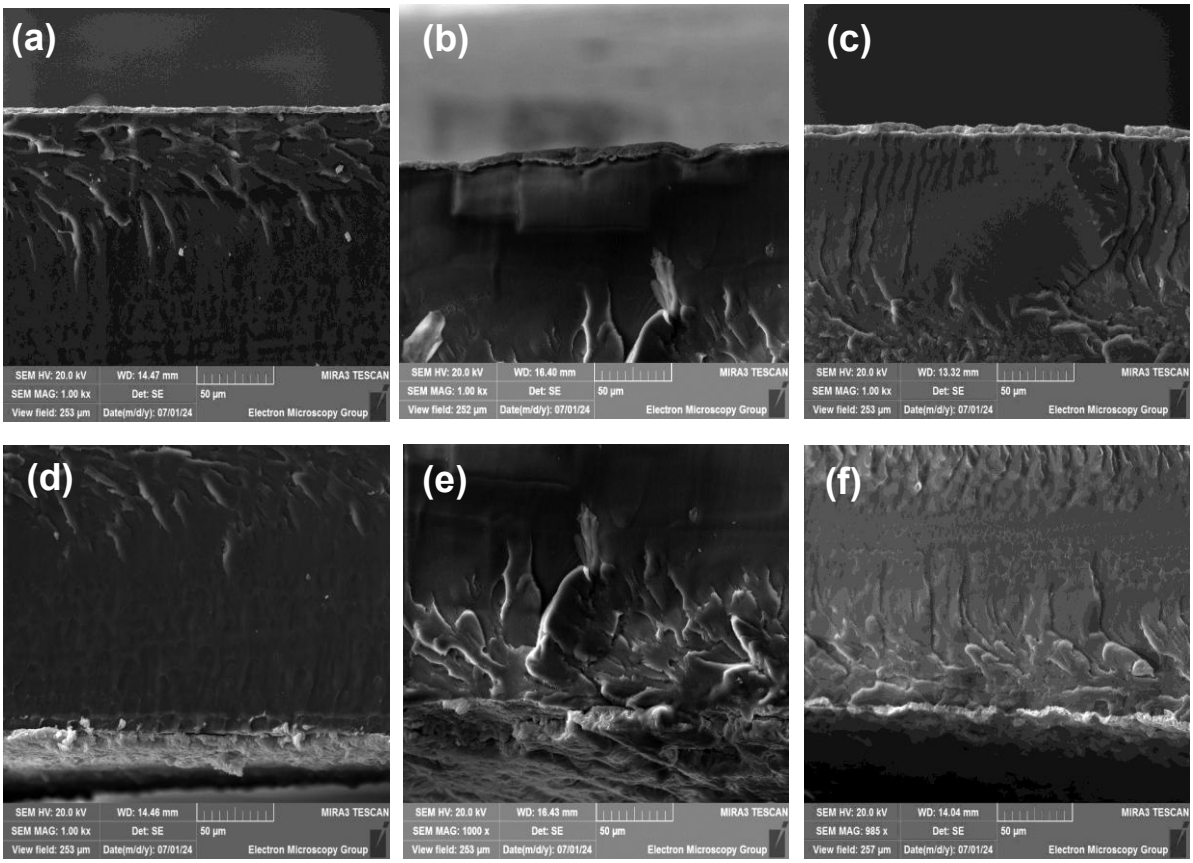

Figure 5.28 Cross-sectional SEM images of the anode catalyst layers (a, b, c) and cathode catalyst layers (d, e, f) for the CCMs prepared under different hot-pressing pressures: 0 lb (a, d), 800 lb (b, e), and 1600 lb (c, f).

The cross-sectional SEM images provide insight into the impact of pressure on the catalyst layer thickness. For the anode catalyst layers (Figure 5.28 (a–c)), the thickness is maintained at approximately 3.3 µm across all tested pressures. In contrast, the cathode catalyst layers (Figure 5.28 (d–f)) show a decrease in thickness as the hot-pressing pressure increases: 7.2 ± 0.22 µm at 0 lb, 6.6 ± 0.58 µm at 800 lb, and 3.92 ± 0.29 µm at 1600 lb. This suggests that the cathode catalyst layer, particularly due to the carbon-supported platinum structure, is more susceptible to mechanical compression than the anode.

While the non-hot-pressed CCM (0 lb) demonstrates acceptable performance, it suffers from poor stability, as previously discussed. Excessive pressure (1600 lb) significantly restricts mass transport and lowers performance. The CCM prepared at 800 lb balances stability and performance. Based on these findings, a hot-pressing pressure of 800 lb was selected for further optimisation.

5.3.3 Hot-pressing duration

Hot-pressing duration is another parameter in hot-pressing process. Insufficient pressing time weakens adhesion between the CLs and the PEMs, while excessive pressing time may lead to degradation of functional groups within the membrane. Despite variations in hot-pressing durations reported in existing studies, a clear standardised time range is still lacking. The optimal duration often depends on the specific hot-pressing equipment and processing conditions. In this study, two pressing times, 90 seconds and 180 seconds were selected. The electrochemical performance of CCMs pressed for 90 and 180 seconds exhibits minimal variation; however, post-test disassembly reveals that CCMs pressed for only 90 seconds still exhibit minor catalyst detachment. The related SEM analysis is shown in Figure 5.29.

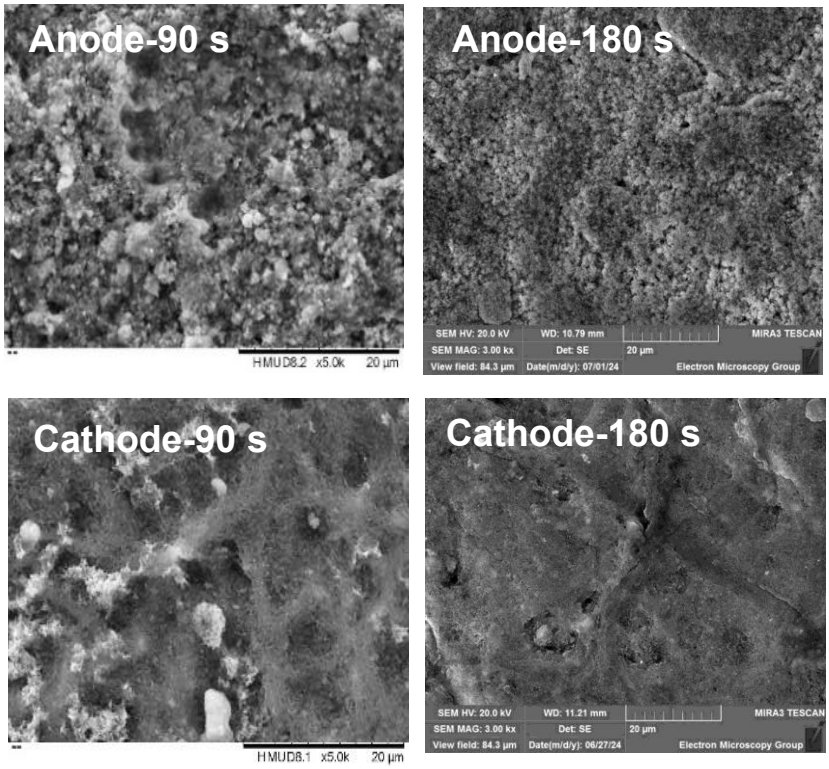

Figure 5.29 SEM images of the anode (top) and cathode (bottom) catalyst layers after hot-pressing for 90 seconds and 180 seconds.

Compared with 90 seconds, the CCM hot pressed for 180 seconds exhibits improved uniformity, which can enhance long-term stability by reducing potential defects and improving mechanical strength and durability. However, extending the hot-pressing time beyond 180 seconds leads to visible darkening of Aquivion® membrane, likely due to carbonisation, as well as signs of dehydration. Based on these results, 180 seconds was selected as the optimal hot-pressing time.

5.4. Ultrasonic spray for CCM fabrication

During the initial optimisation phase, an airbrush gun was used to fabricate CCMs, refining the process from catalyst ink preparation to CCM fabrication. Once the optimal formulation was established, ultrasonic spray coating was introduced to enhance

reproducibility and ensure uniform catalyst deposition. The optimised CCM fabrication process with key findings is illustrated in Figure 5.30. To compare the two different spraying methods, two 5 cm^2 CCMs were fabricated using the optimal recipe by air spray gun and ultrasonic spray, respectively. The polarisation curves for these CCMs, along with recently reported performances are presented in Figure 5.31.

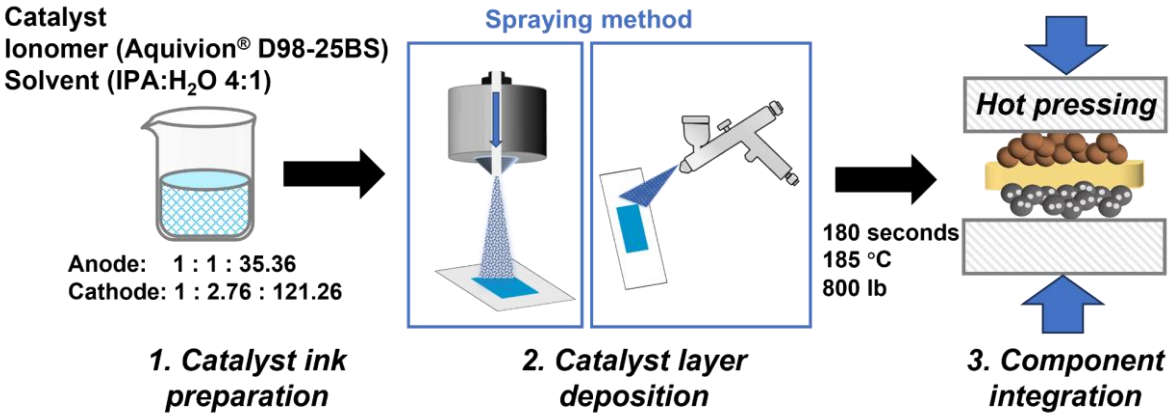

Figure 5.30 Basic CCM fabrication process with key findings.

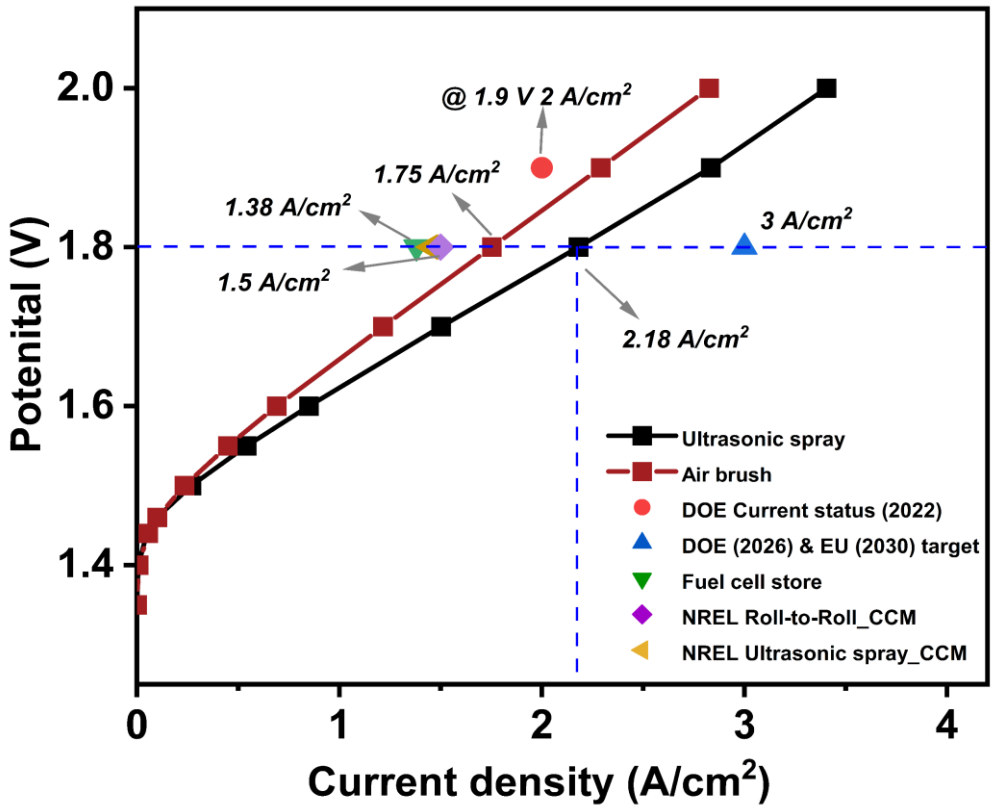

Figure 5.31 Comparison of polarisation curves for CCMs fabricated by airbrush and ultrasonic spray methods, alongside reported CCM performance from DOE, EU targets, NREL, and Fuel Cell Store [265–268].

The results demonstrate a clear performance advantage for the CCM fabricated using ultrasonic spray. At 1.8 V, the ultrasonic spray CCM reaches a current density of 2.18 A/cm^2, a 24.6% improvement over the airbrush CCM, which achieves only 1.75 A/cm^2. This enhanced performance is attributed to the superior dispersion of catalyst ink enabled by ultrasonic atomisation. Unlike airbrush spraying, which relies on high-pressure airflow, ultrasonic atomisation produces droplets with uniformity exceeding 95%, preventing catalyst agglomeration and promoting a homogeneous catalyst layer. The high-frequency vibrations of the ultrasonic nozzle enhance dispersion quality, ensuring finer catalyst deposition and ultimately improving electrochemical

performance. This also validates the focus on dispersion optimisation in earlier sections, highlighting its importance not only during catalyst ink preparation but also throughout the spraying process. Besides the direct comparison between airbrush and ultrasonic spray methods, the performance of the ultrasonic spray CCM also surpasses several recently reported results. A commercial CCM from Fuel Cell Store achieves only a current density of 1.38 A/cm^2 at 1.8 V, despite employing a higher catalyst loading of 3 mg/cm^2 for both iridium and platinum [268]. Similarly, NREL (2020) reported a peak current density of 1.5 A/cm^2, using both ultrasonic spray and roll-to-roll fabrication methods, which is approximately 30% lower than this study [265]. In terms of international technical targets, the present CCM already exceeds the 2022 performance benchmarks set by the DOE [266,267]. However, to meet the 2030 target of 3A/cm^2 (1.8 V), further improvements are required.

These findings demonstrate that the ultrasonic spray method offers significant advantages in performance, making it a promising technique for the following experiments. Based on the above results, the optimal CCM fabrication conditions are summarised in Table 5-1.

Table 5-1 Optimal ultrasonic spraying conditions for the CCM fabrication.

Key step	Specification	HER catalyst layer	OER catalyst layer
Catalyst ink preparation	Catalyst	Pt/C (TKK)	Iridium black (JM)
	ionomer content	69 wt% (to Pt/C)	25 wt% (to Ir)
	Loading	0.5 mg_{Pt}/cm^2	2 mg_{Ir}/cm^2
	Solvent	IPA:H_2O 4:1	IPA:H_2O 4:1
	Solid content	7 mg / mL (to Pt/C)	24 mg / mL (to Ir)
	Dispersing	Ultrasonic bath 30 min Ultrasonic probe 5 mins in ice bath (30% of amplitude, 5 s on, 5 s off)	
Ultrasonic spray	Background set up	Carrier gas: 1 bar	
		Flow rate: 15 mL/h	
		Hot plate temperature: 85 °C,	
		Spray pattern: 4 mm	
		Nozzle speed: 1000 mm/min	
	Nozzle distance	50 mm	35 mm
	Spraying layer	40	15
Hot press	Time	180 s	
	Temperature	185 °C	
	Pressure	800 lb	

5.5. Conclusion

This chapter presented the optimisation of catalyst inks and hot-pressing conditions during the CCM fabrication to enhance both the performance and stability. To ensure stable performance, an anode Ir loading of 2 mg_{Ir}/cm^2, a cathode Pt/C loading of 0.5

mg_{Pt}/cm^2, and I/C ratios of 25 wt% and 69 wt% for the anode and cathode, respectively, were identified as optimal. Furthermore, hot-pressing at 185°C, 800 lb for 180 seconds was determined to be the most effective condition for ensuring adhesion and long-term durability. The introduction of ultrasonic spray coating further improved high-performance CCMs, achieving 24.6% increase in current density compared to the airbrush method, which was achieved through its exceptional atomisation capability. The resulting catalyst layers exhibited greater dispersion uniformity and structural integrity, leading to improved electrochemical performance. With these optimisations, the CCM achieved a current density of 2.18 A/cm^2 at 1.8 V, surpassing the DOE 2022 status benchmark but still falling short of the 2026 target.

A thinner membrane could be used to further improve the performance; however, this might not be suitable for high differential pressure operation for this PhD research. In particular, the significant increase in hydrogen crossover presents a critical challenge, which will be further discussed in Chapter 6.

Chapter 6

Pt functional layer for hydrogen crossover mitigation in proton exchange membrane water electrolysers

The work presented in this chapter has been submitted as *'Platinum Functional Layer for Hydrogen Crossover Mitigation in Proton Exchange Membrane Water Electrolysers'* to Chemical Engineering Journal: Chemical Engineering Journal 512 (2025) 162524. https://doi.org/10.1016/J.CEJ.2025.162524.

6 Pt functional layer for hydrogen crossover mitigation in proton exchange membrane water electrolysers

The previous chapter explored and optimised the comprehensive process for fabricating catalyst-coated membranes (CCMs), from catalyst ink preparation to the CCM assembly to improve the CCM performance for high energy efficiency PEMWEs. Based on the optimised preparation methods, this study further investigates strategies to mitigate hydrogen crossover to improve the performance of the differential pressure PEMWEs. A simplified and scalable method for reducing hydrogen crossover is proposed using sputter coating technology to deposit a thin platinum layer directly onto the PEM. This approach avoids the drawbacks associated with incorporating platinum to the anodic catalyst layer and the limitations of multilayer membrane structures. The performance of this functional platinum layer is evaluated across various loadings and differential pressures ranging from 1 to 10 bar. The optimised design significantly reduces hydrogen crossover rates under high differential pressure conditions. Additionally, accelerated stress testing (AST) is also conducted to validate the long-term stability of the optimised design under conditions mimicking renewable energy coupling.

6.1. Hydrogen crossover behaviour in the standard CCM

Based on the optimised fabrication process, the CCMs evaluated in this chapter were prepared with an iridium loading of 2 mg/cm^2 on the anode and a platinum loading of 0.5 mg$_{Pt}$/cm^2 on the cathode. Aquivion E98-25BS ionomer was used to prepare the catalyst inks, with ionomer-to-catalyst weight ratios of 25% for the anode and 69% for the cathode. Aquivion E98-15S was employed as the membrane. All CCMs were tested under cathode-side pressures of 1, 6, and 11 bar, while the anode side was maintained

at ambient pressure, corresponding to differential pressures of 0, 5, 10 bar. Hydrogen crossover was measured using the integrated hydrogen sensor with the HoribaFuelCon electrolysis testing system. The standard CCMs without any additional treatments are used as a benchmark to assess the effects of differential pressure on polarisation and hydrogen crossover.

6.1.1 Pressure effect on the energy efficiency

The behaviour of the standard CCMs under different differential pressures is shown in Figure 6.1. For a detailed comparison, specific voltage points of 1.5 V and 1.8 V are selected, with the corresponding current densities summarised in Figure 6.2.

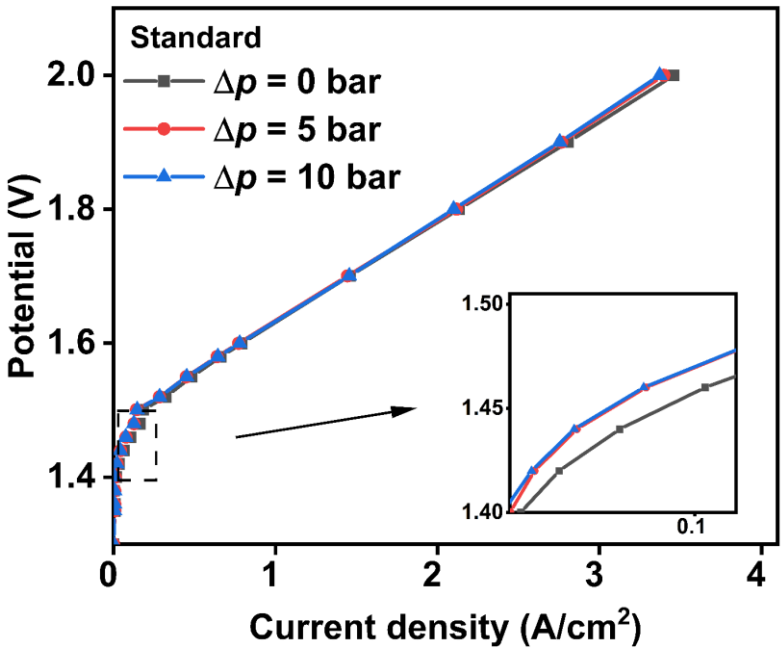

Figure 6.1 Polarisation curves of the standard CCM measured under various cathode-side differential pressures.

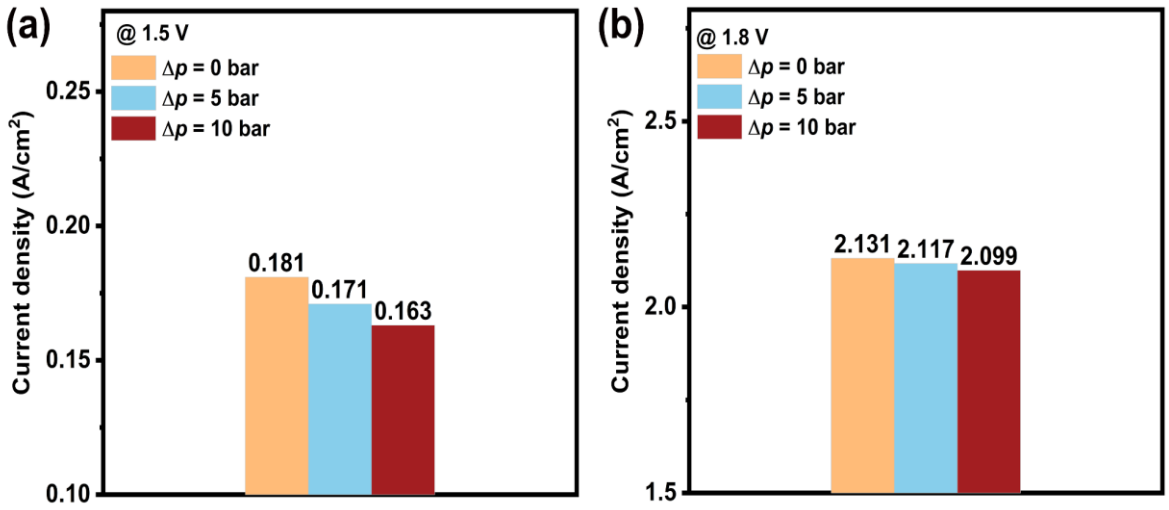

Figure 6.2 Summary of the current densities at specific voltages (1.5 V (a) and 1.8 V (b)) for the standard CCM under differential pressures.

Increasing the pressure affects the cell performance, leading to a decline in current density. This effect is more pronounced at lower voltages. At 1.5 V, the current density decreases from 0.181 A/cm^2 at 1 bar to 0.163 A/cm^2 at 10 bar differential pressures, corresponding to an approximately 10% performance loss. In contrast, at 1.8 V, the current density only drops by approximately 2%, from 2.131 A/cm^2 at 1 bar to 2.099 A/cm^2 at 10 bar differential pressures.

6.1.2 Pressure effect on the hydrogen crossover

To analyse the hydrogen crossover, the hydrogen content in oxygen (Vol%) at anode side was measured across a range of current densities (0.25 A/cm^2 to 2.5 A/cm^2) under varying differential pressures. The results are presented in Figure 6.3, with specific values at representative current densities summarised in Figure 6.4.

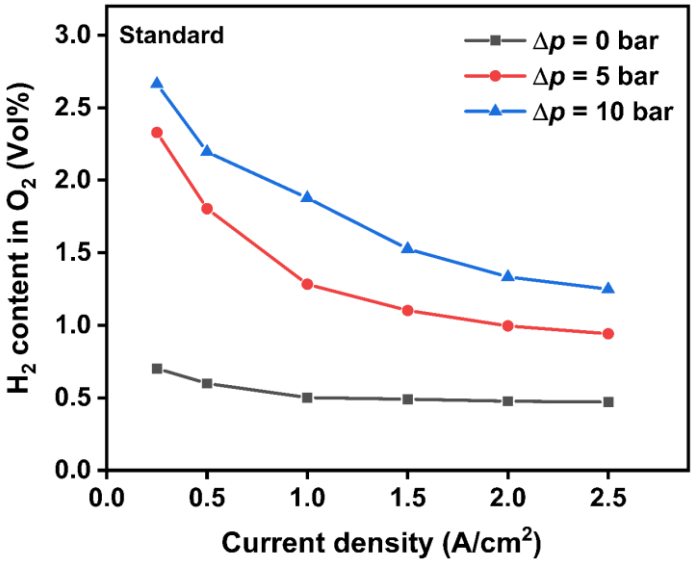

Figure 6.3 Hydrogen content in the anode (Vol%) for the standard CCM. Measurements were conducted under the cathodic pressure of 1, 6, and 11 bar within a current density range from 0.25 to 2.5 A/cm^2.

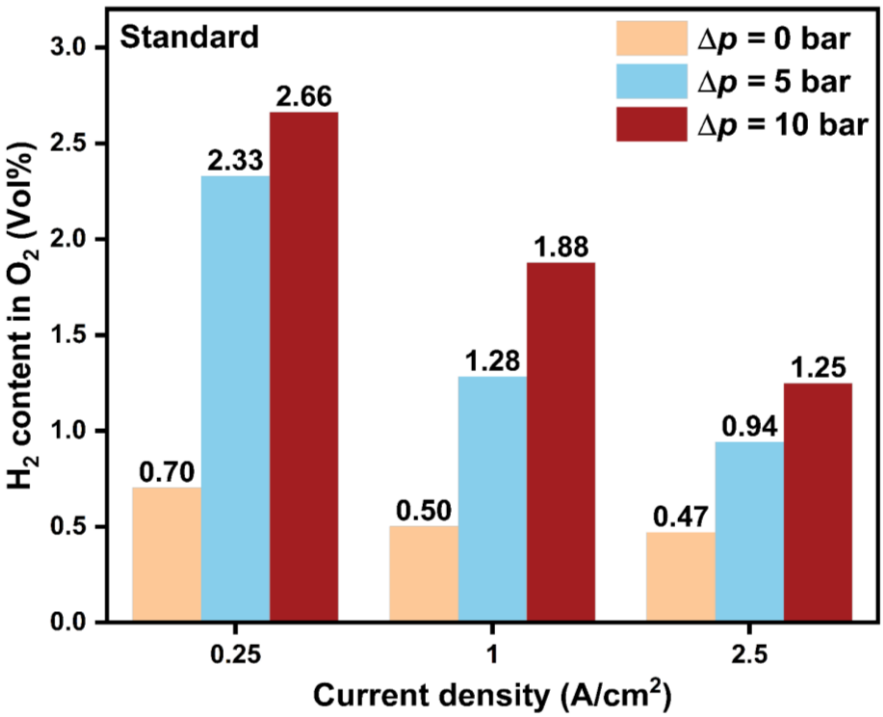

Figure 6.4 Summary of the hydrogen content in the anode at specific current densities (0.25 A/cm^2, 1 A/cm^2, 2.5 A/cm^2) for the standard CCM under various differential pressures.

The data show that hydrogen crossover increases significantly with the increasing differential pressure, primarily driven by the enhanced hydrogen concentration gradient between the cathode and anode. At a low current density of 0.25 A/cm^2, the crossover ratio increases from 0.7% under a differential pressure of 0 bar to 2.33% at 5 bar, and further to 2.66% at 10 bar, representing an approximate 2.8-fold increase. Conversely, increasing the operating current density reduces the hydrogen content in the anode across all pressure conditions. For example, under 0 bar differential pressure, the hydrogen content decreases from 0.7% at 0.25 A/cm^2 to 0.5% at 1 A/cm^2 and further to 0.47% at 2.5 A/cm^2. This trend is attributed to the dilution effect, where higher oxygen production rates at the larger current density reduces the relative hydrogen concentration in the oxygen stream [98,106,107].

It is worth noting that the technical safety threshold for hydrogen crossover is set at 2 vol% H_2 in O_2, corresponding to 50% of the lower explosive limit. However, under a differential pressure of 10 bar, the hydrogen content in the anode reaches 2.2% at 0.5 A/cm^2, exceeding the safety threshold. This raises serious safety concerns, particularly during low-current-density operation, which also limits the flexibility of PEMWEs when integrated with fluctuating renewable energy sources. Effective mitigation strategies are therefore essential to minimise hydrogen crossover and ensure safe, reliable operation across the entire current density range.

6.2. Hydrogen crossover behaviour in CCMs with a platinum functional layer

A platinum functional layer was incorporated into the CCM by sputtering platinum onto dried membranes using a Quorum Q150T-EC chamber. Equivalent thicknesses of 0.5 nm, 1 nm, and 2 nm were achieved under vacuum conditions at a constant current of

20 mA. Platinum deposition was applied to the anode side of the membrane, followed by catalyst spraying using the same procedures as the standard CCM fabrication. The platinum-coated membranes after sputtering coating are shown in Figure 6.5, and a schematic of CCMs with a platinum functional layer is presented in Figure 6.6.

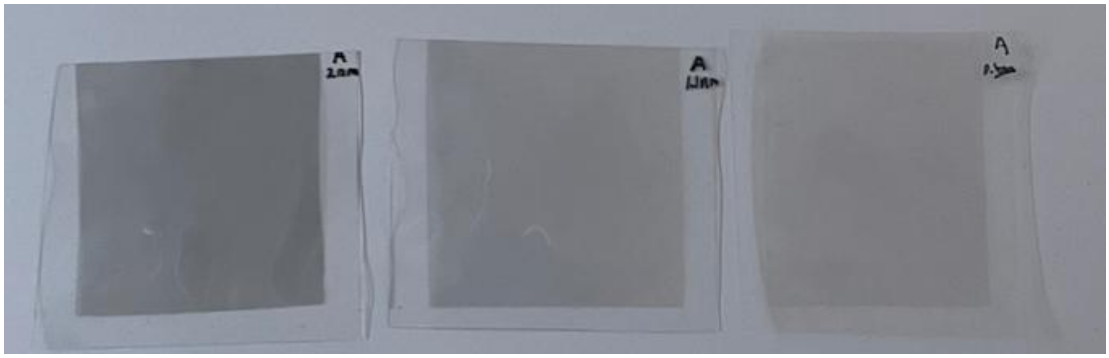

Figure 6.5 Platinum-coated membranes prepared with equivalent platinum layer thicknesses of 2 nm, 0.5 nm, and 1 nm (from left to right).

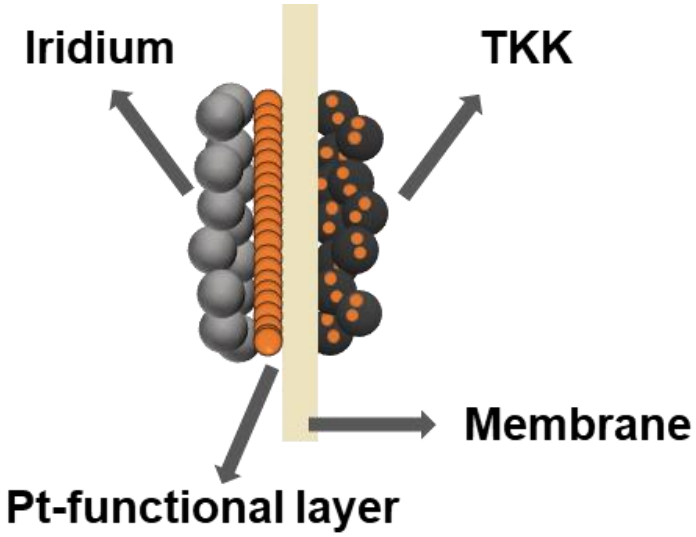

Figure 6.6 Schematic of CCMs incorporating a platinum functional layer.

To confirm the successful platinum deposition, X-ray photoelectron spectroscopy (XPS) analysis was conducted. Figure 6.7 displays the XPS spectra for the treated CCMs.

The presence of Pt4f peaks at binding energies corresponding to $Pt4f_{7/2}$ and $Pt4f_{5/2}$ clearly indicates the introduction of platinum on the membrane.

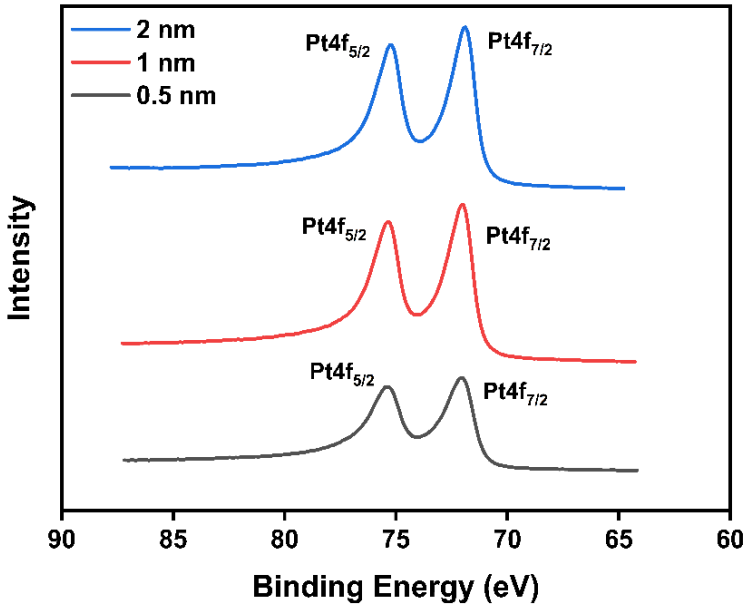

Figure 6.7 High resolution Pt XPS scan for the Pt functional layers deposited on the membrane.

6.2.1 Pressure effect on the treated CCM

To evaluate the effect of the platinum functional layer, the polarisation performance of the CCMs was analysed under various differential pressures. The results are illustrated in Figure 6.8. To enable a detailed comparison, the current densities at specific voltages of 1.5 V and 1.8 V are summarised in Figure 6.9.

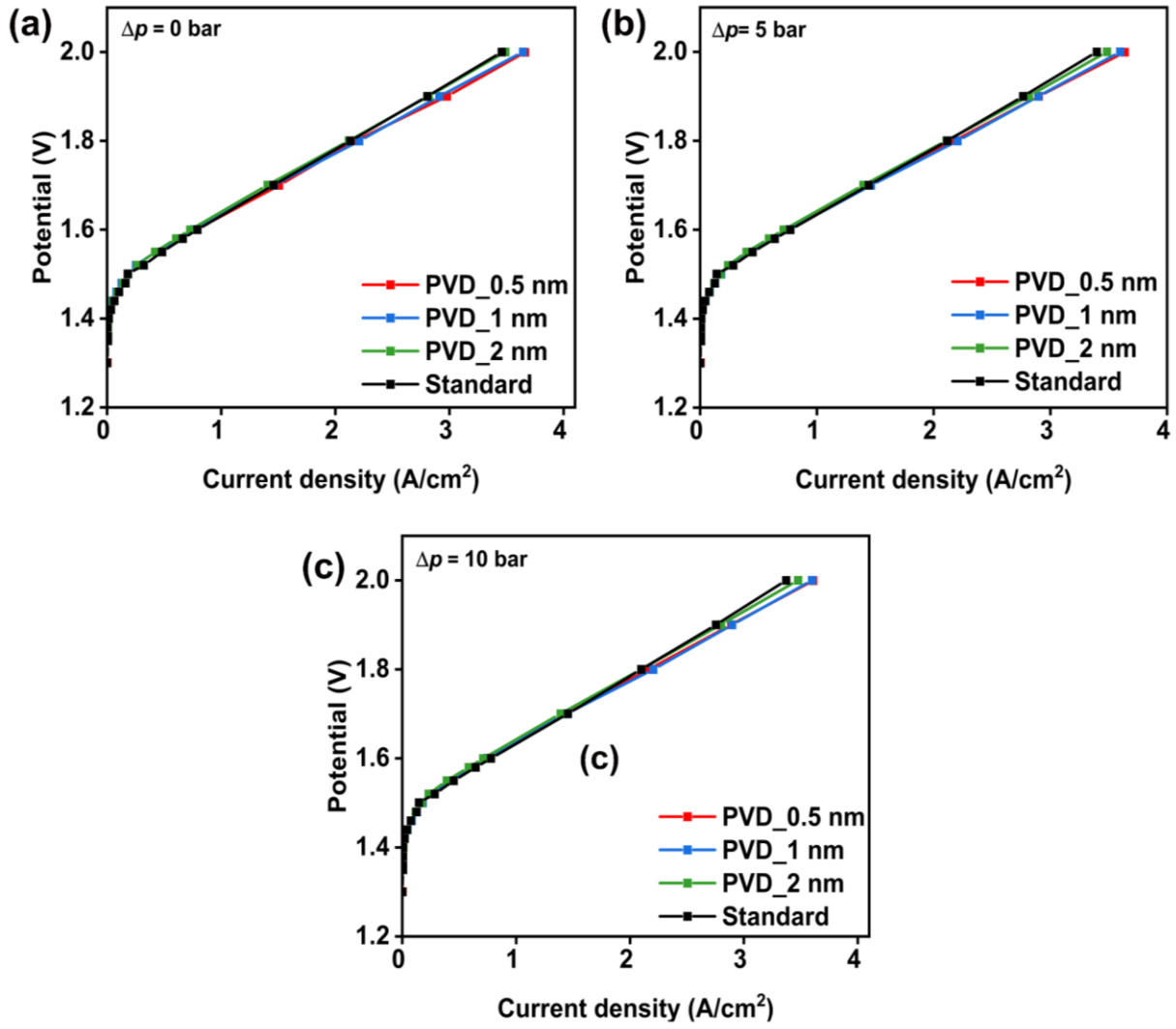

Figure 6.8 Polarisation curves for the standard CCM and the CCMs with the platinum functional layer at various equivalent thicknesses of 0.5 nm, 1 nm, and 2 nm. Measurements were conducted under the differential pressures of (a) 0 bar, (b) 5 bar, and (c) 10 bar.

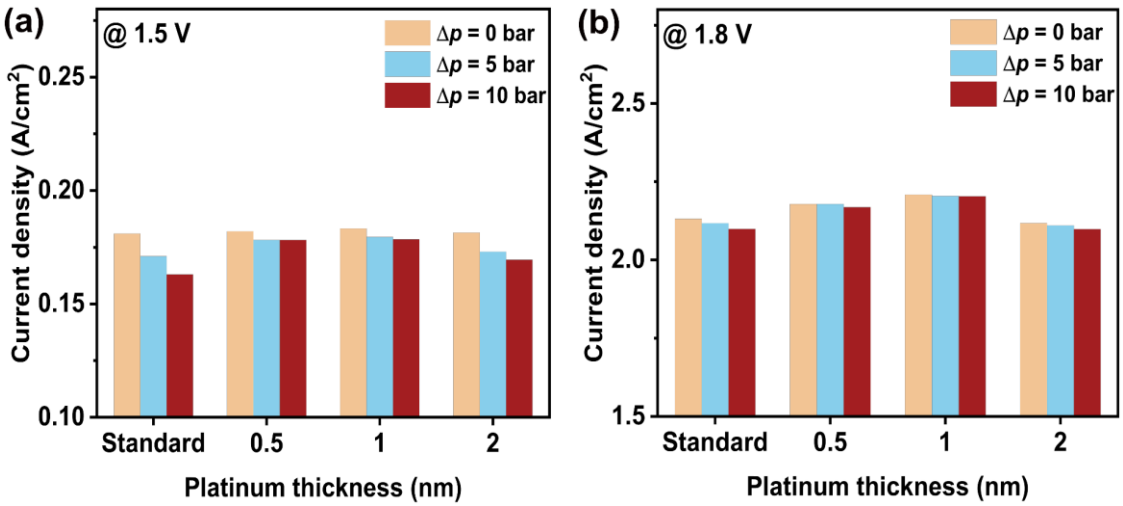

Figure 6.9 Comparison of the current densities at 1.5 V (a) and 1.8 V (b) under various differential pressure operation for the standard CCM and the CCMs with a Pt functional layer coated at different thicknesses.

The polarisation trends observed align with the findings from the standard CCM. These studies highlight that low-pressure operation is favoured in PEM water electrolysis due to the reaction equilibrium of liquid water converting to 1.5 moles of gaseous products (H_2 + $^1/_2$ O_2) [107,269]. Compared to the standard CCM, the CCMs with platinum functional layers show lower current density losses under the differential pressure conditions. For instance, at 1.5 V, the CCM with a 1 nm platinum layer exhibits a minor current density reduction, from 0.183 A/cm^2 at 0 bar to 0.179 A/cm^2 at 10 bar, corresponding to only 2.2% decrease. In comparison, the standard CCM shows a 10% drop under the same condition, highlighting the improved performance stability of the platinum-coated design under the high-differential pressure condition. Overall, the variations in current density at 1.8 V among all tested samples are negligible, with deviations not exceeding 0.05 A/cm^2.

In addition to mitigating pressure-induced performance loss, the platinum-coated

CCMs also exhibit slight improvements in polarisation performance. For example, the CCM with the 1 nm platinum layer achieves current densities of 0.183 A/cm^2 at 1.5 V and 2.21 A/cm^2 at 1.8 V, representing increases of 1.7% and 3.8%, respectively, compared to the standard CCM at 0 bar. These improvements are attributed to the suppression of hydrogen crossover, which will be explored in detail in subsequent sections.

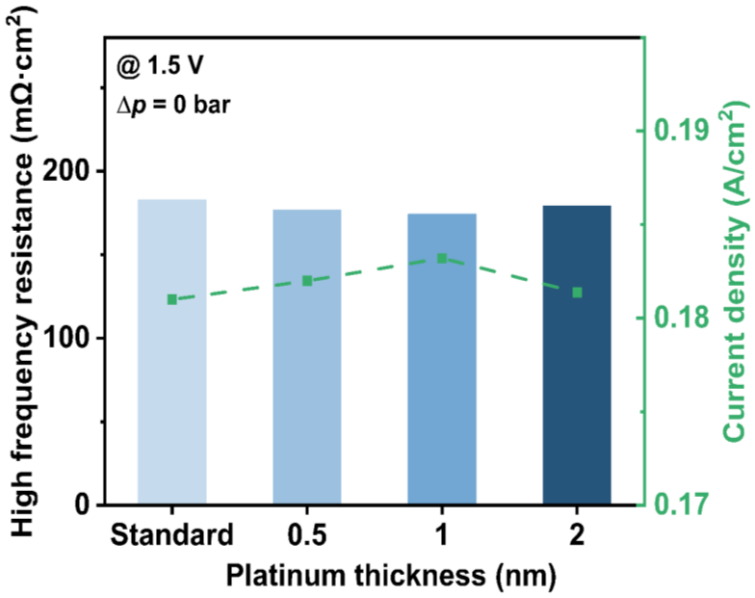

Figure 6.10 High-frequency resistance and current density at 1.5 V for the standard CCM and the CCMs with different platinum coating thicknesses.

To further examine the effect of the platinum interlayer on CCM performance, high-frequency resistance measurement was conducted at 1.5 V for all CCMs (Figure 6.10). The standard CCM shows the highest ohmic resistance of 183 mΩ·cm^2, while the CCM incorporating the 1 nm platinum layer reduces this value to 174 mΩ·cm^2. These results confirm that the platinum interlayer does not hinder proton conductivity between the anodic catalyst layer and the membrane, ensuring effective ion transport within the CCMs. By reducing ohmic resistance, the platinum interlayer enhances overall

performance under operating conditions and establishes a reliable foundation for subsequent hydrogen crossover evaluations. Additionally, the ICP-MS results reveal that 1 nm equivalent Pt layer corresponds to a Pt loading of approximately 2 $\mu g_{Pt}/cm^2$, which represents a minimal addition to the overall CCM structure.

6.2.2 Hydrogen crossover mitigation by the platinum functional layer

To investigate the effectiveness of the platinum functional layer in mitigating hydrogen crossover, measurements were conducted across a current density range of 0.25 A/cm^2 to 2.5 A/cm^2 under three distinct differential pressures. The corresponding results are depicted in Figure 6.11, with representative values at specific current densities summarised in Figure 6.12.

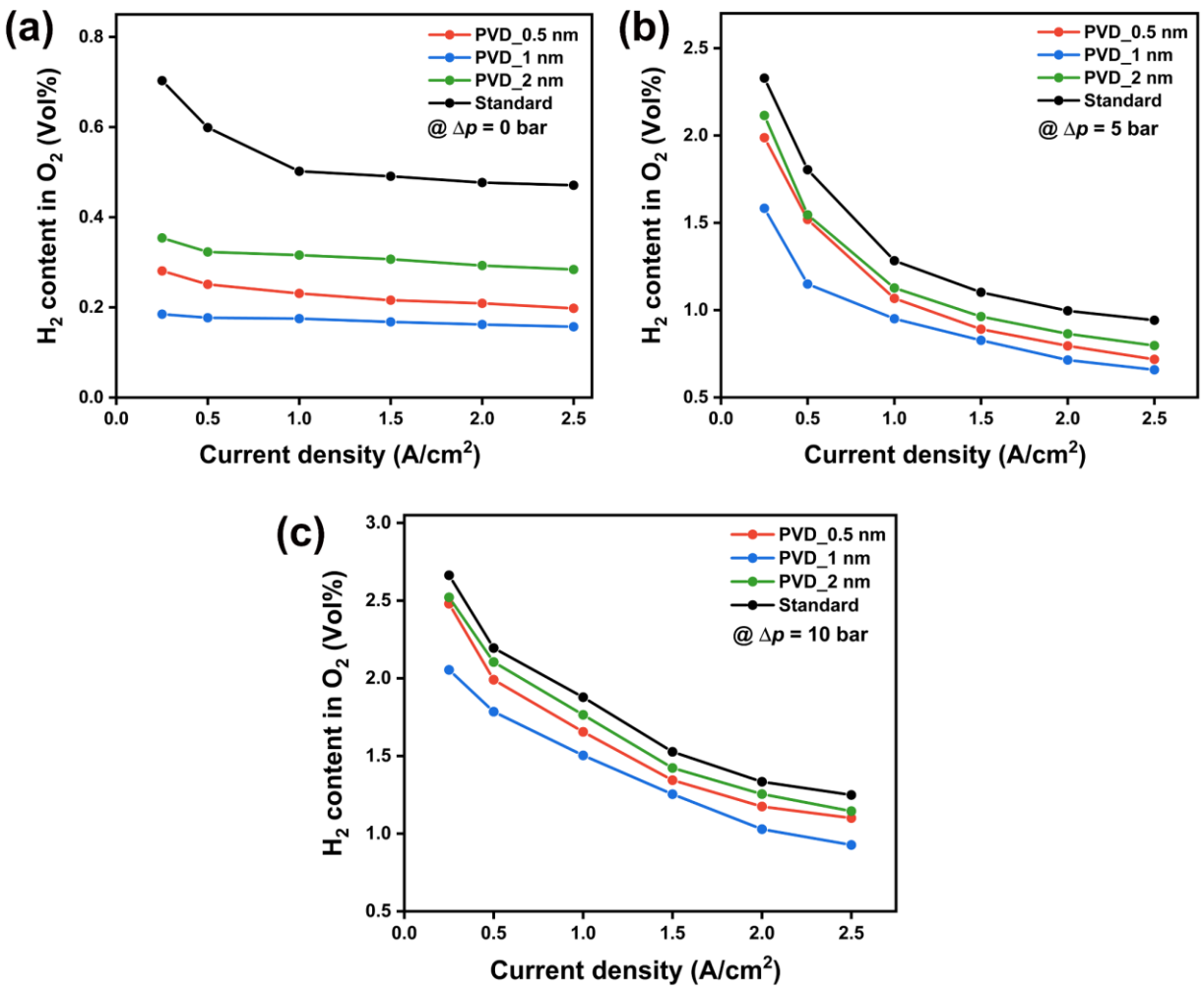

Figure 6.11 Hydrogen content in the anode (Vol%) for the standard CCM and the treated CCMs with the platinum functional layer at the equivalent thicknesses of 0.5 nm, 1 nm, and 2 nm. Measurements were conducted across a current density range of 0.25 A/cm^2 to 2.5 A/cm^2 under three differential pressures of (a) 0 bar, (b) 5 bar, and (c) 10 bar.

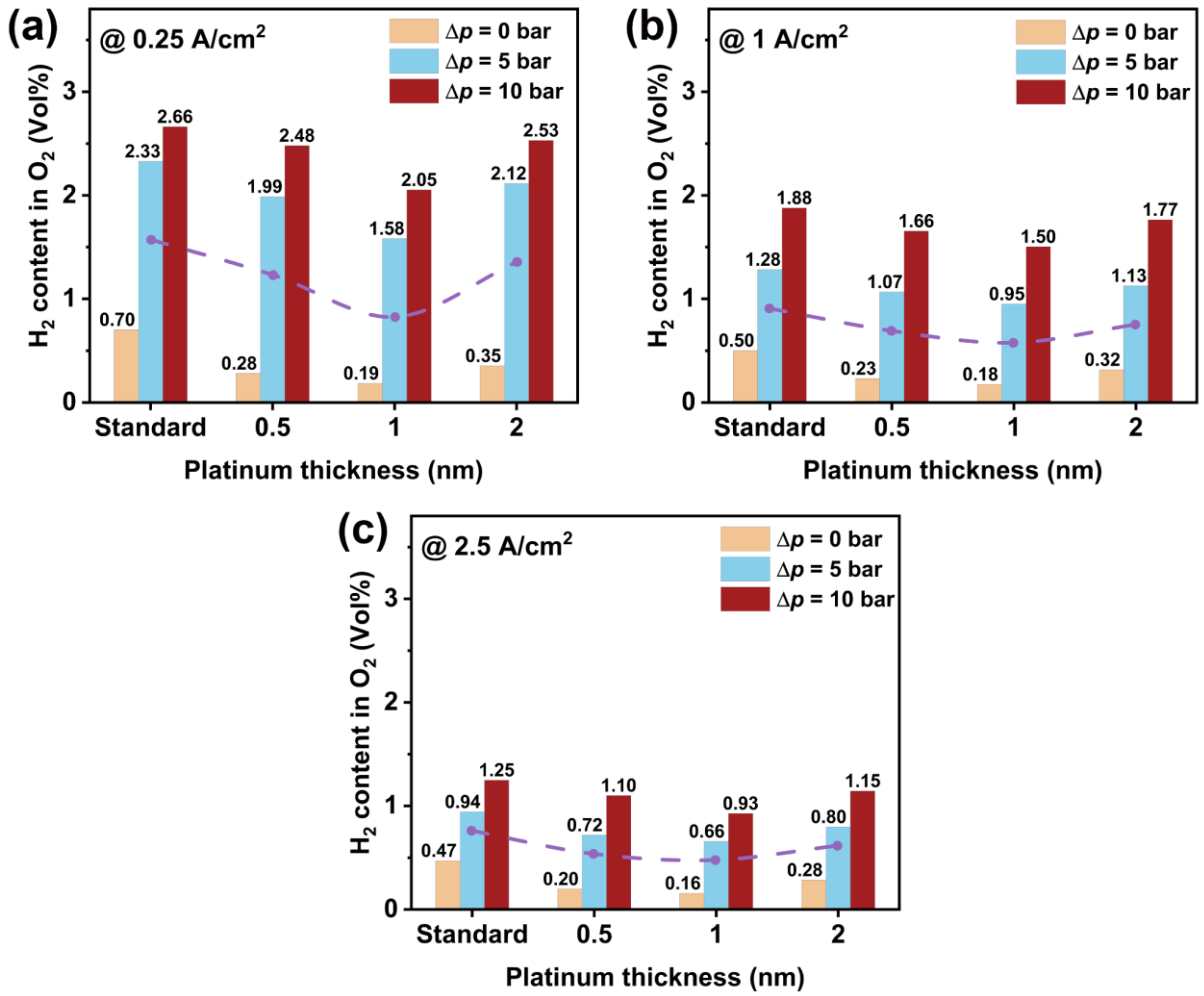

Figure 6.12 Hydrogen crossover (Vol%) at (a) 0.25 A/cm^2, (b) 1 A/cm^2, and (c) 2.5 A/cm^2 for the standard CCM and the treated CCMs with the platinum functional layer at various equivalent thicknesses of 0.5 nm, 1 nm, and 2 nm. Testing was conducted at different differential pressures.

Among the tested configurations, the standard CCM exhibits the highest hydrogen crossover under all differential pressure and current densities conditions. The introduction of the platinum functional layer significantly reduces hydrogen crossover, with the extent of reduction depending on the platinum layer thickness. As iridium remains catalytically inactive for hydrogen oxidation throughout the tests, the observed

improvements can be attributed solely to the platinum functional layer [118].

At 0 bar differential pressure, the standard CCM exhibits highest crossover hydrogen concentration of 0.7%. the CCM with the 1 nm platinum layer demonstrates the most significant reduction in hydrogen crossover. At 0.25 A/cm^2, the hydrogen crossover decreases substantially to 0.28% with the 0.5 nm platinum layer and further to 0.19% with the 1 nm layer, achieving a reduction of 73%. However, the 2 nm platinum layer results in a slight increase in the hydrogen content to 0.35%, indicating that increasing the platinum layer thickness beyond 1 nm does not provide additional reductions. A similar trend is evident at 1 A/cm^2, with the hydrogen content in the anode dropping from 0.50% for the standard CCM to 0.18% for the 1 nm platinum layer, followed by a slight increase to 0.23% for the 2 nm layer. This trend is consistent at 2.5 A/cm^2, with the hydrogen content dropping from 0.47% to 0.16% and then rising to 0.28%. While the reduction percentage is marginally lower at higher current densities, the 1 nm platinum layer still achieves approximately 65% reduction in hydrogen crossover at both 1 A/cm^2 and 2.5 A/cm^2 compared to the standard CCM.

As the differential pressure increases, the platinum functional layer continues to demonstrate its effectiveness in mitigating hydrogen crossover. At 0.25 A/cm^2 and a differential of 5 bar, the hydrogen crossover ratio decreases from 2.33% for the standard CCM to 1.58% with the 1 nm platinum layer, representing a 32% reduction. Under the same current density, at 10 bar differentials, the crossover ratio decreases from 2.66% to 2.05%, achieving 23% reduction. At higher current densities, similar improvements are observed. For instance, at 2.5 A/cm², the crossover ratio drops from 1.25% to 0.72% at 5 bar, and from 1.50% to 0.93% at 10 bar, corresponding to reductions of around 40%. These results underscore that introducing the 1 nm platinum

functional layer not only reduces hydrogen crossover significantly but also ensures safe operation across all current densities, even under the challenging conditions of the 10 bar differential pressure.

6.3. Mechanistic study of hydrogen crossover

In theory, the kinetics of hydrogen oxidation on platinum catalysts are remarkably rapid, enabling effective suppression of hydrogen crossover when sufficient catalyst material is present [270]. Increasing the amount of catalyst is therefore expected to significantly reduce the hydrogen content in the anode. However, experimental findings reveal that the ability of the platinum functional layer to mitigate hydrogen crossover diminishes under higher pressure conditions. At higher differential pressures, the reduction ratio of hydrogen crossover becomes significantly lower compared to that observed under atmospheric conditions, indicating a performance limitation of the platinum layer in suppressing hydrogen permeation. Furthermore, an increase in platinum loading from 1 nm to 2 nm unexpectedly reduced its effectiveness in mitigating hydrogen crossover, which contradicts initial expectations.

To quantitatively analyse the permeated hydrogen flux $N_{H_2}^{Perm}$, the hydrogen concentration at the anode outlet $\mathrm{X}_{H_2\ in\ O_2}$ was measured using a thermal conductivity sensor, and the hydrogen flux values for each CCM are calculated based on Equation (9). The hydrogen flux values for each CCM across the full range of current densities and under various pressure conditions are presented in Figure 6.13.

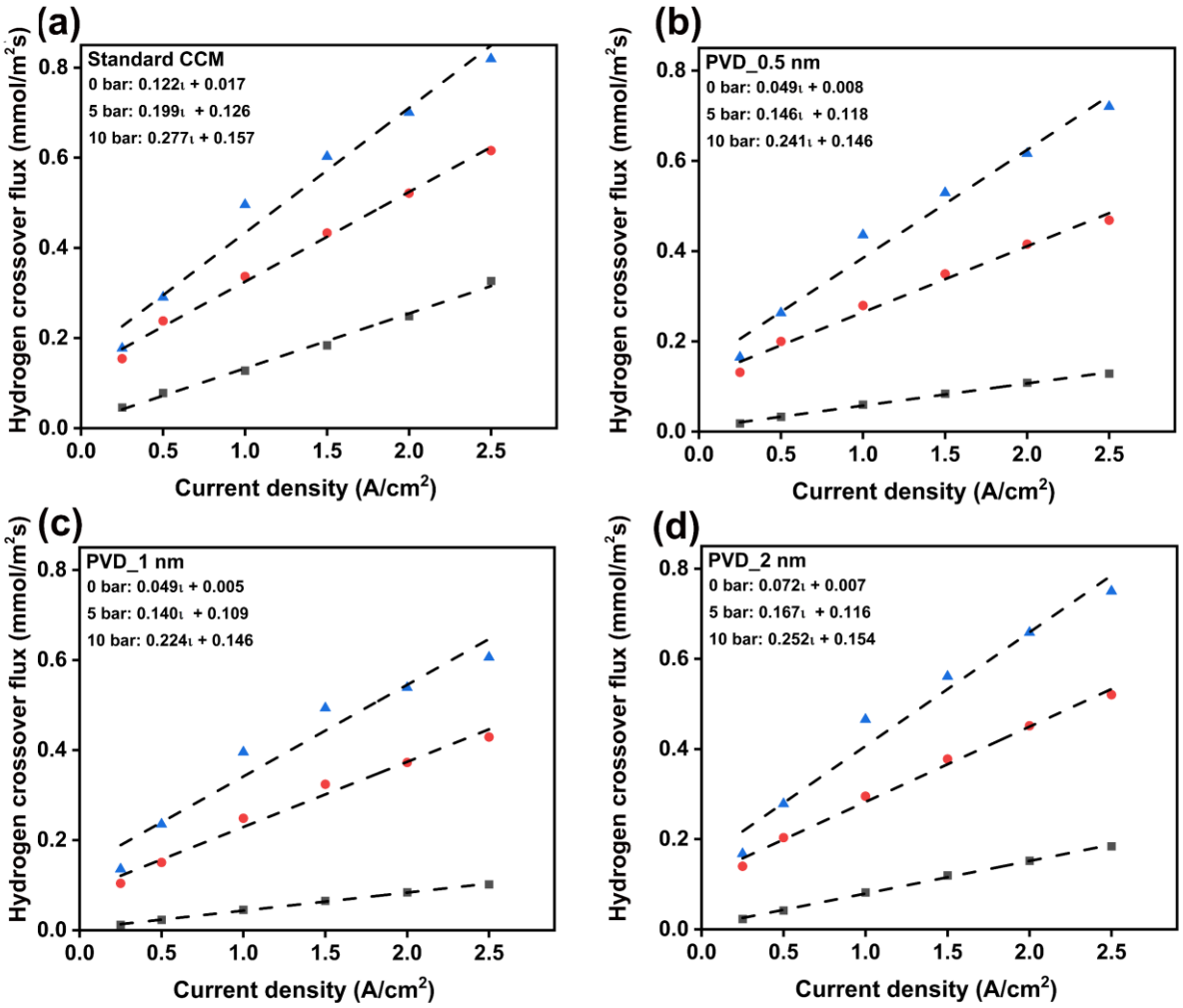

Figure 6.13 Hydrogen crossover flux (mmol/m^2 s) as a function of current density for the standard CCM (a) and the treated CCMs with platinum functional layers of 0.5 nm (a), 1 nm (b), and 2 nm (c). Testing was conducted under differential pressures of 0 bar (black), 5 bar (red), and 10 bar (blue).

The results of hydrogen flux indicate a diminishing effectiveness of the platinum functional layer as the pressure increases, demonstrated by higher flux values under elevated pressure conditions.

Since all CCMs are fabricated using the identical processes, it is reasonable to assume consistent mass transfer characteristics for hydrogen across the membrane. Under this assumption, the total permeation of hydrogen through the membrane remains constant across all CCMs. The CCM without any interlayer (standard CCM) was used to define the baseline total hydrogen flux. Taking the CCM with the 1 nm platinum functional layer as an example, the observed reduction in hydrogen crossover is attributed to hydrogen oxidation reactions (HOR) occurring within the platinum layer. To evaluate the amount of hydrogen consumed via HOR, the residual hydrogen flux is defined as the amount of hydrogen that permeates through the membrane and reaches the outlet after partial consumption within the platinum interlayer. The difference in hydrogen flux between the standard CCM and the treated CCM corresponds to the hydrogen consumed by HOR. Figure 6.14 provides a detailed breakdown of total hydrogen flux (solid bars) and residual flux (hatched bars). The unfilled portions of the bars indicate the amount of hydrogen consumed through HOR within the platinum functional layer.

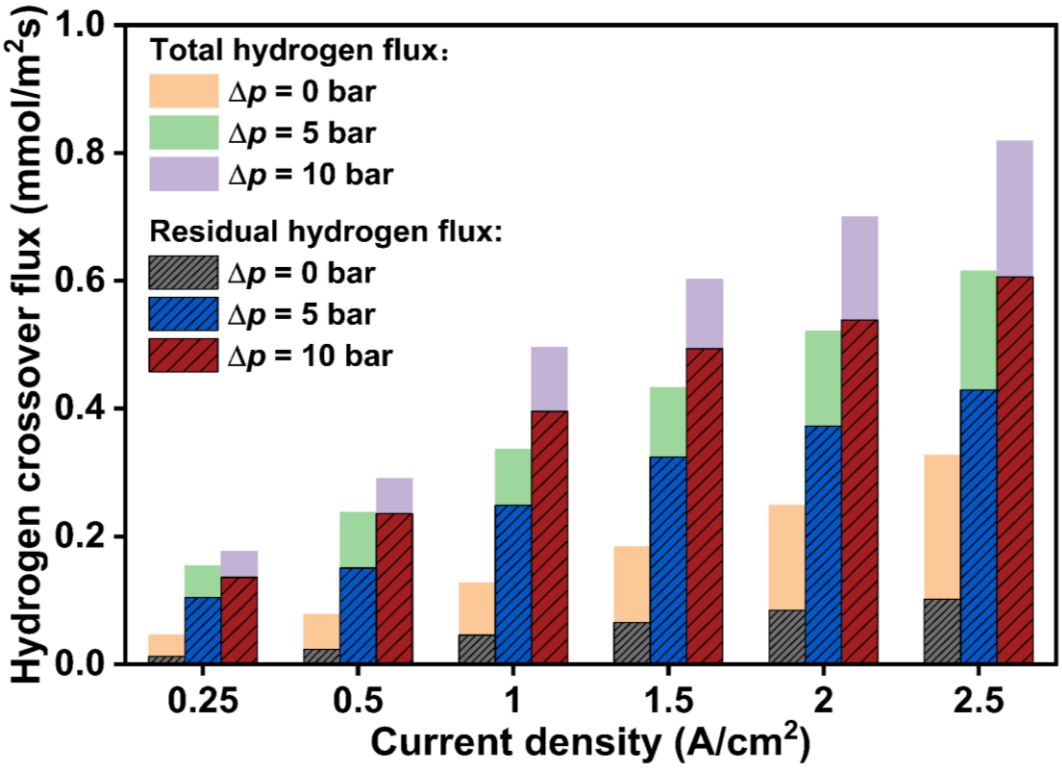

Figure 6.14 Total and residual hydrogen flux under various differential pressures (0, 5, and 10 bar) at different current densities for the CCM with 1 nm equivalent Pt functional layer.

Interestingly, the disparity between total and residual hydrogen flux remains nearly constant across all pressures at each measured current density point. This observation suggests that the amount of hydrogen oxidised within the functional layer is not influenced by increasing pressure. A possible explanation is that the oxidation reaction within the functional layer has already reached its maximum capacity. At elevated pressures, a higher hydrogen permeation flux is observed. Theoretically, increased differential pressures provide more reactants for the HOR at the platinum surface, leading to expectations of higher hydrogen consumption [271]. However, the results deviate from these predictions. Despite the rapid kinetics of HOR on platinum, the amount of hydrogen consumed does not increase proportionally with the higher

permeation rates observed under elevated pressure. This discrepancy may be attributed to the limited availability of the active platinum sites. Essentially, the reaction sites in the functional layer appear to be saturated, preventing further oxidation of the permeated hydrogen.

To further explore the effectiveness of the platinum functional layer in mitigating hydrogen crossover, a schematic is developed to illustrate the local concentration profiles of hydrogen and oxygen gases across the CCM. This model based on previous studies [113,130], is shown in Figure 6.15. In contrast to previous models, where the Pt layer was embedded within the membrane, the present schematic illustrates a platinum interlayer placed between the membrane and the cathode catalyst layer.

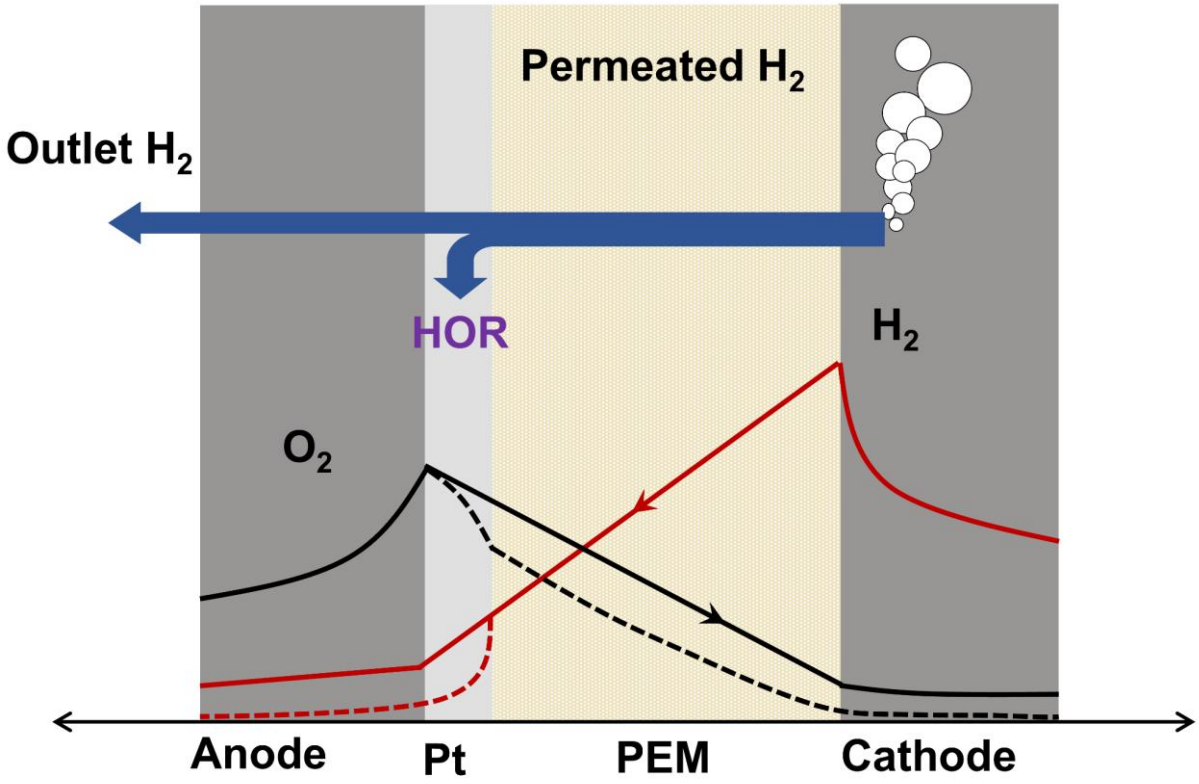

Figure 6.15 Schematic representation of hydrogen and oxygen concentration profiles across the CCM, comparing cases without (solid lines) and with (dashed lines) a platinum functional layer.

As shown in the model, hydrogen generated at the cathode diffuses through the membrane toward the anode, driven by the differential pressure. In the presence of a platinum functional layer, the permeated hydrogen undergoes HOR with oxygen produced at the anode, thereby reducing the concentration of hydrogen reaching the anode outlet. The introduction of a platinum functional layer significantly changes the local concentration profiles of both gases across the CCM. Based on this model, two potential mechanisms are proposed to explain the observed behaviour. The first hypothesis suggests that the platinum functional layer has already reached its maximum reaction capacity under atmospheric condition, limiting its ability to further

reduce hydrogen permeation as pressure increases. The second hypothesis assumes that the platinum layer primarily functions as a physical barrier to hydrogen diffusion, rather than relying on HOR to mitigate crossover.

To evaluate these hypotheses, two modified CCMs were prepared. In the first CCM configuration, gold was deposited onto the membrane surface instead of platinum to assess the effect of a non-catalytic physical barrier. In the second, the platinum functional layer was embedded within the iridium catalyst layer rather than deposited directly on the membrane. This was achieved by first spraying half amount of the iridium catalyst, followed by sputter-coating the platinum layer, and then applying the remaining iridium catalyst to complete the anode. All other fabrication steps remained consistent with the standard process. The hydrogen crossover results for these new CCM configurations under a 10-bar differential pressure are shown in Figure 6.16.

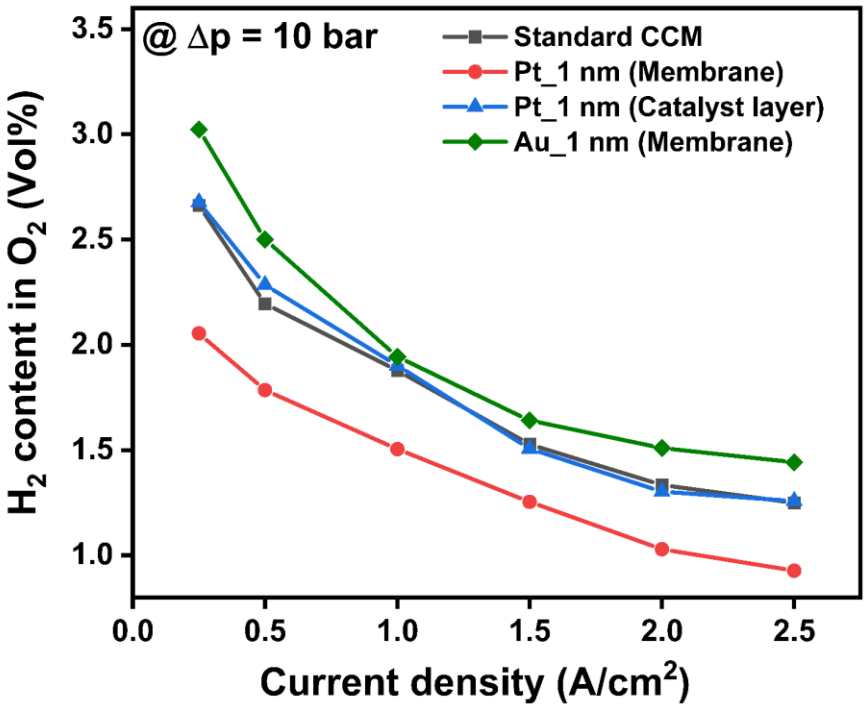

Figure 6.16 Hydrogen crossover results under a 10-bar differential pressure for the

standard CCM, the CCM with a 1 nm platinum functional layer on the membrane (Pt_1 nm (Membrane)), the CCM with a 1 nm platinum functional layer within the anode catalyst layer (Pt_1 nm (Catalyst layer)), and CCM with a 1 nm gold functional layer on the membrane (Au_1 nm (Membrane)).

The experimental results demonstrate that neither of the two modified configurations reduces hydrogen crossover. Considering that HOR occurs only when sufficient hydrogen and oxygen are simultaneously exposed to platinum catalysts [272], the permeated hydrogen available at the Pt layer in this configuration is insufficient. This highlights the importance of the interlayer location. In the other configuration, gold was selected as a non-catalytic material to help distinguish the effect of physical blocking from catalytic HOR. As a result, the hydrogen crossover was not reduced and even slight increase, indicating that the platinum layer does not function as a physical barrier. Consequently, the observed reduction in hydrogen flux for the CCM with the membrane-deposited platinum layer can be attributed primarily to catalytic HOR activity, rather than any physical blocking effect.

This outcome supports the validity of the first hypothesis proposed earlier. However, increasing the platinum loading from 1 nm to 2 nm does not further improve the reaction efficiency and may even introduce adverse effects. To investigate the influence of platinum loading on the functional layer, the TEM analysis was performed by coating 1 nm and 2 nm equivalent platinum layer on TEM grid, as shown in Figure 6.17. At a lower loading, increasing the amount of the deposited platinum provides more active sites for HOR. However, this trend changes at a higher loading. The TEM image reveals that at 2 nm, a nearly continuous film is formed rather than isolated nanoparticles (Figure 6.17 (c)). This structure significantly reduces the number of

accessible surface reaction sites for HOR, which may explain the performance decline observed beyond 1 nm loading.

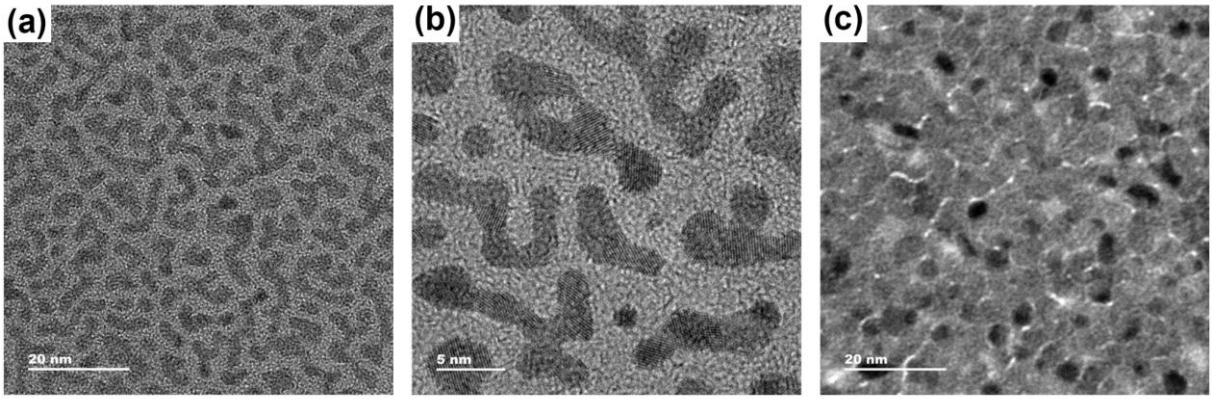

Figure 6.17 TEM images of 1 nm (a, b) and 2 nm (c) platinum functional layer at different magnifications.

These findings suggest that the ability of the platinum functional layer to control hydrogen permeation is inherently constrained by its placement and the local hydrogen and oxygen conditions. Optimising its design requires consideration of these factors to ensure compatibility with specific applications and operating pressures.

6.4. CCM durability under accelerated stress testing

To investigate the stability of the platinum functional layer, an accelerated stress test (AST) was conducted to mimic the PEMWE operation coupled with fluctuating renewable energy sources. The test involves alternating periods of operation and idling to accelerate CCM degradation as outlined by Weiß et al.[273]. During AST, the cathode was subjected to a differential pressure of 11 bar, while the anode remained at atmospheric pressure. After completing 200 AST cycles, corresponding to 100 hours of operation, the polarisation curves and EIS for the CCM with 1 nm Pt functional layer are shown in Figure 6.18.

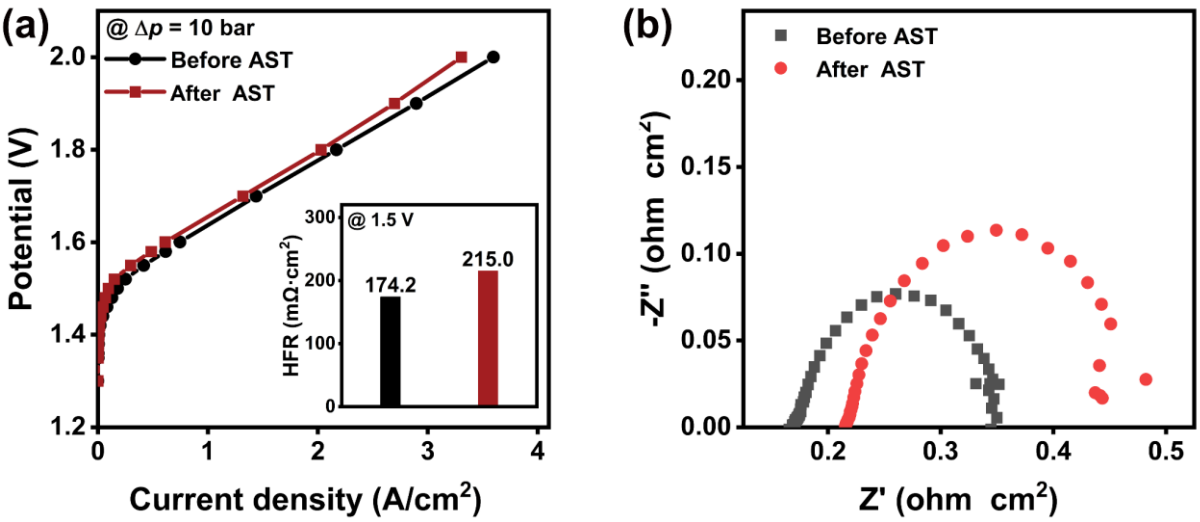

Figure 6.18 Electrochemical performance (a) and EIS recorded at 1.5 V (b) of the CCM with 1 nm Pt functional layer before and after AST.

The EIS pattern after AST reveals an enlarged semi-circle, signifying increased charge transfer resistance and reduced kinetic activity caused by electrode degradation. During AST, ionomer and membrane degradation occur within the catalyst layer due to intermediate species generated from reactions between permeated hydrogen radicals (H•) and oxygen (O_2) at the anode-PEM interface [153,154], leading to a decline in catalyst activity. Additionally, the structural deterioration of the electrode further reduces the number of active reaction sites, leading to increased charge transfer resistance. The ohmic resistance also increases during AST, rising from 174.2 mΩ·cm^2 to 215.0 mΩ·cm^2. This rise reflects the combined effects of ionomer degradation, electrode structural deterioration, and membrane decay induced by chemical attack from reactive intermediates, as evidenced by the rightward shift in the EIS plot. Consequently, the polarisation curves illustrate a loss in power efficiency. These observations align with prior studies, which have reported that the dynamic operation accelerates electrode degradation, significantly impacting durability and performance

274–277.

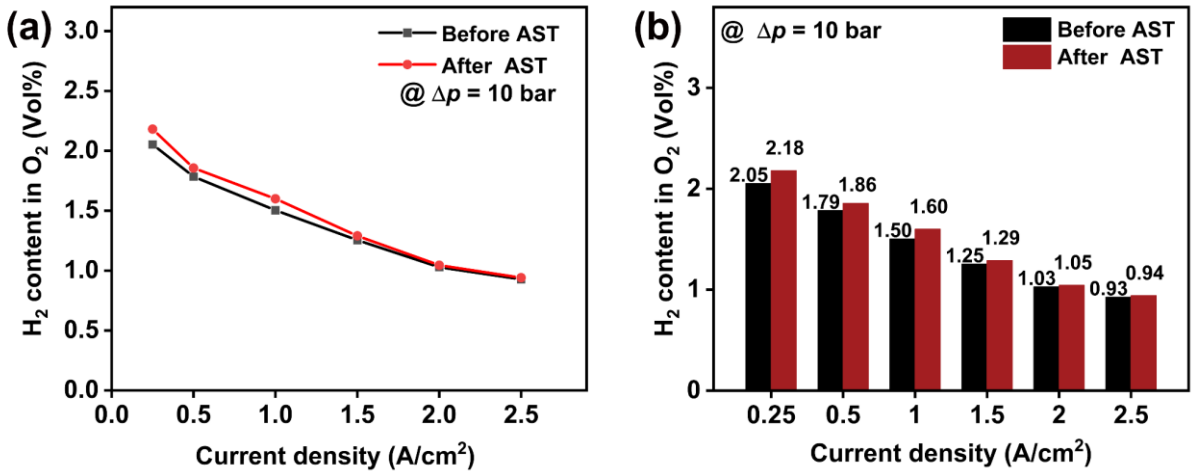

Figure 6.19 The hydrogen crossover characteristics of the CCM with 1 nm Pt functional layer before and after AST.

After AST, the CCM with 1 nm Pt functional layer retains nearly all of its hydrogen crossover mitigation ability at high current densities, as shown in Figure 6.19. For instance, at 2.5 A/cm^2, the functional layer maintains approximately 99% of its original performance. This stability is attributed to the high flux of generated gases at the large current densities, which effectively suppresses the impact of AST-induced degradation. At low current densities, a slight increase in hydrogen crossover ratio is observed. At 0.25 A/cm^2, the functional layer maintains approximately 94% of its initial performance. These results further highlight the functional layer's effectiveness in mitigating hydrogen crossover, even under stress conditions. In contrast, the standard CCM exhibits a significant decline in hydrogen crossover performance after AST, as shown in Figure 6.20. Across the entire current density range, a noticeable upward shift in hydrogen content values is observed, indicating membrane thinning due to dynamic operation. This thinning effect exacerbates hydrogen permeation, further increasing

hydrogen crossover, as reported in previous studies [274,278]. Despite these degradation effects induced by AST, the platinum functional layer effectively preserves its functionality. This demonstrates the potential of this approach to reduce hydrogen crossover and support the feasibility of coupling PEMWE systems with renewable energy sources.

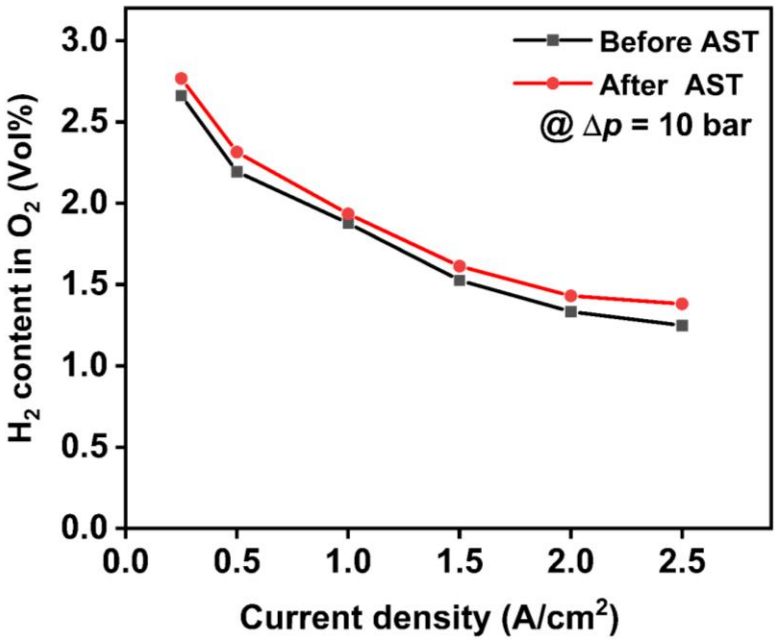

Figure 6.20 Hydrogen crossover performance of the standard CCM before and after AST.

To further understand the AST impact on both electrodes, SEM imaging was performed to analyse the surface morphology of the catalyst layers before and after AST (Figure 6.21 and Figure 6.22). The major crack formation areas have been highlighted in the SEM images to guide visual interpretation.

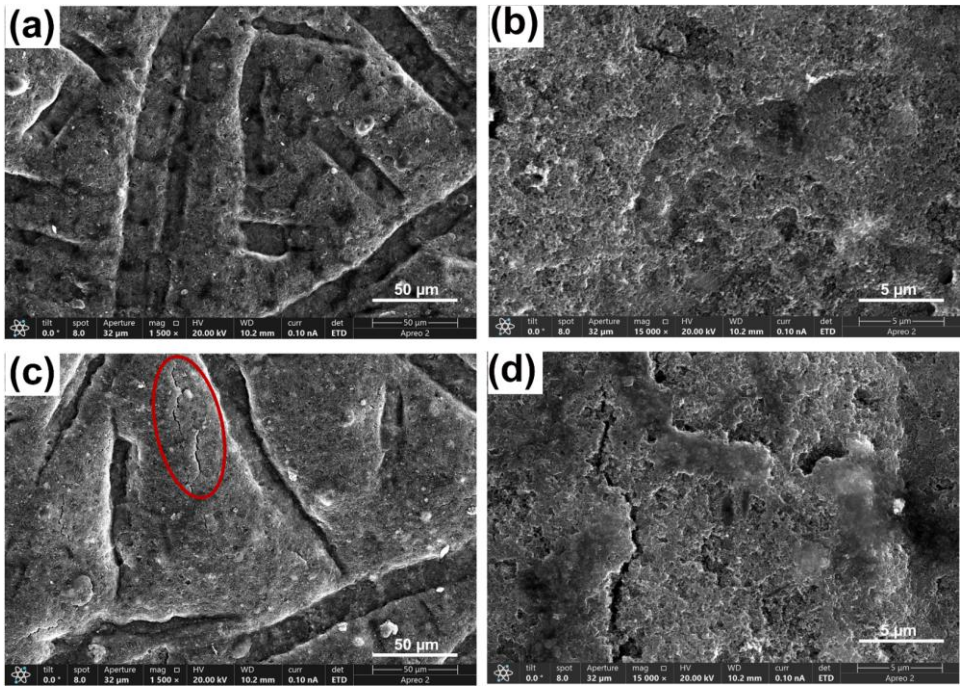

Figure 6.21 SEM images of the cathode catalyst layer surface (CCM with 1 nm Pt functional layer) before (a, b) and after (c, d) AST.

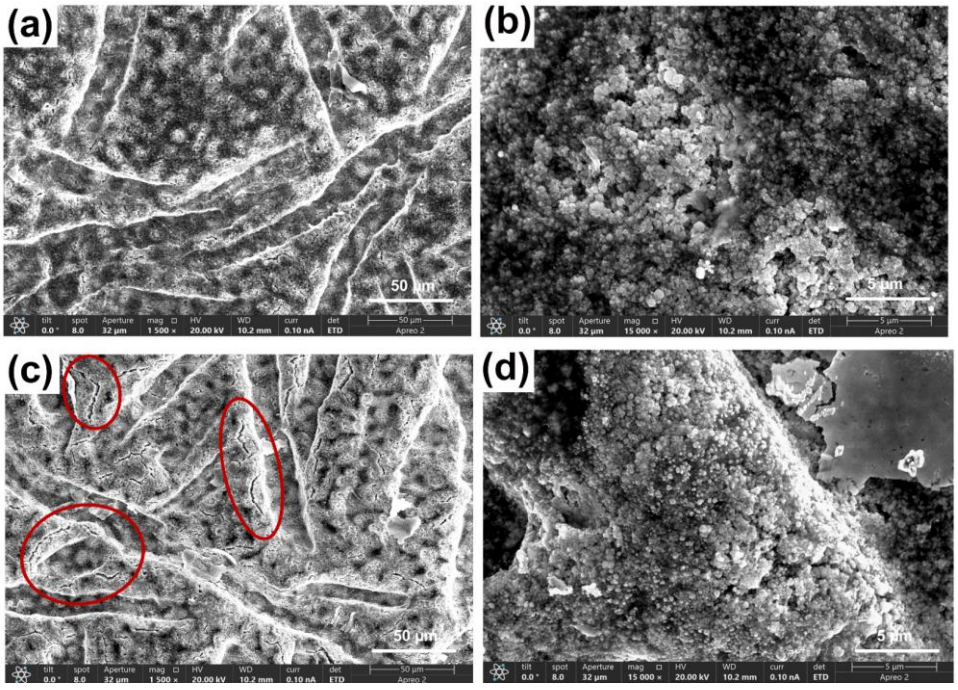

Figure 6.22 SEM images of the anode catalyst layer surface (CCM with 1 nm Pt functional layer) before (a, b) and after (c, d) AST testing.

The SEM images illustrate the surface morphology of the catalyst layers. The indentations visible in the images are associated with the PTL fibre structure and result from the high compression force applied during single-cell assembly, rather than the AST process itself. Similar patterns have been reported in other studies [178,184]. Before AST, the catalyst layer appears more evenly distributed, while after AST, significant cracks and the formation of larger particle clusters are evident. This structural change suggests a progressive electrode degradation, likely caused by nanoparticle detachment, coalescence, and dissolution, as well as the ionomer degradation, which subsequently reduces in-plane electron transport and increases ohmic resistance [184]. Additionally, the increased surface roughness observed after AST further contributes to the elevated charge transfer resistance and ohmic resistance identified in the EIS analysis. Despite these structural degradations, the functional layer maintains its hydrogen mitigation ability under harsh conditions, demonstrating its remarkable robustness and long-term stability.

6.5. Conclusions

This study verifies the effectiveness of incorporating the platinum functional layer at the anode/membrane interface in mitigating hydrogen crossover in PEMWEs. The CCM with a 1 nm equivalent platinum functional layer achieved a reduction in hydrogen content at the anode by 73% and 66% under 0 bar and 10 bar differential pressures at 0.25 A/cm^2, respectively, compared to the standard CCM. However, increasing the platinum loading beyond this point did not offer additional improvement, indicating an optimal configuration for the functional layer. Under elevated differential pressures (5 and 10 bar), the functional layer continued to perform effectively but was limited by the inherent kinetics of the hydrogen oxidation reaction and the finite availability of active

sites. This study confirms that the functional layer reduces hydrogen crossover primarily by facilitating HOR at the anode-electrolyte interface rather than serving as a physical barrier. Localised concentration profiles of hydrogen and oxygen further corroborated this mechanism, demonstrating the functional layer's effectiveness in mitigating hydrogen permeation under high-pressure conditions.

The durability of the platinum functional layer was validated through accelerated stress tests (corresponding to 100 hours) that simulated dynamic operational conditions. Despite some increases in ohmic and charge transfer resistances, the functional layer retained its hydrogen crossover suppression capabilities. The CCM with 1 nm equivalent platinum functional layer maintained 99% of its performance at 2.5 A/cm^2 and 94% at 0.25 A/cm^2, highlighting its durability and adaptability under variable load conditions.

In summary, this work establishes the platinum functional layer as a promising solution for reducing hydrogen crossover while preserving CCM functionality under harsh conditions. These findings underscore its suitability for enabling stable operation in PEMWE systems integrated with renewable energy sources.

Chapter 7

Conclusions and outlook

7 Conclusions and outlook

This study systematically explored the development and optimisation of catalyst-coated membranes for high performance differential pressure proton exchange membrane water electrolysers. Through a combination of experimental investigations and detailed electrochemical and physical characterisations, key insights were obtained into the CCM fabrication and performance evaluation for performance improvement. Additionally, to enhance the operational flexibility of PEMWEs under high differential pressure when coupled with fluctuating loads, the mechanism by which the platinum functional layer mitigates hydrogen crossover was investigated. By reducing hydrogen permeation, this approach extended the operational range of CCMs at low current densities, ensuring safer and more stable performance.

Electrochemical performance and scalability

Performance evaluations across multiple scales, from 5 cm^2 laboratory cells to 50 cm^2 large cells, demonstrated the influence of operational parameters on CCM performance. Optimal configurations, including the 3.5 N·m assembling force with PTFE gaskets and matched PTL thicknesses, achieved reliable performance in the 5 cm^2 setup. When scaled up to the 50 cm^2 testing cell, the scaling effects such as increased interfacial resistance and assembly force sensitivity resulted in reduced current density. Electrochemical impedance spectroscopy revealed the higher ohmic resistance in the large testing cell, underscoring the challenges of maintaining interfacial contact during scale-up. These initial experiments established a stable testing platform and standardised conditions for the subsequent evaluations.

Fabrication and optimisation of CCMs

The development and optimisation of catalyst-coated membranes focused on enhancing both performance and stability through systematic adjustments to catalyst ink formulations and hot-pressing conditions. The formulations of catalysts, ionomers, and solvents were studied to investigate their impact on catalyst layer structure and electrochemical performance. The ionomer-to-catalyst (I/C) ratio of 25 wt% and 69 wt% was employed for the anodic and cathodic catalyst inks, respectively. Additionally, the solvent system used a 4:1 volume ratio of isopropanol to water, ensuring the stability of the dispersion. To enhance the uniformity of the catalyst layer, ultrasonic dispersion was applied to achieve a homogeneous and stable distribution of catalyst nanoparticles in the CCM. For the CCM fabrication, the ultrasonic spray-coating technique demonstrated significant advantages over the airbrush method. Specifically, it achieved a 25.7% increase in current density at 1.8 V, from 1.75 A/cm^2 to 2.2 A/cm^2, due to its superior atomization capability, which produced catalyst layers with improved uniformity and structural integrity. After CCM fabrication, hot-pressing was employed to enhance interfacial adhesion while preserving catalyst layer integrity. A temperature of 185°C, a pressure of 800 lb, and a duration of 180 seconds were identified as the optimal conditions, ensuring stable performance without compromising the structural stability of the catalyst layer. Performance testing was then conducted using the Horiba FuelCon water electrolysis testing system, contributing to the establishment of a well-defined knowledge framework for the CCM preparation and evaluation. The developed CCMs exceeded the DOE's 2022 performance targets but fell short of the more ambitious goals set for 2026. These findings established a systematic fabrication approach, which provides a robust foundation for future experiments.

Mitigation of hydrogen crossover

To reduce hydrogen crossover under differential pressure, a platinum functional layer was introduced. The functional layer, with a thickness equivalent to 1 nm, was deposited on the anode side of the PEM surface using sputter coating. This fabrication method simplifies the overall process and reduces reliance on high-precision equipment, making it both cost-effective and scalable. Experimental results showed a 73% reduction in hydrogen crossover at atmospheric pressure and a 66% reduction at 10 bar differential pressure during single-cell tests at 0.25 A/cm^2, demonstrating the layer's effectiveness across varying pressure conditions.

In addition to the experimental observations, a diffusion-based qualitative analysis model was constructed to provide theoretical insights into reducing hydrogen permeation. This model underscored the importance of optimising the platinum layer's placement within the CCM. Results revealed that the functional layer's position directly impacts its ability to mitigate hydrogen crossover by facilitating hydrogen oxidation at the anode/membrane interface. Improper placement or uneven distribution of the functional layer may reduce its effectiveness.

Durability and Stability Assessments

To evaluate the durability of the platinum functional layer under realistic operating conditions, the accelerated stress test (AST) was conducted. The AST was designed with innovative conditions to simulate fluctuating load scenarios, including intermittent current density variations, closely mimicking operational challenges faced in coupling PEMWEs with renewable energy systems. Over 200 cycles (equivalent to 100 hours of operation), the functional layer demonstrated remarkable stability, retaining over 94% of its hydrogen crossover mitigation ability at 0.25 A/cm^2 and 99% at 2.5 A/cm^2 under

a differential pressure of 10 bar.

These results underscored the robustness of the functional layer in maintaining long-term performance, even under harsh conditions. The functional layer's critical role in reducing hydrogen permeation not only enhances the safety of PEMWE systems but also supports operational flexibility, enabling stable performance under dynamic and high-pressure environments.

Future Strategies for Advancing PEM Water Electrolysis

Based on the findings of this study, several recommendations and perspectives are proposed to further advance the development of the PEMWE technology:

1. **Optimisation of CCMs with lower catalyst loading**: Building on the advancements achieved in this study, future work should focus on the development of CCMs with reduced catalyst loading to meet the DOE’s ambitious targets for 2026. Efforts should emphasise optimising fabrication techniques, such as ultrasonic spray coating, to improve catalyst utilisation and achieve high performance with minimal material use, particularly under high differential pressure conditions.
2. **Theoretical modelling and scaling effects**: The diffusion-based qualitative analysis model developed in this study provided valuable insights into hydrogen permeation mechanisms. Future efforts could focus on refining this model with more quantitative data, addressing scaling effects such as interfacial resistance and gas permeability in larger-scale systems. This work would bridge the gap between laboratory-scale testing and industrial applications.
3. **Exploration of factors limiting the functional layer's activity**: To further reduce hydrogen crossover, it is crucial to investigate the factors restricting the catalytic

activity of the platinum functional layer. A deeper understanding of these limitations could pave the way for enhancing the reaction efficiency and reducing hydrogen permeation under challenging operational conditions.

4. **In-depth characterisation of porous transport layers:** While this work investigates key commercial components such as membranes, PTLs, catalysts (Chapter 4), the analysis of PTLs was limited to porosity. Future work should include a more detailed characterisation of PTLs. Parameters such as tortuosity, pore size, and pore size distribution should be quantitatively assessed to better understand the influence of PTL microstructure on water transport, gas removal, and interfacial resistance in PEMWEs.
5. **Integration of machine learning methods for process optimisation:** Advanced optimisation approaches, such as Bayesian optimisation, could be applied to accelerate the development of high-performance CCMs. By integrating machine learning algorithms with experimental datasets, it is possible to efficiently identify optimal combinations of ink formulation and processing parameters to meet DOE's future performance targets.
6. **Techno-economic evaluation of platinum functional layers:** Although the platinum functional layer demonstrated strong potential in mitigating hydrogen crossover, its cost impact for large-scale applications requires further investigation. A techno-economic analysis is recommended to evaluate how the addition of platinum affects the cost-effectiveness of PEMWE stacks, particularly under large-scale manufacturing conditions.

These future directions aim to build upon the foundation established in this study,

addressing key challenges in the PEMWE research while advancing toward more efficient, cost-effective, and scalable water electrolysis systems capable of meeting the growing demands for green hydrogen production.

References

1. Impram S, Varbak Nese S, Oral B. Challenges of renewable energy penetration on power system flexibility: A survey. Energy Strategy Reviews. 2020 Sep 1;31:100539.

2. UK energy in brief 2019 - GOV.UK [Internet]. [cited 2024 Aug 18]. Available from: https://www.gov.uk/government/statistics/uk-energy-in-brief-2019

3. Hydrogen: A Clean, Flexible Energy Carrier | Department of Energy [Internet]. [cited 2024 Oct 19]. Available from: https://www.energy.gov/eere/articles/hydrogen-clean-flexible-energy-carrier

4. Sharmina M, Edelenbosch OY, Wilson C, Freeman R, Gernaat DEHJ, Gilbert P, et al. Decarbonising the critical sectors of aviation, shipping, road freight and industry to limit warming to 1.5–2°C. Climate Policy [Internet]. 2021 Apr 21 [cited 2024 Aug 18];21(4):455–74. Available from: https://www.tandfonline.com/doi/abs/10.1080/14693062.2020.1831430

5. Hancke R, Ulleberg Ø, Skattum R, Torp V, Jensen JE. High Differential Pressure PEMWE System Laboratory. 2019;

6. Hancke R, Holm T, Ulleberg Ø. The case for high-pressure PEM water electrolysis. Energy Convers Manag. 2022 Jun 1;261:115642.

7. Onda K, Kyakuno T, Hattori K, Ito K. Prediction of production power for high-pressure hydrogen by high-pressure water electrolysis. J Power Sources. 2004 May 20;132(1–2):64–70.

8. Hancke R, Bujlo P, Holm T, Ulleberg Ø. High-pressure PEM water electrolyser performance up to 180 bar differential pressure. J Power Sources. 2024 May 1;601:234271.

9. Hancke R, Bujlo P, Holm T, Ulleberg Ø. High-pressure PEM water electrolyser performance up to 180 bar differential pressure. J Power Sources. 2024 May 1;601:234271.

10. Lee B, Heo J, Kim S, Sung C, Moon C, Moon S, et al. Economic feasibility studies of high pressure PEM water electrolysis for distributed H2 refueling stations. Energy Convers Manag. 2018 Apr 15;162:139–44.

11. Millet P, Durand R, Pineri M. Preparation of new solid polymer electrolyte composites for water electrolysis. Int J Hydrogen Energy. 1990 Jan 1;15(4):245–53.

12. GREEN HYDROGEN COST REDUCTION SCALING UP ELECTROLYSERS TO MEET THE 1.5°C CLIMATE GOAL H 2 O 2. 2020 [cited 2024 Aug 20]; Available from: www.irena.org/publications

13. Smolinka T, Bergmann H, Garche J, Kusnezoff M. The history of water electrolysis from its beginnings to the present. Electrochemical Power Sources: Fundamentals, Systems, and Applications Hydrogen Production by Water

Electrolysis. 2022 Jan 1;83–164.

14. IRENA. Green Hydrogen Cost Reduction: Scaling up Electrolysers to Meet the 1.5^{0}C Climate Goal. International Renewable Energy Agency [Internet]. 2020 [cited 2024 Nov 20];105. Available from: www.irena.org/publications

15. Chatenet M, Pollet BG, Dekel DR, Dionigi F, Deseure J, Millet P, et al. Water electrolysis: from textbook knowledge to the latest scientific strategies and industrial developments. Chem Soc Rev [Internet]. 2022 Jun 6 [cited 2024 Oct 19];51(11):4583–762. Available from: https://pubs.rsc.org/en/content/articlehtml/2022/cs/d0cs01079k

16. Laguna-Bercero MA, Wang Y, Zhou XD, Zhu L. Fundamentals of Solid Oxide Electrolysis Cells (SOEC). Lecture Notes in Energy [Internet]. 2023 [cited 2024 Oct 19];95:5–34. Available from: https://link.springer.com/chapter/10.1007/978-3-031-22508-6_2

17. Liu RT, Xu ZL, Li FM, Chen FY, Yu JY, Yan Y, et al. Recent advances in proton exchange membrane water electrolysis. Chem Soc Rev [Internet]. 2023 Aug 14 [cited 2024 Oct 10];52(16):5652–83. Available from: https://pubs.rsc.org/en/content/articlehtml/2023/cs/d2cs00681b

18. Zeng K, Zhang D. Recent progress in alkaline water electrolysis for hydrogen production and applications. Prog Energy Combust Sci. 2010 Jun 1;36(3):307–26.

19. Manabe A, Kashiwase M, Hashimoto T, Hayashida T, Kato A, Hirao K, et al. Basic study of alkaline water electrolysis. Electrochim Acta. 2013 Jun 30;100:249–56.

20. Sánchez M, Amores E, Abad D, Rodríguez L, Clemente-Jul C. Aspen Plus model of an alkaline electrolysis system for hydrogen production. Int J Hydrogen Energy. 2020 Feb 7;45(7):3916–29.

21. Santoro C, Lavacchi A, Mustarelli P, Di Noto V, Elbaz L, Dekel DR, et al. What is Next in Anion-Exchange Membrane Water Electrolyzers? Bottlenecks, Benefits, and Future. ChemSusChem [Internet]. 2022 Apr 22 [cited 2024 Oct 19];15(8):e202200027. Available from: https://onlinelibrary.wiley.com/doi/full/10.1002/cssc.202200027

22. Miller HA, Bouzek K, Hnat J, Loos S, Bernäcker CI, Weißgärber T, et al. Green hydrogen from anion exchange membrane water electrolysis: a review of recent developments in critical materials and operating conditions. Sustain Energy Fuels [Internet]. 2020 May 6 [cited 2024 Aug 23];4(5):2114–33. Available from: https://pubs.rsc.org/en/content/articlehtml/2020/se/c9se01240k

23. Li C, Baek JB. The promise of hydrogen production from alkaline anion exchange membrane electrolyzers. Nano Energy. 2021 Sep 1;87:106162.

24. Ge Q, Zhu X, Yang Z. Highly Conductive and Water-Swelling Resistant Anion Exchange Membrane for Alkaline Fuel Cells. Int J Mol Sci [Internet]. 2019 Jul 2 [cited 2024 Oct 19];20(14):3470. Available from: https://pmc.ncbi.nlm.nih.gov/articles/PMC6679103/

25. Zhang K, Liang X, Wang L, Sun K, Wang Y, Xie Z, et al. Status and perspectives of key materials for PEM electrolyzer. Nano Research Energy [Internet]. 2022 Dec 1 [cited 2024 Oct 10];1(3):e9120032–e9120032. Available from: https://www.sciopen.com/article/10.26599/NRE.2022.9120032

26. Carmo M, Fritz DL, Mergel J, Stolten D. A comprehensive review on PEM water electrolysis. Int J Hydrogen Energy. 2013 Apr 22;38(12):4901–34.

27. Deng Z, Ye Q, Zhang Z, Tang C, Kang W, Chen M, et al. Application of proton exchange membrane electrolyzers in renewable grid and distributed energy storage. PEM Water Electrolysis [Internet]. 2025 Jan 1 [cited 2024 Nov 6];411–34. Available from: https://linkinghub.elsevier.com/retrieve/pii/B9780443240621000139

28. Eric L. Miller. Hydrogen Production & Delivery Program [Internet]. 2016 [cited 2024 Nov 6]. Available from: https://www.hydrogen.energy.gov/docs/hydrogenprogramlibraries/pdfs/review16/pd000_miller_2016_o.pdf?Status=Master

29. Bakhtiari H, Naghizadeh RA. Multi-criteria optimal sizing of hybrid renewable energy systems including wind, photovoltaic, battery, and hydrogen storage with ε-constraint method. IET Renewable Power Generation [Internet]. 2018 Jun 1 [cited 2024 Nov 6];12(8):883–92. Available from: https://onlinelibrary.wiley.com/doi/full/10.1049/iet-rpg.2017.0706

30. Bareiß K, de la Rua C, Möckl M, Hamacher T. Life cycle assessment of hydrogen from proton exchange membrane water electrolysis in future energy systems. Appl Energy. 2019 Mar 1;237:862–72.

31. Yue M, Lambert H, Pahon E, Roche R, Jemei S, Hissel D. Hydrogen energy systems: A critical review of technologies, applications, trends and challenges. Renewable and Sustainable Energy Reviews. 2021 Aug 1;146:111180.

32. Kopp M, Coleman D, Stiller C, Scheffer K, Aichinger J, Scheppat B. Energiepark Mainz: Technical and economic analysis of the worldwide largest Power-to-Gas plant with PEM electrolysis. Int J Hydrogen Energy. 2017 May 11;42(19):13311–20.

33. Schuler T, De Bruycker R, Schmidt TJ, - al, Roy A, Roenning FH, et al. Critical Review—Identifying Critical Gaps for Polymer Electrolyte Water Electrolysis Development. J Electrochem Soc [Internet]. 2017 Feb 25 [cited 2024 Oct 19];164(4):F387. Available from: https://iopscience.iop.org/article/10.1149/2.1441704jes

34. Grigoriev SA, Fateev VN, Bessarabov DG, Millet P. Current status, research trends, and challenges in water electrolysis science and technology. Int J Hydrogen Energy. 2020 Oct 2;45(49):26036–58.

35. Onda K, Kyakuno T, Hattori K, Ito K. Prediction of production power for high-pressure hydrogen by high-pressure water electrolysis. J Power Sources. 2004 May 20;132(1–2):64–70.

36. Salehmin MNI, Husaini T, Goh J, Sulong AB. High-pressure PEM water

electrolyser: A review on challenges and mitigation strategies towards green and low-cost hydrogen production. Energy Convers Manag. 2022 Sep 15;268:115985.

37. Feng Q, Yuan XZ, Liu G, Wei B, Zhang Z, Li H, et al. A review of proton exchange membrane water electrolysis on degradation mechanisms and mitigation strategies. J Power Sources. 2017 Oct 31;366:33–55.

38. Bessarabov D, Wang H, Li H, Zhao N. PEM electrolysis for hydrogen production: Principles and applications. PEM Electrolysis for Hydrogen Production: Principles and Applications. 2016 Feb 3;1–382.

39. Salehmin MNI, Husaini T, Goh J, Sulong AB. High-pressure PEM water electrolyser: A review on challenges and mitigation strategies towards green and low-cost hydrogen production. Energy Convers Manag. 2022 Sep 15;268:115985.

40. Millet P. Fundamentals of water electrolysis. Electrochemical Power Sources: Fundamentals, Systems, and Applications Hydrogen Production by Water Electrolysis. 2022 Jan 1;37–62.

41. Li W, Tian H, Ma L, Wang Y, Liu X, Gao X. Low-temperature water electrolysis: fundamentals, progress, and new strategies. Mater Adv [Internet]. 2022 Jul 18 [cited 2024 Oct 19];3(14):5598–644. Available from: https://pubs.rsc.org/en/content/articlehtml/2022/ma/d2ma00185c

42. Chen L, Zhao W, Zhang J, Liu M, Jia Y, Wang R, et al. Recent Research on Iridium-Based Electrocatalysts for Acidic Oxygen Evolution Reaction from the Origin of Reaction Mechanism. Small [Internet]. 2024 [cited 2024 Oct 19];2403845. Available from: https://onlinelibrary.wiley.com/doi/full/10.1002/smll.202403845

43. Millet P, Ngameni R, Grigoriev SA, Mbemba N, Brisset F, Ranjbari A, et al. PEM water electrolyzers: From electrocatalysis to stack development. Int J Hydrogen Energy. 2010 May 1;35(10):5043–52.

44. Suen NT, Hung SF, Quan Q, Zhang N, Xu YJ, Chen HM. Electrocatalysis for the oxygen evolution reaction: recent development and future perspectives. Chem Soc Rev [Internet]. 2017 Jan 23 [cited 2024 Oct 19];46(2):337–65. Available from: https://pubs.rsc.org/en/content/articlehtml/2017/cs/c6cs00328a

45. Wang S, Lu A, Zhong CJ. Hydrogen production from water electrolysis: role of catalysts. Nano Converg [Internet]. 2021 Dec 1 [cited 2024 Oct 19];8(1):1–23. Available from: https://nanoconvergencejournal.springeropen.com/articles/10.1186/s40580-021-00254-x

46. Mohamed B, Alli B, Ahmed B. Using the hydrogen for sustainable energy storage: Designs, modeling, identification and simulation membrane behavior in PEM system electrolyser. J Energy Storage. 2016 Aug 1;7:270–85.

47. Shan J, Zheng Y, Shi B, Davey K, Qiao SZ. Regulating electrocatalysts via surface and interface engineering for acidic water electrooxidation. ACS Energy

Lett [Internet]. 2019 Nov 8 [cited 2024 Oct 19];4(11):2719–30. Available from: https://pubs.acs.org/doi/full/10.1021/acsenergylett.9b01758

48. Dau H, Limberg C, Reier T, Risch M, Roggan S, Strasser P. The Mechanism of Water Oxidation: From Electrolysis via Homogeneous to Biological Catalysis. ChemCatChem [Internet]. 2010 Jul 12 [cited 2024 Oct 19];2(7):724–61. Available from: https://onlinelibrary.wiley.com/doi/full/10.1002/cctc.201000126

49. Biaku CY, Dale N V., Mann MD, Salehfar H, Peters AJ, Han T. A semiempirical study of the temperature dependence of the anode charge transfer coefficient of a 6 kW PEM electrolyzer. Int J Hydrogen Energy. 2008 Aug 1;33(16):4247–54.

50. Fritz DL, Mergel J, Stolten D. PEM Electrolysis Simulation and Validation. ECS Trans [Internet]. 2014 Feb 27 [cited 2024 Oct 19];58(19):1–9. Available from: https://iopscience.iop.org/article/10.1149/05819.0001ecst

51. Schalenbach M, Carmo M, Fritz DL, Mergel J, Stolten D. Pressurized PEM water electrolysis: Efficiency and gas crossover. Int J Hydrogen Energy. 2013 Nov 22;38(35):14921–33.

52. Bühre L V., Mourali M, Trinke P, Brandt J, Brinker D, Kardeş G, et al. Analysis of Kinetic and Ohmic Resistances in PEM Water Electrolysis through Reference Electrode Measurements. J Electrochem Soc [Internet]. 2024 May 29 [cited 2024 Oct 19];171(5):054518. Available from: https://iopscience.iop.org/article/10.1149/1945-7111/ad4b5d

53. Mauger SA, Neyerlin KC, Yang-Neyerlin AC, More KL, Ulsh M. Gravure Coating for Roll-to-Roll Manufacturing of Proton-Exchange-Membrane Fuel Cell Catalyst Layers. J Electrochem Soc [Internet]. 2018 Sep 11 [cited 2024 Oct 10];165(11):F1012–8. Available from: https://iopscience.iop.org/article/10.1149/2.0091813jes

54. Moradi Nafchi F, Afshari E, Baniasadi E, Javani N. A parametric study of polymer membrane electrolyser performance, energy and exergy analyses. Int J Hydrogen Energy. 2019 Jul 12;44(34):18662–70.

55. Vogt H. The bubble coverage of gas-evolving electrodes in a flowing electrolyte. Electrochim Acta. 2000 Sep 1;45(27):4449–56.

56. Nafeh AESA. Hydrogen production from a PV/PEM electrolyzer system using a neural-network-based MPPT algorithm. International Journal of Numerical Modelling: Electronic Networks, Devices and Fields [Internet]. 2011 May 1 [cited 2024 Oct 19];24(3):282–97. Available from: https://onlinelibrary.wiley.com/doi/full/10.1002/jnm.778

57. Suermann M, Pătru A, Schmidt TJ, Büchi FN. High pressure polymer electrolyte water electrolysis: Test bench development and electrochemical analysis. Int J Hydrogen Energy. 2017 Apr 27;42(17):12076–86.

58. Schalenbach M, Tjarks G, Carmo M, Lueke W, Mueller M, Stolten D. Acidic or Alkaline? Towards a New Perspective on the Efficiency of Water Electrolysis. J Electrochem Soc [Internet]. 2016 Aug 31 [cited 2024 Dec 30];163(11):F3197–208. Available from: https://iopscience.iop.org/article/10.1149/2.0271611jes

59. Marshall A, Børresen B, Hagen G, Tsypkin M, Tunold R. Hydrogen production by advanced proton exchange membrane (PEM) water electrolysers—Reduced energy consumption by improved electrocatalysis. Energy. 2007 Apr 1;32(4):431–6.

60. Sartory M, Wallnöfer-Ogris E, Salman P, Fellinger T, Justl M, Trattner A, et al. Theoretical and experimental analysis of an asymmetric high pressure PEM water electrolyser up to 155 bar. Int J Hydrogen Energy. 2017 Dec 28;42(52):30493–508.

61. Ayers KE, Anderson EB, Capuano C, Carter B, Dalton L, Hanlon G, et al. Research Advances towards Low Cost, High Efficiency PEM Electrolysis. ECS Trans [Internet]. 2010 Oct 1 [cited 2024 Oct 14];33(1):3–15. Available from: https://iopscience.iop.org/article/10.1149/1.3484496

62. Overview of PEM Electrolysis for Hydrogen Production. PEM Electrolysis for Hydrogen Production [Internet]. 2016 Feb 3 [cited 2024 Oct 14];13–22. Available from: https://www.taylorfrancis.com/chapters/edit/10.1201/b19096-5/overview-pem-electrolysis-hydrogen-production-nicola-briguglio-vincenzo-antonucci

63. Leimbach M, Kurniawan M, Zimmermann CP, Höß CE, Fritz M, Bund A. Characterization of Protective Coatings on Stainless Steel Bipolar Plates for PEM Electrolyzers. ECS Meeting Abstracts [Internet]. 2022 Oct 9 [cited 2024 Oct 14];MA2022-02(22):935. Available from: https://iopscience.iop.org/article/10.1149/MA2022-0222935mtgabs

64. Grigor'ev SA, Khaliullin MM, Kuleshov N V., Fateev VN. Electrolysis of water in a system with a solid polymer electrolyte at elevated pressure. Russian Journal of Electrochemistry [Internet]. 2001 [cited 2025 Jan 1];37(8):819–22. Available from: https://link.springer.com/article/10.1023/A:1016735003101

65. Bernt M, Schröter J, Möckl M, Gasteiger HA. Analysis of Gas Permeation Phenomena in a PEM Water Electrolyzer Operated at High Pressure and High Current Density. J Electrochem Soc [Internet]. 2020 Aug 7 [cited 2024 Nov 6];167(12):124502. Available from: https://iopscience.iop.org/article/10.1149/1945-7111/abaa68

66. Omrani R, Shabani B. Hydrogen crossover in proton exchange membrane electrolysers: The effect of current density, pressure, temperature, and compression. Electrochim Acta. 2021 May 1;377:138085.

67. Wrubel JA, Milleville C, Klein E, Zack J, Park AM, Bender G. Estimating the energy requirement for hydrogen production in proton exchange membrane electrolysis cells using rapid operando hydrogen crossover analysis. Int J Hydrogen Energy. 2022 Aug 1;47(66):28244–53.

68. Feng Q, Yuan XZ, Liu G, Wei B, Zhang Z, Li H, et al. A review of proton exchange membrane water electrolysis on degradation mechanisms and mitigation strategies. J Power Sources. 2017 Oct 31;366:33–55.

69. Khatib FN, Wilberforce T, Ijaodola O, Ogungbemi E, El-Hassan Z, Durrant A, et al. Material degradation of components in polymer electrolyte membrane (PEM)

electrolytic cell and mitigation mechanisms: A review. Renewable and Sustainable Energy Reviews. 2019 Sep 1;111:1–14.

70. Barbir F. PEM electrolysis for production of hydrogen from renewable energy sources. Solar Energy. 2005 May 1;78(5):661–9.

71. Roy A, Watson S, Infield D. Comparison of electrical energy efficiency of atmospheric and high-pressure electrolysers. Int J Hydrogen Energy. 2006 Nov 1;31(14):1964–79.

72. Mohammadi A, Mehrpooya M. A comprehensive review on coupling different types of electrolyzer to renewable energy sources. Energy. 2018 Sep 1;158:632–55.

73. Wang T, Cao X, Jiao L. PEM water electrolysis for hydrogen production: fundamentals, advances, and prospects. Carbon Neutrality 2022 1:1 [Internet]. 2022 Jun 2 [cited 2024 Oct 10];1(1):1–19. Available from: https://link.springer.com/article/10.1007/s43979-022-00022-8

74. Hiroshi Ito. PEM Electrolysis for Hydrogen Production-Membranes [Internet]. 2015 [cited 2024 Oct 10]. Available from: https://www-taylorfrancis-com.bham-ezproxy.idm.oclc.org/reader/read-online/003ec59d-b4f0-4e13-95b6-8a1deceaabfe/chapter/pdf?context=ubx

75. Ito H, Maeda T, Nakano A, Takenaka H. Properties of Nafion membranes under PEM water electrolysis conditions. Int J Hydrogen Energy. 2011 Aug 1;36(17):10527–40.

76. Zawodzinski TA, Derouin C, Radzinski S, Sherman RJ, Smith VT, Springer TE, et al. Water Uptake by and Transport Through Nafion® 117 Membranes. J Electrochem Soc [Internet]. 1993 Apr 1 [cited 2024 Oct 10];140(4):1041–7. Available from: https://iopscience.iop.org/article/10.1149/1.2056194

77. Abdol Rahim AH, Tijani AS, Kamarudin SK, Hanapi S. An overview of polymer electrolyte membrane electrolyzer for hydrogen production: Modeling and mass transport. J Power Sources. 2016 Mar 31;309:56–65.

78. Ito H. Current collectors (gdls) and materials. PEM Electrolysis for Hydrogen Production: Principles and Applications [Internet]. 2016 Feb 3 [cited 2024 Oct 10];147–56. Available from: https://www-taylorfrancis-com.bham-ezproxy.idm.oclc.org/chapters/edit/10.1201/b19096-12/current-collectors-gdls-materials-hiroshi-ito

79. Maier M, Smith K, Dodwell J, Hinds G, Shearing PR, Brett DJL. Mass transport in PEM water electrolysers: A review. Int J Hydrogen Energy. 2022 Jan 1;47(1):30–56.

80. Mo J, Kang Z, Yang G, Retterer ST, Cullen DA, Toops TJ, et al. Thin liquid/gas diffusion layers for high-efficiency hydrogen production from water splitting. Appl Energy. 2016 Sep 1;177:817–22.

81. Gabbasa M, Sopian K, Fudholi A, Asim N. A review of unitized regenerative fuel cell stack: Material, design and research achievements. Int J Hydrogen Energy.

2014 Oct 22;39(31):17765–78.

82. Grigoriev SA, Millet P, Volobuev SA, Fateev VN. Optimization of porous current collectors for PEM water electrolysers. Int J Hydrogen Energy. 2009 Jun 1;34(11):4968–73.

83. Doan TL, Lee HE, Shah SSH, Kim MJ, Kim CH, Cho HS, et al. A review of the porous transport layer in polymer electrolyte membrane water electrolysis. Int J Energy Res [Internet]. 2021 Aug 1 [cited 2025 Jan 21];45(10):14207–20. Available from: https://onlinelibrary.wiley.com/doi/full/10.1002/er.6739

84. Chen Z, Guo L, Pan L, Yan T, He Z, Li Y, et al. Advances in Oxygen Evolution Electrocatalysts for Proton Exchange Membrane Water Electrolyzers. Adv Energy Mater [Internet]. 2022 Apr 1 [cited 2025 Jan 21];12(14):2103670. Available from: https://onlinelibrary.wiley.com/doi/full/10.1002/aenm.202103670

85. Cheng T. Bipolar plates and plate materials. Proton Exchange Membrane Fuel Cells: Materials Properties and Performance [Internet]. 2009 Jan 1 [cited 2024 Oct 11];305–42. Available from: https://www-taylorfrancis-com.bham-ezproxy.idm.oclc.org/chapters/edit/10.1201/b19096-11/bipolar-plates-plate-materials-conghua-ch-wang

86. Włodarczyk R. Properties of graphite-stainless steel composite in bipolar plates in simulated anode and cathode environments of PEM fuel cells. Materials Science-Poland 2014 32:3 [Internet]. 2016 May 18 [cited 2024 Oct 14];32(3):487–97. Available from: https://link.springer.com/article/10.2478/s13536-014-0229-6

87. Olesen AC, Rømer C, Kær SK. A numerical study of the gas-liquid, two-phase flow maldistribution in the anode of a high pressure PEM water electrolysis cell. Int J Hydrogen Energy. 2016 Jan 5;41(1):52–68.

88. Dang J, Yang F, Li Y, Zhao Y, Ouyang M, Hu S. Experiments and microsimulation of high-pressure single-cell PEM electrolyzer. Appl Energy. 2022 Sep 1;321:119351.

89. Marangio F, Pagani M, Santarelli M, Calì M. Concept of a high pressure PEM electrolyser prototype. Int J Hydrogen Energy. 2011 Jul 1;36(13):7807–15.

90. Suermann M, Schmidt TJ, Büchi FN. Overpotential Analysis in High Pressure Water Electrolysis. ECS Meeting Abstracts [Internet]. 2016 Sep 1 [cited 2025 Feb 3];MA2016-02(38):2407. Available from: https://iopscience.iop.org/article/10.1149/MA2016-02/38/2407

91. Bin S, Chen Z, Zhu Y, Zhang Y, Xia Y, Gong S, et al. High-pressure proton exchange membrane water electrolysis: Current status and challenges in hydrogen production. Int J Hydrogen Energy. 2024 May 20;67:390–405.

92. Ito H, Maeda T, Nakano A, Takenaka H. Properties of Nafion membranes under PEM water electrolysis conditions. Int J Hydrogen Energy. 2011 Aug 1;36(17):10527–40.

93. Ring RW, Stott JE, Hales C. Modeling the Risk of Fire/Explosion Due to

Oxidizer/Fuel Leaks in the Ares I Interstage. 2008.

94. Eikerling MH, Berg P. Poroelectroelastic theory of water sorption and swelling in polymer electrolyte membranes. Soft Matter [Internet]. 2011 Jun 21 [cited 2025 Feb 20];7(13):5976–90. Available from: https://pubs.rsc.org/en/content/articlehtml/2011/sm/c1sm05273j

95. Schalenbach M, Hoefner T, Paciok P, Carmo M, Lueke W, Stolten D. Gas Permeation through Nafion. Part 1: Measurements. Journal of Physical Chemistry C [Internet]. 2015 Nov 12 [cited 2025 Feb 20];119(45):25145–55. Available from: https://pubs.acs.org/doi/full/10.1021/acs.jpcc.5b04155

96. Trinke P, Bensmann B, Hanke-Rauschenbach R. Current density effect on hydrogen permeation in PEM water electrolyzers. Int J Hydrogen Energy. 2017 May 25;42(21):14355–66.

97. Bessarabov D, Kruger A, Luopa SM, Park J, Molnar AA, Lewinski KA. Gas Crossover Mitigation in PEM Water Electrolysis: Hydrogen Cross-over Benchmark Study of 3M's Ir-NSTF Based Electrolysis Catalyst-Coated Membranes. ECS Trans [Internet]. 2016 Aug 22 [cited 2025 Feb 20];75(14):1165–73. Available from: https://iopscience.iop.org/article/10.1149/07514.1165ecst

98. Zhang Z, Baudy A, Testino A, Gubler L. Cathode Catalyst Layer Design in PEM Water Electrolysis toward Reduced Pt Loading and Hydrogen Crossover. ACS Appl Mater Interfaces [Internet]. 2024 [cited 2024 Dec 23];16. Available from: https://pubs.acs.org/doi/full/10.1021/acsami.4c01827

99. Fahr S, Engel FK, Rehfeldt S, Peschel A, Klein H. Overview and evaluation of crossover phenomena and mitigation measures in proton exchange membrane (PEM) electrolysis. Int J Hydrogen Energy. 2024 May 28;68:705–21.

100. Trinke P, Bensmann B, Hanke-Rauschenbach R. Experimental evidence of increasing oxygen crossover with increasing current density during PEM water electrolysis. Electrochem commun. 2017 Sep 1;82:98–102.

101. Sakai T, Takenaka H, Wakabayashi N, Kawami Y, Torikai E. Gas Permeation Properties of Solid Polymer Electrolyte (SPE) Membranes. J Electrochem Soc [Internet]. 1985 Jun 1 [cited 2024 Nov 28];132(6):1328–32. Available from: https://iopscience.iop.org/article/10.1149/1.2114111

102. Li S, Wei X, Dai H, Yuan H, Ming P. Voltammetric and galvanostatic methods for measuring hydrogen crossover in fuel cell. iScience [Internet]. 2021 Jan 21 [cited 2025 Feb 2];25(1):103576. Available from: https://pmc.ncbi.nlm.nih.gov/articles/PMC8692992/

103. Jeong J, Jeong J, Kim S, Ahn B, Ko J, Park K. Measurement of hydrogen crossover by gas chromatograph in PEMFC. Korean Chemical Engineering Research [Internet]. 2014 [cited 2025 Feb 2];52(4):425–9. Available from: https://www.researchgate.net/publication/284369525_Measurement_of_Hydrogen_Crossover_by_Gas_Chromatograph_in_PEMFC

104. Wrubel JA, Milleville C, Klein E, Zack J, Park AM, Bender G. Estimating the

energy requirement for hydrogen production in proton exchange membrane electrolysis cells using rapid operando hydrogen crossover analysis. Int J Hydrogen Energy. 2022 Aug 1;47(66):28244–53.

105. Schalenbach M, Carmo M, Fritz DL, Mergel J, Stolten D. Pressurized PEM water electrolysis: Efficiency and gas crossover. Int J Hydrogen Energy. 2013 Nov 22;38(35):14921–33.

106. Stähler M, Stähler A, Scheepers F, Carmo M, Lehnert W, Stolten D. Impact of porous transport layer compression on hydrogen permeation in PEM water electrolysis. Int J Hydrogen Energy. 2020 Feb 7;45(7):4008–14.

107. Martin A, Trinke P, Bensmann B, Hanke-Rauschenbach R. Hydrogen Crossover in PEM Water Electrolysis at Current Densities up to 10 A cm−2. J Electrochem Soc [Internet]. 2022 Sep 20 [cited 2024 Nov 24];169(9):094507. Available from: https://iopscience.iop.org/article/10.1149/1945-7111/ac908c

108. Martin A, Trinke P, Stähler M, Stähler A, Scheepers F, Bensmann B, et al. The Effect of Cell Compression and Cathode Pressure on Hydrogen Crossover in PEM Water Electrolysis. J Electrochem Soc [Internet]. 2022 Jan 5 [cited 2025 Feb 2];169(1):014502. Available from: https://iopscience.iop.org/article/10.1149/1945-7111/ac4459

109. Trinke P, Keeley GP, Carmo M, Bensmann B, Hanke-Rauschenbach R. Elucidating the Effect of Mass Transport Resistances on Hydrogen Crossover and Cell Performance in PEM Water Electrolyzers by Varying the Cathode Ionomer Content. J Electrochem Soc [Internet]. 2019 Apr 25 [cited 2025 Feb 2];166(8):F465–71. Available from: https://iopscience.iop.org/article/10.1149/2.0171908jes

110. Alia S. HydroGEN: Low Temperature Electrolysis. 2021;

111. Choi E, Kang H, Jang Y, Kim JH, Ahn HS, Kim SM, et al. Construction of PTFE/Nafion Composite Membrane with Ultrathin Graphene Oxide Layer for Durable Fuel Cells. Adv Mater Technol [Internet]. 2024 Jan 1 [cited 2025 Feb 21];9(1):2301191. Available from: https://onlinelibrary.wiley.com/doi/full/10.1002/admt.202301191

112. Lee S, Jang W, Kim M, Eun Shin J, Bum Park H, Jung N, et al. Rational Design of Ultrathin Gas Barrier Layer via Reconstruction of Hexagonal Boron Nitride Nanoflakes to Enhance the Chemical Stability of Proton Exchange Membrane Fuel Cells. Small [Internet]. 2019 Oct 1 [cited 2025 Feb 21];15(44):1903705. Available from: https://onlinelibrary.wiley.com/doi/full/10.1002/smll.201903705

113. Fan Y, Chao L, Arthur G, Robert S, Cortney. MITTELSTEADT. US20220243339A1 - Proton exchange membrane water electrolyzer membrane electrode assembly - Google Patents. 2022. p. 2–2.

114. Martin A, Abbas D, Trinke P, Böhm T, Bierling M, Bensmann B, et al. Communication—Proving the Importance of Pt-Interlayer Position in PEMWE Membranes for the Effective Reduction of the Anodic Hydrogen Content. J Electrochem Soc [Internet]. 2021 Sep 24 [cited 2025 Feb 2];168(9):094509.

Available from: https://iopscience.iop.org/article/10.1149/1945-7111/ac275b

115. Lee J, Ricardo Carreon-Ruiz E, Siegwart M, - al, Rastedt M, Javier Pinar F, et al. Scalable Implementation of Recombination Catalyst Layers to Mitigate Gas Crossover in PEM Water Electrolyzers. J Electrochem Soc [Internet]. 2022 Mar 21 [cited 2024 Dec 22];169(3):034522. Available from: https://iopscience.iop.org/article/10.1149/1945-7111/ac5c9b

116. Klose C, Trinke P, Böhm T, Bensmann B, Vierrath S, Hanke-Rauschenbach R, et al. Membrane Interlayer with Pt Recombination Particles for Reduction of the Anodic Hydrogen Content in PEM Water Electrolysis. J Electrochem Soc [Internet]. 2018 Nov 21 [cited 2024 Nov 6];165(16):F1271–7. Available from: https://iopscience.iop.org/article/10.1149/2.1241814jes

117. Zeng Z, Ouimet R, Bonville L, Niedzwiecki A, Capuano C, Ayers K, et al. Degradation Mechanisms in Advanced MEAs for PEM Water Electrolyzers Fabricated by Reactive Spray Deposition Technology. J Electrochem Soc [Internet]. 2022 May 31 [cited 2024 Nov 6];169(5):054536. Available from: https://iopscience.iop.org/article/10.1149/1945-7111/ac7170

118. Schalenbach M, Stolten D. High-pressure water electrolysis: Electrochemical mitigation of product gas crossover. Electrochim Acta. 2015 Feb 20;156:321–7.

119. Stähler A, Stähler M, Scheepers F, Lehnert W, Carmo M. Scalable Implementation of Recombination Catalyst Layers to Mitigate Gas Crossover in PEM Water Electrolyzers. J Electrochem Soc [Internet]. 2022 Mar 21 [cited 2024 Nov 6];169(3):034522. Available from: https://iopscience.iop.org/article/10.1149/1945-7111/ac5c9b

120. Abbas D, Martin A, Trinke P, Bierling M, Bensmann B, Thiele S, et al. Effect of Recombination Catalyst Loading in PEMWE Membranes on Anodic Hydrogen Content Reduction. J Electrochem Soc [Internet]. 2022 Dec 23 [cited 2024 Nov 6];169(12):124514. Available from: https://iopscience.iop.org/article/10.1149/1945-7111/aca6a0

121. Ouimet RJ, Yu H, Mirshekari G, Zeng Z, Bonville LJ, Bliznakov S, et al. Development of Recombination Layers to Reduce Gas Crossover for Proton Exchange Membrane Water Electrolyzers By Reactive Spray Deposition Technology. ECS Meeting Abstracts [Internet]. 2020 Nov 23 [cited 2024 Dec 1];MA2020-02(38):2469. Available from: https://iopscience.iop.org/article/10.1149/MA2020-02382469mtgabs

122. Chen Z, Guo L, Pan L, Yan T, He Z, Li Y, et al. Advances in Oxygen Evolution Electrocatalysts for Proton Exchange Membrane Water Electrolyzers. Adv Energy Mater [Internet]. 2022 Apr 1 [cited 2024 Nov 6];12(14):2103670. Available from: https://onlinelibrary.wiley.com/doi/full/10.1002/aenm.202103670

123. Liu C, Wrubel J, Padgett E, Bender G. The impacts of membrane pinholes on PEM water electrolysis. J Power Sources. 2023 Oct 15;581:233507.

124. Briguglio N, Siracusano S, Bonura G, Sebastián D, Aricò AS. Flammability reduction in a pressurised water electrolyser based on a thin polymer electrolyte

membrane through a Pt-alloy catalytic approach. Appl Catal B. 2019 Jun 5;246:254–65.

125. Briguglio N, Pantò F, Siracusano S, Aricò AS. Enhanced performance of a PtCo recombination catalyst for reducing the H2 concentration in the O2 stream of a PEM electrolysis cell in the presence of a thin membrane and a high differential pressure. Electrochim Acta. 2020 Jun 1;344:136153.

126. Pantò F, Siracusano S, Briguglio N, Aricò AS. Durability of a recombination catalyst-based membrane-electrode assembly for electrolysis operation at high current density. Appl Energy. 2020 Dec 1;279:115809.

127. Johnson Matthey PLC. GB202113808D0-Catalyst coated proton exchange membranes for green hydrogen producing water electrolysers. 2021.

128. Nemanja D, David E, Syed Dawar S, Jigish T. AU2023232652A1-Methods, devices, and systems for mitigating hydrogen crossover within an electrochemical cell. 2023.

129. Joshua B, Navya J. WO2022038540A1 - Improved electrochemical membrane - Google Patents [Internet]. 2021 [cited 2025 Feb 2]. Available from: https://patents.google.com/patent/WO2022038540A1/en

130. Brundiers S, Trinke P, Bensmann B, Hanke-Rauschenbach R. Model-Based Investigation of Recombination Interlayers in PEM Water Electrolysis: Concentration Profiles, Efficiency, and Operational Limits. J Electrochem Soc [Internet]. 2024 Jul 26 [cited 2024 Nov 28];171(7):074509. Available from: https://iopscience.iop.org/article/10.1149/1945-7111/ad6212

131. Goñi-Urtiaga A, Presvytes D, Scott K. Solid acids as electrolyte materials for proton exchange membrane (PEM) electrolysis: Review. Int J Hydrogen Energy. 2012 Feb 1;37(4):3358–72.

132. Nicola Briguglio, Vincenzo Antonucci. PEM Electrolysis for Hydrogen Production-Overview of PEM Electrolysis for Hydrogen Production [Internet]. 2015 [cited 2024 Oct 10]. Available from: https://www-taylorfrancis-com.bham-ezproxy.idm.oclc.org/reader/read-online/08c9ee55-8c9c-4ade-a8dc-d5288d7975f7/chapter/pdf?context=ubx

133. Aricò AS, Di Blasi A, Brunaccini G, Sergi F, Dispenza G, Andaloro L, et al. High Temperature Operation of a Solid Polymer Electrolyte Fuel Cell Stack Based on a New Ionomer Membrane. Fuel Cells [Internet]. 2010 Dec 1 [cited 2025 Feb 19];10(6):1013–23. Available from: https://onlinelibrary.wiley.com/doi/full/10.1002/fuce.201000031

134. Bazaid M, Huang Y, Goddard WA, Jang SS. Proton transport through interfaces in nanophase-separation of hydrated aquivion membrane: Molecular dynamics simulation approach. Colloids Surf A Physicochem Eng Asp. 2023 Nov 5;676:132187.

135. Siracusano S, Baglio V, Stassi A, Merlo L, Moukheiber E, Arico' AS. Performance analysis of short-side-chain Aquivion® perfluorosulfonic acid polymer for proton exchange membrane water electrolysis. J Memb Sci. 2014 Sep 15;466:1–7.

136. Otero J, Sese J, Michaus I, Santa Maria M, Guelbenzu E, Irusta S, et al. Sulphonated polyether ether ketone diaphragms used in commercial scale alkaline water electrolysis. J Power Sources. 2014 Feb 1;247:967–74.

137. Aili D, Kraglund MR, Tavacoli J, Chatzichristodoulou C, Jensen JO. Polysulfone-polyvinylpyrrolidone blend membranes as electrolytes in alkaline water electrolysis. J Memb Sci. 2020 Mar 15;598:117674.

138. Mader J, Xiao L, Schmidt TJ, Benicewicz BC. Polybenzimidazole/Acid Complexes as High-Temperature Membranes. Advances in Polymer Science [Internet]. 2008 [cited 2025 Jan 25];216(1):63–124. Available from: https://link.springer.com/chapter/10.1007/12_2007_129

139. Wei G, Xu L, Huang C, Wang Y. SPE water electrolysis with SPEEK/PES blend membrane. Int J Hydrogen Energy. 2010 Aug 1;35(15):7778–83.

140. Siracusano S, Baglio V, Lufrano F, Staiti P, Aricò AS. Electrochemical characterization of a PEM water electrolyzer based on a sulfonated polysulfone membrane. J Memb Sci. 2013 Dec 15;448:209–14.

141. Klose C, Saatkamp T, Münchinger A, Bohn L, Titvinidze G, Breitwieser M, et al. All-Hydrocarbon MEA for PEM Water Electrolysis Combining Low Hydrogen Crossover and High Efficiency. Adv Energy Mater [Internet]. 2020 Apr 1 [cited 2024 Nov 10];10(14):1903995. Available from: https://onlinelibrary.wiley.com/doi/full/10.1002/aenm.201903995

142. Eisenstein O, Milani J, Perutz RN. Selectivity of C-H Activation and Competition between C-H and C-F Bond Activation at Fluorocarbons. Chem Rev [Internet]. 2017 Jul 12 [cited 2025 Feb 19];117(13):8710–53. Available from: https://pubmed.ncbi.nlm.nih.gov/28653537/

143. Phan TT, Kim SK, Islam J, Kim MJ, Lee JH. Degradation analysis of polymer electrolyte membrane water electrolyzer with different membrane thicknesses. Int J Hydrogen Energy. 2024 Jan 2;49:875–85.

144. Khedekar K, Li K, Gebhardt R, - al, Cho Y, Miura YN, et al. Analysis of Gas Permeation Phenomena in a PEM Water Electrolyzer Operated at High Pressure and High Current Density. J Electrochem Soc [Internet]. 2020 Aug 7 [cited 2025 Jan 24];167(12):124502. Available from: https://iopscience.iop.org/article/10.1149/1945-7111/abaa68

145. Ma L, Sui S, Zhai Y. Investigations on high performance proton exchange membrane water electrolyzer. Int J Hydrogen Energy. 2009 Jan 1;34(2):678–84.

146. Millet P, Ranjbari A, De Guglielmo F, Grigoriev SA, Auprêtre F. Cell failure mechanisms in PEM water electrolyzers. Int J Hydrogen Energy. 2012 Nov 1;37(22):17478–87.

147. Khatib FN, Wilberforce T, Ijaodola O, Ogungbemi E, El-Hassan Z, Durrant A, et al. Material degradation of components in polymer electrolyte membrane (PEM) electrolytic cell and mitigation mechanisms: A review. Renewable and Sustainable Energy Reviews. 2019 Sep 1;111:1–14.

148. Feng Q, Yuan XZ, Liu G, Wei B, Zhang Z, Li H, et al. A review of proton exchange membrane water electrolysis on degradation mechanisms and mitigation strategies. J Power Sources. 2017 Oct 31;366:33–55.

149. Lapicque F, Belhadj M, Bonnet C, Pauchet J, Thomas Y. A critical review on gas diffusion micro and macroporous layers degradations for improved membrane fuel cell durability. J Power Sources. 2016 Dec 30;336:40–53.

150. Lai YH, Fly GW, Clapham S. In-situ membrane hydration measurement of proton exchange membrane fuel cells. J Power Sources. 2015 Jan 15;274:324–37.

151. Liu H, Coms FD, Zhang J, Gasteiger HA, Laconti AB. Chemical Degradation: Correlations Between Electrolyzer and Fuel Cell Findings. Polymer Electrolyte Fuel Cell Durability [Internet]. 2009 [cited 2025 Jan 25];71–118. Available from: https://link.springer.com/chapter/10.1007/978-0-387-85536-3_5

152. Lapicque F, Belhadj M, Bonnet C, Pauchet J, Thomas Y. A critical review on gas diffusion micro and macroporous layers degradations for improved membrane fuel cell durability. J Power Sources. 2016 Dec 30;336:40–53.

153. Kuhnert E, Heidinger M, Sandu D, Hacker V, Bodner M. Analysis of PEM Water Electrolyzer Failure Due to Induced Hydrogen Crossover in Catalyst-Coated PFSA Membranes. Membranes (Basel) [Internet]. 2023 Mar 1 [cited 2024 Nov 6];13(3):348. Available from: https://www.mdpi.com/2077-0375/13/3/348/htm

154. LaConti AB, Hamdan M, McDonald RC. Mechanisms of membrane degradation. Handbook of Fuel Cells [Internet]. 2010 Dec 15 [cited 2024 Nov 6]; Available from: https://onlinelibrary.wiley.com/doi/full/10.1002/9780470974001.f303055

155. Liu C, Shviro M, Bender G, Gago AS, Morawietz T, Dzara MJ, et al. Degradation Effects at the Porous Transport Layer/Catalyst Layer Interface in Polymer Electrolyte Membrane Water Electrolyzer. J Electrochem Soc [Internet]. 2023 Mar 29 [cited 2025 Feb 19];170(3):034508. Available from: https://iopscience.iop.org/article/10.1149/1945-7111/acc1a5

156. Lim C, Ghassemzadeh L, Van Hove F, Lauritzen M, Kolodziej J, Wang GG, et al. Membrane degradation during combined chemical and mechanical accelerated stress testing of polymer electrolyte fuel cells. J Power Sources. 2014 Jul 1;257:102–10.

157. Kuhnert E, Heidinger M, Sandu D, Hacker V, Bodner M. Analysis of PEM Water Electrolyzer Failure Due to Induced Hydrogen Crossover in Catalyst-Coated PFSA Membranes. Membranes (Basel) [Internet]. 2023 Mar 1 [cited 2025 Feb 19];13(3):348. Available from: https://www.mdpi.com/2077-0375/13/3/348/htm

158. Kobayashi Y, Kosaka K, Yamamoto T, Tachikawa Y, Ito K, Sasaki K. A solid polymer water electrolysis system utilizing natural circulation. Int J Hydrogen Energy. 2014 Oct 2;39(29):16263–74.

159. Jang IY, Kweon OH, Kim KE, Hwang GJ, Moon SB, Kang AS. Covalently cross-linked sulfonated poly(ether ether ketone)/tungstophosphoric acid composite membranes for water electrolysis application. J Power Sources. 2008 Jun 15;181(1):127–34.

160. Pang Y, Duan Y, Li Q, Liu B, Hu X, Liu Q, et al. Immobilized hindered amine radical scavenger for durability enhancement of perfluorosulfonic acid membrane in PEMFCs. J Memb Sci. 2023 Nov 15;686:121999.

161. Huang H, Zeng X, Zhong Z, Fan J, Li H. Low hydrogen permeability and high durability proton exchange membrane with three-dimensional acid-base crosslink structure for water electrolysis. J Memb Sci. 2024 Feb 1;694:122408.

162. Yuan XZ, Shaigan N, Song C, Aujla M, Neburchilov V, Kwan JTH, et al. The porous transport layer in proton exchange membrane water electrolysis: perspectives on a complex component. Sustain Energy Fuels [Internet]. 2022 Apr 12 [cited 2025 Feb 19];6(8):1824–53. Available from: https://pubs.rsc.org/en/content/articlehtml/2022/se/d2se00260d

163. Ito H, Maeda T, Nakano A, Hwang CM, Ishida M, Kato A, et al. Experimental study on porous current collectors of PEM electrolyzers. Int J Hydrogen Energy. 2012 May 1;37(9):7418–28.

164. Weber CC, Wrubel JA, Gubler L, Bender G, De Angelis S, Büchi FN. How the Porous Transport Layer Interface Affects Catalyst Utilization and Performance in Polymer Electrolyte Water Electrolysis. ACS Appl Mater Interfaces [Internet]. 2023 Jul 26 [cited 2025 Feb 20];15(29):34750–63. Available from: https://pubs.acs.org/doi/full/10.1021/acsami.3c04151

165. Kumar SS, Lim H. Recent advances in hydrogen production through proton exchange membrane water electrolysis – a review. Sustain Energy Fuels [Internet]. 2023 Jul 25 [cited 2024 Oct 10];7(15):3560–83. Available from: https://pubs.rsc.org/en/content/articlehtml/2023/se/d3se00336a

166. Rakousky C, Reimer U, Wippermann K, Carmo M, Lueke W, Stolten D. An analysis of degradation phenomena in polymer electrolyte membrane water electrolysis. J Power Sources. 2016 Sep 15;326:120–8.

167. Kang Z, Mo J, Yang G, Li Y, Talley DA, Retterer ST, et al. Thin film surface modifications of thin/tunable liquid/gas diffusion layers for high-efficiency proton exchange membrane electrolyzer cells. Appl Energy. 2017 Nov 15;206:983–90.

168. Mayyas A, Ruth M, Pivovar B, Bender G, Wipke K. Manufacturing Cost Analysis for Proton Exchange Membrane Water Electrolyzers. 2019 [cited 2025 Feb 19]; Available from: https://www.nrel.gov/docs/fy10osti/72740.pdf.

169. Liu C, Carmo M, Bender G, Everwand A, Lickert T, Young JL, et al. Performance enhancement of PEM electrolyzers through iridium-coated titanium porous transport layers. Electrochem commun. 2018 Dec 1;97:96–9.

170. Rakousky C, Keeley GP, Wippermann K, Carmo M, Stolten D. The stability challenge on the pathway to high-current-density polymer electrolyte membrane water electrolyzers. Electrochim Acta. 2018 Jul 10;278:324–31.

171. Kornherr M, Schramm C, Felix Ernst M, - al, Højgaard Jensen S, Knudsen Kaer S, et al. Effect of the IrOx Conductivity on the Anode Electrode/Porous Transport Layer Interfacial Resistance in PEM Water Electrolyzers. J Electrochem Soc [Internet]. 2021 Aug 27 [cited 2025 Feb 19];168(8):084513. Available from:

https://iopscience.iop.org/article/10.1149/1945-7111/ac1eb4

172. Moriau L, Stojanovski K, Jovanovič P, Escalera-López D, Cherevko S, Hodnik N. Towards electrochemical iridium recycling in acidic media: effect of the presence of organic molecules and chloride ions. RSC Adv [Internet]. 2023 Mar 8 [cited 2025 Feb 19];13(12):7980–7. Available from: https://pubs.rsc.org/en/content/articlehtml/2023/ra/d2ra07142h

173. Liu C, Wippermann K, Rasinski M, Suo Y, Shviro M, Carmo M, et al. Constructing a Multifunctional Interface between Membrane and Porous Transport Layer for Water Electrolyzers. ACS Appl Mater Interfaces [Internet]. 2021 Apr 14 [cited 2025 Feb 19];13(14):16182–96. Available from: https://pubs.acs.org/doi/full/10.1021/acsami.0c20690

174. Liu C, Shviro M, Gago AS, Zaccarine SF, Bender G, Gazdzicki P, et al. Exploring the Interface of Skin-Layered Titanium Fibers for Electrochemical Water Splitting. Adv Energy Mater [Internet]. 2021 Feb 1 [cited 2025 Feb 19];11(8):2002926. Available from: https://onlinelibrary.wiley.com/doi/full/10.1002/aenm.202002926

175. Mandal M, Secanell M. Improved polymer electrolyte membrane water electrolyzer performance by using carbon black as a pore former in the anode catalyst layer. J Power Sources. 2022 Sep 1;541:231629.

176. Khajeh-Hosseini-Dalasm N, Sasabe T, Tokumasu T, Pasaogullari U. Effects of polytetrafluoroethylene treatment and compression on gas diffusion layer microstructure using high-resolution X-ray computed tomography. J Power Sources. 2014 Nov 15;266:213–21.

177. Borgardt E, Giesenberg L, Reska M, Müller M, Wippermann K, Langemann M, et al. Impact of clamping pressure and stress relaxation on the performance of different polymer electrolyte membrane water electrolysis cell designs. Int J Hydrogen Energy. 2019 Sep 3;44(42):23556–67.

178. Cruz Ortiz E, van Treel N, Koch S, Vierrath S, Bühler M. The effect of compression on PEM Electrolyzer membrane electrode Assemblies. J Power Sources. 2024 Sep 15;614:235018.

179. Liu J, Yang Y, Kerner F, Schröder D. Unraveling the impact of compression on the performance of porous transport layers in water Electrolyzers. Appl Energy. 2025 Mar 1;381:124982.

180. Liu C, Carmo M, Bender G, Everwand A, Lickert T, Young JL, et al. Performance enhancement of PEM electrolyzers through iridium-coated titanium porous transport layers. Electrochem commun. 2018 Dec 1;97:96–9.

181. Yang G, Mo J, Kang Z, List FA, Green JB, Babu SS, et al. Additive manufactured bipolar plate for high-efficiency hydrogen production in proton exchange membrane electrolyzer cells. Int J Hydrogen Energy. 2017 May 25;42(21):14734–40.

182. Yang G, Mo J, Kang Z, Dohrmann Y, List FA, Green JB, et al. Fully printed and integrated electrolyzer cells with additive manufacturing for high-efficiency water splitting. Appl Energy. 2018 Apr 1;215:202–10.

183. Li H, Nakajima H, Inada A, Ito K. Effect of flow-field pattern and flow configuration on the performance of a polymer-electrolyte-membrane water electrolyzer at high temperature. Int J Hydrogen Energy. 2018 May 3;43(18):8600–10.

184. Liu J, Liu H, Yang Y, Tao Y, Zhao L, Li S, et al. Efficient and Stable Proton Exchange Membrane Water Electrolysis Enabled by Stress Optimization. ACS Cent Sci [Internet]. 2024 [cited 2024 Oct 10]; Available from: https://pubs.acs.org/doi/full/10.1021/acscentsci.4c00037

185. Li Q, Ghadiani H, Jalilvand V, Alam T, Farhat Z, Islam MA. Hydrogen Impact: A Review on Diffusibility, Embrittlement Mechanisms, and Characterization. Materials 2024, Vol 17, Page 965 [Internet]. 2024 Feb 19 [cited 2025 Jan 27];17(4):965. Available from: https://www.mdpi.com/1996-1944/17/4/965/htm

186. Campari A, Ustolin F, Alvaro A, Paltrinieri N. A review on hydrogen embrittlement and risk-based inspection of hydrogen technologies. Int J Hydrogen Energy. 2023 Nov 9;48(90):35316–46.

187. Monjid H. Review of Hydrogen Embrittlement in Metals: Hydrogen Diffusion, Hydrogen Characterization, Hydrogen Embrittlement Mechanism and Prevention | Acta Metallurgica Sinica (English Letters) [Internet]. 2008 [cited 2025 Feb 20]. Available from: https://link.springer.com/article/10.1007/s40195-020-01039-7#Sec4

188. U.S. DEPARTMENT of ENERGY. PEM Electrolyzer Incorporating an Advanced Low-Cost Membrane [Internet]. 2008 [cited 2025 Feb 20]. Available from: https://www.osti.gov/servlets/purl/1091385/

189. He RY, Jiang J, Wang RF, Yue Y, Chen Y, Pan TJ. Anti-corrosion and conductivity of titanium diboride coating on metallic bipolar plates. Corros Sci. 2020 Jul 1;170:108646.

190. Zhao J, Shahgaldi S, Ozden A, Alaefour IE, Li X, Hamdullahpur F. Effect of catalyst deposition on electrode structure, mass transport and performance of polymer electrolyte membrane fuel cells. Appl Energy. 2019 Dec 1;255:113802.

191. Shahgaldi S, Alaefour I, Li X. Impact of manufacturing processes on proton exchange membrane fuel cell performance. Appl Energy. 2018 Sep 1;225:1022–32.

192. Immerz C, Paidar M, Papakonstantinou G, Bensmann B, Bystron T, Vidakovic-Koch T, et al. Effect of the MEA design on the performance of PEMWE single cells with different sizes. J Appl Electrochem [Internet]. 2018 Jun 1 [cited 2024 Oct 10];48(6):701–11. Available from: https://link.springer.com/article/10.1007/s10800-018-1178-2

193. Leonard E, Shum AD, Danilovic N, Capuano C, Ayers KE, Pant LM, et al. Interfacial analysis of a PEM electrolyzer using X-ray computed tomography. Sustain Energy Fuels [Internet]. 2020 Feb 4 [cited 2024 Dec 28];4(2):921–31. Available from: https://pubs.rsc.org/en/content/articlehtml/2020/se/c9se00364a

194. Chen Z, Guo L, Pan L, Yan T, He Z, Li Y, et al. Advances in Oxygen Evolution Electrocatalysts for Proton Exchange Membrane Water Electrolyzers. Adv

Energy Mater [Internet]. 2022 Apr 1 [cited 2024 Dec 28];12(14):2103670. Available from: https://onlinelibrary.wiley.com/doi/full/10.1002/aenm.202103670

195. Holzapfel P, Bühler M, Van Pham C, Hegge F, Böhm T, McLaughlin D, et al. Directly coated membrane electrode assemblies for proton exchange membrane water electrolysis. Electrochem commun. 2020 Jan 1;110:106640.

196. Kang Z, Fan Z, Zhang F, Zhang Z, Tian C, Wang W, et al. Studying Performance and Kinetic Differences between Various Anode Electrodes in Proton Exchange Membrane Water Electrolysis Cell. Materials 2022, Vol 15, Page 7209 [Internet]. 2022 Oct 16 [cited 2024 Oct 10];15(20):7209. Available from: https://www.mdpi.com/1996-1944/15/20/7209/htm

197. Park J, Kang Z, Bender G, Ulsh M, Mauger SA. Roll-to-roll production of catalyst coated membranes for low-temperature electrolyzers. J Power Sources. 2020 Dec 15;479:228819.

198. Zainoodin AM, Tsujiguchi T, Masdar MS, Kamarudin SK, Osaka Y, Kodama A. Performance of a direct formic acid fuel cell fabricated by ultrasonic spraying. Int J Hydrogen Energy. 2018 Mar 22;43(12):6413–20.

199. Holzapfel P, Bühler M, Van Pham C, Hegge F, Böhm T, McLaughlin D, et al. Directly coated membrane electrode assemblies for proton exchange membrane water electrolysis. Electrochem commun. 2020 Jan 1;110:106640.

200. Xu C, Ma L, Li J, Zhao W, Gan Z. Synthesis and characterization of novel high-performance composite electrocatalysts for the oxygen evolution in solid polymer electrolyte (SPE) water electrolysis. Int J Hydrogen Energy. 2012 Feb 1;37(4):2985–92.

201. Minke C, Suermann M, Bensmann B, Hanke-Rauschenbach R. Is iridium demand a potential bottleneck in the realization of large-scale PEM water electrolysis? Int J Hydrogen Energy. 2021 Jul 6;46(46):23581–90.

202. Parry SJ. Abundance and distribution of palladium, platinum, iridium and gold in some oxide minerals. Chem Geol. 1984 Feb 1;43(1–2):115–25.

203. Hubert MA, King LA, Jaramillo TF. Evaluating the Case for Reduced Precious Metal Catalysts in Proton Exchange Membrane Electrolyzers. ACS Energy Lett [Internet]. 2022 Jan 14 [cited 2024 Oct 22];7(1):17–23. Available from: https://pubs.acs.org/doi/full/10.1021/acsenergylett.1c01869

204. Yasutake M, Kawachino D, Noda Z, - al, Bernt EM, Schramm C, et al. Analysis of Voltage Losses in PEM Water Electrolyzers with Low Platinum Group Metal Loadings. J Electrochem Soc [Internet]. 2018 Mar 28 [cited 2024 Oct 22];165(5):F305. Available from: https://iopscience.iop.org/article/10.1149/2.0641805jes

205. Taie Z, Peng X, Kulkarni D, Zenyuk I V., Weber AZ, Hagen C, et al. Pathway to Complete Energy Sector Decarbonization with Available Iridium Resources using Ultralow Loaded Water Electrolyzers. ACS Appl Mater Interfaces [Internet]. 2020 Nov 25 [cited 2024 Oct 22];12(47):52701–12. Available from: https://pubs.acs.org/doi/full/10.1021/acsami.0c15687

206. Ferner KJ, Litster S. Composite Anode for PEM Water Electrolyzers: Lowering Iridium Loadings and Reducing Material Costs with a Conductive Additive. ACS Appl Energy Mater [Internet]. 2024 Sep 23 [cited 2025 Jan 30];7:8135. Available from: https://pubs.acs.org/doi/full/10.1021/acsaem.4c01866

207. Yuan S, Zhao C, Li H, Shen S, Yan X, Zhang J. Rational electrode design for low-cost proton exchange membrane water electrolyzers. Cell Rep Phys Sci. 2024 Mar 20;5(3):101880.

208. Hegge F, Lombeck F, Cruz Ortiz E, Bohn L, Von Holst M, Kroschel M, et al. Efficient and Stable Low Iridium Loaded Anodes for PEM Water Electrolysis Made Possible by Nanofiber Interlayers. ACS Appl Energy Mater [Internet]. 2020 Sep 28 [cited 2024 Nov 20];3(9):8276–84. Available from: https://pubs.acs.org/doi/full/10.1021/acsaem.0c00735

209. Rozain C, Mayousse E, Guillet N, Millet P. Influence of iridium oxide loadings on the performance of PEM water electrolysis cells: Part I–Pure IrO2-based anodes. Appl Catal B. 2016 Mar 1;182:153–60.

210. Siracusano S, Baglio V, Van Dijk N, Merlo L, Aricò AS. Enhanced performance and durability of low catalyst loading PEM water electrolyser based on a short-side chain perfluorosulfonic ionomer. Appl Energy. 2017 Apr 15;192:477–89.

211. Alia SM, Reeves KS, Baxter JS, Cullen DA. The Impact of Ink and Spray Variables on Catalyst Layer Properties, Electrolyzer Performance, and Electrolyzer Durability. J Electrochem Soc [Internet]. 2020 Nov 18 [cited 2025 Jan 31];167(14):144512. Available from: https://iopscience.iop.org/article/10.1149/1945-7111/abc746

212. Taie Z, Peng X, Kulkarni D, Zenyuk I V., Weber AZ, Hagen C, et al. Pathway to Complete Energy Sector Decarbonization with Available Iridium Resources using Ultralow Loaded Water Electrolyzers. ACS Appl Mater Interfaces [Internet]. 2020 Nov 25 [cited 2025 Jan 30];12(47):52701–12. Available from: https://pubs.acs.org/doi/full/10.1021/acsami.0c15687

213. Ferner KJ, Litster S. Composite Anode for PEM Water Electrolyzers: Lowering Iridium Loadings and Reducing Material Costs with a Conductive Additive. ACS Appl Energy Mater [Internet]. 2024 Sep 23 [cited 2024 Nov 24]; Available from: https://pubs.acs.org/doi/full/10.1021/acsaem.4c01866

214. Kwan JTH, Daniel L, Wang WJ, Yao KLW, Shehata DS, Wilkinson DP. New multi-functional catalyst coated membrane structure for improved water electrolysis. J Power Sources. 2024 Jan 30;591:233872.

215. Hansen KU, Lee A, Jiao F. Enabling low-IrO2 proton exchange membrane water electrolysis via microporous layer-supported catalyst-coated membranes. Chem Catalysis [Internet]. 2024 Jul 18 [cited 2024 Nov 24];4(7). Available from: http://www.cell.com/article/S2667109324001945/fulltext

216. Tian B, Li Y, Liu Y, Ning F, Dan X, Wen Q, et al. Ordered Membrane Electrode Assembly with Drastically Enhanced Proton and Mass Transport for Proton Exchange Membrane Water Electrolysis. Nano Lett [Internet]. 2023 Jul 26 [cited

2025 Jan 30];23(14):6474–81. Available from: https://pubs.acs.org/doi/full/10.1021/acs.nanolett.3c01331

217. Pham C Van, Bühler M, Knöppel J, Bierling M, Seeberger D, Escalera-López D, et al. IrO2 coated TiO2 core-shell microparticles advance performance of low loading proton exchange membrane water electrolyzers. Appl Catal B. 2020 Jul 15;269:118762.

218. Shi W, Shen T, Xing C, Sun K, Yan Q, Niu W, et al. Ultrastable supported oxygen evolution electrocatalyst formed by ripening-induced embedding. Science (1979) [Internet]. 2025 Feb 14 [cited 2025 Feb 19];387(6735):791–6. Available from: https://www.science.org/doi/10.1126/science.adr3149

219. Rozain C, Mayousse E, Guillet N, Millet P. Influence of iridium oxide loadings on the performance of PEM water electrolysis cells: Part II – Advanced oxygen electrodes. Appl Catal B. 2016 Mar 1;182:123–31.

220. Huang M, Tao J, Ma L, Zhuang X, Wang H, Bing Tao H, et al. Is it stable for the asymmetric pressure operation of PEM water Electrolyzer? Chemical Engineering Journal. 2024 Oct 15;498:155209.

221. Huang M, Tao J, Ma L, Zhuang X, Wang H, Bing Tao H, et al. Is it stable for the asymmetric pressure operation of PEM water Electrolyzer? Chemical Engineering Journal. 2024 Oct 15;498:155209.

222. Hsu WY, Gierke TD. Ion transport and clustering in nafion perfluorinated membranes. J Memb Sci. 1983 Feb 1;13(3):307–26.

223. Bühler M, Hegge F, Holzapfel P, Bierling M, Suermann M, Vierrath S, et al. Optimization of anodic porous transport electrodes for proton exchange membrane water electrolyzers. J Mater Chem A Mater [Internet]. 2019 Dec 3 [cited 2025 Jan 2];7(47):26984–95. Available from: https://pubs.rsc.org/en/content/articlehtml/2019/ta/c9ta08396k

224. Kim YS, Welch CF, Hjelm RP, Mack NH, Labouriau A, Orler EB. Origin of toughness in dispersion-cast Nafion membranes. Macromolecules [Internet]. 2015 Apr 14 [cited 2025 May 10];48(7):2161–72. Available from: /doi/pdf/10.1021/ma502538k

225. Mardle P, Thirunavukkarasu G, Guan S, Chiu YL, Du S. Comparative Study of PtNi Nanowire Array Electrodes toward Oxygen Reduction Reaction by Half-Cell Measurement and PEMFC Test. ACS Appl Mater Interfaces [Internet]. 2020 Sep 23 [cited 2024 Oct 23];12(38):42832–41. Available from: https://pubs.acs.org/doi/full/10.1021/acsami.0c11531

226. Garsany Y, Baturina OA, Swider-Lyons KE, Kocha SS. Experimental methods for quantifying the activity of platinum electrocatalysts for the oxygen reduction reaction. Anal Chem [Internet]. 2010 Aug 1 [cited 2024 Oct 19];82(15):6321–8. Available from: https://pubs.acs.org/doi/full/10.1021/ac100306c

227. Bender G, Carmo M, Smolinka T, Gago A, Danilovic N, Mueller M, et al. Initial approaches in benchmarking and round robin testing for proton exchange membrane water electrolyzers. Int J Hydrogen Energy. 2019 Apr 5;44(18):9174–

87.

228. Lickert T, Fischer S, Young JL, Klose S, Franzetti I, Hahn D, et al. Advances in benchmarking and round robin testing for PEM water electrolysis: Reference protocol and hardware. Appl Energy. 2023 Dec 15;352:121898.

229. Bazarah A, Majlan EH, Husaini T, Zainoodin AM, Alshami I, Goh J, et al. Factors influencing the performance and durability of polymer electrolyte membrane water electrolyzer: A review. Int J Hydrogen Energy. 2022 Oct 15;47(85):35976–89.

230. Mason TJ, Millichamp J, Shearing PR, Brett DJL. A study of the effect of compression on the performance of polymer electrolyte fuel cells using electrochemical impedance spectroscopy and dimensional change analysis. Int J Hydrogen Energy. 2013 Jun 18;38(18):7414–22.

231. Jo M, Cho HS, Na Y. Comparative Analysis of Circular and Square End Plates for a Highly Pressurized Proton Exchange Membrane Water Electrolysis Stack. Applied Sciences 2020, Vol 10, Page 6315 [Internet]. 2020 Sep 10 [cited 2024 Nov 11];10(18):6315. Available from: https://www.mdpi.com/2076-3417/10/18/6315/htm

232. Moreno Soriano R, Rojas N, Nieto E, de Guadalupe González-Huerta R, Sandoval-Pineda JM. Influence of the gasket materials on the clamping pressure distribution in a PEM water electrolyzer: Bolt torques and operation mode in pre-conditioning. Int J Hydrogen Energy. 2021 Jul 26;46(51):25944–53.

233. Teuku H, Alshami I, Goh J, Masdar MS, Loh KS. Review on bipolar plates for low-temperature polymer electrolyte membrane water electrolyzer. Int J Energy Res [Internet]. 2021 Dec 1 [cited 2024 Nov 9];45(15):20583–600. Available from: https://onlinelibrary.wiley.com/doi/full/10.1002/er.7182

234. Majasan JO, Cho JIS, Dedigama I, Tsaoulidis D, Shearing P, Brett DJL. Two-phase flow behaviour and performance of polymer electrolyte membrane electrolysers: Electrochemical and optical characterisation. Int J Hydrogen Energy. 2018 Aug 16;43(33):15659–72.

235. Selamet OF, Pasaogullari U, Spernjak D, Hussey DS, Jacobson DL, Mat M. In Situ Two-Phase Flow Investigation of Proton Exchange Membrane (PEM) Electrolyzer by Simultaneous Optical and Neutron Imaging. ECS Trans [Internet]. 2011 Oct 4 [cited 2024 Nov 9];41(1):349–62. Available from: https://iopscience.iop.org/article/10.1149/1.3635568

236. Tsotridis Georgios, Pilenga A. EU harmonised protocols for testing of low temperature water electrolysers. Publications Office of the European Union [Internet]. 2021 Jul 26 [cited 2024 Nov 9];171. Available from: https://publications.jrc.ec.europa.eu/repository/handle/JRC122565

237. Mo J, Steen SM, Zhang FY, Toops TJ, Brady MP, Green JB. Electrochemical investigation of stainless steel corrosion in a proton exchange membrane electrolyzer cell. Int J Hydrogen Energy. 2015 Sep 28;40(36):12506–11.

238. Toops TJ, Brady MP, Zhang FY, Meyer HM, Ayers K, Roemer A, et al. Evaluation

of nitrided titanium separator plates for proton exchange membrane electrolyzer cells. J Power Sources. 2014 Dec 25;272:954–60.

239. Grigoriev SA, Millet P, Volobuev SA, Fateev VN. Optimization of porous current collectors for PEM water electrolysers. Int J Hydrogen Energy. 2009 Jun 1;34(11):4968–73.

240. Ito K, Sakaguchi T, Tsuchiya Y, Inada A, Nakajima H, Saito R. Gas Crossover Suppression by Controlling Wettability of Cathode Current Collector. ECS Trans [Internet]. 2016 Aug 22 [cited 2024 Nov 10];75(14):1107–12. Available from: https://iopscience.iop.org/article/10.1149/07514.1107ecst

241. Xu C, Wang J, Wang J, Yang K, Li G, Gao W, et al. Structural optimization study on porous transport layers of sintered titanium for polymer electrolyte membrane electrolyzers. Appl Energy [Internet]. 2024 Mar 1 [cited 2025 May 12];357:122541. Available from: https://www.sciencedirect.com/science/article/abs/pii/S0306261923019050

242. Hasa B, Aryal UR, Higashi S, Tolouei NE, Lang JT, Erb B, et al. Porous transport layer influence on overpotentials in PEM water electrolysis at low anode catalyst loadings. Applied Catalysis B: Environment and Energy [Internet]. 2025 Feb 1 [cited 2025 May 12];361:124616. Available from: https://linkinghub.elsevier.com/retrieve/pii/S0926337324009305

243. Giesbrecht PK, Freund MS. Operando Three-Electrode Analysis of Nafion-Based Polymer Electrolyte Membrane Water Electrolyzers - Thermodynamic Relations. ACS Appl Energy Mater [Internet]. 2024 Sep 9 [cited 2024 Nov 10];7(17):7272–84. Available from: https://pubs.acs.org/doi/full/10.1021/acsaem.4c01289

244. Kim S, Hyun K, Kwon Y. Effects of voltage stress conditions on degradation of iridium-based catalysts occurring during high-frequency operation of PEM water electrolysis. Chemical Engineering Journal. 2024 Sep 15;496:154288.

245. Lettenmeier P, Wang R, Abouatallah R, Helmly S, Morawietz T, Hiesgen R, et al. Durable Membrane Electrode Assemblies for Proton Exchange Membrane Electrolyzer Systems Operating at High Current Densities. Electrochim Acta. 2016 Aug 20;210:502–11.

246. Cherevko S, Geiger S, Kasian O, Mingers A, Mayrhofer KJJ. Oxygen evolution activity and stability of iridium in acidic media. Part 2. – Electrochemically grown hydrous iridium oxide. Journal of Electroanalytical Chemistry [Internet]. 2016 Aug 1 [cited 2025 May 10];774:102–10. Available from: https://www.sciencedirect.com/science/article/pii/S1572665716302405?via%3Dihub

247. Bender G, Carmo M, Smolinka T, Gago A, Danilovic N, Mueller M, et al. Initial approaches in benchmarking and round robin testing for proton exchange membrane water electrolyzers. Int J Hydrogen Energy. 2019 Apr 5;44(18):9174–87.

248. Alia SM, Stariha S, Borup RL. Electrolyzer Durability at Low Catalyst Loading

and with Dynamic Operation. J Electrochem Soc [Internet]. 2019 Oct 24 [cited 2024 Nov 10];166(15):F1164–72. Available from: https://iopscience.iop.org/article/10.1149/2.0231915jes

249. Padgett E, Adesso A, Yu H, Wrubel J, Bender G, Pivovar B, et al. Performance Losses and Current-Driven Recovery from Cation Contaminants in PEM Water Electrolysis. J Electrochem Soc [Internet]. 2024 Jun 27 [cited 2024 Nov 11];171(6):064510. Available from: https://iopscience.iop.org/article/10.1149/1945-7111/ad576b

250. Cho YH, Kim J, Yoo SJ, Jeon TY, Ahn M, Jung N, et al. Enhancement of polymer electrolyte membrane fuel cell performance by boiling a membrane electrode assembly in sulfuric acid solution. J Power Sources. 2010 Sep 15;195(18):5952–6.

251. Hjuler HA, Aili D, Jensen JO. High temperature polymer electrolyte membrane fuel cells: Approaches, status, and perspectives. High Temperature Polymer Electrolyte Membrane Fuel Cells: Approaches, Status, and Perspectives. 2016 Jan 1;1–545.

252. Zhao J, Guo H, Xing Y, Ping S, Lin W, Yang Y, et al. A review on the sealing structure and materials of fuel-cell stacks. Clean Energy [Internet]. 2023 Feb 1 [cited 2024 Nov 12];7(1):59–69. Available from: https://dx.doi.org/10.1093/ce/zkac096

253. Khandavalli S, Park JH, Kariuki NN, Myers DJ, Stickel JJ, Hurst K, et al. Rheological Investigation on the Microstructure of Fuel Cell Catalyst Inks. ACS Appl Mater Interfaces [Internet]. 2018 Dec 19 [cited 2024 Dec 26];10(50):43610–22. Available from: https://pubs.acs.org/doi/abs/10.1021/acsami.8b15039

254. Sasabe T, Iida K, Sakai K, Uemura S, Shinohara K, Hirai S. Impact of Solvent Decomposition on Dispersion Structure of PEFC Catalyst Ink. ECS Trans [Internet]. 2021 Oct 1 [cited 2024 Dec 26];104(8):191–6. Available from: https://iopscience.iop.org/article/10.1149/10408.0191ecst

255. Wang C, Cheng X, Yan X, Shen S, Ke C, Wei G, et al. Respective Influence of Ionomer Content on Local and Bulk Oxygen Transport Resistance in the Catalyst Layer of PEMFCs with Low Pt Loading. J Electrochem Soc [Internet]. 2019 Feb 23 [cited 2024 Dec 26];166(4):F239–45. Available from: https://iopscience.iop.org/article/10.1149/2.0401904jes

256. Yoshimune W, Harada M. Impact of Nonadsorbed Ionomer on Viscosity of Catalyst Inks for Polymer Electrolyte Fuel Cells. Bull Chem Soc Jpn [Internet]. 2020 Feb 15 [cited 2024 Dec 26];93(2):302–7. Available from: https://dx.doi.org/10.1246/bcsj.20190321

257. Hoffmann E, Zhang S, Thoma M, Damm C, Peukert W. Formulation of carbon black-ionomer dispersions for thin film formation in fuel cells. Particuology. 2019 Jun 1;44:7–21.

258. Sharma R, Andersen SM. Zoom in Catalyst/Ionomer Interface in Polymer Electrolyte Membrane Fuel Cell Electrodes: Impact of Catalyst/Ionomer

Dispersion Media/Solvent. ACS Appl Mater Interfaces [Internet]. 2018 Nov 7 [cited 2024 Dec 26];10(44):38125–33. Available from: https://pubs.acs.org/doi/abs/10.1021/acsami.8b14622

259. Liu H, Ney L, Zamel N, Li X. Effect of Catalyst Ink and Formation Process on the Multiscale Structure of Catalyst Layers in PEM Fuel Cells. Applied Sciences 2022, Vol 12, Page 3776 [Internet]. 2022 Apr 8 [cited 2024 Dec 26];12(8):3776. Available from: https://www.mdpi.com/2076-3417/12/8/3776/htm

260. Andersen SM, Dhiman R, Larsen MJ, Skou E. Importance of electrode hot-pressing conditions for the catalyst performance of proton exchange membrane fuel cells. Appl Catal B. 2015 Aug 1;172–173:82–90.

261. Leader JO, Walluk MR, Waller MG, Trabold TA. Optimizing The Hot-Press Procedure Of High-Temperature Proton Exchange Membrane Fuel Cells For Adhesion Strength And Conductivity. ECS Meeting Abstracts [Internet]. 2022 Jul 7 [cited 2025 Feb 24];MA2022-01(37):1644. Available from: https://iopscience.iop.org/article/10.1149/MA2022-01371644mtgabs

262. Benítez R, Chaparro AM, Daza L. Electrochemical characterisation of Pt/C suspensions for the reduction of oxygen. J Power Sources. 2005 Oct 10;151(1–2):2–10.

263. Meyer Q, Mansor N, Iacoviello F, Cullen PL, Jervis R, Finegan D, et al. Investigation of Hot Pressed Membrane Electrode Assemblies using X-ray Computed Tomography. [cited 2025 Feb 24]; Available from: www.ucl.ac.uk/electrochemical-innovation-lab

264. Zhang J, Yin GP, Wang ZB, Lai QZ, Cai K Di. Effects of hot pressing conditions on the performances of MEAs for direct methanol fuel cells. J Power Sources. 2007 Feb 25;165(1):73–81.

265. Park J, Kang Z, Bender G, Ulsh M, Mauger SA. Roll-to-roll production of catalyst coated membranes for low-temperature electrolyzers. J Power Sources. 2020 Dec 15;479:228819.

266. Technical Targets for Proton Exchange Membrane Electrolysis | Department of Energy [Internet]. [cited 2025 Feb 24]. Available from: https://www.energy.gov/eere/fuelcells/technical-targets-proton-exchange-membrane-electrolysis

267. Andrenacci S, Choi Y, Raka Y, Talic B, Colmenares-Rausseo L. Electrolysers towards EU MAWP 2023 targets and beyond. [cited 2025 Feb 24]; Available from: https://zenodo.org/records/7144913

268. Electrolyzer MEA - 3 Layer [Internet]. [cited 2025 Feb 24]. Available from: https://www.fuelcellstore.com/electrolyzer-ccm

269. Hancke R, Bujlo P, Holm T, Ulleberg Ø. High-pressure PEM water electrolyser performance up to 180 bar differential pressure. J Power Sources. 2024 May 1;601:234271.

270. Gasteiger HA, Kocha SS, Sompalli B, Wagner FT. Activity benchmarks and

requirements for Pt, Pt-alloy, and non-Pt oxygen reduction catalysts for PEMFCs. Appl Catal B. 2005 Mar 10;56(1–2):9–35.

271. Cheng X, Shen Z, Jiao L, Yang L, Wang X, Wu Q, et al. Tuning metal catalysts via nitrogen-doped nanocarbons for energy chemistry: From metal nanoparticles to single metal sites. EnergyChem. 2021 Nov 1;3(6):100066.

272. Xu G, Du X, Ding W, Ma S, Zhang L, Li J, et al. Nano-Pd loaded composite membrane for reduced hydrogen crossover in proton exchange membrane water electrolysis via recasting method. Renew Energy. 2024 Nov 1;235:121285.

273. Weiß A, Siebel A, Bernt M, Shen TH, Tileli V, Gasteiger HA. Impact of Intermittent Operation on Lifetime and Performance of a PEM Water Electrolyzer. J Electrochem Soc [Internet]. 2019 Apr 29 [cited 2024 Nov 29];166(8):F487–97. Available from: https://iopscience.iop.org/article/10.1149/2.0421908jes

274. Kuhnert E, Hacker V, Bodner M. A Review of Accelerated Stress Tests for Enhancing MEA Durability in PEM Water Electrolysis Cells. Int J Energy Res [Internet]. 2023 Jan 1 [cited 2024 Nov 29];2023(1):3183108. Available from: https://onlinelibrary.wiley.com/doi/full/10.1155/2023/3183108

275. Rakousky C, Keeley GP, Wippermann K, Carmo M, Stolten D. The stability challenge on the pathway to high-current-density polymer electrolyte membrane water electrolyzers. Electrochim Acta. 2018 Jul 10;278:324–31.

276. Alia SM, Stariha S, Borup RL. Electrolyzer Durability at Low Catalyst Loading and with Dynamic Operation. J Electrochem Soc [Internet]. 2019 Oct 24 [cited 2024 Dec 24];166(15):F1164–72. Available from: https://iopscience.iop.org/article/10.1149/2.0231915jes

277. Siracusano S, Hodnik N, Jovanovic P, Ruiz-Zepeda F, Šala M, Baglio V, et al. New insights into the stability of a high performance nanostructured catalyst for sustainable water electrolysis. Nano Energy. 2017 Oct 1;40:618–32.

278. Grigoriev SA, Dzhus KA, Bessarabov DG, Millet P. Failure of PEM water electrolysis cells: Case study involving anode dissolution and membrane thinning. Int J Hydrogen Energy. 2014 Dec 3;39(35):20440–6.